CHALMERS

Influence of the processing route on oxide transformation in austenitic Fe-19Mn-18Cr-C-N PM steel

Bachelor Thesis 2012

Department of Materials and Manufacturing Technology
CHALMERS UNIVERSITY OF TECHNOLOGY
Gothenburg, Sweden, 2012

by

Maximilian Walter

Gothenburg, 2012

Performed at: Department of Materials and Manufacturing Technology
Chalmers University of Technology
SE-41296 Gothenburg

Examiner and
Supervisor: Eduard Hryha Ph.D.
Department of Materials and Manufacturing Technology
Chalmers University of Technology
SE-41296 Gothenburg

Contents

Nomenclature

Symbols

E_B	characteristic binding energy	[eV]
E_K	kinetic energy	[eV]
G	Gibbs free energy	[J]
h	Planck constant	[Js]
K	equilibrium constant	
R	general gas constant	[J/(mol · K)]
t	time	[s]
T	temperature	[°C]
T_{Sol}	solidus temperature	[°C]
T_{Liq}	liquidus temperature	[°C]
W_S	spectrometer work function	[J]
X_S	solidus composition	
X_L	liquidus composition	

α	ferritic phase
γ	austenitic phase
ϑ	frequency

Acronyms

at.-%	Atom-%
EDX	Energy Dispersive X-Ray Analysis
ESCA	Electron Spectroscopy of Chemical Analysis
HNS	High Nitrogen Steels
HIP	Hot Isostatic Pressing
LWT	Lehrstuhl Werkstofftechnik Ruhr-Universität Bochum
mass.-%	Mass-%
PM	Powder Metallurgy
PREN	Pitting Resistance Equivalent Number
SEM	Scanning Electron Microscope
SLPS	Super Solidus Liquid Phase Sintering
UHV	Ultra High Vacuum
vol.-%	Volume-%
XPS	X-ray Photoelectron Spectroscopy

Chapter 1

Abstract

The present work deals with the analysis of oxide state in the Fe-19Mn-18Cr-C-N (X40MnCrN19-18) powder steel in densified state by surface sensitive analysis techniques.
The steel powder was densified by different powder metallurgical manufacturing techniques (hot isostatic pressing (HIP), supersolidus liquid phase sintering (SLPS) and solid state sintering (SSS)). Further the surface composition was studied using X-ray photoelectron spectroscopy, scanning electron microscopy and energy dispersive X-ray analysis. This was done to gain information about the included oxides in the densified powder mass and their state depending on the different applied consolidation techniques.
The results are discussed considering former investigations which analyzed the loose powder. Hence the development of the oxides is related to the initial composition of the powder surface. The results show large differences in consolidation between the different techniques related to the different thermodynamic conditions during consolidation and therefore oxide states of the produced samples. The samples produced by HIP and SLPS show the best densification and in contrast the sintered samples are much more porous even though a vacuum dwelling step during heating stage was applied.
Focusing on oxides the outcome is that highly thermodynamically stable mixed Mn-Si-Cr-O-oxides exist in the HIP and SLPS powder masses and that their shape and size depends on the applied consolidation principle.

The sintered samples contain a much higher amount of oxides with lower thermodynamic stability. Only the dwelling at 700°C under technical vacuum showed an improvement of the oxide reduction for solid state sintering and it is concluded that a dwelling temperature should not overstep this temperature.
Furthermore it is estimated that HIP and SLPS consolidation overcome the initial state of the powder very well, which is not achieved by solid state sintering.

Keywords: PM steel, austenitic HNS, high manganese steel, XPS, fracture surface oxides, manufacturing techniques

Chapter 2

Introduction

This thesis deals with the fracture surface analysis of Fe-19Mn-18Cr-C-N (X40MnCrN19-18) steel powder in densified state. The Fe-19Mn-18Cr-C-N steel is an austenitic stainless steel of superior strength based on the C+N alloying concept developed by the Chair of Materials Technology (LWT) at the Ruhr-University Bochum. In consequence of the combination of carbon and nitrogen in high interstitial amount the steel features a high toughness and ductility together with superior strength. Therefore the C+N concept enables the strengthening of an austenitic steel while keeping a high toughness.
By the reason that the manufacturing of high nitrogen steels (HNS) via conventional casting techniques has proved itself as very difficult, because of low solubility of N in the molten state, the powder metallurgical manufacturing of the Fe-19Mn-18Cr-C-N steel is applied and further investigated.

Thus, in this thesis the gas-atomized prealloyed steel powder has been densified by different powder metallurgical techniques like hot isostatic pressing (HIP), supersolidus liquid phase sintering (SLPS) and solid state sintering (SSS). The produced compacts are further analyzed and compared to each other with focus on vital properties for the densification.

A special attention was focused on the distribution and chemistry of oxide phases resulting from different applied PM processing routes because former investigations of the same material revealed a significant influence of oxides in the bulk material on the mechanical properties of the densified parts.

Thus, different manufacturing techniques, atmospheres and annealing steps have been combined to point out how the oxide distribution and hence the solid state densification mechanisms can be affected by the manufacturing parameters, to find an appropriate way to produce the Fe-19Mn-18Cr-C-N steel via powder metallurgical techniques. Further, the steel powder shall be alloyed with nitrogen during consolidation as well. This is required to ensure an aspired nitrogen content and the ideal C+N ratio and makes it necessary to perform consolidation at least partly under increased nitrogen partial pressure.
Furthermore, the aim of this work is to comprehend the surface processes that take place depending on manufacturing of this high alloyed steel powder and especially the oxide distribution, transformation and reduction.
For this reason surface sensitive analysis techniques like X-ray photoelectron spectroscopy and high resolution electron microscopy combined with EDX analysis were applied to investigate fracture surfaces of the sintered parts. To achieve information about the interior composition and morphology of the different samples.

These investigations are necessary, because the production of the Fe-19Mn-18Cr-C-N steel via powder metallurgy didn't succeed until now. Due to the fact that the investigated steel has a high oxidation tendency and stable oxides form on its surface during densification the consolidation mechanism is very complex and influenced by many parameters.

Chapter 3

Theoretical background

3.1. High nitrogen steels

Austenitic steels containing nitrogen include several fields of application. They can be found as standard CrNi stainless steels, high strength stainless steels, low cost stainless steels, steels of high corrosion resistance and in diverse other applications due to their wide range of properties [1]. The similarity of all those steels is the use of a high amount of nitrogen in their composition and an adaption of their alloy concept due to the higher nitrogen content.

Considering austenitic steels, nitrogen and of course carbon condition a higher strength by increasing solid solution hardening and further stabilize the austenite strongly. Additionally nitrogen increases the corrosion resistance and delays the formation of precipitates, therefore allows a higher content of interstitial atoms in solid solution [2].

Nevertheless the disadvantage of a high nitrogen steel is the complicated manufacturing. High nitrogen steels (HNS) usually have to be manufactured using complex and expensive pressurized melting techniques because of the low N solubility in the melt. In this case nitrogen behaves contrarily to carbon while the solubility of carbon in the melt is very high the solubility of nitrogen is almost zero. This changes in solid state. Considering the austenite the N solubility arises with increasing temperature strongly and further outrages the C solubility, but in contrast the decrease of the solubility in ferrite is even higher for nitrogen than for carbon too [1].

Thus, nitrogen is mainly used in the austenite which results in austenitic and martensitic high nitrogen steels [3].

The solubility of nitrogen furthermore depends on several parameters which are the temperature, the nitrogen partial pressure and the alloy composition.
Higher nitrogen partial pressure increases the nitrogen solubility in the steel matrix which is described by the Sieverts-law [3.1] and used in pressurized casting.

$$[N\%] = K \cdot \sqrt{p_{N_2}} \tag{3.1}$$

The Sieverts'law describes the equilibrium between N_2-pressure and atomically dissolved N. It's transferable for engineering alloys till 0.8% dissolved nitrogen, but strongly affected by the presence of other elements like chromium [2].
A more easy and common way to increase the nitrogen solubility is to adapt the alloy composition. The use of components which decrease the nitrogen activity leads to a higher solubility of nitrogen. With ascending influence these elements are W, Mo, Mn, Cr, Nb, V and Ti. The highest increase of the N solubility is given by Nb, V and Ti but their use is not common because they are strong nitride formers. In opposite Cu, Co, Ni, Al and Si increase the N activity and so descend the solubility. Thus, in general the combination of Cr, Mn, N and C is used. Mn has to be pointed out notably because it replaces nickel in standard austenites with lower costs and better influence on the nitrogen solubility [1]. These steels can further be melted without increasing nitrogen pressure and therefore are much cheaper in production.

Recent investigations showed [4, 5], that even better mechanical properties were obtained if carbon was added to austenitic CrMnN steels. Their alloying composition follows the C+N concept, which has been developed at the Chair of Materials Technology (LWT) at the Ruhr-Universität-Bochum. Using the C+N concept the strength of austenitic steels is improved about three times compared to a standard CrNi stainless steels (X5CrNi18-10) without entailing lower ductility [6]. Thus a high strength and yet ductile behavior is reached by the combination of nitrogen and carbon. This behavior is based on the exceptionally high concentration of free electrons in the C+N austenite because these support the metallic character of interatomic bondings.
The number of free electrons in general determines the character of an interatomic bonding.
If their content is low the bond type is rather covalent and thus brittle. A high content of free electrons strengthens the metallic character which is ductile and so the toughness is improved [2].

Researches in this topic resulted in the conclusion that nitrogen increases the number of free electrons significantly while just carbon has no noteworthy influence on their number [7]. Furthermore the concentration of free electrons is increased ascending from C over N to C+N. C+N increases the number of free electrons the most and further shifts the maximum of the free electron concentration to higher interstitial content [6]. Therefore by using the C+N concept the strength of an austenitic steel is improved while in parallel the ductility remains high, even for an high content of interstitial elements.

3.2. Powder metallurgy

3.2.1. Introduction

Powder metallurgy (PM) is the umbrella term for several master forming techniques that produce metallic products out of an disperse state. It's mainly used for near-net-shaped products or products with superior properties and has become widely accepted as a predominant way of producing high-quality products for diverse applications.

The principle of all PM methods is to densify the powderous material by using temperatures below the melting point and in some cases additionally pressure. This is done in many different ways by techniques like solid state sintering, liquid phase sintering, hot and cold isostatic pressing, powder forging, metal injection molding etc. [8].

Main benefits of the PM route compared to other manufacturing techniques are the high exploitation of the raw material, which is usually about 95%, less machining and the lower energy need of conventional sintering processes. Special PM-products also focus on the improved microstructure and properties and accept the loss of energy advantage because of this [9].

At this point it is necessary to border the conventional PM manufacturing from the PM manufacturing of high-alloyed steel powders. Conventional PM is more effective than casting and machining. It uses mixed elementary powders and/ or ferrous alloys which are produced by water atomization. These powders are in a first step annealed in reducing atmosphere and in a second step heated up to $\frac{2}{3}$ till $\frac{4}{5}$ of the solidus temperature to sinter to the net shape. Their entire manufacturing needs less energy and costs, which is mostly because of less machining, and is thus advantageous.

PM of high-alloyed powders in opposite uses the more expensive gas atomization and more expensive and energy consuming manufacturing techniques like hot isostatic pressing.

It focuses on high density and unequilibrium microstructures and thus achieves special results in significant advantages.
Therefore the production effort is much higher, but the properties improved as well.
The work in this thesis considers manufacturing of PM parts focused on higher properties and an improved microstructure, therefore this energy handicap is accepted.
Another focus is on the production of nearly full density PM products. Ordinary press-and-sinter processes leave a porosity of 5-10% the approach in this thesis is focused on nearly full density (solid state sintering, supersolidus liquid phase sintering and hot isostatic pressing) [8].
Furthermore PM-production always avoids casting defects as well as macro segregations in the finished product. By this it promises superior mechanical properties compared to casting [8].
In the field of high N-containing steels one has to consider one more substantial benefit, the possibility of solid state alloying of the powder material through gas phase during the sintering process. Therefore, the nitrogen content of the product sintered under nitrogen containing atmosphere can be adjusted by chosing an appropriate nitrogen partial pressure and the reached N-content can extend the N-content of cast products

3.2.2. Manufacturing of steel powders

Nowadays there are several commercial routes for the production of metal powders, which consist of powder fabrication by chemical, mechanical or atomization techniques [9].
For the production of prealloyed steel powders the dominant fabrication route is the water or gas atomization. These production methods further differ from each other, for example in the shape of the particles, the productivity, oxidation potential etc. [8].
Figure 3. 1 shows a drawing of the atomization principle for water and gas atomization. During the atomization process, high pressure water or gas jets impact the molten metal stream and disintegrate it into droplets that are in turn rapidly solified [8].
The pressure and the media, that are used to atomize the liquid metal stream, determine the possible cooling rate of the metal drops and by this define the shape and the fineness of microstructure of the produced powder particles. It's important to point out, that the cooling rate of PM powders despite of all always overtops the casting cooling rate [9].

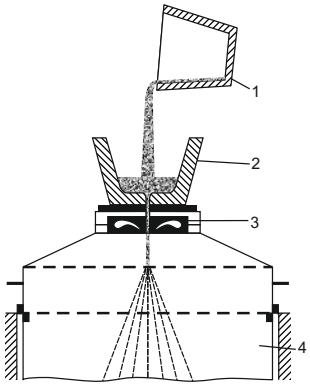

Figure 3.1.: Atomization principle for prealloyed steel powder (1.prealloyed melt; 2.gathering cup; 3.gas or water jets; 4.melt droplets)

The cooling rate for water atomization lies in general between 10^4-10^8 K/s and therefore the particles have an irregular and rough shape [8]. Figure 3.2 depicts the appearance of a water atomized powder particle and compares it to a spherical, gas atomized particle.

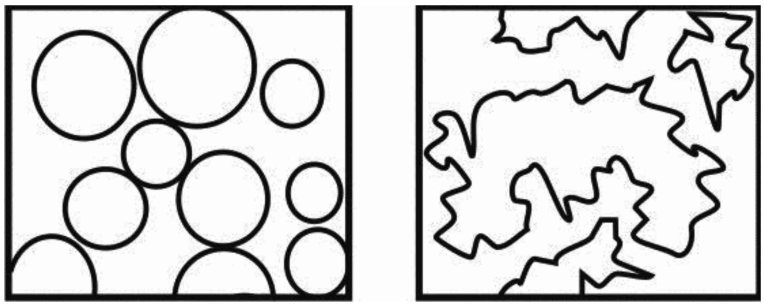

Figure 3.2.: Comparison of spherical, gas atomized particles and irregular, water atomized particles

Due to their shape water atomized particles have some advantages over gas atomized powder particles. The irregular shape leads to a larger surface area and because the driving force of the sintering process is related to the surface energy the sinterability of water atomized powders is better compared to spherical particles [10]. Additionally the compressibility of irregular particles is much better than those of spherical particals. But on the other hand the spherical shape enables the highest possible apparent density without compression [11]. This is an advantage for high-alloyed powders which can't be compressed properly either.
Another disadvantage of water atomization is that the oxide content of water atomized steel powders is much higher than those of gas atomized, caused by the larger surface area and the use of highly-oxidizing water.

Thus water atomization, although the output is much higher than using gas atomization, is only used for elemental iron or low alloyed steel powder. The atomization of high alloyed steels makes it necessary to use inert gas atomization, for which utilized gases are helium, argon and nitrogen. In common nitrogen is mainly used for gas atomization because it's the cheapest gas and has acceptable cooling rates.
Another advantage is that it doesn't leave inclusions in the compacted powder mass after HIP, because in opposite to the other gases nitrogen is solutable in the solid steel matrix. Thus nitrogen inclusions can be eliminated afterwards. Because of this number of high alloyed steels, like the one studied in this thesis, are atomized with nitrogen [11].
However, even though using inert gas atomization the oxidation of highly reactive metallic elements is too powerful and can't be prevented completely [12]. Thus the specific role and disadvantages of remaining oxides on the densification of powder particles will be explained later in section 3.2.4.

3.2.3. Manufacturing techniques

Before densifying the steel powders these usually have to be mixed and compacted. In this thesis only loose and prealloyed powder is considered therefore compaction methods are not regarded. The blending though is vital to minimize the segregation of small particles in advance to achieve a homogeneous packing density and enables maximal compactness of the mix [9].
To achieve higher performances and properties only manufacturing techniques which lead to high density of the PM product are considered for the manufacturing in the frame of this thesis. Consolidation techniques applied in this work are solid state sintering, supersolidus liquid phase sintering and hot isostatic pressing.

Solid State Sintering

Sintering is a heat treatment which has the goal to densify a loose or compacted powder body by heating it up to $\frac{2}{3}$ till $\frac{4}{5}$ of the solidus temperature and maintain it at this temperature. It's further the process that includes different mechanisms which lead to the bonding of loose powder particles and can be illustrated by figure 3. 3.

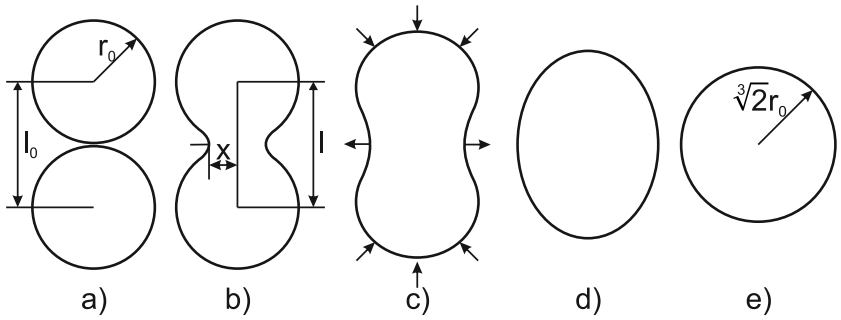

Figure 3.3.: Different sintering states after Frenkel, repainted from [13]: a) two particle adhesion; b) building of sintering necks; c) growth of sintering necks; d) non circular shape; e) spherical shape [13]

The conventional sintering process is a pure solid state process and includes only solid masstransfer, the additional appearance of a liquid phase will be discussed later on [13].
Driving force of the sintering process is the difference between the enthalpy at the beginning and the end of the process. Minimizing this free enthalpy is achieved by decreasing outer and inner surfaces as well as structural defects. Outcome is a less porous, densified state of the powder mass with minimized surface [9]. The main densification mechanisms are surface diffusion, grain-boundary diffusion and volume diffusion. The importance of these mechanisms is furthermore temperature and particle-size dependent and changes during the sintering process. In practice the sintering process can be divided into two main sections. During the first period local bonding and the formation of sintering-necks between the powder particles takes place. In this step the volume of the sintering compact stays nearly the same because there is only bonding through masstransport from convex regions to the necks but no shrinkage. In the second step sintering necks are more intensively developed and pore-shrinkage takes place actively. During this step nearly the whole volume shrinkage takes place and the final density is reached [11]. The main parameters which influence the sintering process are further the temperature, the annealing time, the particle size and the diffusion coefficient. Due to the fact that it's a diffusion based process higher temperatures, longer annealing time and higher diffusion coefficients advance the densification by increasing diffusion. This is further the reason why low diffusion coefficients of a component are very unprofitable for such a process and border densification because they depress diffusion. This will be further considered in section 3.2.4.

Supersolidus Liquid Phase Sintering

The formation of a liquid during sintering is a common technique to enhance densification of a loose powder mass. But contrary to conventional liquid-phase-sintering processes SLPS doesn't use a mixed powder, which consists of multiple components with different melting points, to achieve this.

The conventional mixtures densify because of the melting and spreading of a low melting component which embeds higher melting components and thus produce rather a composite [9].

SLPS in opposite uses a prealloyed steel powder and the fact that alloys have no exact melting point. Alloys have a melting range between the solidus- and the liquidus-line and melt continually in this range [figure 3. 4].

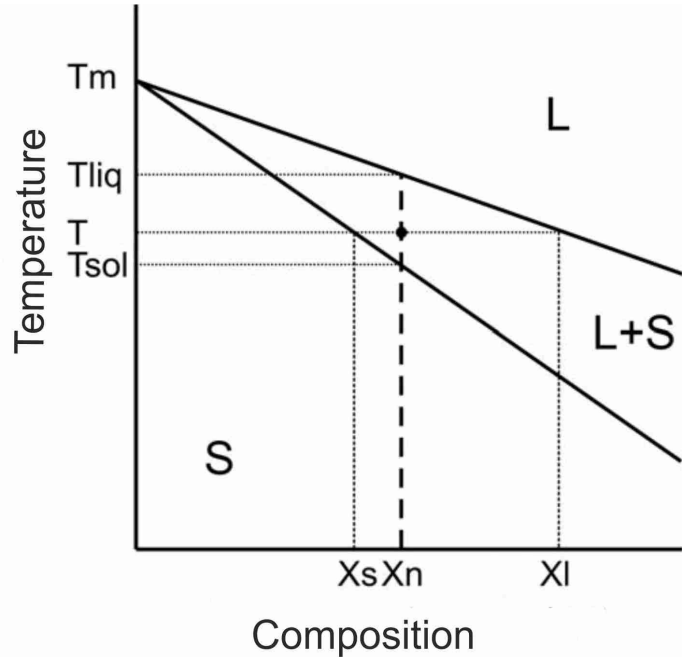

Figure 3. 4.: Schematic depiction of the SLPS conditions [14]

In the section between the solidus- and the liquidus-line, the so called sintering window, the state of the alloy therefore is partial fluid, which is further used to densify the powder mass by sintering it in the solid-liquid temperature range [15].

The SLPS process of densification starts rapidly with the overstepping of the solidus-line and the formation of first liquid parts. The melt wets the remaining solid parts and resulting capillary forces between the particles and the melt cause rapid densification of the powder mass. Furthermore, the partial liquid material wants to minimize it's surface area and thus rearrangement processes start.

These rearrangements of the solid parts are the main densification process of SLPS and depend primary on the microstructure and the amount of liquid phase. To achieve full density usually a quantity of 25-35 Vol.-% liquid phase is used [15].

The generation of a liquid phase during the SLPS process is mainly caused by the melting of low melting eutectics, even for an atomized powder microsegregations and thus different local compositions are included and the melting is not homogeneous. These different local compositions enable a continuous fusing, because they have different melting points and thus melt step by step in a spacing [15].

Local fusion usually starts at the grain boundaries and the sintering-necks because these are the finally solified areas. Thus the fusion of SLPS begins in the powder particle itself and at the contact spots of the particles.

The single steps of this process can be seen in figure 3.5 and show the division of the powder particles by the fusion process which makes the powder particle size irrelevant for SLPS. This is further the reason why SLPS is applicable to densify powders that are normally too coarse for use in solid state sintering and traditional liquid phase sintering. Because the size of powder particles has only less influence, the size of the microstructural parts counts [16].

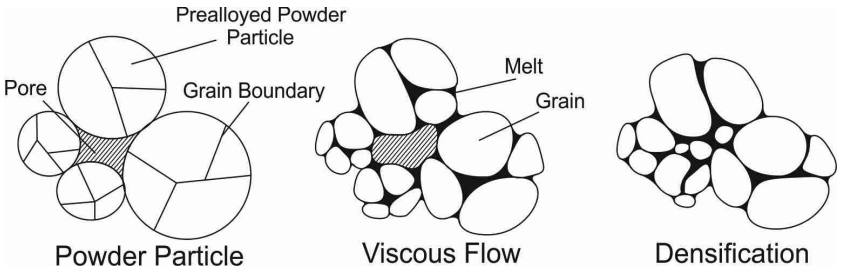

Figure 3.5.: Fusion process of prealloyed particles during SLPS [14]

To apply SLPS it's important to consider the width of the melting range [Figure 3.4] from T_{Sol} to T_{Liq}. As a smooth increase of the amount of liquid phase is desirable, this range should be very wide. A flat increase of the liquid amount is requested to control the sintering process more easy and to assure a reproduceable amount of liquid and thus quality. Further a low solidus-line is worthwhile because this shifts the densification to lower temperatures and thus saves energy and costs.

Furthermore the alloy composition itself shouldn't differ much because widely differing phases usually moisten each other poorly. Thus the composition range from X_S to X_L should be kept small [15].

Hot Isostatic Pressing

Hot isostatic pressing (HIP) is a common technique to densify high alloyed steel powders. Using this technique the loose powder mass is not densified using a liquid phase but applying high temperatures combined with high isostatic pressure. Typically the temperatures of HIP are about 700°C to 2200°C, the pressure about 100 MPa - 200 MPa and the holding time about 1 h to 4 h [9].

HIP has the advantage of a high densification, even though the sinterability is low, and low coarsening of the microstructure, compared to other techniques like casting. Despite of this the disadvantages like long cyclic times, expensive and sensible molds and limited product shape shouldn't be underestimated [9].

The HIP process usually takes place in an high pressure vessel which includes a radiation heating device made out of graphite or molybdenum. The encapsulated powder mass is positioned in this vessel and pressure is allied by a gas which is in general argon of high purity.

The isostatic pressure is a main advantage of the HIP process because thus the densification takes place homogeneous in the whole mass and the result after the HIP process is a fully and homogeneously densified powder compact with isotropic properties [9].

Driving force of the HIP process is besides the already discussed solid state sintering mechanisms (3.2.3) the exterior pressure. Plastic deformation, dislocation creep and viscous flow as densifying mechanisms are therefore added to the sintering mechanisms [8].

Because the consolidation in HIP is isostatic, there is further only a little shear on the particle surfaces. Hence contaminated prior particle boundaries can exist even in full-density compacts. Such boundaries are weak and limit properties intensely [8].

Their origin, influence and role in entire PM is considered in the next section.

3.2.4. Influence of surface oxide layer on densification, oxide reduction and effect of processing atmosphere

From the description of the densification process given in earlier sections it can be concluded that the surface properties of a powder are of vital importance for the consolidation of the compact. This issue leads to the topic of the surface characteristics of a steel powder, because that's the key parameter for chemical and mechanical properties which a powder can achieve [12].

The formation of sintering necks requires the contact of clean metallic surface zones, because it's a diffusion based process and thus is dependent on the diffusion coefficient of the participating elements. Oxides act as a diffusion barrier and retard the neck building between the powder particles because of their ceramic character.
This topic is even more important when dealing with high alloyed steels, because they form very stable oxides. Elements with high affinity to oxygen like Cr, Mn and Si are optionally oxidized and form thin oxides films and/or particulates on the surface which aren't easy to reduce. Low alloyed steels in opposite only form less stable iron oxides which can be reduced below the sintering temperature and thus don't limit the neck formation process [12].
In this thesis gas atomized high alloyed steel powders are discussed which are better applicable than water atomized powders because of lower initial oxide content.
Also prealloying of the steel powder is profitable in this case because it is possible to overcome, up to a limited extent, the high affinity to oxygen of some elements such as Cr and Mn by having them in solution [17]. Their reactivity is weakened by prealloying in comparison to admixed powders.
However, the used powder due to it's large specific surface area and it's high Mn and Cr content is very reactive, thus an oxidation of the surface during further handling won't be preventable completely [18].

Previous studies of several prealloyed CrMn steel powders showed that, as a result of the atomization and further handling, the surface of the powder particles was covered by an inhomogeneous oxide layer. This layer is build up as following: more than 90% of the surface is covered by a thin Fe-oxide layer which is about 6 nm thick, the rest of the surface is coated with small, ca. 200 nm thick, spherical particulates. These particulates are rich in elements like Cr and Mn which form thermodynamically stable oxides and are even more complicated to reduce [19, 20].
Figurative this enrichment of Cr and Mn on the powder surface can be depicted as "oxide-islands" in the iron layer [20].

The reduction of these surface oxides during a heating stage while sintering is further crucial in order to facilitate the development of strong sinter necks. Therefore a suitable atmosphere during the sintering process is vital.

In general the atmosphere shall prevent further oxidation of the powder particles during the sintering process, reduce already existing oxide layer to improve mass transport and in the case of easy volatile components prevent loss of elements like N and Mn [9, 12].
In the absence of a reducing agent, what means sintering and heating in vacuum or nitrogen atmosphere, the main removal of oxides is caused by their dissociation. This reaction follows equation 3.2.

$$\frac{2}{n}M_mO_n = \frac{2m}{n}M + O_2 \tag{3.2}$$

In general such a reaction takes place when the change in Gibbs free energy ΔG^0 is negative, what means the energy state after the reaction is lower than before.
ΔG^0 is linked with the temperature (T) and the equilibrium constant K by equation 3.3, where R is the general gas constant. Equation 3.3 further shows the direct dependence of ΔG^0 and K, it underlines that if the value of K is bigger ΔG^0 is more negative and the driving force is improved.

$$\Delta G^0 = -RTlnK \tag{3.3}$$

Equation 3.4 expresses the change of the free energy (per mole O_2) during dissociation of oxide, at a standard pressure of 1 bar.

$$\Delta G^0 = \frac{2m}{n}G^0(M) + G^0(O_2) - \frac{2}{n}G^0(M_mO_n) \tag{3.4}$$

The equilibrium constant K is furthermore determined out of the activities of the reaction products and reactants [3.5].

$$K = \frac{[a(M)]^{\frac{2m}{n}} \cdot a(O_2)]}{[a(M_mO_n)]^{\frac{2}{n}}} \tag{3.5}$$

The activity is the " effective concentration " of an element in its alloy and for a gas like O_2 equal to its partial vapor pressure. In the case of a solid metal M and its oxide M_mO_n the activity is unity for both [12]. The outcome of this is equation 3.6 which shows that K is equal to the partial pressure of O_2.

$$K = p(O_2) \tag{3.6}$$

Converting equation 3.2 and substitute K by $p(O_2)$ the equilibrium oxygen partial pressure can be determined as:

$$p(O_2) = exp(-\frac{\Delta G^0}{RT}) \tag{3.7}$$

As information about ΔG^0 is known and included in several thermodynamic databases, the equilibrium oxygen partial pressure can be plotted for different types of oxides dependent on the temperature and thus their stability can be depicted and compared depending on T. A plot of the oxygen partial pressure for different oxides is given in figure [3.6].

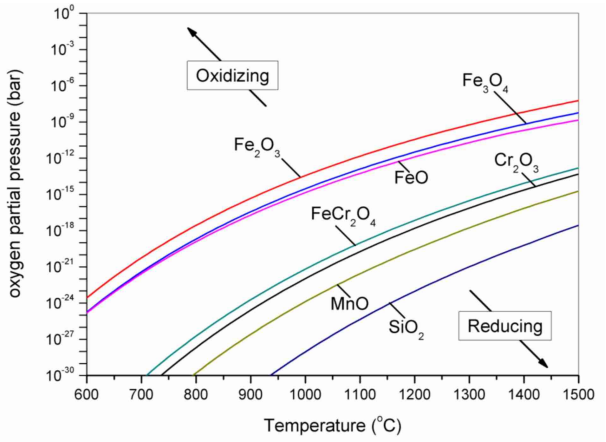

Figure 3.6.: Equilibrium oxygen partial pressure as a function of temperature for some metal oxides, from [21]

This plot visualizes the common way of oxide dissociation in vacuum. Oxides are only stable for higher oxygen partial pressures and low temperatures, if the temperature increases and the oxygen partial pressure decreases they were reduced. To the right of each curve the depicted oxide can be reduced by either lowering the partial pressure for a given temperature or by increasing the temperature for a constant oxygen partial pressure. The system then descends to a more stable state. To the left of the considered oxide, the oxide is stable and the metal is oxidized. Because of this it's a matter of environmental conditions which oxide is stable and if oxides transform [22, 18].

Indeed the necessary pressures to reduce highly stable oxides is very low and so only relatively unstable oxides like iron-oxides can be reduced economically via dissociation.
Hence, in industrial applications other methods are used which lead to reduction at lower temperatures and higher oxygen partial pressures. These applications are techniques where reducing agents like hydrogen and carbon are used [17].
The reduction by hydrogen follows equation 3.8 and even a small amount of H_2 is very effective to reduce Fe-oxides at lower temperatures from ca. 300°C on.

$$Me_xO_y + yH_2 = xMe + yH_2O \tag{3.8}$$

The direct [3.9] and indirect [3.10] carbothermal reduction are rather used to reduce more stable oxides like Cr- and Mn-Oxides. This happens at higher temperatures, starting at ca. 800°C with a first maximum between 800-1000°C [17]. At this temperatures carbon becomes more active, and the carbothermal reactions start. In a first step oxides can be reduced by graphite out of the mixture to form CO [3.9] and in a second step CO reduces oxides itself to form CO_2 [3.10]. Furthermore the second step can take place with CO originating from the sintering atmosphere and thus graphite in the powder is not essentially needed.
In the case of reduction by solid carbon the present graphite reacts with oxygen originating from oxide dissociation and forms volatile CO. This can further be seen as the reduction mechanism in inert atmospheres (Vacuum/ N_2), here the reducing agent exists in solid state and reduces the oxides from this point of origin. Thus, reduction by solid carbon is more notable in inert atmospheres and the carbon loss is higher compared to CO containing atmospheres [17, 22].
Considering prealloyed steel powders with carbon there is no pure graphite in the compact. Despite it is well known that the carbon activity in the steel matrix increases strongly with raised temperature and carbon as an interstitial element is very mobile [3]. Consequently the needed carbon for the carbothermal reaction originates out of the steel matrix itself.

$$yC + Me_xO_y = xMe + yCO \tag{3.9}$$

$$yCO + Me_xO_y = xMe + yCO_2 \tag{3.10}$$

The third method to reduce oxides with the help of a reducing agent is the water gas reaction [3.11], this reaction keeps the balance in reducing/ oxidizing gas between all the gas components and produces again CO out of CO_2 which can further reduce more oxides [17].

$$H_2 + CO_2 = H_2O + CO \tag{3.11}$$

Oxide reducing reactions take place when the change in the Gibbs free energy ΔG^0 is negative and a oxide is more stable the lower ΔG^0 is.
Thus oxides with lower Gibbs energy are more difficult to reduce.
In practice it's possible and conventional to depict all the possible oxidizing and reducing reactions in the common Ellingham-Richardson diagram [3. 7]. From this chart it's possible to evaluate the stability of different oxides by considering ΔG^0 over the temperature and compare it with CO, CO_2 and H_2O.

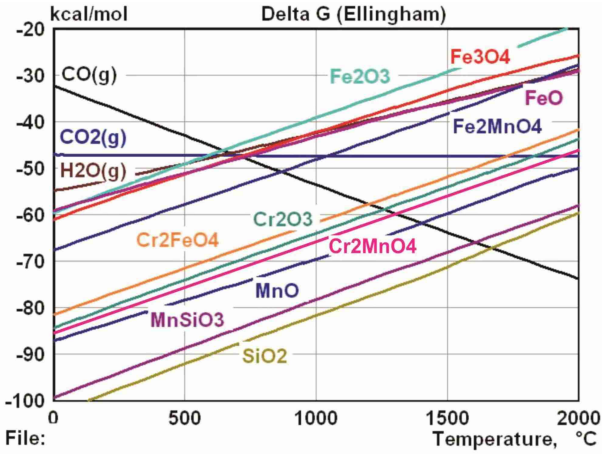

Figure 3. 7.: Ellingham-Richardson diagram for selected metal oxides from [23].

It's essential that always the products with the lowest ΔG^0 and thus the lowest line are stable. So reactions from one state to the other take place if two lines cross. By this the Ellingham-Richardson diagram shows at which temperature a reduction or oxidation can take place and can be used for the qualitative choice of parameters [22].

Concluding the topic of the microclimate shall be described shortly. Considering the reduction of a powder mass the conditions for the oxide reduction aren't the same at any site of the compact. Thus differences in the reduction state between the edge and the core of a sample have been found in earlier researches [17].
The conditions for the reduction of the surface are more favorable in areas close to the surface since the the local microclimate is improved. This is due to the continuous sintering atmosphere interchange with the "constant flow" in case of flowing gases and the better evacuation of reaction products, "sucking out", during vacuum sintering [22]. This further accentuates reduction in vacuum compared to nitrogen, since the zone of reduction is larger, because the "sucking out" is more effective and the microclimate in the core is improved [22, 24].
Furthermore no re-oxidation because of cumulation of reduction products is possible and oxide transformation at higher temperatures is prevented [25].

3.3. X-ray photoelectron spectroscopy

X-ray Photoelectron Spectroscopy (XPS) is a common surface sensitive technique for analyzing the elemental composition, the chemical state and the nature of bonding of solid surfaces. More often it is known as Electron Spectroscopy of Chemical Analysis (ESCA).
The physical principle of XPS is based on the photoelectric effect, by irradiating a samples surface with monoenergetic soft X-rays electrons are emitted and further analyzed.
The energies of these photoelectrons and their number outcomes a unique spectrum which is characteristic for the irradiated element [26].
The output of an XPS measurement therefore is a plot of the number of emitted electrons per energy unit versus their kinetic energy.
The special photoemission form of XPS is caused by the ejection of an electron from a core level by an X-ray with the energy hϑ. An electron can be ejected if the energy of the radiation exceeds the binding energy of the electron in the atom. As shown in equation 3.12 the kinetic energy of the emitted electron is the deviation between the radiation energy and the binding energy and thus depends on the used radiation source. Therefore the kinetic energy (E_K) is no intrinsic material property.

$$E_K = h\vartheta - E_B - W_S \tag{3.12}$$

In fact the binding energy is the parameter which defines the electron and it's origin precisely. Equation 3.13 shows the relationship between the photon energy hϑ, the kinetic energy of the emitted electron (E_K) and the characteristic binding energy (E_B).

$$E_B = h\vartheta - E_K - W_S \tag{3.13}$$

The parameter W_S in this equation is the spectrometer work function, it's identified during calibration of the spectrometer and makes the calculation of the binding energy independent of the samples work function [27].
Figure 3.8 emphasizes schematically the emission of a photoelectron from the 1s shell by an X-ray photon.

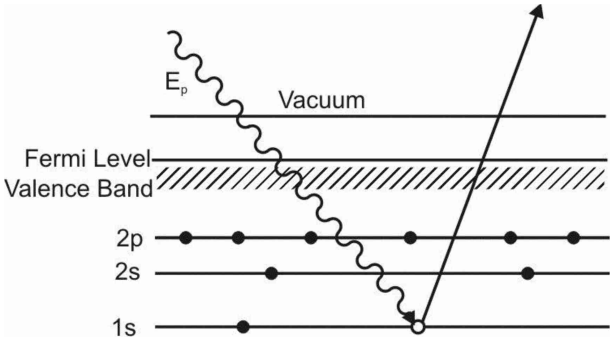

Figure 3.8.: Process of photoemission, repainted from [28]

Irradiating an atom with radiation of the energy hϑ further ejects every electron with a binding energy less than the radiation energy. Thus the result of an XPS measurement is a spectrum of emitted photoelectrons. The combination of these different photoelectrons is used to characterizes the excited element completely by reconstructing its electronic structure [28].
By this way every element can be distinctively identified. A mixture of elements is further the sum of several elemental peaks [26]. This makes it possible to determine the whole surface composition of an alloy out of single peaks.
But not every emitted photoelectron is characteristic for the irradiated atom. Only those who leave the solid surface without loss of energy, due to inelastic scattering, carry the specific information and form the unique elemental peaks. Photoelectrons, which have lost energy while escaping, form the background of the spectrum.
This is furthermore the reason of the surface sensitivity of the XPS measurements.

Although, ionization occurs much deeper than only some angstroms only the electrons that originate within tens of angstroms below the surface can leave without impacts and produce characteristic peaks [26]. So the XPS information depth is only in the range of the top 2 till 15 atom layers, which is about 5 to more than 30 angstroms [27].
After the emission of the photoelectron the ion remains excited, because of the loss of the electron. This excited state is not stable and needs to relax. The consequence of this relaxation is the radiationless emission of an auger-electron, which thus also occur in the XPS spectra.
So photoionization normally leads to two emitted electrons, a photoelectron and an auger-electron [28].

The chemical state of an element can be detected by slight shifts of the peaks in the spectrum. When an element is in a chemical bond its configuration differs from the ground state. This leads to a shift of a few electron Volts in the spectrum, because of a different binding energy. Mostly the shifts are very low and therefore the binding energy scale has to be well calibrated. This XPS feature can be used to identify different oxidation states by the difference in their chemical state [27].
The quantitative information about the surface composition can be determined from the area under the peak (peak intensity) because this area is related to the concentration of the elements in the alloy. In the past methods have been developed for quantifying XPS measurements, by utilizing the peak height and unique sensitivity factors for each element [26].

In the simplest terms, an electron spectrometer consist of a X-ray source, an electron energy analyzer and the sample under investigation. These main components are contained within an ultra-high vacuum (UHV) chamber to exclude impurities caused by the atmosphere and minimize errors of the analytical signal because low energy electrons are easily scattered by residual gas molecules. In practice, there is often a second UHV chamber with various sample preparation facilities and additional analytical facilities.
An associated data system is used for data gathering and analysis for following processes.
Common used X-ray sources are Al and Mg monochromated K_α X-rays, with 1486.6 eV for Al and 1253.6 eV in case of Mg [28].

Because the measured factor in XPS is the kinetic energy of the emitted electrons, a formalism is needed to describe their origin. This is done by describing them via the shell they were emitted from. Thus the so-called spectroscopists' or chemists' notation describes the electrons by means of their quantum numbers.

In this concept peaks are labeled corresponding to the scheme nl_j. Where n is the principal quantum number or the electron shell, which takes positive integer values of 1, 2, 3 etc., and l is the quantum number which describes the orbital angular momentum of the electron, the possible values of l depend on the value of n and range from 0 to n-1. Usually the l-quantum number, which determines the shape of the orbital, is given a letter rather than a number which is shown in Table 3. 1.

Table 3. 1.: Notation of l-quantum numbers as letters, from [28]

Value of l	Usual notation
0	s
1	p
2	d
3	f

Exemplarily the calculation of the l values can be shown as following, if n has the value (n=3) l can range from 0 to 2. Thus the l values are limited to s, p and d.

XPS peaks usually split into two if the angular momentum number is greater than 0, what means that there are more than one electron in the same orbital. This is a result of the interaction of the electron angular momentum because of the spin with its orbital angular momentum. The quantum number is further associated with its spin, s^2. And s can be either $+\frac{1}{2}$ or $-\frac{1}{2}$, to avoid two electrons with the same quantum number which is forbidden after Pauli's principle. This variation influences the j in the nl_j-scheme, because the two angular momenta are added vectorially to produce the quantity j. Thus j can have different values because of the different prefix of s. For example an electron from a d orbital can have j values of $\frac{3}{2}$ and $\frac{5}{2}$, equally an electron from a p orbital can have $\frac{1}{2(l-s)}$ and $\frac{3}{2(l+s)}$ as j values, with the same spin s^2 for both electrons but different quantum numbers for each. Therefore double peaks of electrons with the same spin but different quantum numbers occur.

The ratio of the double peaks depends on their relative populations and can be looked up in according literature. The gap between the doublets furthermore depends on the strength of the spin orbit and increases with the atomic number [28].
Figure 3. 9 shows an XPS spectrum from iron with the peaks labeled according to the chemists' notation and illustrated double peaks [26].

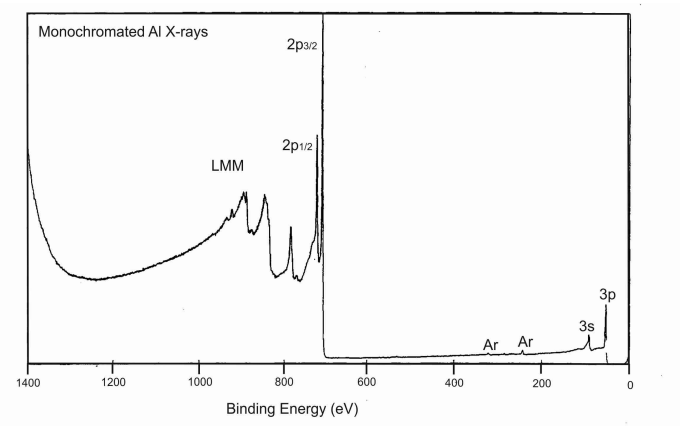

Figure 3. 9.: XPS spectrum of iron, repainted from [26]

The XPS spectrum in general is a plot of the number of detected electrons per energy interval versus their kinetic energy. As already said every element has an unique spectrum, because every element has a characteristic set of binding energies.
A binding energy of 0 eV, with reference to the Fermi level, corresponds in this spectrum from the position on the kinetic energy scale equal to the photon excitation energy minus the spectrometer work function. This is the origin of the scale and from this point the scale increases to the left [26].
To handle the spectrum correctly one has to know the types of peaks which occur and their sense. Following the characteristic features of the spectrum are described and their meanings pointed out.
Photoelectron lines are usually the most intense lines in a spectrum, they are relatively symmetrical and typically the narrowest lines observed in the spectra. They enable the determination of the chemical composition of the specimens surface from the binding energy of the photoelectron and are listed in several catalogues for Mg and Al radiation sources.
Auger lines are groups of lines in rather complex patterns, they can yield valuable chemical information about an atom and are a consequence of the photoemission process [28].
When non-monochromatic X-ray sources are used so called satellites occur in the spectrum.

Mg and Al X-ray sources mainly emitt $K_{\alpha 1,2}$ X-rays, but also $K_{\alpha 3,4}$ and K_{β} X-rays. Thus minor peaks at lower binding energies appear additionally to the characteristic main peaks in the spectrum.

These peaks are called satellites and their displacement and relatively height can be looked up in particular tables [27].

Contamination of the X-ray source with other elements might also cause small peaks corresponding to the most intense spectral peaks. These X-ray ghost lines may result from Mg impurity in the Al anode or vice versa. Because such ghost lines are not possible with monochromatic X-ray sources and rarely appear with nonmonochromatic X-ray sources they should not be considered in line identification, except in special cases [26].

Shake-Up lines are a consequence of the photoelectric process too, because not every process is a simple one which leads to ions in the ground state. There is a possibility that the ion will be left in an excited state, a few electron volts above the ground state. Thus the kinetic energy of the emitted photoelectron is reduced and a satellite peak a few volts lower in kinetic energy, than the main peak, is observed in the spectrum. These lines are again characteristic for the exact state of the ion and thereby the displacements and relative intensities of them can be useful to identify the chemical state of an element [26].

Another possible aspect in a XPS spectrum could be the multiplet splitting of photoelectron lines, in this case a line is asymmetrically split into two or more components. These occur because the emission of an electron, from a core level of an atom that itself has a spin, can create a vacancy in two or more ways. New unpaired electrons can therefore form an orbital with other unpaired electrons and so several final states are possible. This leads to more than one peak in the spectrum [26].

Energy loss lines are the results of energy loss of the photoelectrons due to the interaction with other electrons and occur especially in metals spectra [26].

The last lines of the spectra that have to be mentioned are the valence lines. These are lines of low intensities which occur in the binding energy region between the Fermi level and 10-20 eV binding energy. They are produced by photoelectrons from solid state energy bands and can determine the difference between insulators and conductors, because of the presence or absence of electrons from conduction bands [26].

3.4. Scanning electron microscopy

The scanning electron microscope (SEM) is an often used optical device to explore the surface of solid specimens, with higher magnification and depth of focus than a light microscope.
This is done by scanning the surface with a highly focused electron beam.
The short wavelength and the high parallelism of this electron beam makes it possible to achieve high magnification combined with high resolution and high depth of focus. Thus the theoretical enlargement of the scanned area can reach up to 1.000.000 : 1 [29].
Furthermore, the SEM image is a product of the interaction of the electron beam with the specimens surface. The image is mainly created by reflected or scattered electrons and thus only black and white images are created because electrons carry no color-information. To avoid interactions of the electron beam with atoms or molecules of the atmosphere and thus interferences the whole SEM scanning has to take place under high vacuum conditions [30].

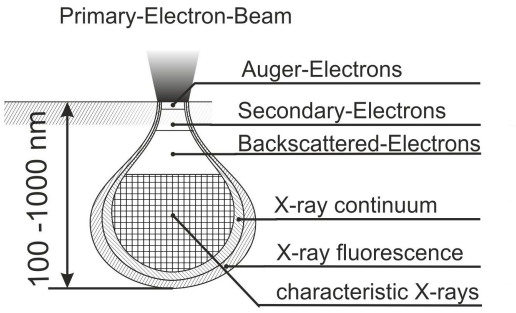

Figure 3. 10.: Interaction volume of the primary electron beam and the specimen, repainted from [30]

The electron beam actively interacts with the specimen in the interaction volume shown in figure 3. 10 and creates secondary products, which can be used for imaging and analysis.
In general used signals are the secondary electrons and backscattered electrons, as well as X-rays.
Secondary electrons (SE) originate from inelastic scattering of the electron beams primary electrons with the atoms of the sample. They have only lower energy yield (<50 eV) and are grouped in three sections.

1. SE1 are emitted directly from the surface in the beam focus.
2. SE2 occur because of multiple diffusion and leave the sample with larger distance to the beam spot.
3. SE3 occur because of backscattered electrons, leave from the largest distance to the spot and create no image.

SE are employed to image the topography of the surface because areas that are facing the detector appear brighter as more emitted electrons can reach the detector than from areas that are shadowed, thus the edge effect is pronounced.
Secondary electrons are further measured by two different detectors, the SE2-Detector and the Inlens-Detector. The SE2-Detector detects secondary electrons (90%) and also the backscattered electrons (10%).
The Inlens-Detector in contrast only detects SE1 and SE2 electrons and therefore has a much higher surface sensitivity. It only detects the SE which originate from the top surface layer and carry primary surface information. This surface information is even higher when the energy of the electron beam is lower, because of lower penetration depth [31].
Backscattered electrons (BE) are of much higher energy (>50 eV) than the SE and origin from the primary electron beam itself. They are generated by elastic scattering of the primary electrons much deeper in the sample and carry depth information about the sample. Because the backscattering coefficient depends on the atomic number of the excited element heavier elements reflect more BE and hence appear brighter.
For this reason the backscatter electron detector is positioned right under the the final electron lens and directly above the sample, to detect every emitted BE and avoid topography contrasts. Further the effectiveness increases with higher energy of the electron beam, because more BE are emitted [31].
Besides the generation of images the SEM also allows it to characterize the local chemical composition of a sample. This is done by the so called EDX-Analysis (Energy Dispersive X-Ray Analysis). In the case of EDX-Analysis a continuous energy spectrum is emitted by the retarding of high energetic electrons in the sample. These emissions are element characteristic X-rays and make it possible to identify the composition of constituent parts [30].
In this thesis a SEM Leo 1550 is used, equipped with INCA-EDX (Oxford instruments). The used acceleration voltage was 15 kV and the work distance was about 9 mm.

3.5. Chemical analysis

The hot extraction is a measurement method to detect the nitrogen and oxygen content of metallic samples. It uses the fact that metallic meltings nearly have no solubility for N and O and that these elements therefore exhaust as gases while melting the samples.
Thus the samples are melted by an induced electrical current in a graphite cup. So all components of the sample, including nitrides and oxides, are molten and exhaust as gases that are now detected.
To avoid measurement errors in advance the atmosphere in the hot extraction measurement chamber has to be free of detectable gases. So it's flooded with helium (99,995 % purity) in advanced to assure an inert surrounding.
Additionally the helium blows off the residues of nitrogen and oxygen out of the sample, so they can be analyzed completely.
From this point on the measurement principles of N and O differ from each other.
Gaseous oxygen immediately reacts with the graphite cup and forms carbonmonoxide (CO), which is furthermore transformed to carbondioxide (CO_2). This amount of (CO_2) is quantified via infrared spectroscopy. Infrared spectroscopy uses the nature of some gases to absorb infrared-radiation. Each gas absorbs characteristic spectral ranges of the radiation and due to its volume concentration this absorbation is more or less strong. If the amount of O increase the amount of absorbed radiation also increases and the measured infrared intensity decreases. Thus, the concentration of the absorbing gas can be quantified. The identification of the gas is made by the main wavelengths that are absorbed because these are characteristic for each absorber.
In contrast the nitrogen content is measured by heat conductance. A thermal conductivity cell measures the amount of nitrogen by measuring changes in the heat conductance of the chambers atmosphere. This is done by comparing the measured heat conductance with a reference factor, which is usually helium. To avoid the influence of CO_2 on the nitrogen measurement it has to be removed. This is done by binding it in sodium hydroxide (NaOH).
Before measuring N and O the hot extraction device has to be calibrated with some standard specimens. To cover a wider range of nitrogen and oxygen contents a detector for low and one for high concentrations is used and calibrated. So contents from 0.01 ppm till 2 Mass.-% can be detected, while the precision of the measurement depends on the specimens weigth and decreases with lower weigth of the speciment [32].

Chapter 4

Material and experimental procedure

4.1. Material

In this thesis the prealloyed austenitic steel powder Fe-19Mn-18Cr-C-N (X40MnCrN19-18) is examined. It is produced out of a prealloyed melt by gas atomization using nitrogen and contains in initial state 0.396 mass.-% carbon and 0.315 mass.-% nitrogen. The complete chemical composition of the powder is given in table 4.1.

Table 4.1.: Composition of the Fe-19Mn-18Cr-C-N steel in original condition

Content/ Element	C	N	Cr	V	Mn	Ni	Mo	Co	W	Si	Fe
mass.-%	0.39	0.31	17.08	0.02	19.67	0.46	0.99	0.38	0.05	0.45	39.81
at.-%	1.77	1.21	17.65	0.02	19.24	0.42	0.55	0.35	0.01	0.86	57.92

The Fe-19Mn-18Cr-C-N steel is a austenitic, high strength, stainless CrMn-steel which follows the (C+N) alloying concept for high nitrogen steels (HNS) [2].
The combined alloying of C+N has several advantages. It widens the homogeneous austenite field strongly to lower temperatures and stabilizes the austenite stronger than C or N on their own. Additionally the short-range-ordering is increased leading to higher solubility of C and N which conditions a higher solubility in solid solution and furthermore decreases solution annealing temperatures.

Another advantages is the insolubility of N in $M_{23}C_6$ carbides which prohibits their precipitation and increases resistance against intercrystalline corrosion, which would occur if only interstitial carbon is used [33]. Moreover the high amount of interstitials conditions a high strength in this steel. The increased short-range-order in combination with the low stacking-fault-energy of austenitic steels further improves the hardening potential. Additionally the metallic, ductile nature of bonding is increased by the C+N alloying concept and thus Fe-19Mn-18Cr-C-N is a high strength and yet ductile austenitic steel. This becomes clear when the properties of the Fe-19Mn-18Cr-C-N steel are compared to the austenitic standard steel X5CrNi18-10 because the yield strength is increased about three times and the toughness only slightly effected [2].
The alloying elements chromium and manganese improve the nitrogen solubility in this steel by decreasing the N-activity and thus enable a pressureless casting of the prealloy. Further Cr conditions the high corrosion resistance and Mn replaces the expensive Ni as austenite stabilizing element.
Molybdenum increases the corrosion resistance and nitrogen solubility too, it further delays the precipitation of carbides and nitrides to higher temperatures and so raises the pitting resistance equivalent number (PREN) [2].

4.2. Previous investigations

Previous surface investigations focusing on the Fe-19Mn-18Cr-C-N steel powder built the fundament of this thesis. These investigations considered the loose steel powder with a look at the as-received surface composition and the oxide distribution during heat treatment under ultra high vacuum of about 10^{-7} mbar [19] and under a nitrogen atmosphere of 1 bar nitrogen partial pressure [34].
The analysis of the as-received surface indicated that the single powder particles are coated with a heterogeneous oxide layer which consists of a 4 nm thick homogeneous iron oxide layer with small particulates and larger agglomerates. The small particulates are about 30 nm large and the larger, "flaky" agglomerates have a size up to some hundreds of nanometers. The model of this layer can be seen in figure 4.1.
Studies showed that chromium and manganese only form the small particulates distributed in the iron oxide layer. Hence mainly iron oxide covers the surface.

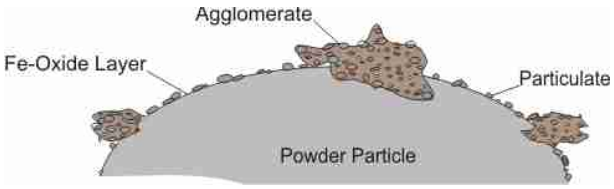

Figure 4. 1.: Model of the oxide distribution on the powder surface in as-received state [19]

Furthermore manganese and chromium form the larger agglomerates of the surface coating. Their amount on the whole oxide quantity thus increases with increasing etch depth, so that they dominate the oxide partition in deeper etched areas.

The investigations during vacuum heat treatment further depict the processes that take place during the sintering process of the Fe-19Mn-18Cr-C-N steel under UHV. They show till which temperature oxides are stable and characterize changes in the surface composition with increasing annealing temperature.

For iron it is shown that oxide reduction starts well under 500°C and for chromium that reduction starts below 600°C, both reduction processes are nearly finished at 700°C and only negligible amount of Fe and Cr is left in oxidic state.

In contrast first up from 700°C a starting Mn-evaporation indicates a Mn-reduction which increases further on with higher temperature.

The results of annealing the powder at 1000°C finally showed a nearly oxide free surface state, at this temperature most oxides that were present in initional state and during sintering are reduced.

Furthermore, it is observed that oxides transform into more stable oxides from 700°C on, what means that the thermodynamic lower stable oxides undergo a transformation during heating stages resulting in more stable Mn-Si-O-spinells.

Additionally it was pointed out that a main disadvantage of annealing the powder under UHV is the strong evaporation of Mn. The measurements show a decreasing Mn content from 700°C on and because this loss of manganese changes the alloy composition uncontrollable a heat treatment over 700°C is assumed to be problematically. It is concluded that a higher amount of oxide-free surface thus conditions a too intensive loss of manganese and because of this the use of high vacuum to reduce oxides from the powder surface is limited [19].

Previous investigations during heat treatment under 1 bar nitrogen partial pressure indicated a similar development of the oxide distribution as it was detected under UHV heat treatment.

The analyses show an iron oxide reduction at 500°C and it is assumed that this reduction took place by forming more stable oxides like manganese oxides because no carbothermal reaction could take place.

For chromium the oxide reduction further shifts to a higher temperature of 700°C and hence starts much later without the influence of a vacuum.

Between 500°C and 600°C additionally further oxidation of the contained manganese is detected which leads to an increased manganese fraction in oxidic state.

These manganese oxides moreover transform into more stable Si containing oxides from 800°C on and form mixed oxides of manganese base. Thus mixed Mn and Si containing oxides distributed in spherical shape at the powder surface from 800°C on.

The topic of manganese evaporation was also considered in this investigation. It outcame that the evaporation again starts at 700°C, but that it takes place in much lower amount compared to the UHV heat treatment.

The furthermore investigated nitrogen uptake of the powder started at 700°C and lead to a formation of chromium nitrides at the powder surface. Therefore not only oxides were reduced during heat treatment also the uptake of nitrogen took place [34].

4.3. Manufacturing and heat-treatment

In this thesis considered manufacturing techniques shall all lead to high density products, thus hot isostatic pressing (HIP), supersolidus liquid phase sintering (SLPS) and solid state sintering (SSS) were chosen. Further some variations of the solid state sintering process are tested to advance the oxide reduction and improve the densification using this technique. An overview of the techniques and their parameters is given in table 4. 2.

Table 4. 2.: Parameters of the different manufacturing techniques

Parameters/ Technique	HIP	SLPS	SSS	V700	V1050	V1150
max. temperature in °C	1150	1360	1340	1340	1340	1340
final atmosphere in bar	1000	1.75 N_2	1.75 N_2	1.75 N_2	1.75 N_2	1.75 N_2
final annealing time in min	240	120	360	360	360	360
annealing step temperature in °C	–	–	–	700	1050	1150
annealing vacuum in mbar	–	–	–	0.1	0.1	0.1
annealing step time in min	–	–	–	7	30	30

The first sample is produced by hot isostatic pressing (HIP). Using this technique the Fe-19Mn-18Cr-C-N steel powder is capsuled in a ferritic mould and compacted by using high temperature and isostatic external pressure. The HIP parameters are T=1150°C, p=100 MPa and t=4h and argon is used as compression gas.

Due to no interaction with the atmosphere the composition of the HIP specimen does not differ from the initial state. It's important to notice that this specimen, in opposite to the others, hasn't uptaken any nitrogen.

The SLPS specimen in opposite has been produced under 1.75 bar nitrogen pressure to alloy the powder with nitrogen to 0.825 mass.-% during manufacturing. This amount was chosen because former investigations and calculations showed it as the most promising for a balanced C+N ratio and high interstitial amount in this steel. Further it was done by solid state alloying via atmosphere during the sintering processs because previous researches revealed that the reachable nitrogen content via casting is bordered to 0.6 mass.-% [5] and thus the aspired C+N ratio only accessible by nitriding the solid, austenitic state.

In this trial and in the solid state sintering trials the loose powder mass was put into an aluminum-oxide ceramic cup without a cap and heat treated with direct interaction with the surrounding nitrogen atmosphere.

The used maximum temperature for SLPS was 1360°C and reached by heating up with 10 K/min. The measured SLPS Time-Temperature-Profile can be seen in figure 4.2 (a).

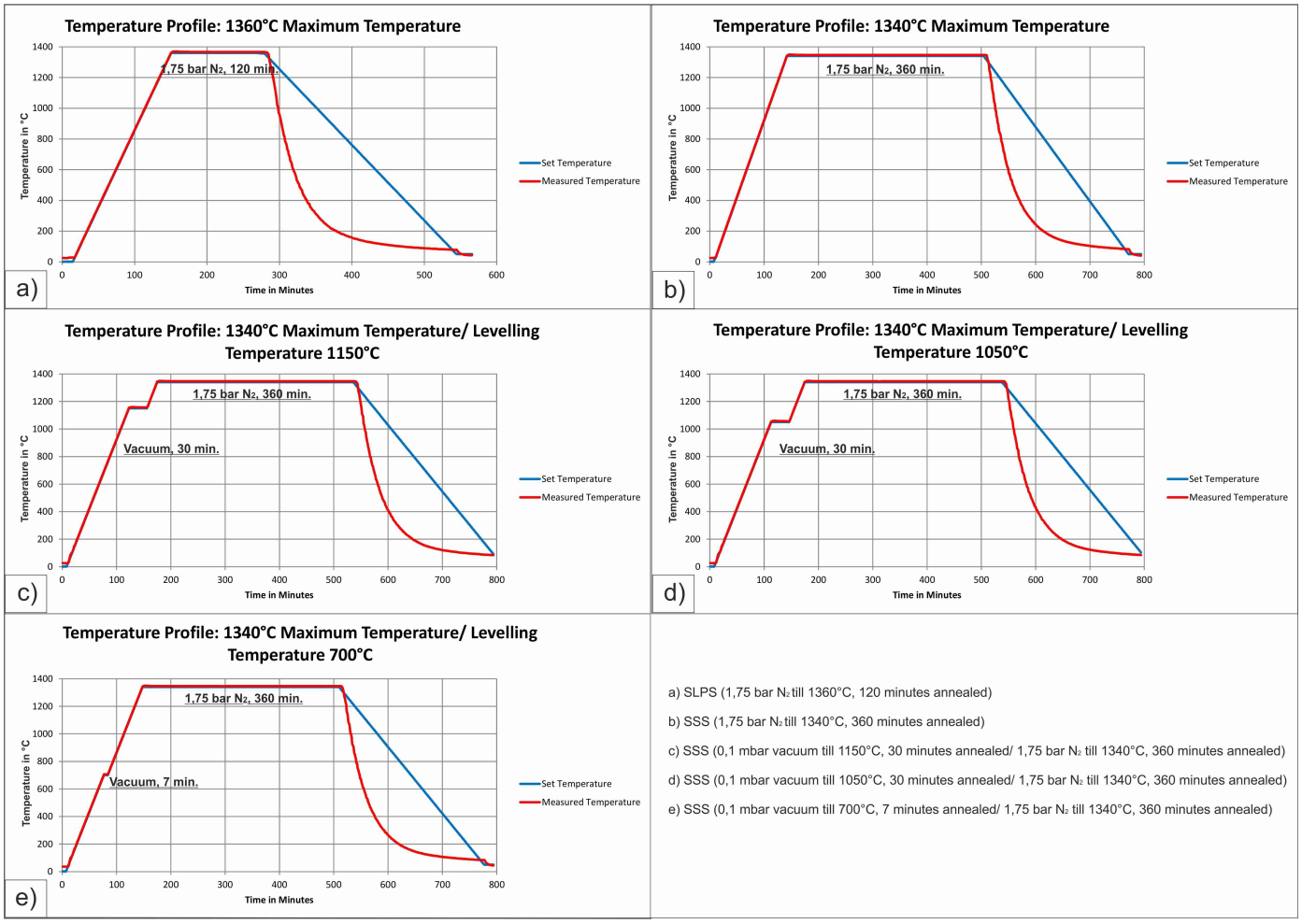

Figure 4.2.: Different temperature profiles of the densification processes used for Fe-19Mn-18Cr-C-N steel powder

The maximum temperature of 1340°C used for solid state sintering was slightly under the SLPS temperature. It was the same for every solid state sintering run and also reached by heating up with 10 K/min.

In the case of the solid state sintering trials thus only the atmospheres and annealing steps differed between the several variations.

The pure solid state sintering trial was performed under 1.75 bar N_2 from the beginning of the heating, see figure 4. 2 (b). Here the powder mass was densified and alloyed with nitrogen during consolidation as well.

The other solid state sintering trials included an annealing step under vacuum atmosphere before 1.75 bar nitrogen partial pressure was set on. They differ from each other in the used annealing temperature, for which 1150°C, 1050°C and 700°C were chosen. Till these temperatures a vacuum of 0.1 mbar was set on the powder mass. Afterwards a nitrogen atmosphere was set. Figures 4. 2 (c) - (d) show the variation of annealing steps during solid state sintering. The use of these annealing steps during sintering was chosen to investigate the influence of a vacuum on the oxide distribution during the sintering process at defined temperatures. 700°C, as the temperature where iron and chromium oxides should be fully reduced, was chosen to further look on the manganese-oxide distribution influenced by a vacuum. Further it's the highest annealing temperature where no evaporating of manganese is estimated. 1050°C and 1150°C were chosen as temperatures well over the stability of every expected oxide and thus, their influence to support reduction is tested. Furthermore the amount of expected manganese loss should be investigated.

Because grain boundary precipitations were found in every sample after manufacturing they were additionally solution annealed before further use. This was done by annealing them under argon atmosphere at 1200°C for 30 minutes and afterwards cooling them rapidly using water. This annealing was necessary, because carbides and nitrides have a strong influence on the properties of the Fe-19Mn-18Cr-C-N steel. They decrease the toughness strongly and are thus unwanted. Furthermore they should not be considered in the surface analysis of this thesis and are excluded by solution annealing of the samples in advance.

4.4. XPS analysis

With the help of X-ray photoelectron spectroscopy (XPS) the fracture surfaces of the manufactured samples have been analyzed. This was done after breaking the samples in the extended vacuum chamber of the XPS device.

For this reason specific specimens have been manufactured out of the produced sample material. They were cut out of the middle of each densified compact to avoid any contamination of previous handling and to characterize the oxide distribution in the main applicable area of the samples. The geometric profile and the analyzed area of the used XPS-specimens is further depicted in figure 4.3.

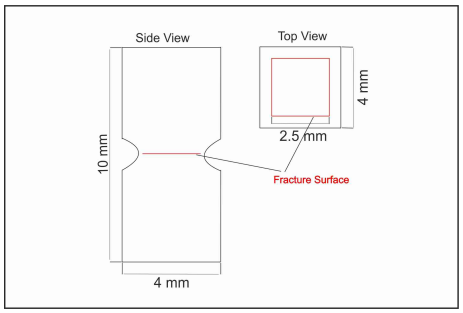

Figure 4.3.: XPS specimen and position of the fracture surface

To be able to break the specimens in the XPS vacuum chamber notches were made at two sides of the specimens. This was necessary because of the high toughness of the used steel alloy.
Afterwards these specimens have been positioned in the extended vacuum chamber of the XPS device and were broken under ultra high vacuum (UHV) of about 10^{-7} mbar to analyze the pure fracture face and avoid further contamination.
The actual XPS investigations were performed using the instrument PHI 5500. The as-fractured surface was investigated and with the help of controlled argon ion etching the composition depending on the etch depth was analyzed up to 50 nm.
Afterwards the surface composition was estimated by curve fitting and analysis of the characteristic XPS peaks.

4.5. SEM analysis

The as-fractured surface of the samples was investigated using a high resolution SEM (HR SEM), type Leo Gemini 1550. The chemical analysis using the SEM was done by using the EDX detector, type INCA.

4.6. Chemical analysis

Via hot extraction the manufactured samples were analyzed due to their nitrogen and oxygen content. The knowledge about the nitrogen content is important to check how much nitrogen has been alloyed during manufacturing and how the composition changed along the sample geometry. The amount of oxygen further shows the oxidation potential and enables to compare different manufacturing techniques due to their influence on the oxygen content in the sintered powder mass.

For this reason specimens out of three different sections of each sample were analyzed [Figure 4. 4] to further compare the N and O profile over the samples cross-section. The several specimens were taken from the top of the sample which actively was in contact with the atmosphere, the middle of the sample and the bottom, which touched the crucible.

With a view on the XPS analysis the N and O contents from the middle of the samples are of larger importance because this is were the XPS samples were taken from.

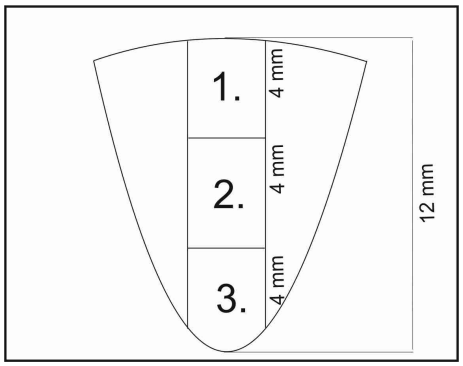

Figure 4. 4.: Specimen sampling for the N/O analysis (1.Top; 2.Middle; 3.Bottom)

For the analysis the ONH 2000 analysis device produced by the Eltra GmbH was used and in advanced cleaned and calibrated. Thus an atmosphere without N and O influence is guaranteed. The actual measurements were done by first weighing the specimens and then evaporating them by an electric arc in a graphite cup.

The result of each measurement is the average of three measurements per specimen and is presented in mass.-%.

Chapter 5

Results

5.1. Fracture surface analysis of the compact produced by hot isostatic pressing

XPS analysis

The XPS analysis of the HIP fracture surface indicates carbon, oxygen, chromium, manganese and iron as the main peaks in the XPS survey spectrum. Further nitrogen, sulfur, selenium, molybdenum and nickel are detected, but in much lower content. These quantitative results of the measured element fractions on the as-fractured surface and after ion etching till 50 nm are presented in table 5. 1.

Table 5. 1.: Content of elements on the fracture surface of the HIP sample, in at.-%

Content/ Element	C	N	O	Si	S	Cr	Mn	Fe	Se	Mo	Ni
Fracture surface	13.1	1.0	20.3	0	1.1	11.4	14.0	38.1	0.4	0.6	0
Etched 1 nm	9.9	1.2	19.5	0	0.8	12.4	13.8	41.3	0.4	0.7	0.1
Etched 5 nm	8.8	0.6	14.3	0	0.5	13.7	12.1	48.2	0.6	1.1	0.1
Etched 10 nm	8.3	0.8	13.5	0	0	14.0	12.9	49.2	0	1.1	0.1
Etched 50 nm	7.5	0.6	13.5	0	0	15.1	11.8	50.0	0	1.3	0.2

Figure 5. 1 furthermore depicts the results of table 5. 1 graphically to underline the development of the elements distribution.

It shows, that on the outermost surface there is a higher percentage of carbon and oxygen which decreases with the first etching steps and then indicates no changes. Manganese decreases as well during first etching steps but only slightly and levels equally to the oxygen development from 5 nm etch depth on. Contrary the content of iron and chromium increases proportionally and levels after 5 nm etch depth too.

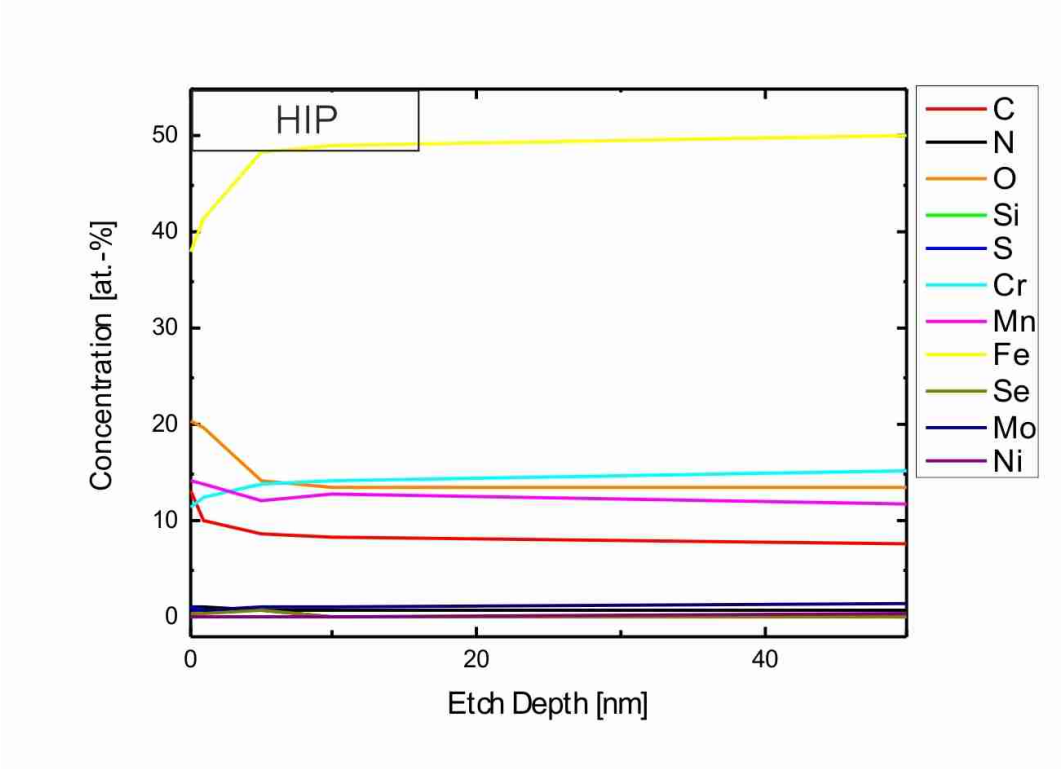

Figure 5. 1.: Development of the element content distribution with etching depth, HIP specimen

Still these deviations in concentration are very low and concentrated on the first etch steps compared to former investigations of the loose powder [19] and do not exceed 10 at.-%.

So there is virtually no change in the elements profile after 5 nm etching depth.

This is connected to the high roughness of the fracture surfaces which are presented later during SEM study description. The Fe-19Mn-18Cr-C-N samples fracture very ductile and thus have a rather rough fracture surface which causes difficulties during ion etching. The etching is not successful because it does not remove the surface homogeneously. The fracture surface is etched very partial and it cannot be estimated that the etching really took place in vertical depth because the roughness shadows parts of the surface from etching. Hence the XPS results after etching are not characteristic for an etched state.

There is no real information about the composition over the etch depth contained in the XPS results and only assumptions about the as-fractured surface can be made.
Still the HIP and the SLPS samples are even the most planar fractured samples and do not show large differences in hight like the solid state sintered samples because of much less porosity.
In figure 5. 2 non-metallic elements are further excluded to depict the development trends of Cr, Mn, Fe, Mo and Si separately.
The developments of the element concentrations are despite of all similar in both measurements [figure 5. 1 and 5. 2] and thus non-metallic elements don't influence the courses of the metallic elements.
At this point it has to be additionally mentioned that silicon was only measured in traces on the HIP fracture surface and thus silicon is excluded from evaluations for the HIP sample.

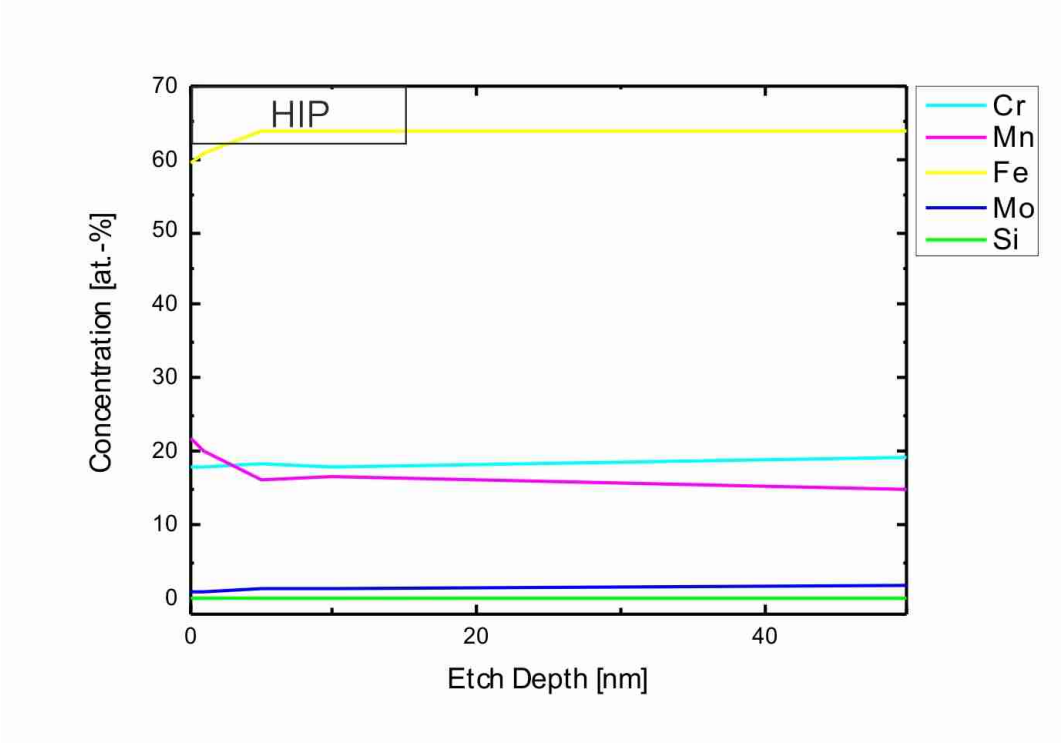

Figure 5. 2.: Relative concentration of metallic elements over etching depth, HIP specimen

Moreover it is desirable to know in which state, oxidic or metallic, the elements exist on the fracture surface. For molybdenum this is obvious because the analysis of its characteristic peak indicates its presence only in metallic state in all cases. Therefore Mo is excluded from all evaluations of oxide cations. For the other elements their state has to be analyzed by considering shifts in their binding energy. For this reason high resolution narrow scans are used to gain information about the chemical state of Mn, Cr and Fe.

The development of the measured iron, chromium and manganese peaks over the etching depth thus is shown in figures 5.3 to 5.5. The XPS spectra are presented as-fractured and till 50 nm of ion etching.

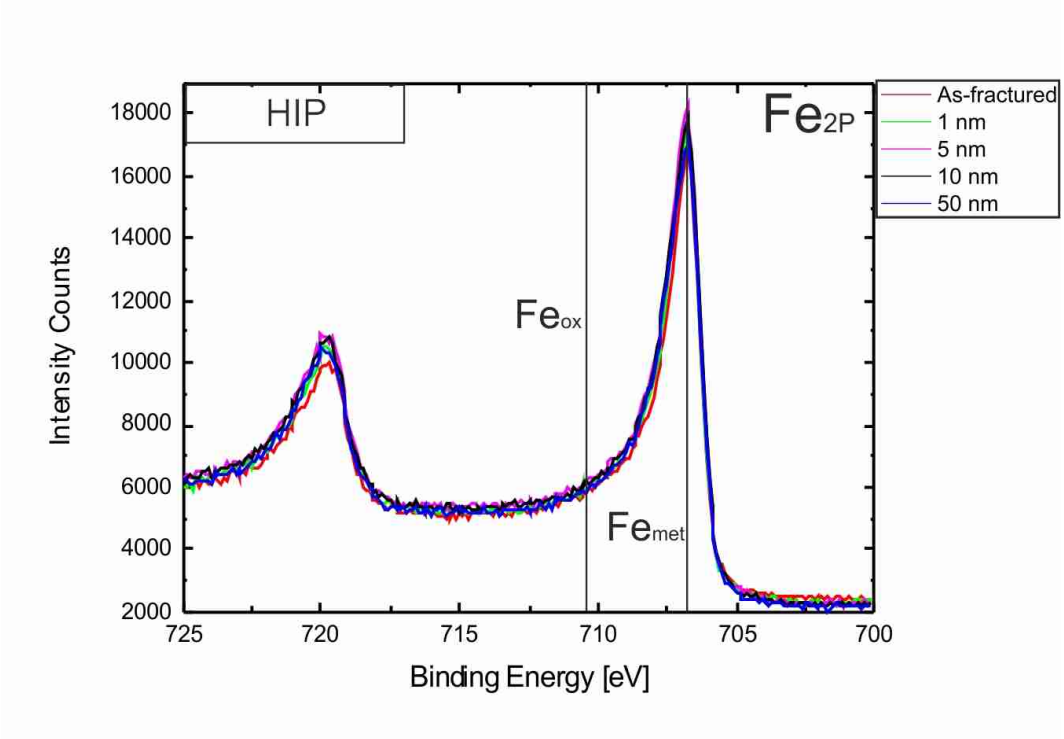

Figure 5.3.: Detailed XPS spectra of Fe 2p peak for HIP specimen

These results point out that for iron, chromium and manganese the metallic fraction of the peak is always dominant. Iron is nearly fully metallic from the as-fractured surface on and metallic chromium content increases till 50 nm etching depth from 85 at.-% to 93 at.-%. Metallic manganese content instead first decreases slightly from 71.4 at.-% to 61.6 at.-% and then levels at 66 at.-%, but still is in high metallic amount.

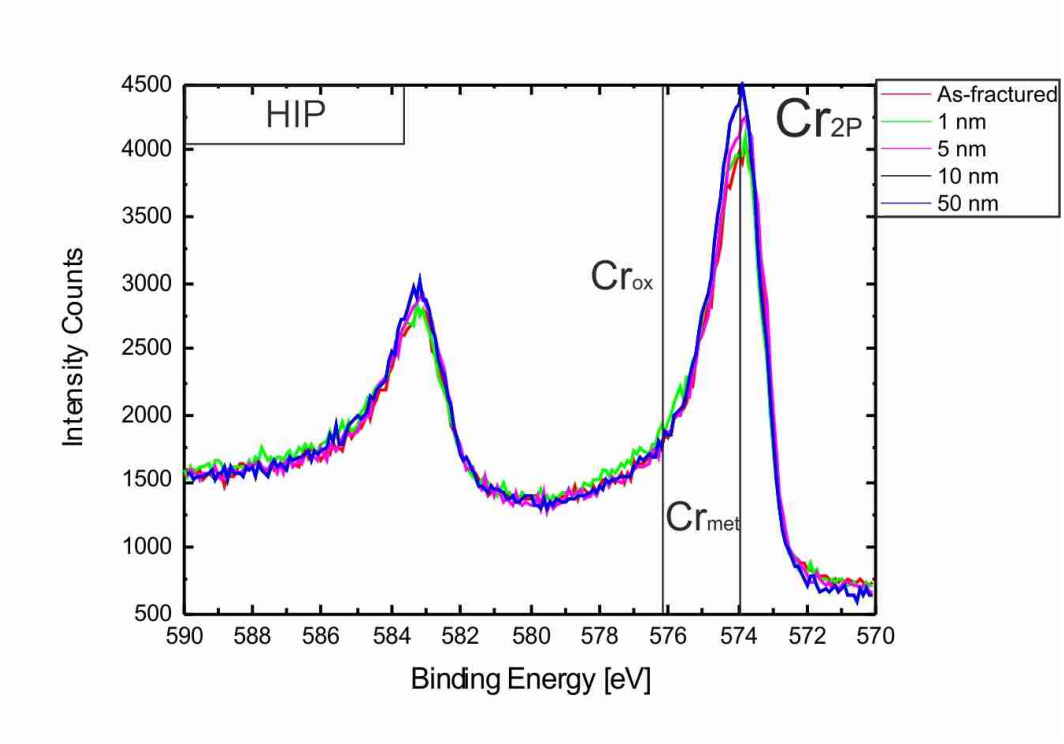

Figure 5. 4.: Detailed XPS spectra of Cr 2p peak for HIP specimen

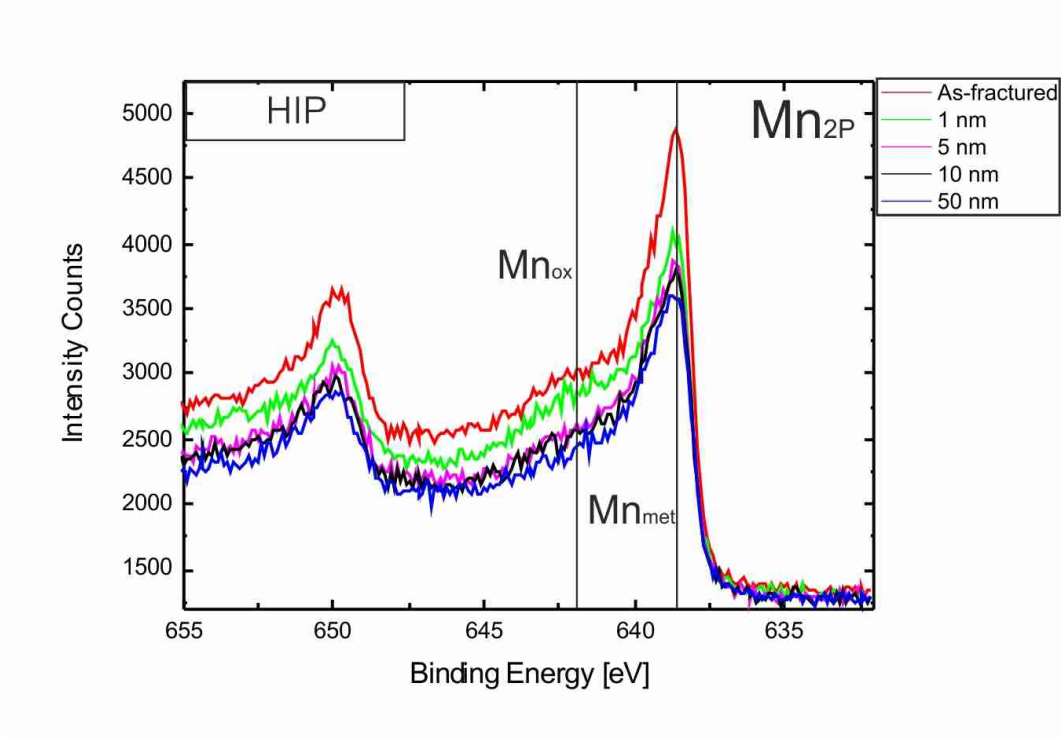

Figure 5. 5.: Detailed XPS spectra of Mn 2p peak for HIP specimen

These developments are detected by curve fitting of the considered element peaks and are depicted in figure 5.6 altogether.

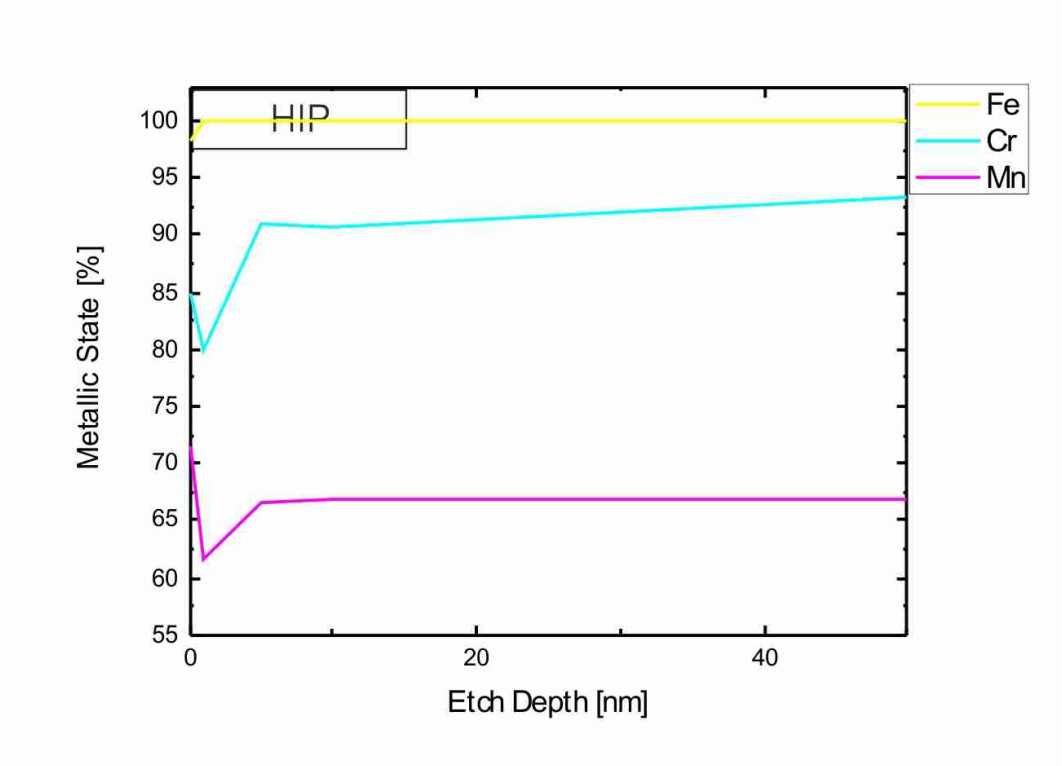

Figure 5.6.: Content of the metallic state of Fe, Cr and Mn over the etching depth, HIP specimen

The results indicate the absence of a continuous oxide layer on the fracture surface because all elements are mostly present in metallic state [19]. Only because of the manganese oxide fraction it can be estimated that oxide particulates are present on the fracture surface, formed preferably by Mn.

To describe the identification of elemental state the principle of curve fitting shall be described shortly. This principle enables to divide an elemental peak into metallic and oxidic fraction and thus to calculate the cation composition. An example for the curve fitting procedure for Fe, Cr and Mn is given in figure 5.7.

Doing curve fitting it is intended to reconstruct the measured element curve by fitting single peaks for metallic and oxidic states to it. Further the curve areas are proportional to the amount of atoms of the element in the corresponding chemical state and thus the amount of metallic and oxidic part of an element can be distinguished.

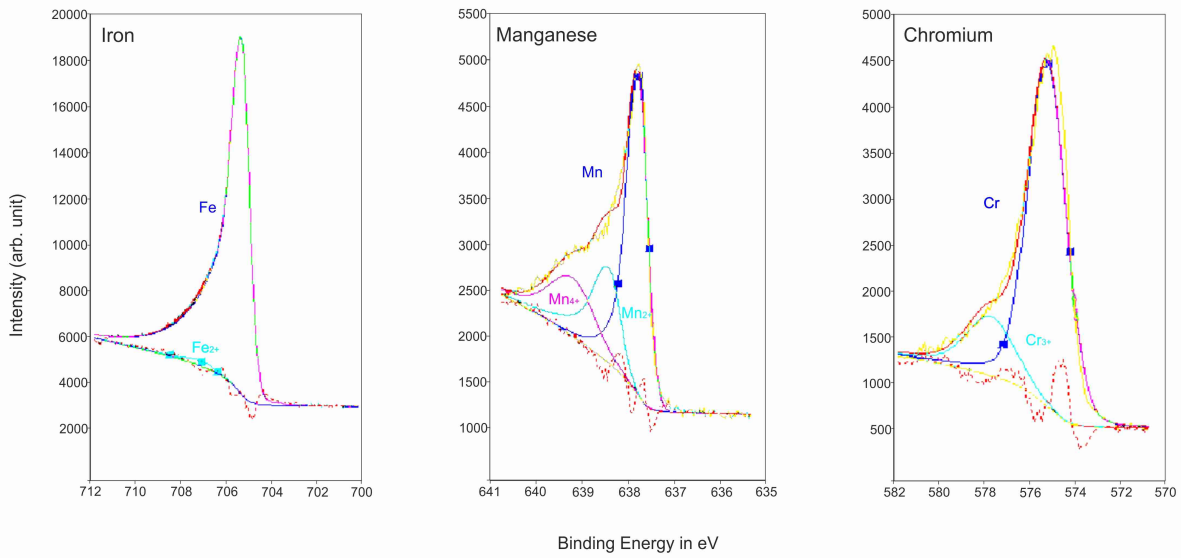

Figure 5. 7.: Analysis of the chemical state of Fe, Mn and Cr with the help of curve fitting. The measured peak is composed of a metallic component (blue) and an oxidic component (magenta and cyan)

Due to the fact that the states of some oxides change because of the ion etching it is impossible to distinguish the exact cation composition. Thus for example the individual contents of Fe^{2+} and Fe^{3+} cant't be determined correctly, only their sum.

To evaluate the fraction of the total oxidic state of each element the normalized relative cation concentrations are depicted in figure 5.8.

This composition is determined by considering the fraction of each element in the oxidic state in relation to the total concentration of the oxide forming element on the surface and normalizing the sum of all elements in oxidic state to 100 %.
This representation therefore provides information about the fraction of each element in the oxides and offers valuable information about their composition.
Oxide forming cations in the HIP sample are mostly manganese cations and their amount slightly increases with etching. In contrast the chromium cation amount decreases proportionally from 30 % in 1 nm to 20 % at 50 nm etch depth.

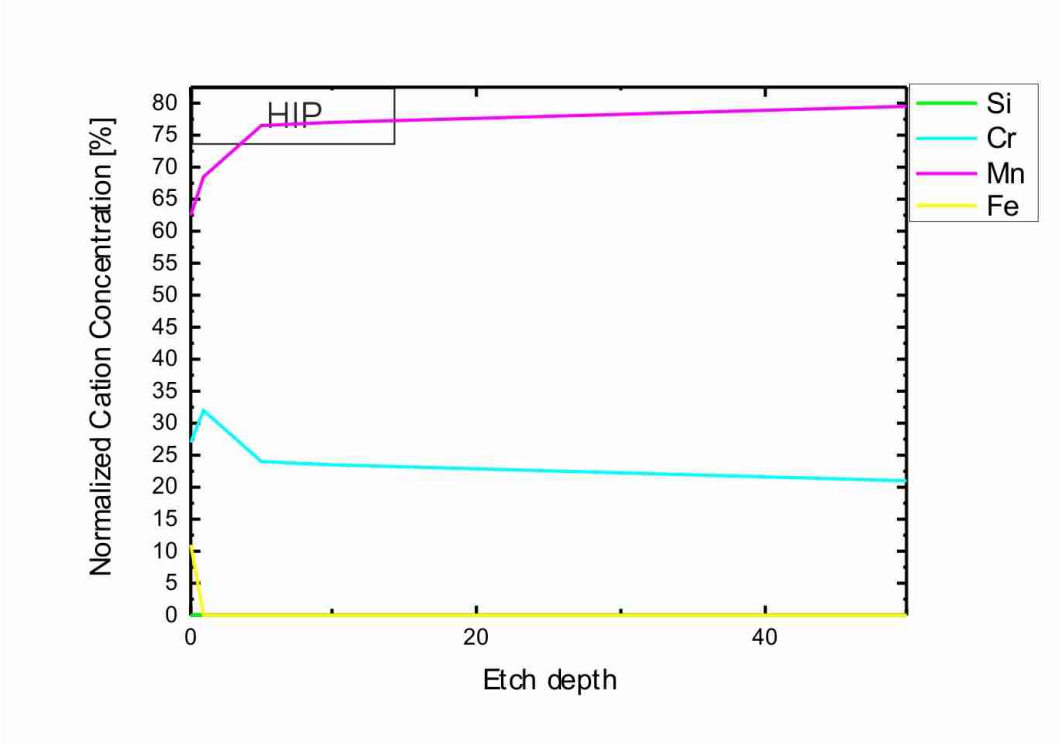

Figure 5. 8.: Normalized relative cation concentration of the oxidic state, HIP specimen

At the surface even 10 % of iron cations are present which lowers the Mn- and Cr-cation amount at the as-fractured surface, but does not influence the major trend of increasing Mn-fraction and decreasing Cr-fraction which leads to a dominance of Mn in deeper etched areas.
Silicon cations have further no portion because they were only detected in traces on the HIP fracture surface.

In general the total oxide in the HIP sample is very low, the total cation concentration is always well under 12 at.-% and even decreases to 6.3 at.-% in 50 nm etch depth. This developement is presented in figure 5. 9 which furthermore underlines that the oxides in the HIP sample are composed of Mn and Cr.
The jump in cation concentration after the first etching step is furthermore connected to the removal of contamination layer from the pure surface. The intensity of the signal increases from the pure surface resulting in increased cation concentration.

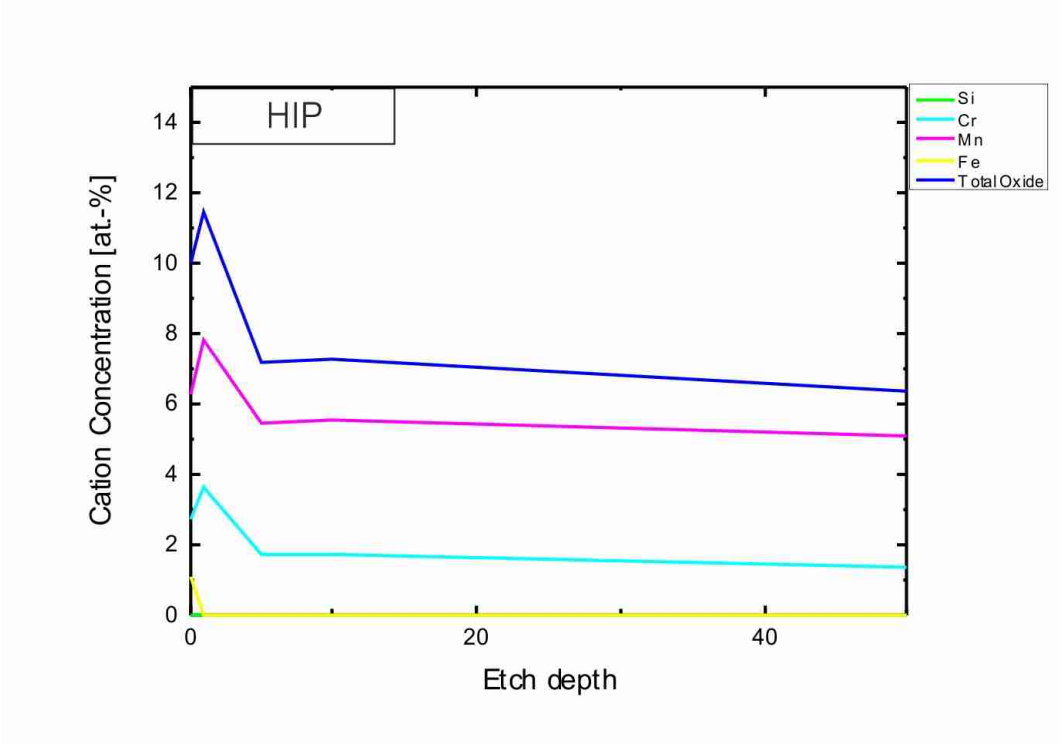

Figure 5. 9.: Total sum of the cations and single cation concentrations depicted over the etching depth, HIP specimen

SEM and EDX

Figure 5. 10 displays the appearance of the densified powder mass after hot isostatic pressing. It shows a very fine and highly densified state [a) and b)] of the consolidated powder and further low remaining porosity and no visible precipitations in the microstructure [c) and d)].
Remaining pores in the microstructure are very small and mainly appear at the grain boundaries. Concluded from these SEM pictures the average grain size of the HIP sample is about 25 μm and thus slightly coarser as the average particle size of the loose powder which was about 20 μm [19].
Considering the surface conditions of the HIP sample after fracturing [figure 5. 11] the surface appears rough and shows no large inclusions. Moreover inter- and transparticle dimple ductile fracturing is the main failure mechanism of the HIP sample and is present dominant.
Figure 5. 12 in addition depicts the appearance of the fracture surface at higher magnification, showing a high amount of spherical particulates on the as-fractured surface. These particulates size up to 500 nm in average.

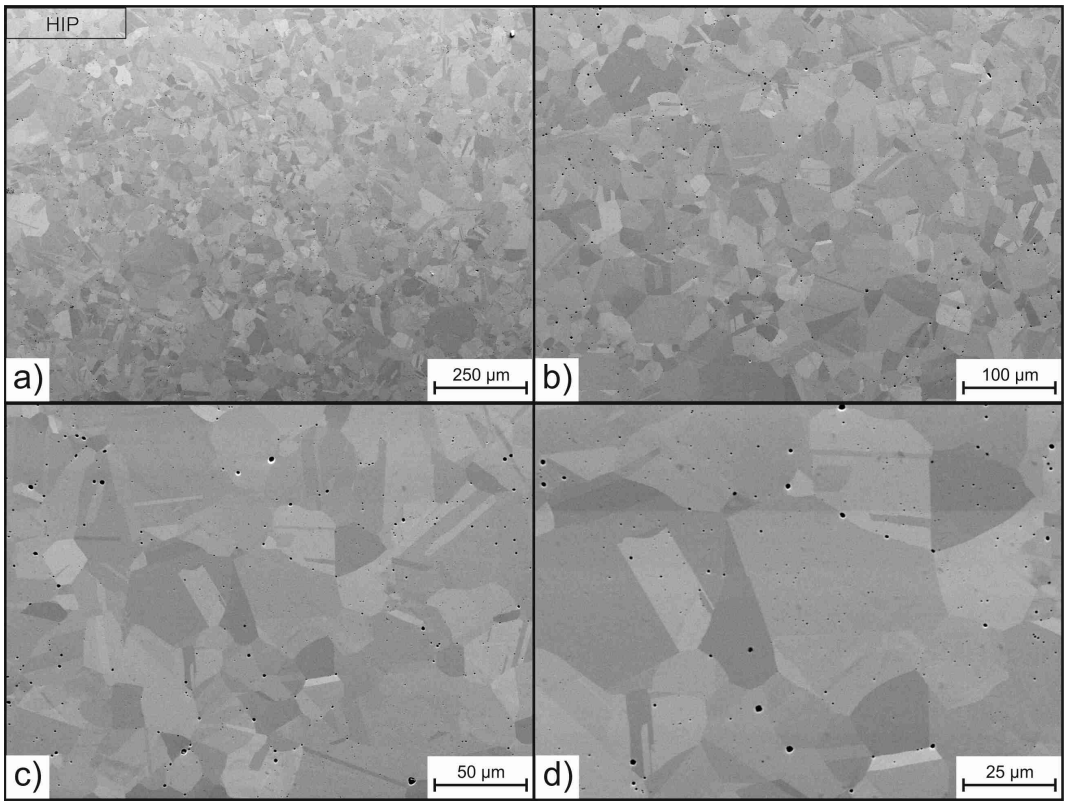

Figure 5.10.: Overview of the densified powder mass, polished HIP specimen

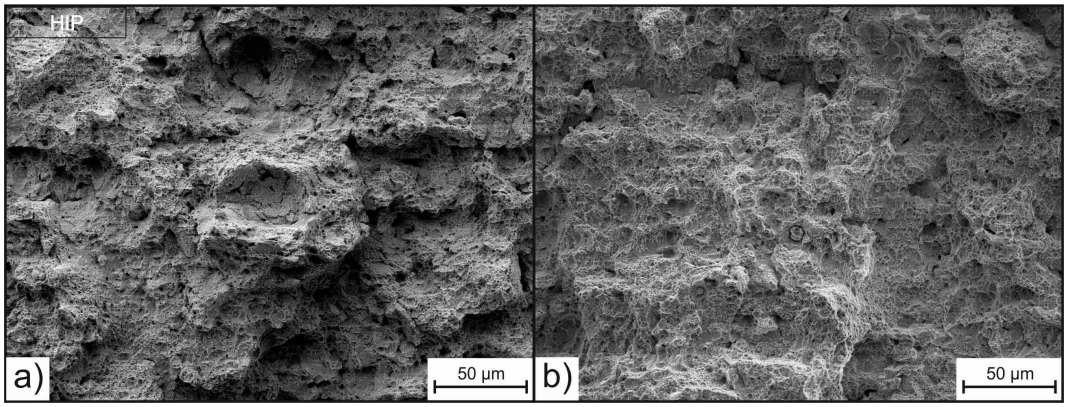

Figure 5.11.: Overview of fracture surface, HIP specimen

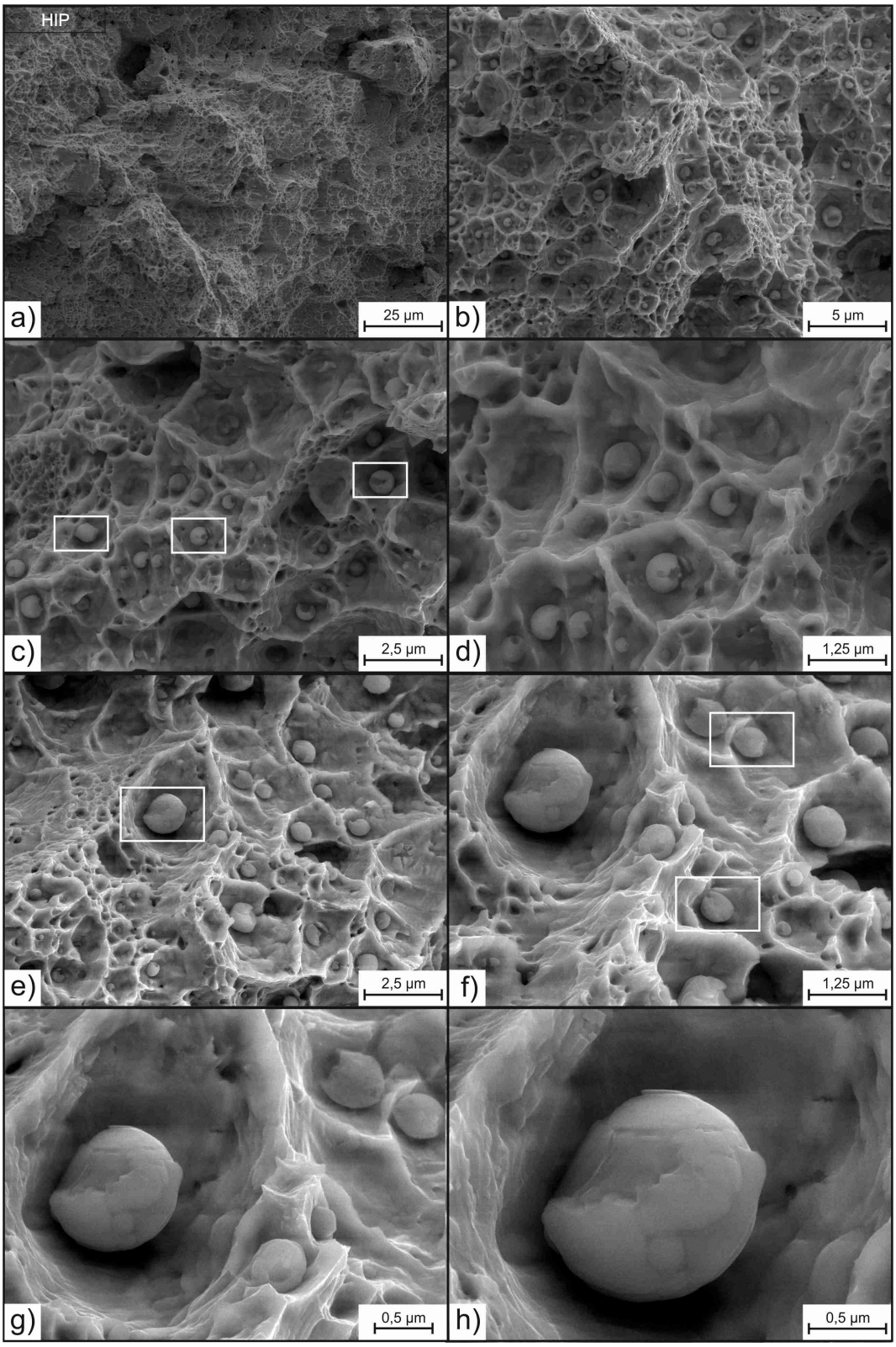

Figure 5. 12.: Closeup of the particulates distributing in the densified powder mass, HIP specimen

Figure 5. 12 g) and h) show a close-up picture of one of these particulates and depict its complex structure composed of a number of fine particulates itselve. The dominant interparticle ductile fracturing mode is initiated by these particulates originating on the powder surface [35]. It seems as if during consolidation original particulates and agglomerates were conserved and thus distribute in the powder mass.

This assumption can be underlined by considering figure 5. 13 [a) and b)] which shows a weak connected, former powder particle in the densified HIP sample. It is lying in a large dimple and small and fine dimples estimate a weak connection to the adjacent matrix.
The surface of this particle [c) and d)] is covered with a huge amount of small oxides, they cover dominant parts of the surface and thus limit the connection to other particles.
In this case especially the number and size of the particulates is disadvantageous because a large number of small particulates, like in this case, coats a very large surface area and thus limits inter-partical connection most. The same amount of oxide distributed in larger but less particulates could be even better for the densification because it would allow better connection between the particles.

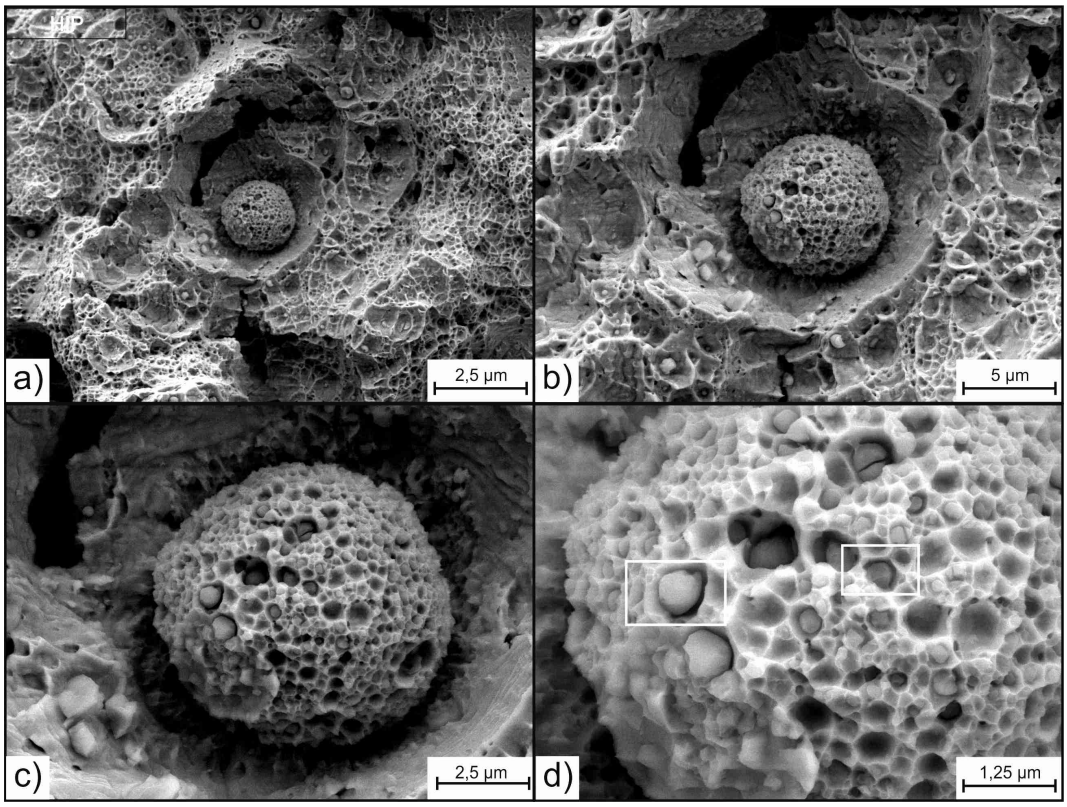

Figure 5. 13.: Weak connected former powder particle in the densified powder mass, HIP specimen

To furthermore complete the surface investigations of the HIP fracture site EDX analyses have been performed to gain information about the surface particulates and their composition. These results are presented in appendices B. 1, B. 2, B. 3 and B. 4 and were performed at a magnification of 20.000 times.

Appendices B. 1 and B. 2 show the analyses of the oxide inclusions existing on the surface and verify that these particulates are oxides because their oxygen content is very high compared to the matrix (about 50 at.-%). These oxides are composed out of a large amount of manganese (about 30 at.-%) and a quite high amount of silicon (about 6 at.-%). In opposite their chromium (4 to 6 at.-%) and iron (7 to 15.8 at.-%) amount is rather low.
Some measurements additionally detected molybdenum, aluminum, selenium and sulfur, but only in trace amounts of about 2 at.-%.

The EDX analysis of the particulate regarded in figure 5. 12 g) and h) [appendix B. 2 spectrum 1] further shows that this particulate is a pure oxide, it contains no iron and is mainly composed out of silicon and manganese as oxide forming elements.

Therefore it can be concluded that the spherical, oxidic particulates in the HIP sample are mainly heterogeneous Si-Mn-O-oxides.
These measurements can further be refered to the matrix composition. The matrix consists of only manganese, chromium and iron in an ratio 1:1:3 and fits to the in advanced estimated bulk composition well. Hence the composition of the oxides can be estimated as significant.

Appendices B. 3 and B. 4 present the EDX results of the powder particle regarded in figure 5. 13 and the surrounding matrix interface. The analyses of the particulates show again a high oxygen amount and underline the conglomeration of oxides on the powder particle surface. But in contrast to the earlier discussed EDX results the regarded particulates of this analysis contain a higher amount of aluminum and lower content of manganese. Thus the composition of the oxides differs. The oxides now contain manganese and aluminum in equal parts (both about 15 at.-%), only less silicon (0 to 2 at.-%) and additionally contents of titanium till 3 at.-%. The chromium and iron content instead stays stable and low. Hence, at this site of interest Mn-Al-O-oxides are dominant.

Further figures and EDX results that underline the conclusions about the HIP specimen are attached in the appendices B. 5 to B. 7.

5.2. Fracture surface analysis of the compact produced by supersolidus liquid phase sintering

XPS analysis

The XPS analysis results of the fracture surface of the SLPS specimen are very similar to the results of the HIP sample and show mainly carbon, oxygen, chromium, manganese and iron peaks in the spectrum. Other elements like nitrogen, sulfur, selenium, molybdenum and nickel are again only detected in traces.
Table 5. 2 and figure 5. 14 present the measured results and further depict the development of the element contents over the etching depth.

Table 5. 2.: Content of elements on the fracture surface of the SLPS sample, in at.-%

Content/ Element	C	N	O	Si	S	Cr	Mn	Fe	Se	Mo	Ni
Fracture surface	19.3	3.0	19.3	0	0.7	11.6	12.5	32.4	0.4	0.6	0.1
Etched 1 nm	10.7	3.5	19.1	0	0.7	13.2	12.3	39.6	0	0.8	0.2
Etched 5 nm	7.5	3.2	16.9	0	0	14.3	11.7	45.0	0	1.2	0.3
Etched 10 nm	7.5	3.0	16.6	0	0	14.2	11.5	45.7	0	1.3	0.2
Etched 50 nm	4.8	2.8	15.5	0	0	15.4	11.3	48.7	0	1.5	0

As already said the development of the elemental contents are very similar to the HIP sample and thus trends and distributions of the HIP sample apply for the SLPS sample as well. The only difference is that the SLPS sample has a higher amount of carbon and nitrogen on its surface.
The carbon amount on the as-fractured surface of the SLPS sample (19 at.-%) is much higher and decreases more steep in deeper etched regions to a lower amount of carbon (ca. 5 at.-% in an etching depth of 50 nm). This underlines the removal of carbon contaminations and further shows that the other elements are less affected in their development by the carbon distribution because they behave similar despite of the carbon content and development.
The much higher nitrogen content on the SLPS surface, 3.0 at.-% versus 1.0 at.-% of HIP, shows that the SLPS sample was alloyed with nitrogen during manufacturing.

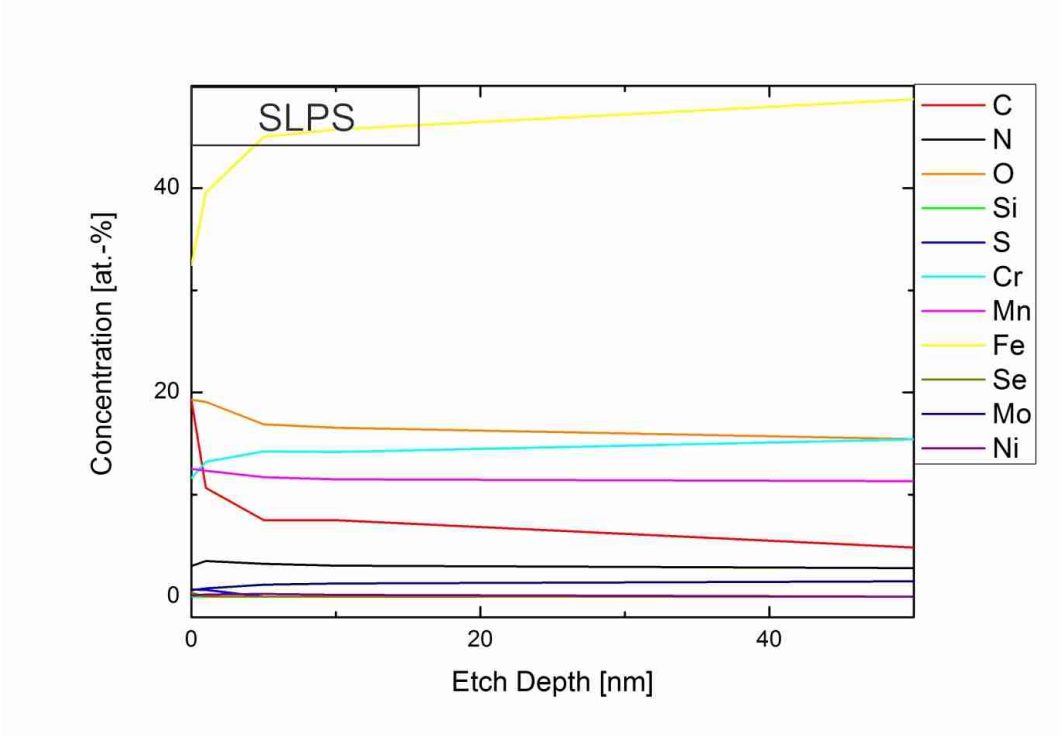

Figure 5. 14.: Development of the element content distribution with etching depth, SLPS specimen

The N-content in comparison to the C-content is much more stable over the etching steps and thus a homogeneous alloying instead of an absorption on the surface can be estimated.
To furthermore exclude the influence of lighter elements on the development of metallic elements figure 5. 15 depicts only the development of Fe, Cr, Mn, Mo and Si. Silicon was again detected only in trace amount and so not quantified.
It is obvious that both graphs (5. 14 and 5. 15) follow the same developments and that again the SLPS sample is very similar to the HIP sample. The carbon and nitrogen content thus does not influence the metallic elements.

The high resolution narrow scans (appendices B. 8 to B. 10) of Fe, Cr and Mn again show that a high portion of iron, chromium and manganese exists in metallic state and that the oxidic part especially for chromium and iron is very low.
This is further presented in figure 5. 16 which shows the content of metallic Mn, Cr and Fe over the etching depth.
It shows that the metallic iron and chromium contents increase with deeper etching depth and that metallic manganese content first decreases with first etching and then rises steadily from 48 % to 60 %.

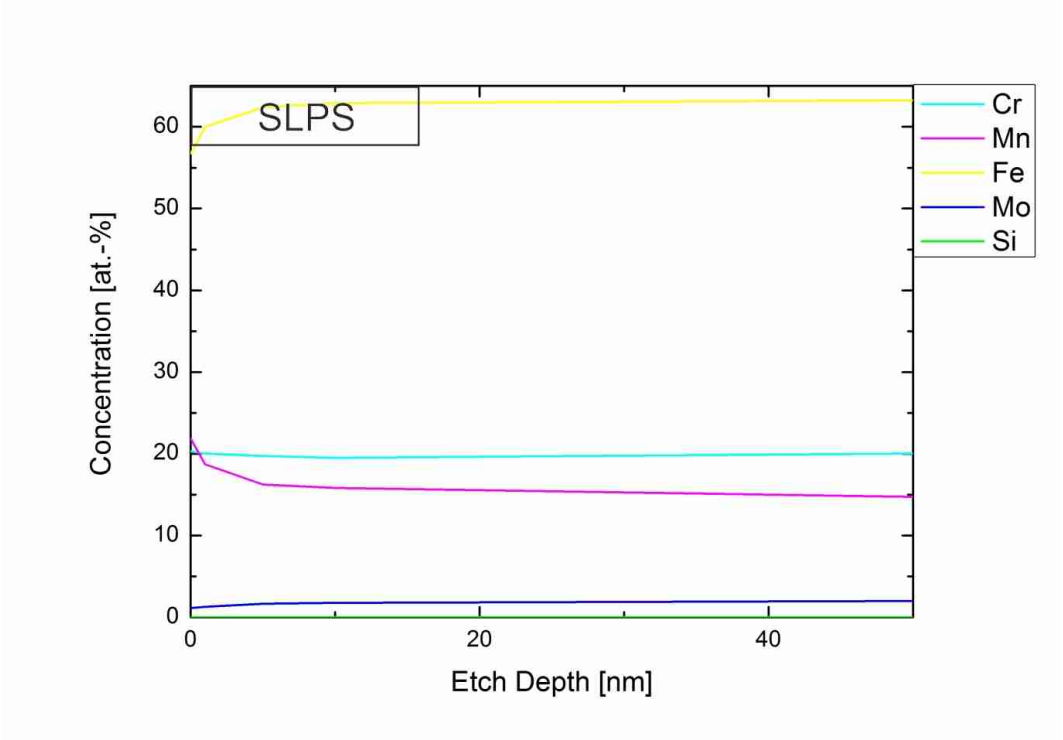

Figure 5.15.: Relative concentration of metallic elements over etching depth, SLPS specimen

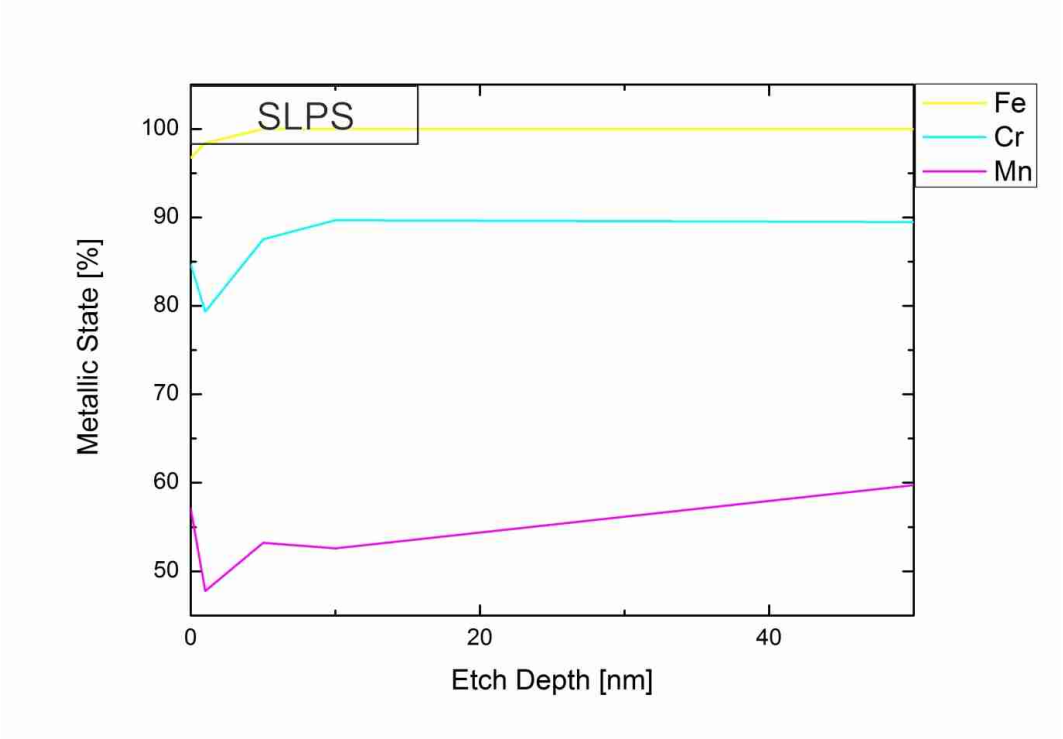

Figure 5.16.: Content of the metallic state of Fe, Cr and Mn over the etching depth, SLPS specimen

The differences compared to the HIP sample are slightly lower amounts of metallic contents for Fe and Cr. So oxidic iron exists in the SLPS sample till 1 nm of etching depth, but only in very low amount of 1.6 %. Metallic chromium follows the same trend, it increases but to a sligtly lower amount (89.5 % compared to 93.2 % in 50 nm etch depth of the HIP specimen). For metallic manganese the trend is again the same as measured in the HIP sample, but for manganese the metallic amount is much lower for SLPS as for HIP. Metallic Mn content of the HIP specimen was 66.8 % in 50 nm etching depth, for the SLPS specimen this value is around 60 %.
These results indicate a weaker reduction of oxides during SLPS consolidation, especially for manganese.

Additionally the normalized, relative cation concentrations [figure 5.17] show that the composition of the oxides in the SLPS sample is again manganese based.
At the pure surface and in 1 nm etch depth they still comprehend 12.9 % till 6.4 % of iron in oxidic state, but from 5 nm on they only consist of manganese and chromium in an ratio of 3:1. Figure 5.17 further shows that the chromium fraction in the oxidic state is rather constant around 25 % and that mainly the manganese fraction increases with decreasing iron content.

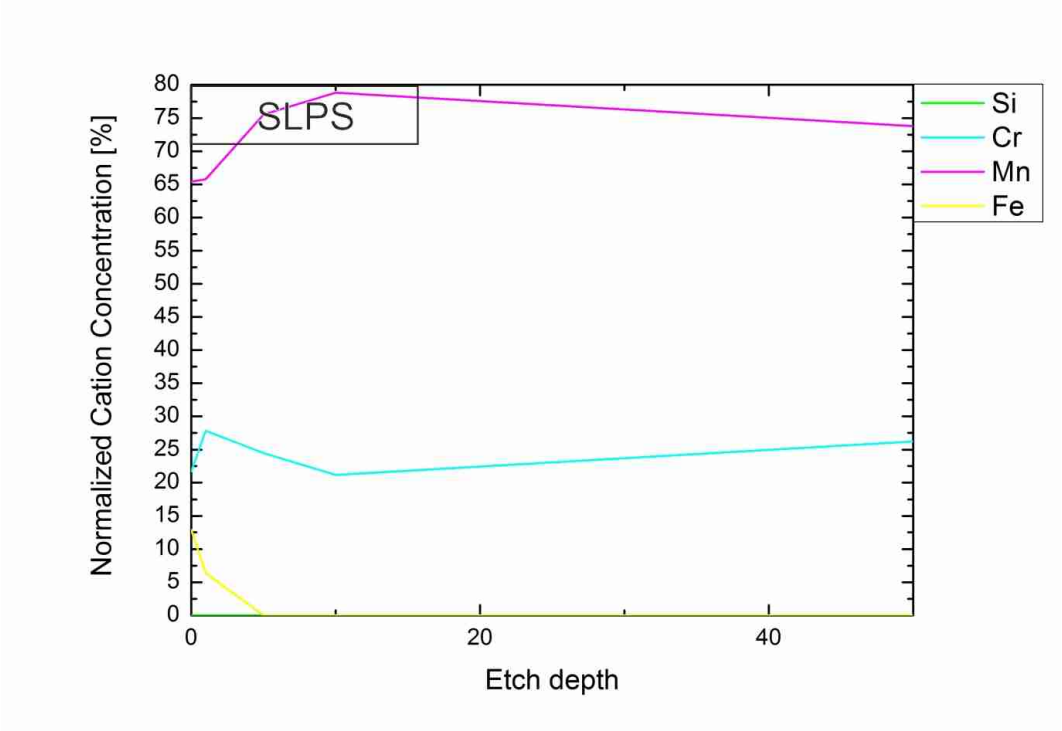

Figure 5.17.: Normalized relative cation concentration of the oxidic state, SLPS specimen

Figure 5.18 underlines this conclusion and further shows that the total oxide amount of the SLPS sample is higher than those of the HIP sample. It ranges from 14.3 at.-% on the as-fractured surface till 8 at.-% in 50 nm etch depth, the HIP sample only contained 10 at.-% to 6.3 at.-%.

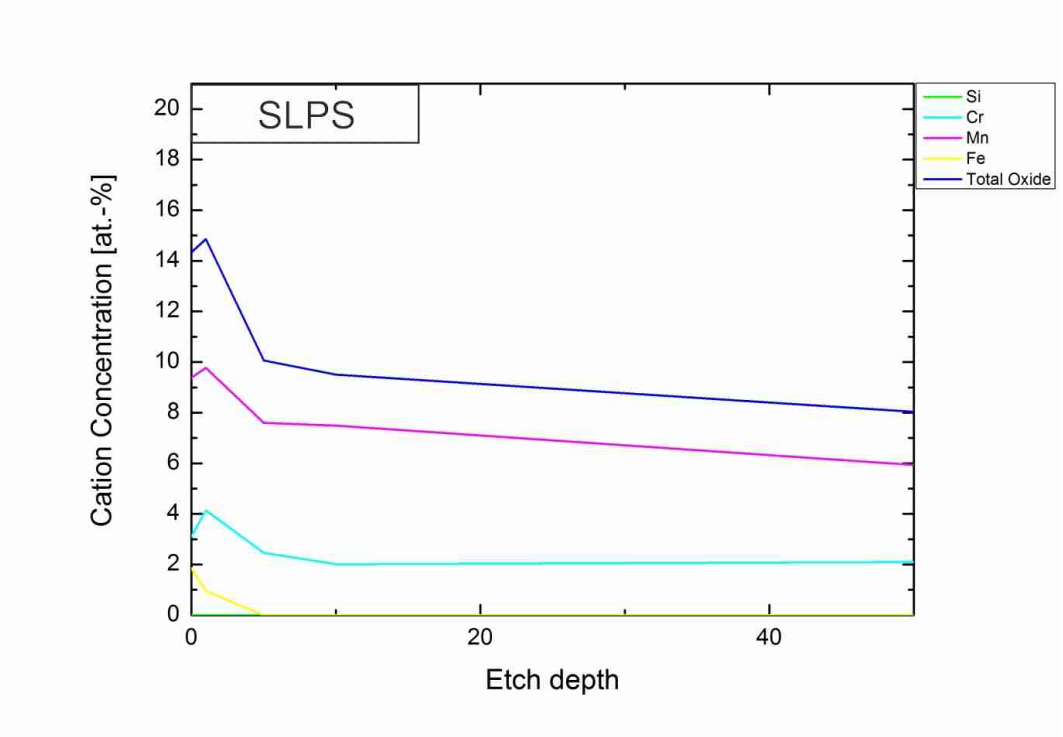

Figure 5.18.: Total sum of the cations and single cation concentrations depicted over the etching depth, SLPS specimen

SEM and EDX

The appearance of the densified powder mass after SLPS is presented in figure 5.19 and shows a highly densified sample with only a few larger pores. These pores are much larger compared to the HIP sample and do not only distribute at the grain boundaries, they even exist in the middle of some grains [b)].

The microstructure of this sample is more coarse compared to the HIP sample. The average grain size is about 150 μm and thus six times larger than in the HIP sample. Therefore the SLPS manufacturing influenced the size of the structure much more.

Again this sample is free of precipitations and so figure 5.19 d) shows a microstructure without carbides or nitrides.

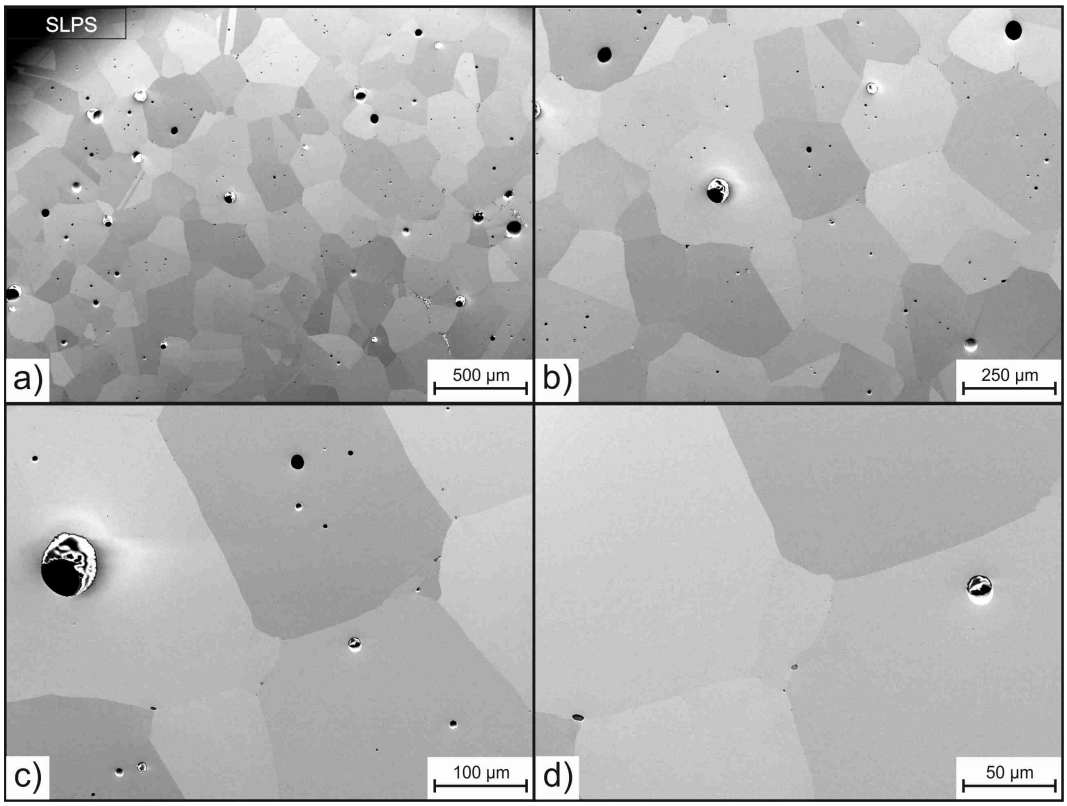

Figure 5. 19.: Overview of the densified powder mass, polished SLPS specimen

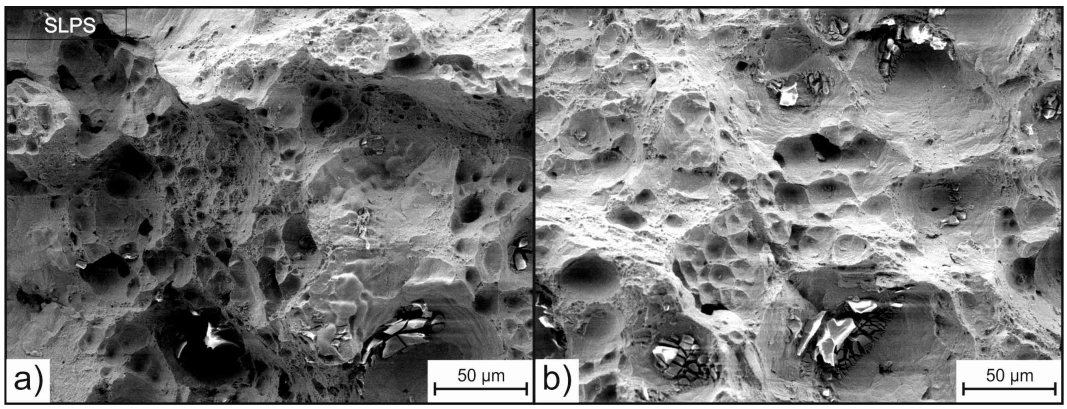

Figure 5. 20.: Overview of fracture surface, SLPS specimen

In addition the appearance of the SLPS sample after fracturing is shown in figure 5. 20. The fracture surface appears rather smooth and without deep dimples. In comparison to the HIP sample it shows much larger dimples but in lower amount and is not that fine structured because of the much larger grains.
Another characteristic feature is the existence of large agglomerated angular particulates which lie in larger dimples.

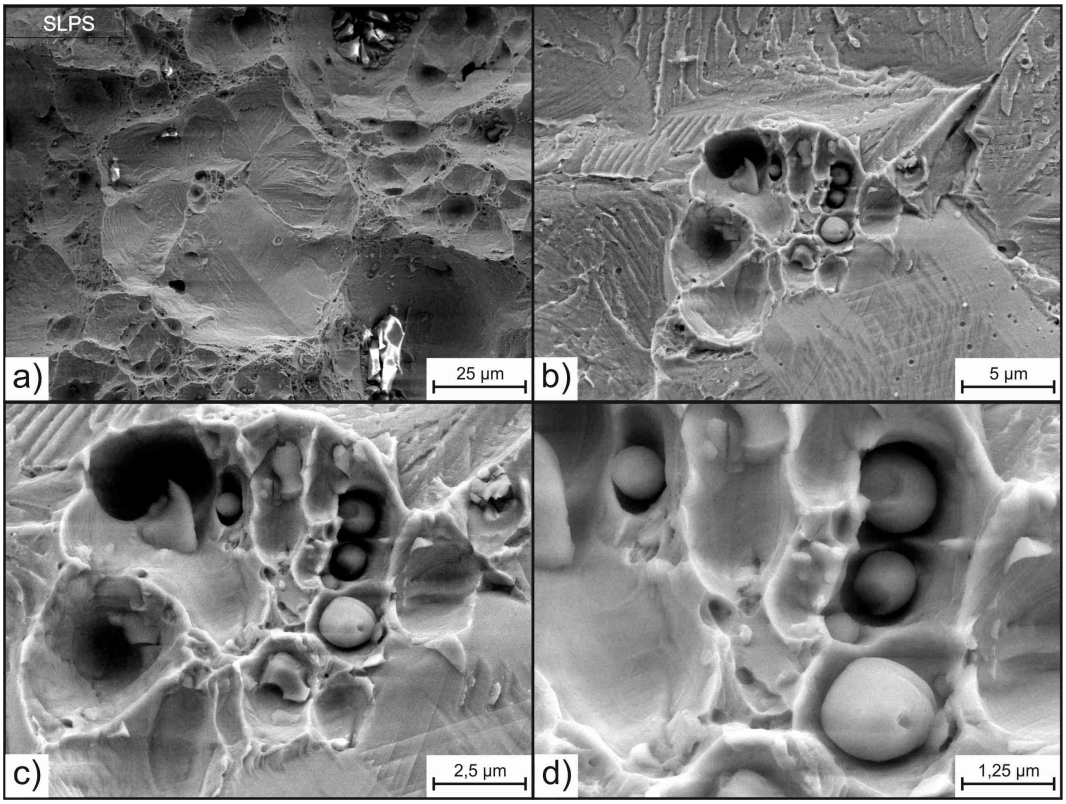

Figure 5. 21.: Close-up picture of spherical particulates on the fracture surface, SLPS specimen

Figure 5. 21 further shows that in the SLPS sample spherical particulates, similar to the particulates of the HIP sample, exist as well. These particulates appear much larger as in the HIP sample (average size of about 1 μm) and can be found in the middle of a smooth fracture site [Figure a) and b)].
Additionally figure 5. 22 shows another fracture site of the SLPS sample. This site is very smooth and with a closer look spherical particulates can be found in it as well.
The fracture mode of this sample furthermore looks different and appears to be a mixture out of different failure mechanisms. At some places it seems to be ductile and shows extensive deformation, but in some places it's rather brittle and smooth fractured. Therefore it can be concluded that different failure modes are present in the SLPS sample.

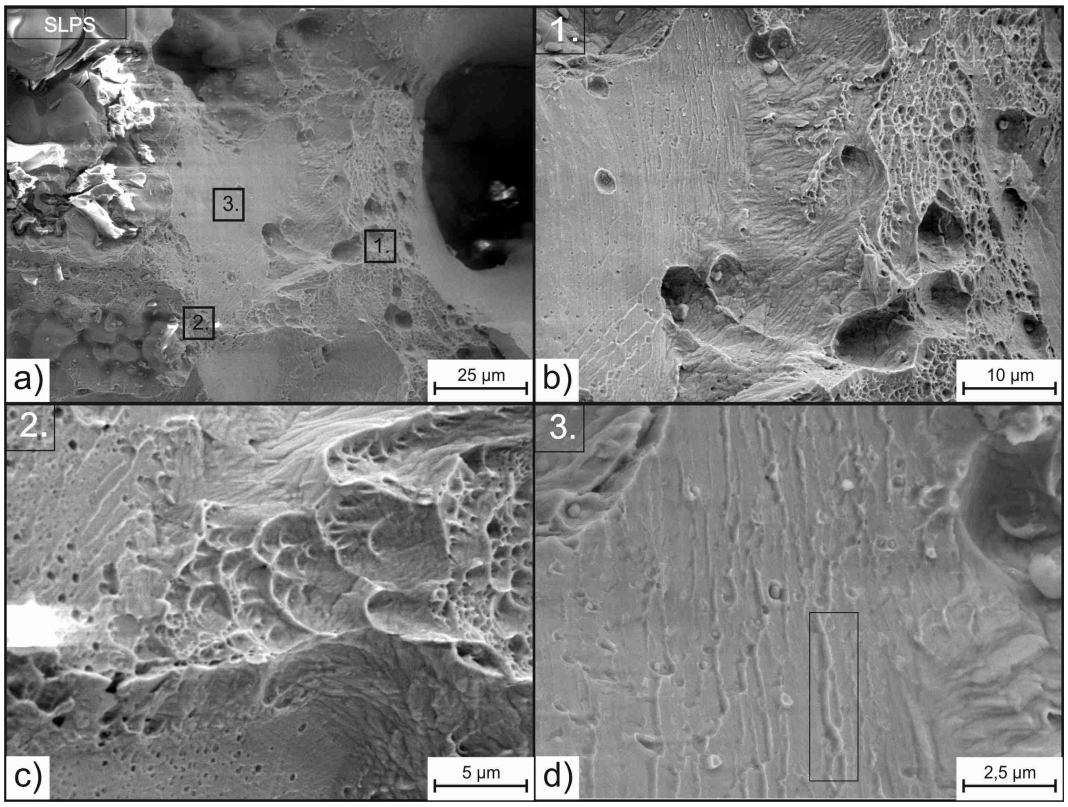

Figure 5. 22.: Mixed fracture surface, SLPS specimen

This can be understood best by analyzing the different areas of figure 5. 22 [b) to d)] which can be divided in three different fractured places.

Site one failed transparticle ductile along the particulates and also partly intergranular along the grain boundaries.

The second site contrarily shows a ductile interparticle failure indicated by fine inclusions.

The third site moreover indicates the presence of a brittle failure mode that can be either transgranular cleavage or intergranular decohesion [35].

When it comes to decohesion the surface does not appear to be smooth for such type of failure and grain boundaries of the neighboring surface are not visible. Further this type of failure mode appears to transform to transparticle transgranular ductile failuring inside area one.

Therefore the description above and the presence of river patterns are more characteristic for transgranular cleavage failuring. At the same time transgranular cleavage is only possible in the body-centered cubic and the hexagonal closed-packed structure and not in the austenitic face-centered cubic structure. Thus this fracturing mode is questionable in this type of site and it is more likely to conclude that the failure mode is rather intergranular decohesion, if the face-centered cubic structure is preconditioned [35].

These mixed failure mechanisms further show a rather high heteroginity of the SLPS sample and border it from the very homogeneous HIP sample.

Furthermore the appearance of different types of particulates distinguishes the SLPS sample and the HIP sample as well. Figures 5. 23, 5. 24 and 5. 25 show additionally particulates that exist in the SLPS sample and can't be found in the HIP specimen.

Figure 5. 23 presents large and rather spherical particulates distributing at SLPS sintering necks.

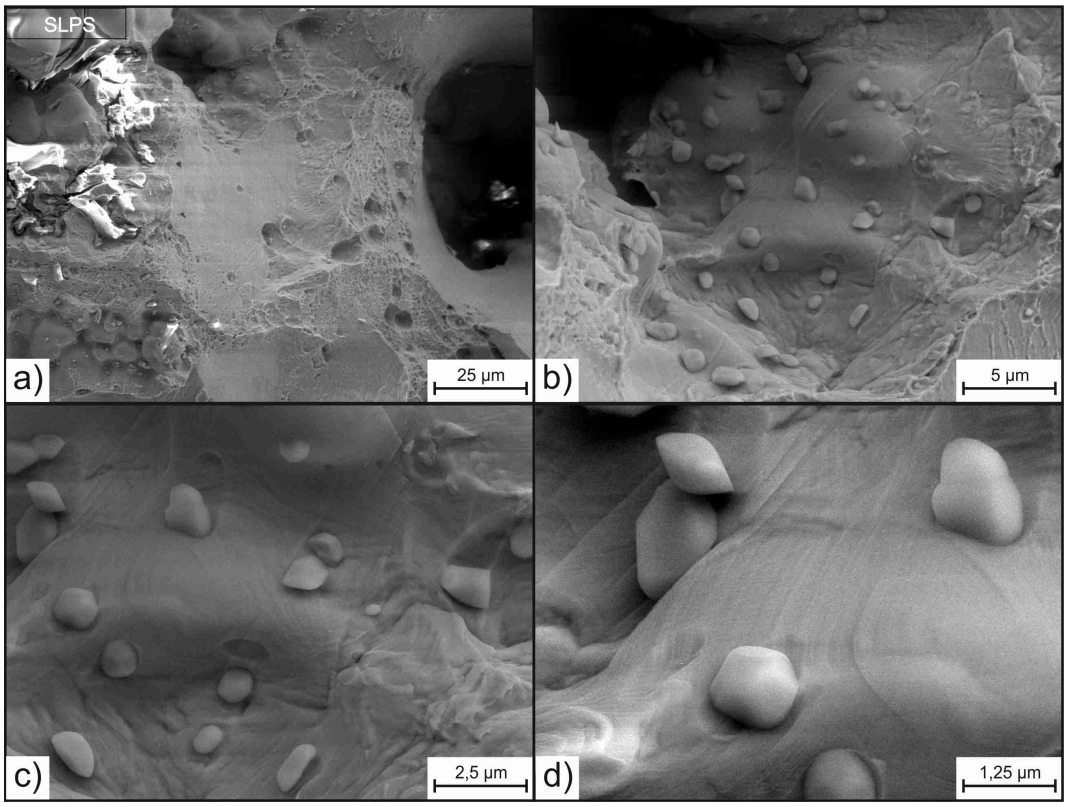

Figure 5. 23.: Large, spherical particulates at sintering necks, SLPS specimen

Figures 5. 24 and 5. 25 in opposite show very angular particulates which are quite large (about 2 μm in 5. 24).

The particulates in figure 5. 24 even distribute in the same positions as the spherical particulates which can be found in the HIP sample and the matrix failed very ductile around them. This indicates an inter- and transparticle dimple ductile fracturing at this site of interest as found in the HIP sample homogeneously which is only initiated by different shaped particulates. Further their assembly seems to be a composite of different phases as different shells can be distinguished exactly in image d).

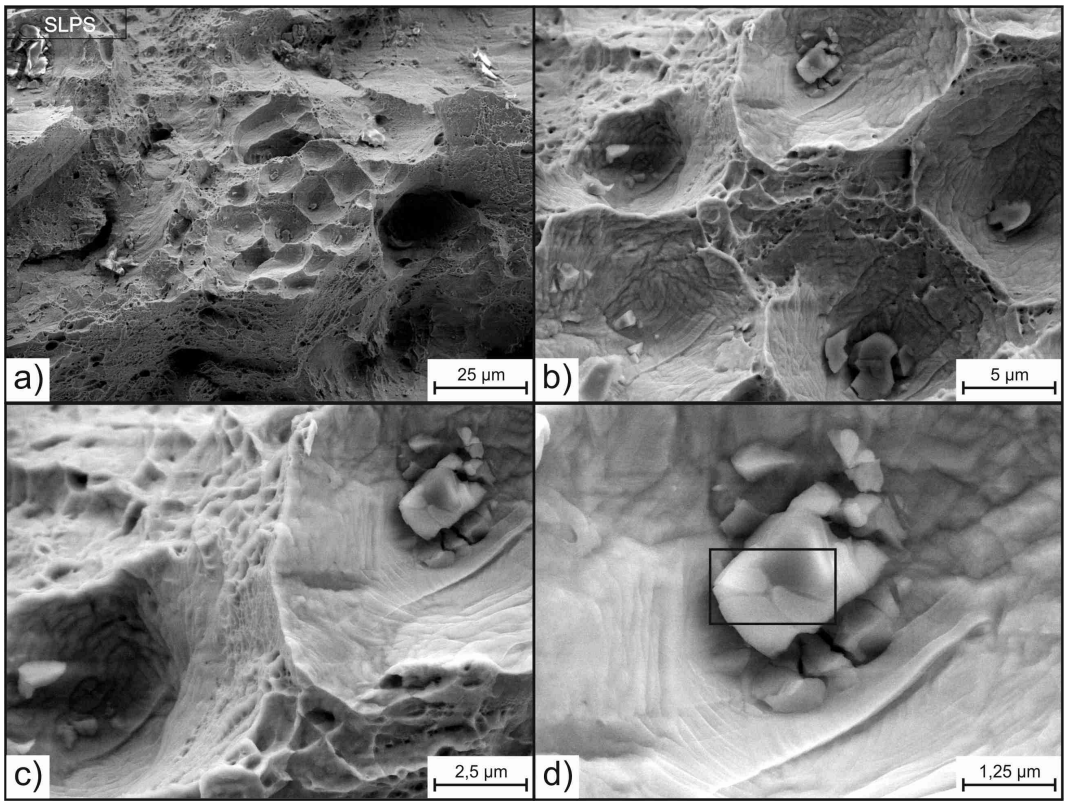

Figure 5. 24.: Closeup of angular particles distributing in the densified powder mass, SLPS specimen

Figure 5. 25 in contrast shows a very large and homogeneous agglomerate of particulate. These single particulates are very large and the agglomerates accumulate in larger dimples of the fracture surface. A detailed look [c) and d)] shows clean cracks trough them and estimates the brittle breakup of a single, large phase to many small ones.

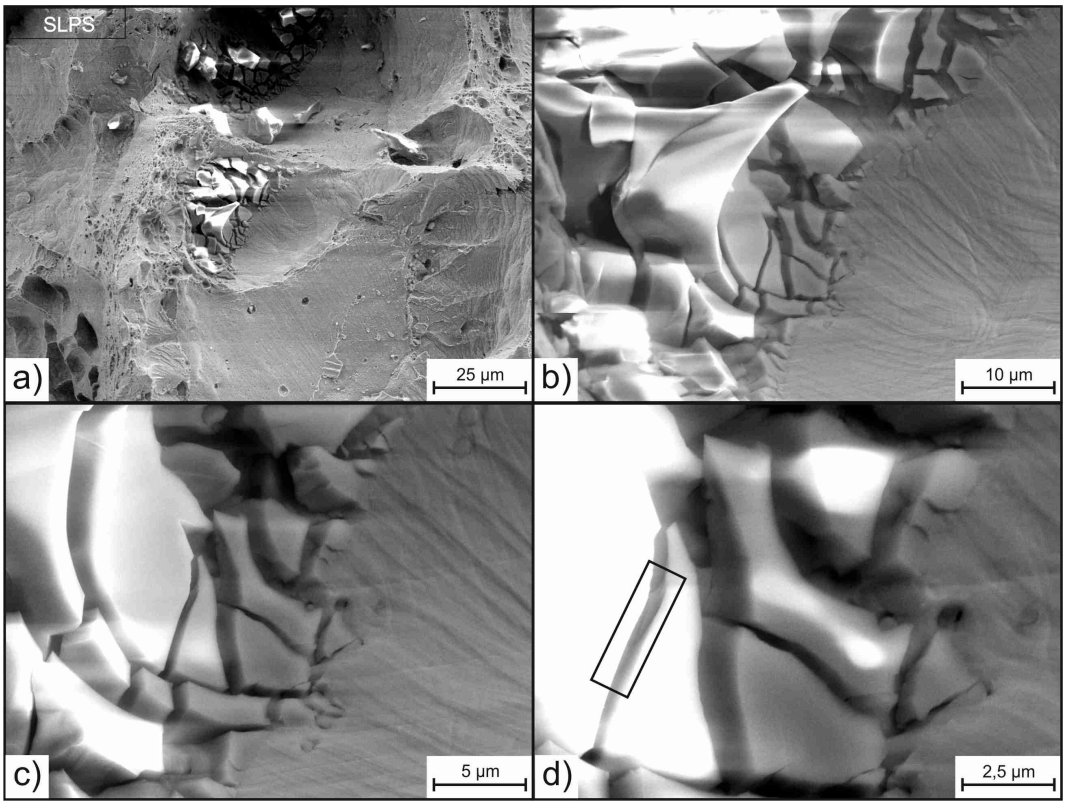

Figure 5. 25.: Agglomerated, angular particulates, SLPS specimen

In the next section EDX results are presented to complete the analysis of the till now considered fracture surface parts of the SLPS sample. These analyses focus on the different existing particulates and are presented in appendices B. 11 to B. 13.

The results of the analysis of the spherical particulates of figure 5. 21 show a very huge amount of manganese (44 to 57 at.-%) and sulfur (13 to 25 at.-%), but only a small fraction of oxygen (4 to 7 at.-%). Therefore it can be concluded that these particulates are not oxides and furthermore have a sulfidic character. Other elements are only contained in trace amounts and especially chromium and iron are only contained in less fractions than 10 at.-% [appendix B. 11].

The results presented in appendix B. 12 in opposite show that the particulates of figure 5. 23 are oxides. They contain about 50 to 60 at.-% oxygen and their fraction of manganese (20 -30 at.-%) and silicon (10 at.-%) is very high. The Si-conten is furthermore even higher as in the Mn-Si-O-oxides found in the HIP sample and in parallel the chromium (only 1.3 to 4.5 at.-%.) and iron (2 to 8 at.-%) amount decreases to lower values. Hence it can be estimated that these Mn-Si-O-oxides are more pure than the till now considered ones.

Although appendix B. 13 shows only low oxygen contents for the large, brittle particulates of figure 5. 25 it's obvious that these are oxides as well.
Because at least spectrum three of this measurements shows a high oxygen content of about 30 at.-% and additional measurements of similar particulates [appendices B. 17 and B. 18] show oxygen contents of 40 - 60 at.-%. Therefore these particulates can be identified as manganese and silicon rich oxides. The manganese and silicon ration is similar to the Mn-Si-O-oxides of measurement B. 12 and again only low chromium and iron fractions are detected. Concluding it can be stated that these particulates are of the same composition as the particulates of B. 12 and only their shape differs.
The different shape can be connected to the presence of a liquid phase in this sample and the fact that the particulates exist in different places of the fracture surface. While the particulates of appendix B. 12 exist at a liquid phase free solid state sintering neck the particulates of appendix B. 13 exist in the center of the densified powder mass.
They were influenced by the SLPS liquid phase which changed and dominated their shape. Hence the spherical oxides are molded-in in this sample and are found as large agglomerates.

Also the particulates depicted in figure 5. 24 and analyzed in appendix B. 14 can be identified as oxides. They consist mainly out of oxygen, manganese and aluminum and contain slightly higher amounts of chromium and titanium as the earlier discussed particulates in the SLPS sample.
Their composition fits quite well to the oxides found in appendix B. 3 in the HIP sample and they are also identified as Mn-Al-O-oxides.

Further figures and EDX results that underline the conclusions about the SLPS specimen are attached in the appendices B. 15 to B. 18.

5.3. Fracture surface analysis of the compact produced by solid state sintering

5.3.1. Solid state sintering without additional treatment

XPS analysis

The surface of the solid state sintered sample again mainly contains carbon, oxygen, chromium, manganese and iron. Other detected elements are nitrogen, sulfur, selenium, molybdenum, nickel and silicon. However the ratios and fractions differ much from the earlier discussed HIP and SLPS samples.
Table 5. 3 and figure 5. 26 present this values and depict their development over the etch depth.

Table 5. 3.: Content of elements on the fracture surface of the SSS sample, in at.-%

Content/ Element	C	N	O	Si	S	Cr	Mn	Fe	Se	Mo	Ni
Fracture surface	16.4	2.9	40.7	2.0	1.5	5.0	12.4	17.9	1.0	0.3	0
Etched 1 nm	6.0	1.7	43.7	1.9	1.8	5.7	15.7	22.3	1.1	0.3	0
Etched 5 nm	4.3	1.4	41.7	1.3	1.8	6.8	15.0	26.2	1.1	0.4	0
Etched 10 nm	6.7	1.9	38.7	1.4	1.4	7.5	14.4	26.3	1.1	0.5	0.1
Etched 50 nm	4.6	1.6	26.1	1.2	1.1	11.4	13.9	38.2	0.9	0.8	0.2

The carbon and nitrogen development of this sample is likewise the SLPS sample. The carbon content sharply decreases after the first etch step and then levels around 6 at.-%. The nitrogen content in contrast is much more stable and levels around 2.9 at.-% to 1.7 at.-% which again indicates a homogeneous alloying with nitrogen instead of an absorbtion.
The development of manganese is further similar to previous investigated samples too and levels in a range from 12.4 at.-% to 15.7 at.-%.
Further the chromium content is very low, at the fracture surface there is only 5.0 at.-% of Cr which increases with deeper ion etching to 11.4 at.-% in 50 nm etch depth.
And the iron content increases from only 17.9 at.-% on the as-fractured surface to 38.2 at.-% in 50 nm etch depth.
Contrarily to these low values the surface of the SSS sample shows a larger amount of oxygen.

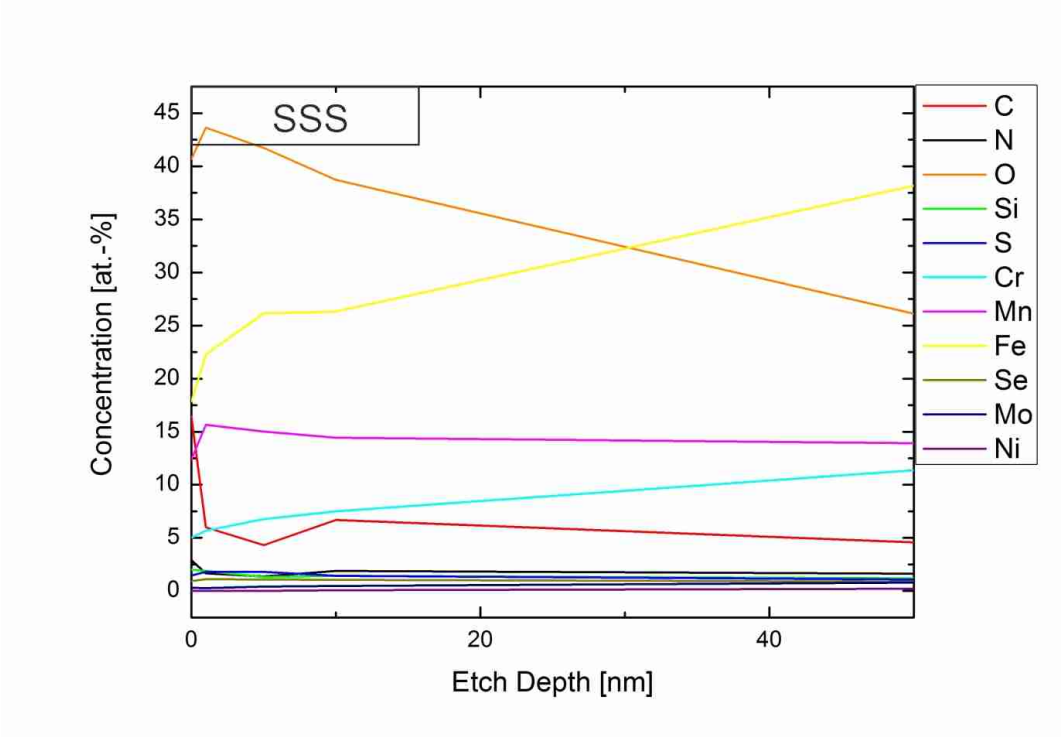

Figure 5. 26.: Development of the element content distribution with etching depth, SSS specimen

This amount starts with 40.7 at.-% at the as-fractured surface, increases slightly to 43.7 at.-% in 1 nm etch depth and then decreases steadily to 26.1 at.-% in 50 nm depth.
Additionally the SSS sample shows traces of 2 at.-% to 1.2 at.-% silicon which is the first quantification of Si during XPS investigations.
These results imply another configuration of the SSS specimens fracture surface in comparison to the HIP and SLPS sample and suggest that this sample is much more coated by cations in oxidic state.
Figure 5. 27 thus shows the distribution of metallic elements in the SSS sample with the etch depth.

It gets clear that a higher fraction of manganese (34.2 at.-% in 1 nm to 21.3 at.-% in 50 nm) exists and that in opposite chromium (12.4 at.-% in 1 nm to 17.4 at.-% in 50 nm) and iron (48.6 at.-% in 1 nm to 58.3 at.-% in 50 nm) have lower fractions. Additionally silicon exists with 5.4 at.-% on the as-fractured surface decreasing to 1.8 at.-% in 50 nm etch depth.

The high resolution narrow scans of the SSS specimens surface for Fe, Cr and Mn (appendices B. 19 to B. 21) underline the assumption of more oxides on the fracture surface. They show a much higher occurrence of the oxidic state for each element and less fraction of the metallic

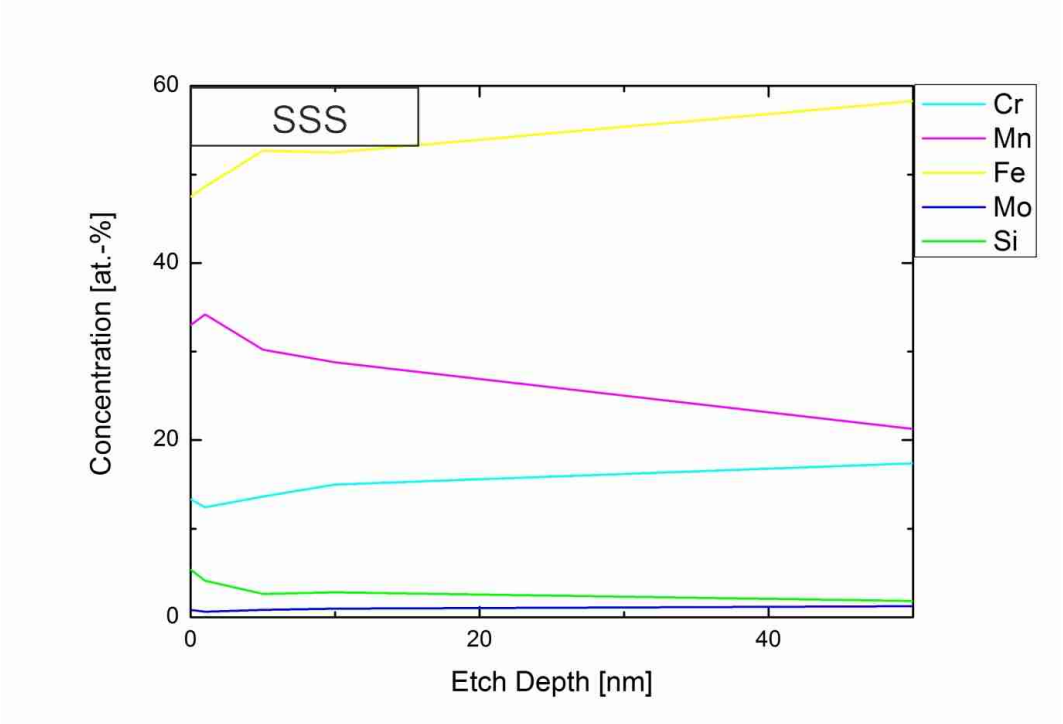

Figure 5. 27.: Relative concentration of metallic elements over etching depth, SSS specimen

state. The fracture surface differs much from the HIP and SLPS specimens which nearly have only metallic iron and chromium on their surface.

Figure 5. 28 sums this conclusion up and shows that iron (81 % in 1 nm to 92 % in 50 nm), chromium (73 % in 1 nm to 79 % in 50 nm) and manganese (10 % in 1 nm to 36 % in 50 nm) are in lower quantity in metallic state.
For the as-fractured surface it further has to be pointed out that even more Fe, Cr and Mn is in metallic state as for the ion etched state of 1 nm. Especially for iron and manganese 10 % more of the elements are metallic.

To consider the different fractions of the oxidic state [figure 5. 29] on the SSS specimens fracture surface now also silicon has to be taken into account.
This leads to a changed composition of the oxides on the surface. Even though still 60 % to 65 % of the cations are manganese, also 10 % to 15 % of silicon and chromium and 10 % to 25 % iron are present.

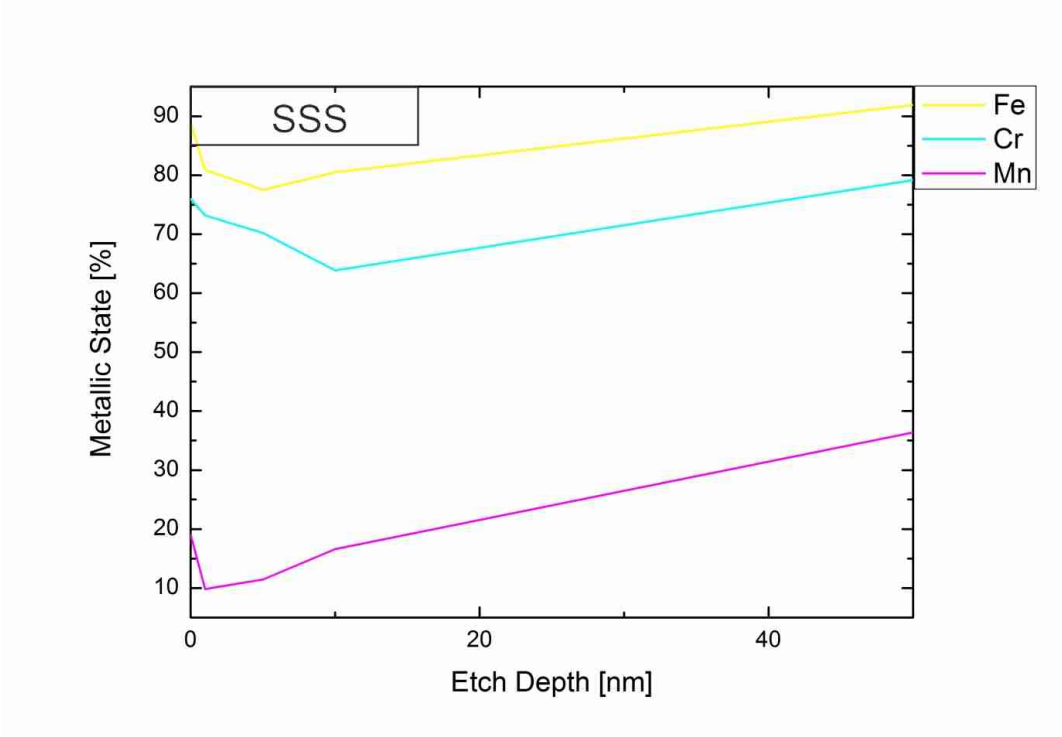

Figure 5.28.: Content of the metallic state of Fe, Cr and Mn over the etching depth, SSS specimen

Furthermore the manganese and silicon amount decreases during the first etching steps and then levels constantly, while chromium and iron increase parallel. Thus the dominance of Mn and Si cations on the top surface layer seems to drop with deeper ion etching.

Figure 5.30 completes this consideration as it shows a decreasing amount of manganese cations. This figure shows that the number of manganese cations decreases, from 30.8 at.-% in 1 nm to 13.5 at.-% in 50 nm, and that the fraction of silicon cations decreases as well. However it does not show the increase of chromium and iron cations. So these cations and thus the oxide value of chromium and iron do not increas in quantity. Their fraction of the total oxide amount only increases because their amount does not decrease as steep as the amount of manganese.
The high manganese amount and thus the total oxide amount in contrast decrease rapidly and so the chromium and iron amount of the normalized oxidic state increase because the rather constant Cr and Fe cation values take a greater fraction in the normalized consideration of the oxidic state. Hence the normalization virtually changes the oxide composition.

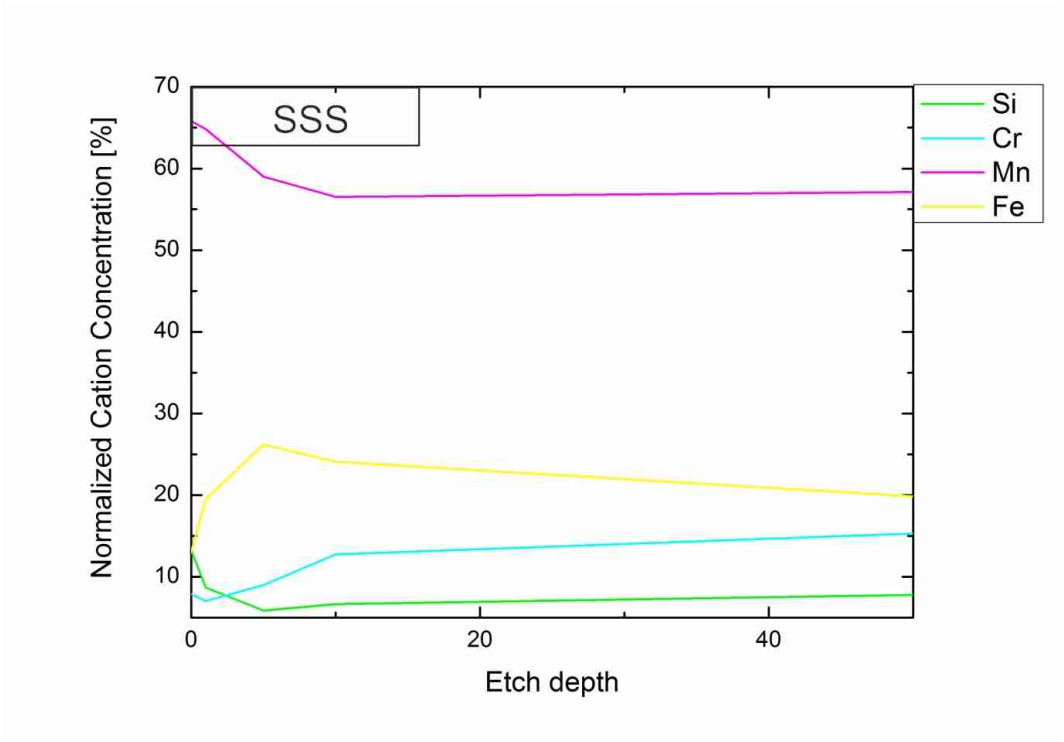

Figure 5. 29.: Normalized relative cation concentration of the oxidic state, SSS specimen

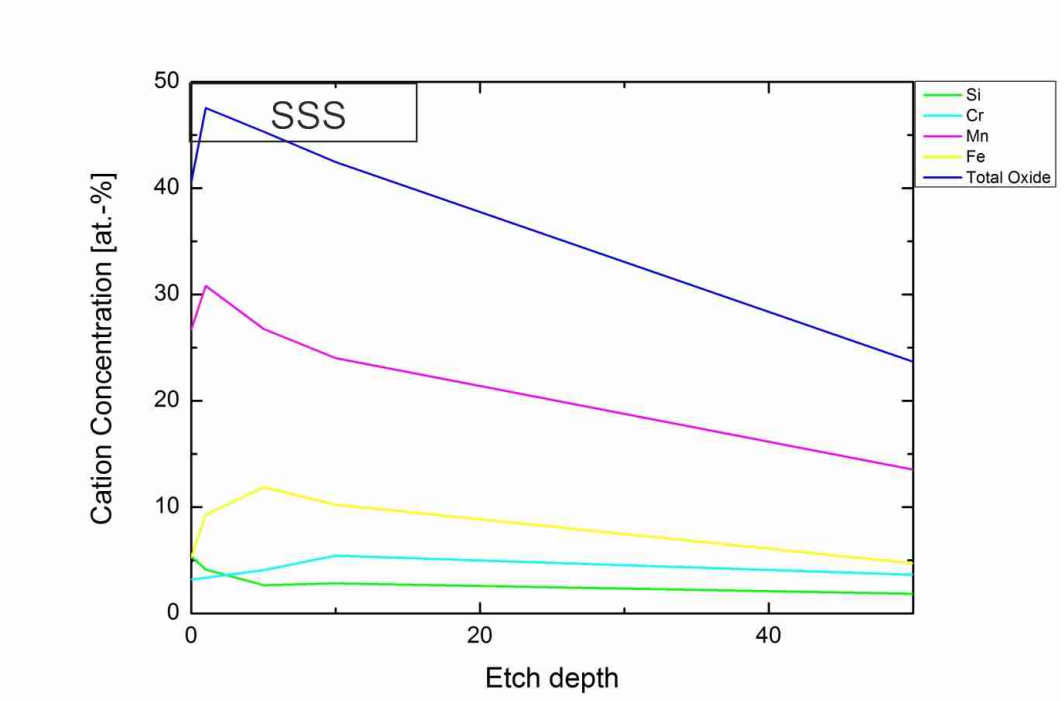

Figure 5. 30.: Total sum of the cations and single cation concentrations depicted over the etching depth, SSS specimen

The total amount of oxides in the SSS sample is indeed much higher as in the HIP and in the SLPS samples and ranges between 47.6 at.-% in 1 nm to 23.7 at.-% in 50 nm, still dominated by manganese which takes the largest fraction.

SEM and EDX

In figure 5.31 the densified state of the solid state sintered powder mass is displayed. This figure shows a much more coarsened microstructure compared to the HIP sample, but with an average grain size of 100 μm much smaller grains as of the SLPS sample [a) and b)]. In contrast to the HIP and the SLPS sample this sample has a much higher porosity after manufacturing. The pores are larger and in higher number existent. A closer look on the grain boundaries [c) and d)] further shows remaining precipitation in the microstructure. Hence the solution annealing after manufacturing didn't led to a carbide and nitride free state.

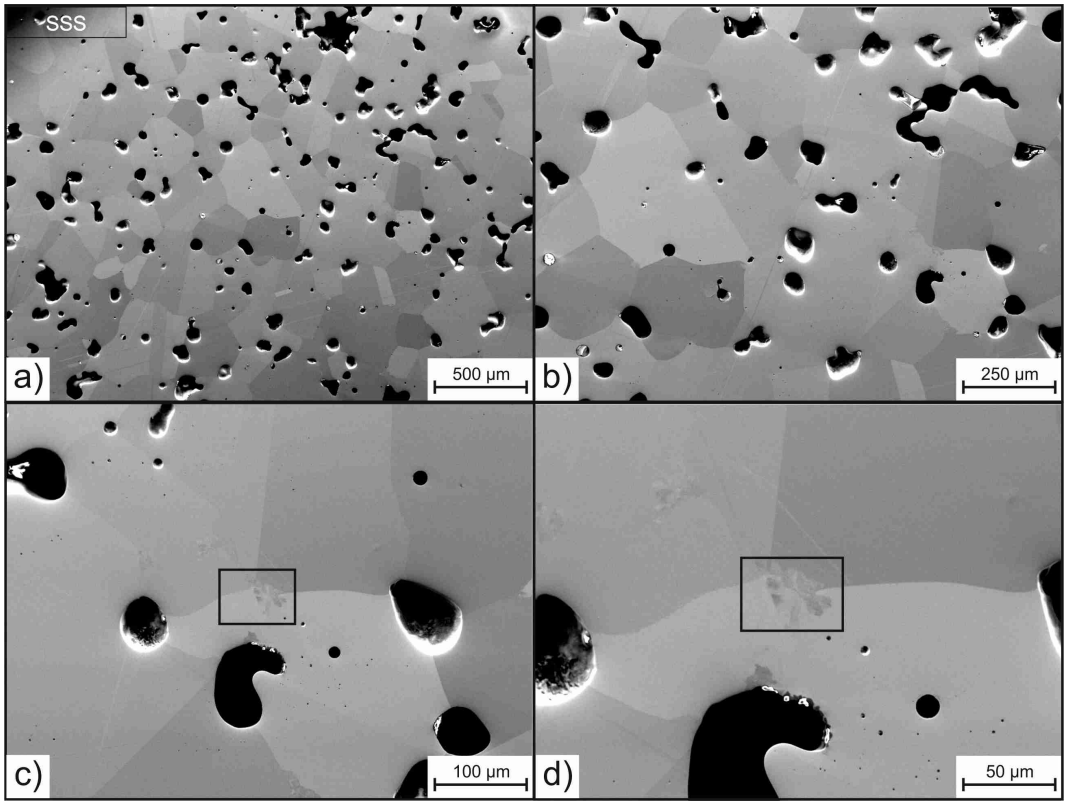

Figure 5.31.: Overview of the densified powder mass, polished SSS specimen

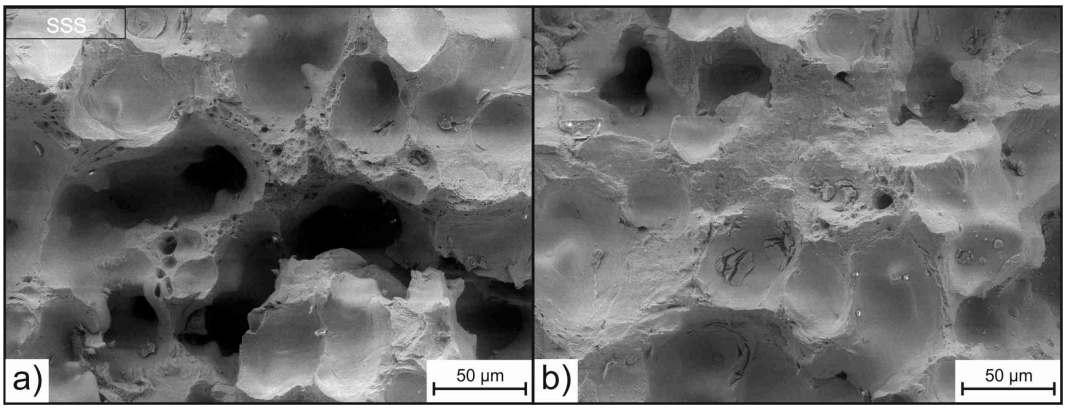

Figure 5. 32.: Overview of fracture surface, SSS specimen

Likewise the fracture surface of the SSS sample looks different compared to the till now considered ones. Figure 5. 32 shows a much more porous surface with deeper caviations [a)] and large differences in height.
Furthermore it can be seen that this sample consolidated via sintering necks between the particles and fractured localized at these places. Further the larges buckets of the fracture surface are remained pores and exist in the powder mass from the beginning on.

Figure 5. 33 depicts a sintering neck and its failure mechanism. The fracturing mode is interparticle ductile with large dimples at coarse inclusions [35]. This mechanism of failure is very homogeneous and residues along the former sintering necks.
The size of the spherical particulates is similar to the spherical oxides of the HIP sample and has an average value of about 550 nm.

At this point additionally particulates which exist on the fracture surface are regarded. These particulates were not enclosed in the sintering necks during consolidation, they furthermore exist on the surface of the sintering necks. Figures 5. 34 to 5. 36 present the different types of particulates.

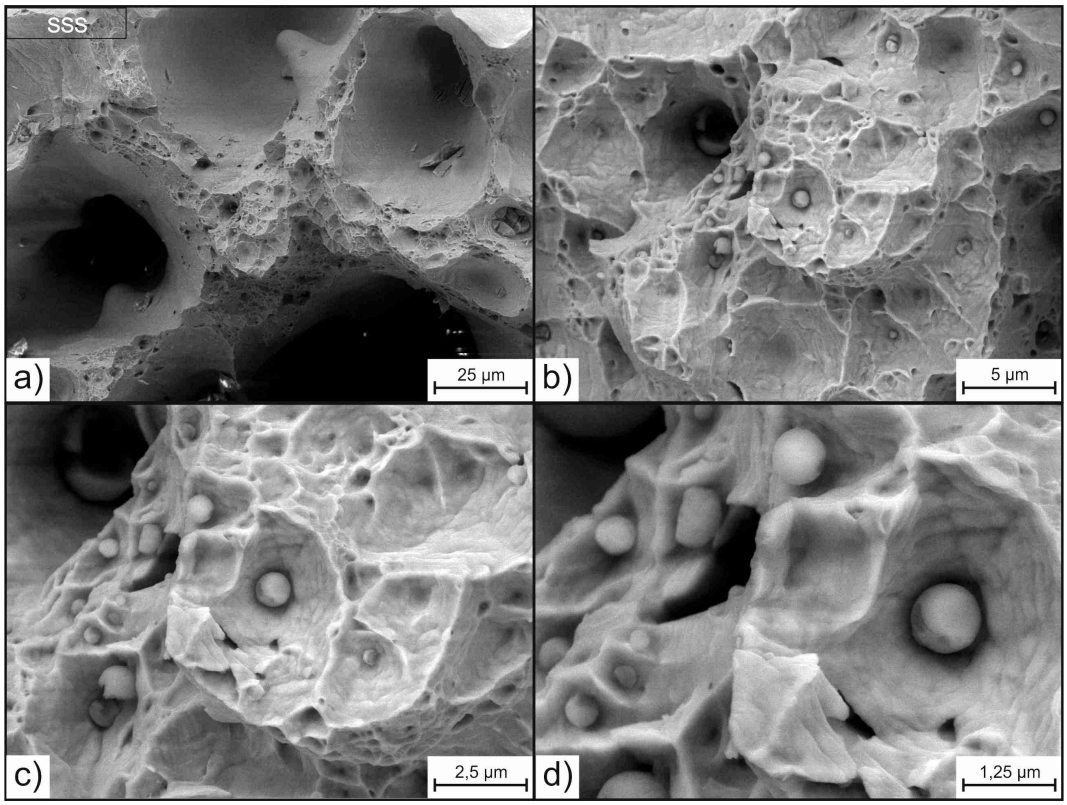

Figure 5.33.: Closeup of the spherical particulates distributing in the densified powder mass, SSS specimen

The first type of such particulates is shown in figure 5.34 and presents loose particulates of spherical shape. These particulates are not connected to each other or the matrix and the matrix looks rather oxidized too. It is not as clean as before and seems to be coated with oxide. The second type of particulate is a large, irregular formed particulate lying in a pore [figure 5.35]. This particulates looks like the large, agglomerated Mn-Si-O-oxides found in the SLPS compact and lies on the uncoated matrix. At this site evaporation lines indicate the presence of pure metallic matrix [c)]. The particulates itself is angular and cracks through it indicate again a brittle character [d)].

The third type of particulate is new in the line of these steel powder compacts. Its complete shape reminds of a large flake and it is furthermore build up by different modules. First the flake is covered with a inhomogeneous coating itself. This coating consists of a thin film and porous, complicated shaped isles in it. In this film and on the flake additionally large, angular particulates distribute which have the form of a pyramid.

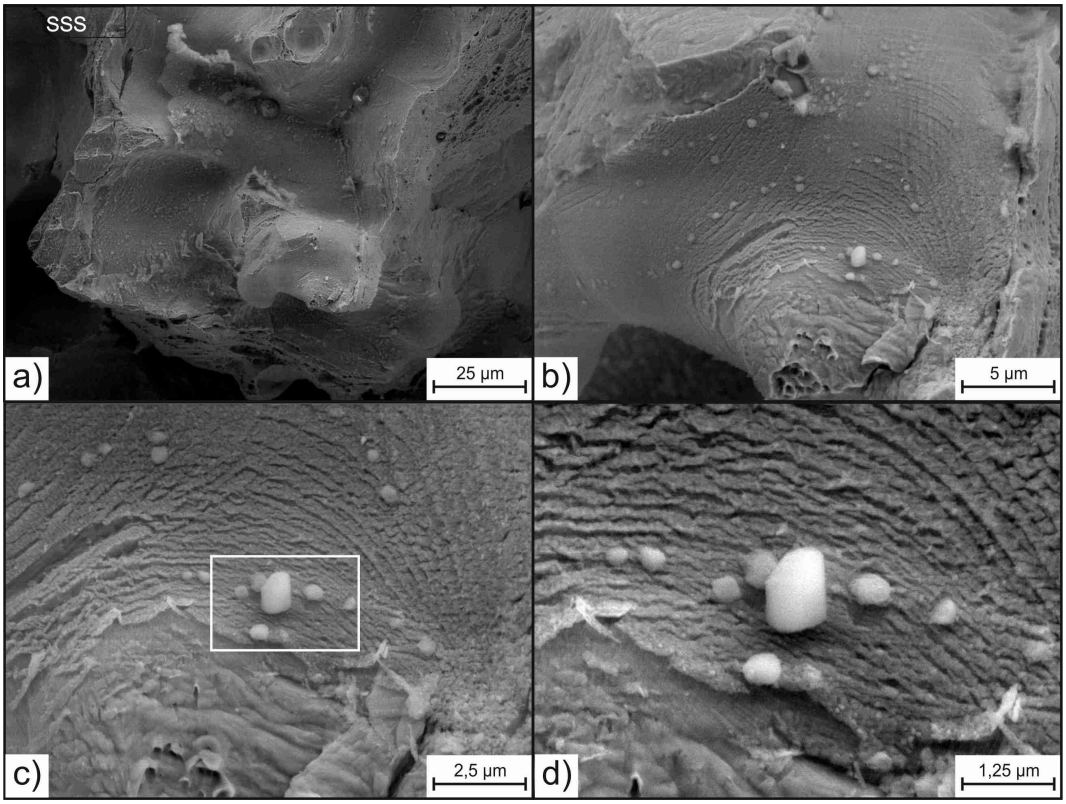

Figure 5. 34.: Loose particulates on the sintering necks distributing in an oxidic layer on the surface, SSS specimen

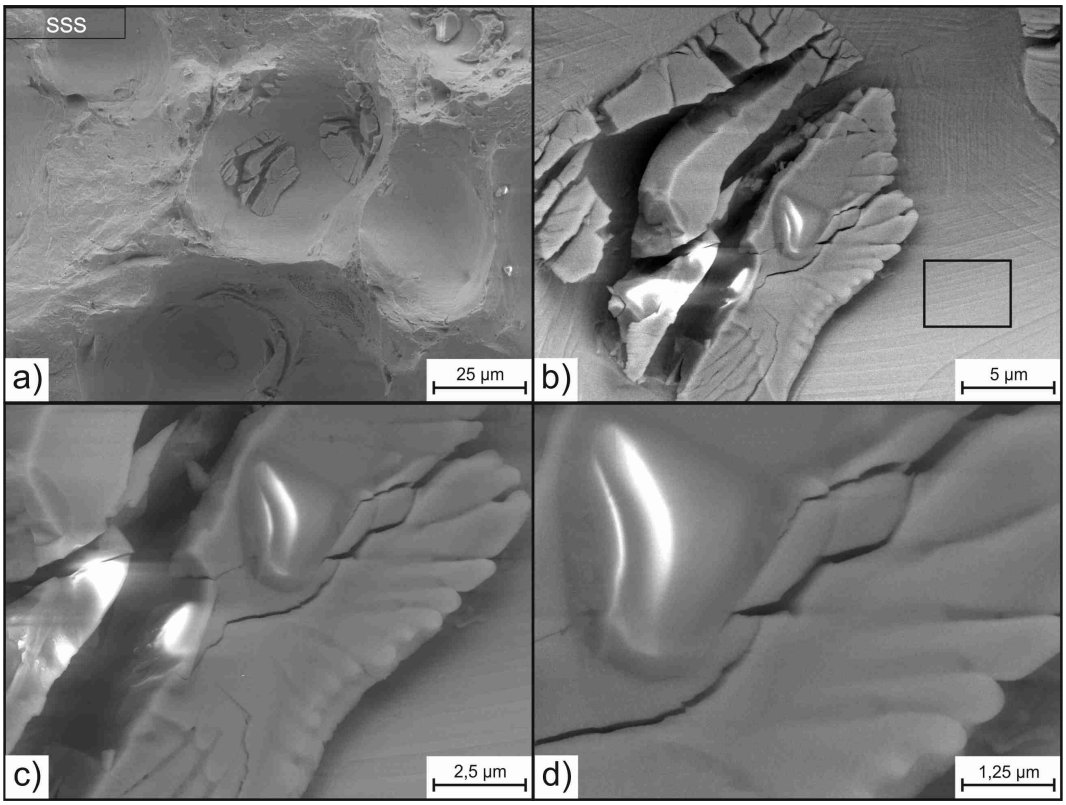

Figure 5. 35.: Agglomerated, angular particulates distributing in pores, SSS specimen

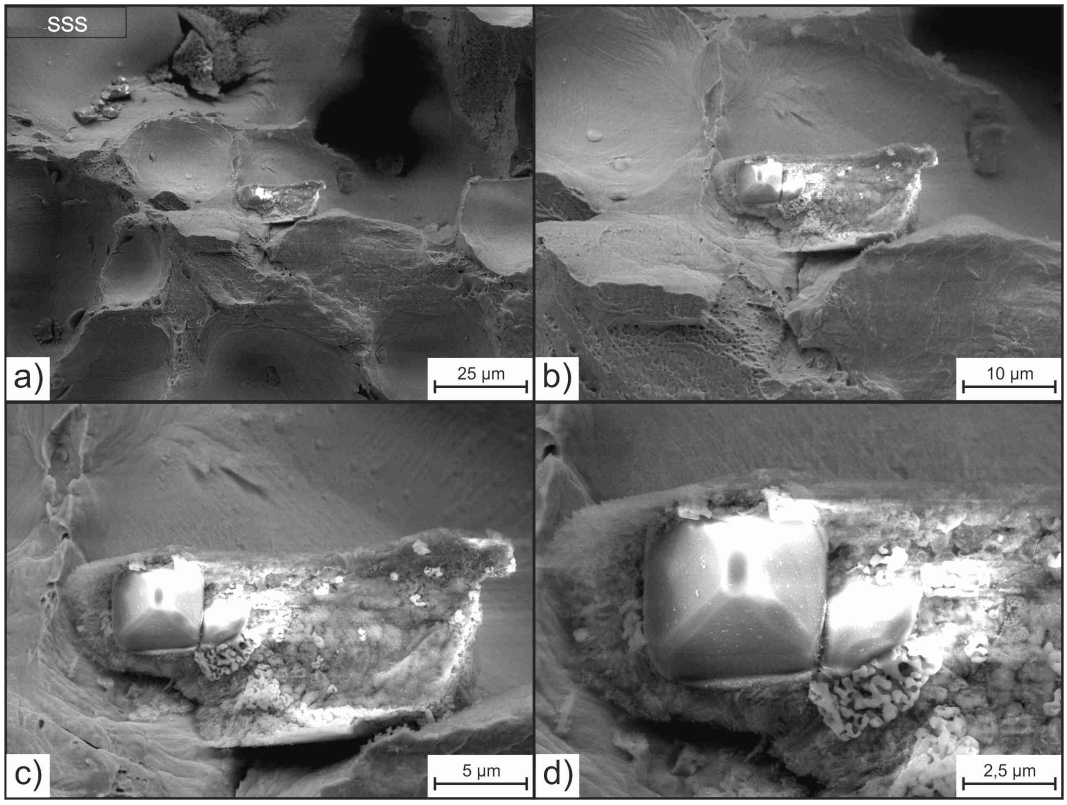

Figure 5.36.: Loose, irregular shaped particulate in former sintering pore, SSS specimen

To gain knowledge about the composition and the character of these many different particulates of the SSS sample following EDX measurements are regarded.

These analyses are presented in appendices B. 22 to B. 25 and depict the composition of the single particulates.
Appendix B. 22 presents the results of the analysis of the spherical particulates found in the fracture face. It indicates an oxidic character of these particulates (22 to 56 at.-% oxygen content) and further shows a high amount of manganese (17 to 36 at.-%). Furthermore they contain aluminum (7.5 to 15 at.-%), selenium (0.7 to 8.6 at.-%) and sulfur (1.7 to 8.4 at.-%). Here it is essential to mention that Se and S contents are high when the Al content reaches its lowest level and vice versa, thus they seem somehow connected in their summarized amount which is always about 20 at.-%.

The results of the EDX analysis presented in appendix B. 23 show that the particulates of figure 5. 34 are oxides and that the matrix, which was measured in spectrum 4, contains a lot of oxygen too. The matrix thus is coated with an oxidic layer, but further only contains the typical matrix elements Cr, Mn and Fe in a normal ratio 1:1:3 which allows no evaluation of the composition of this layer.
The particulates contain a high amount of manganese (13 to 20 at.-%) and iron (11.6 to 18.7 at,-%). The manganese content is typically for Mn-O-oxides but the iron content is the highest measured for oxidic particulates till now. Thus it can be concluded that these particulates indeed contain a larger iron fraction or that because of their small size the matrix was measured in larger fractions and thus the iron originates from this point.

The large, agglomerated particulate of figure 5. 35 is analyzed in appendix B. 24. These measurements show a high manganese amount (12.4 to 53.6 at.-%) for every measured spot and in opposite low chromium and iron contents (under 4 at.-%). Measurements 2 and 3 further show a huge amount of oxygen.
However it can be estimated that the composition of this particulate is very mixed. While spectrum 1 and 3 show much selenium, sulfur and molybdenum additionally to the high manganese amount. Spectrum 2 mainly shows aluminum and traces of titanium. Thus the composition changes much over the particulate profile and fits to different earlier observed compositions.

The measurements presented in appendices B. 25, B. 31 and B. 32 analyze the particulate of figure 5. 36 and a very similar one. They show that these particulates can be clearly divided into different parts.

At first the background, metallic matrix [appendix B. 25 spectrum 4] contains much oxygen and Cr, Mn and Fe in the typical 1:1:3 ratio.

Secondly the matrix of the flaky particulates itself [appendices B. 25 and B. 31 spectrum 3] contains more oxygen and only less iron. It moreover consists of manganese, selenium and sulfur. For which the fractions change but the sum stays stable.

The third place are the porous, complicated shaped precipitations on the flake [appendix B. 25 spectrum 2, appendix B. 32 spectrum 2 and 3]. These contain lower oxygen contents as the flake-matrix and much less manganese. In opposite their selenium (about 30 at.-%), sulfur (about 20 at.-%) and molybdenum (about 11 at.-%) fractions are extremely high. Thus these parts of the microstructure can be identified as selenides.

The large, smooth particulates on the flake in opposite containe no Se, S or Mo [appendices B. 25, B. 31 and B. 25 spectra 1]. The composition is very exactly always 60 at.-% of oxygen, 11 to 13 at.-% manganese and 20 at.-% aluminum. Thus they have a similar composition like the earlier identified Mn-Al-O-oxides.

Further figures and EDX results that underline the conclusions about the SSS specimen are attached in the appendices B. 26 to B. 32.

5.3.2. Solid state sintering with dwelling at 700°C under vacuum

XPS analysis

Carbon, oxygen, chromium, manganese and iron dominate the surface composition of the solid state sintered sample dwelled at 700°C. But for this sample additionally selenium and sulfur take a larger fraction of the surface composition. The V700 sample contains the highest amounts of selenium and sulfur of all samples and they decrease steadily with the etch depth.
In opposite the amount of oxygen is quite low for a solid state sintered samples, it only ranges from 36 at.-% in 1 nm etch depth to 22 at.-% in 50 nm and is the lowest oxygen value of all solid state sintered samples. The other detected elements like nitrogen, molybdenum, nickel and silicon are detected in similar amounts and developments as in the other sintered samples and show no characteristic differences.
These fractions and developments are depicted in table 5. 4 and figure 5. 37.

Table 5. 4.: Content of elements on the fracture surface of the V700 sample, in at.-%

Content/ Element	C	N	O	Si	S	Cr	Mn	Fe	Se	Mo	Ni
Fracture surface	12.6	2.7	34.4	1.1	8.9	4.4	13.0	15.4	6.4	1.1	0
Etched 1 nm	5.6	2.4	35.9	1.5	7.0	5.8	15.6	20.5	4.7	1.0	0
Etched 5 nm	4.5	1.7	34.7	1.0	7.5	6.8	15.5	23.1	3.9	1.3	0.1
Etched 10 nm	5.7	1.3	33.9	1.1	5.3	7.7	14.4	25.7	3.5	1.3	0.2
Etched 50 nm	4.7	2.6	22.0	0.4	2.8	11.1	14.2	38.5	2.3	1.3	0.2

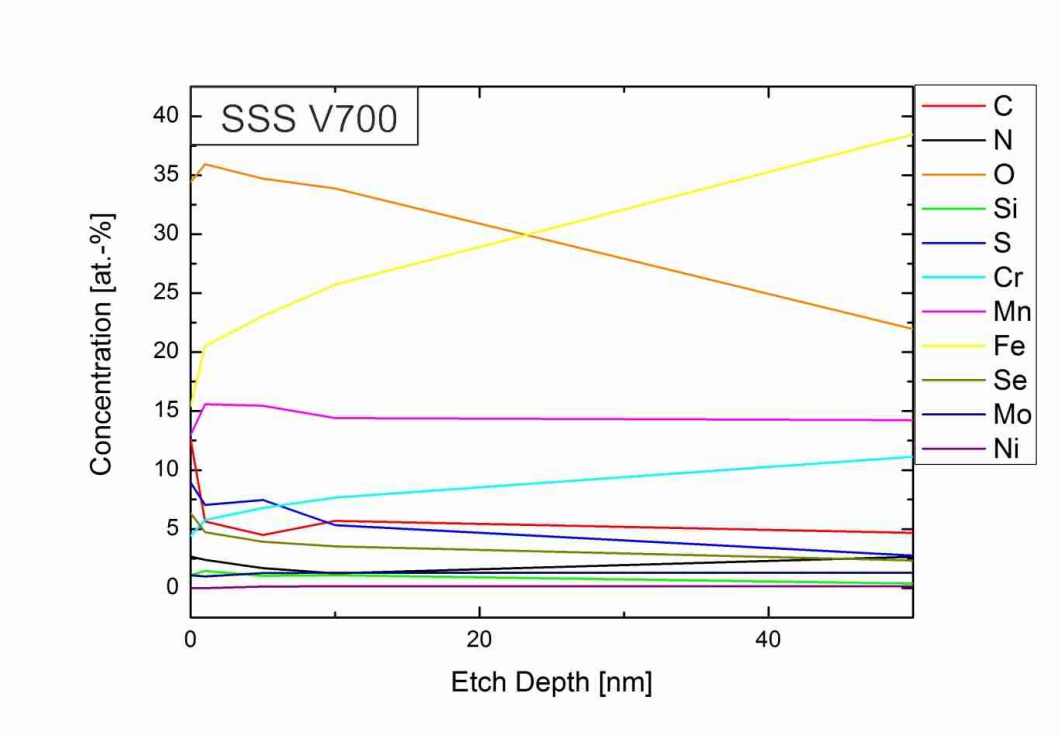

Figure 5.37.: Development of the element content distribution over etching depth, V700 specimen

Figure 5.38 moreover depicts only the development of the metallic elements with the etching depth. Here selenium and sulfur are excluded and therefore do not influence the distribution of metallic elements. This presentation moreover does not show any characteristic difference to the earlier discussed simply sintered sample.

The high resolution narrows scans (appendices B.33 to B.35) and the depiction of the metallic content of Fe, Cr and Mn [figure 5.39] show again a similar state of the V700 sample as for the SSS sample. The oxidic fractions are quite high and especially for manganese only a small part is metallic.

For chromium even less part is metallic in the V700 sample as in the SSS sample. The values lay around 5 % to 10 % under the SSS values and only increase to a higher amount in an etch depth of 50 nm.

Considering the composition of the relative cation concentration only a slightly lower silicon fraction and a very stable iron fraction around 20 % needs to be mentioned, the remaining distribution is the same as for the the SSS sample [figure 5.40].

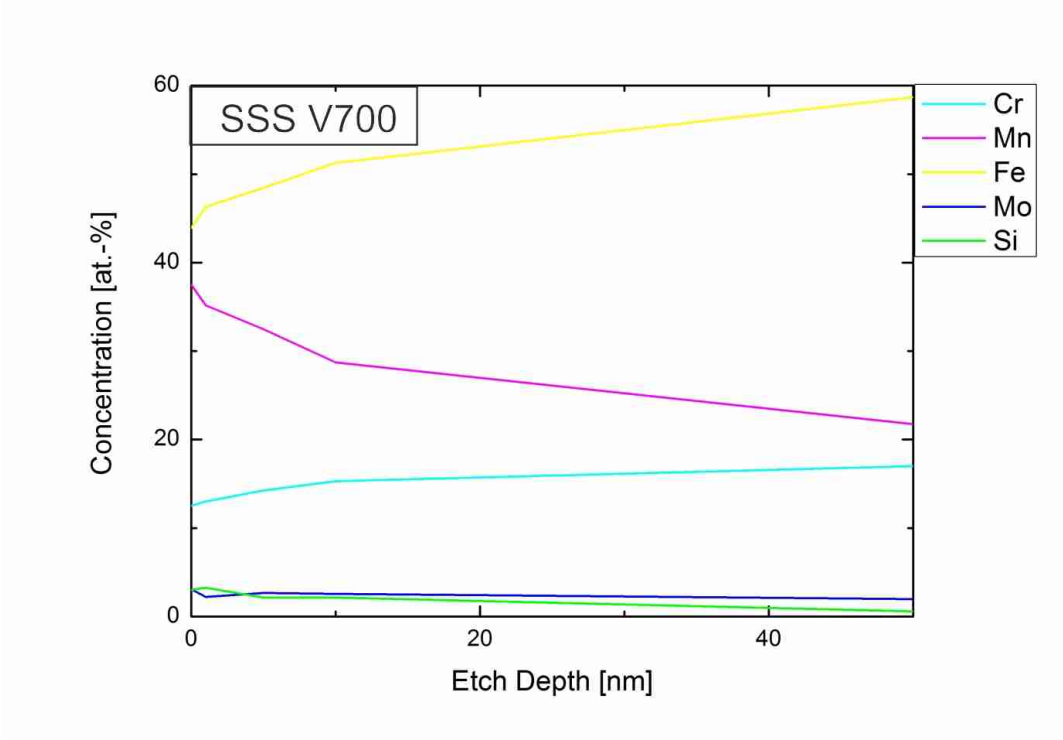

Figure 5. 38.: Relative concentration of metallic elements with etching depth, V700 specimen

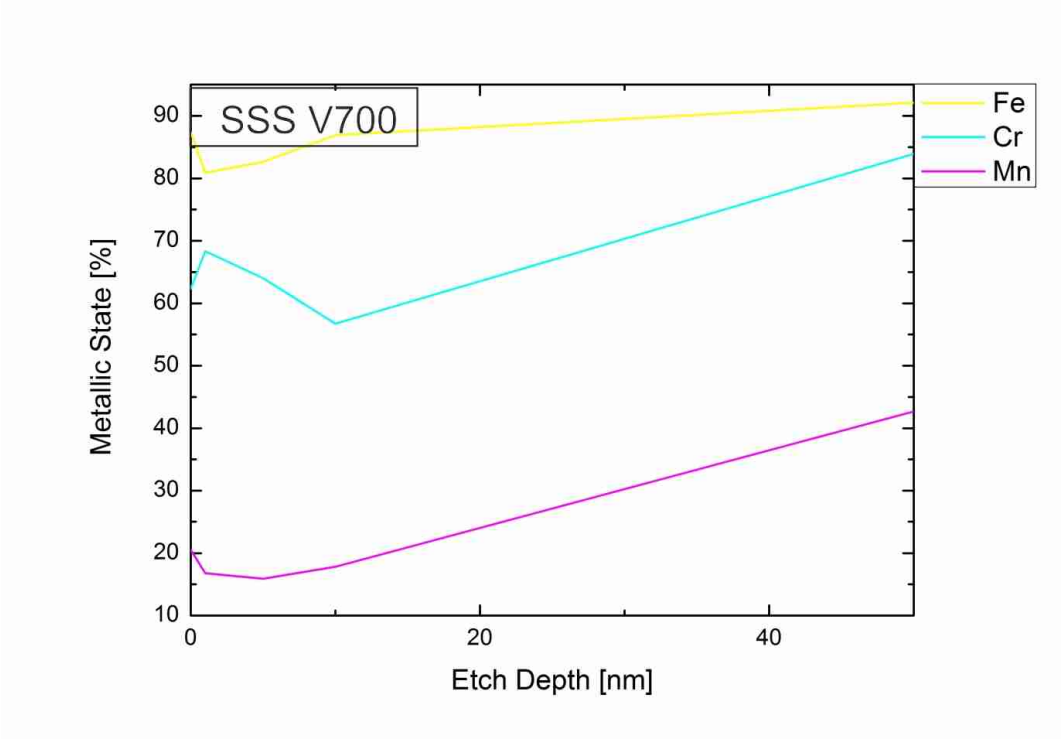

Figure 5. 39.: Content of the metallic state of Fe, Cr and Mn over the etching depth, V700 specimen

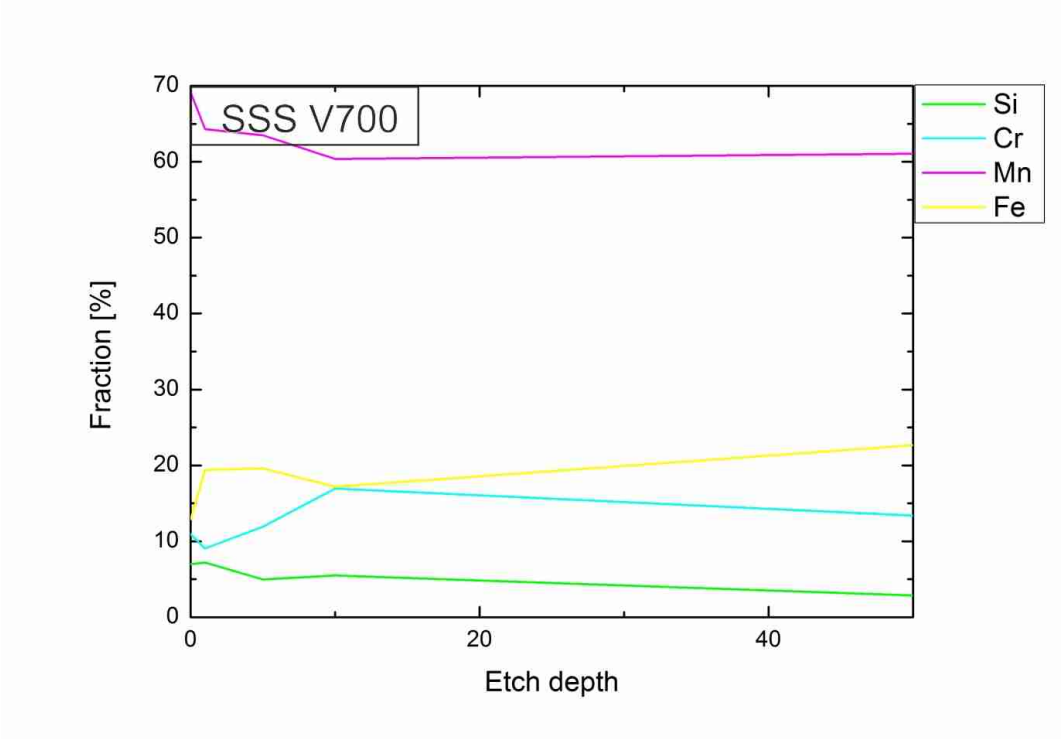

Figure 5. 40.: Normalized relative cation concentration of the oxidic state, V700 specimen

Figure 5. 41 shows complementary that the total oxide amount is nearly the same for the V700 sample as for the SSS sample as well. The developments do not differ and everything that was said for the SSS sample without dwelling under vacuum conditions applies for the V700 sample as well. The oxides are manganese based and only the silicon content is slightly lower.

Concluding the state of the oxides in sintered V700 sample does not differ much from the SSS sample. Their value, composition and development over the etch depth are very similar and show no noteworthy influence of the dwelling step at 700°C under vacuum.
The most characteristic feature that distintcs the V700 sample from the other samples is thus the larger selenium and sulfur amount.

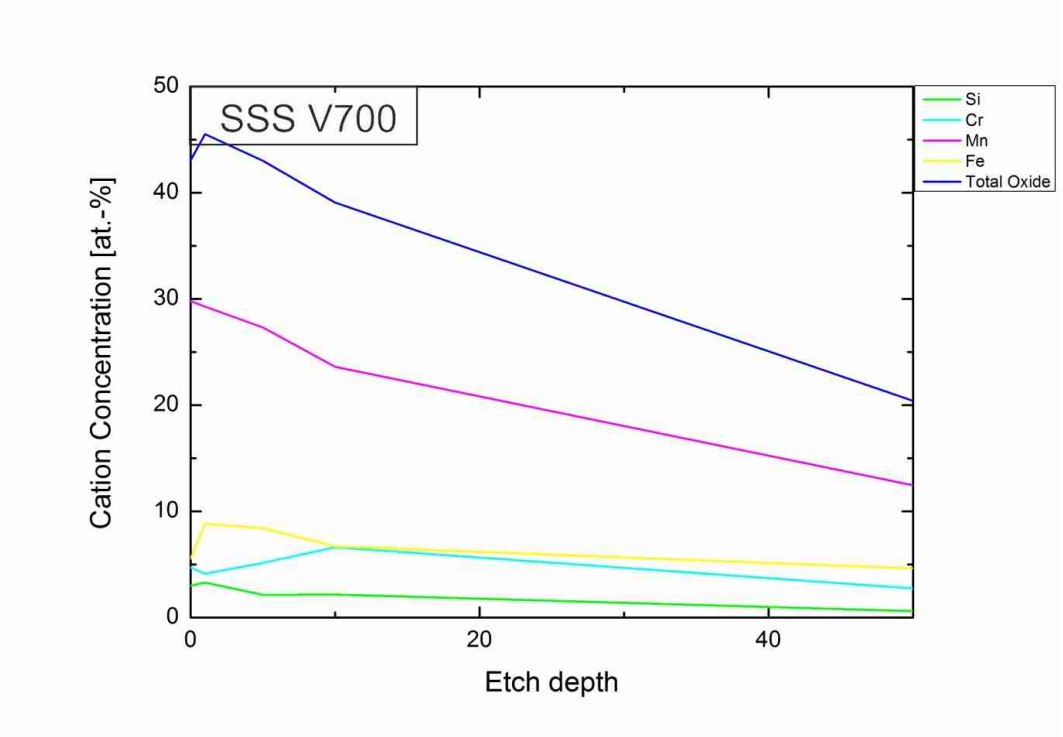

Figure 5. 41.: Total sum of the cations and single cation concentrations depicted over the etching depth, V700 specimen

SEM and EDX

Figure 5. 42 presents an overview of the solid state sintered sample which was dwelled at 700°C under vacuum before final consolidation at 1340°C.

Figures a) and b) show a rather porous structure which appears similar to the only sintered sample. Additionally the grain size is 100 μm as well and the amount of pores seems equal. The closeup in figure d) furthermore shows a precipitation free structure and no carbides or nitrides at the grain boundaries. Therefore the solution annealing was successful for this sample.

The figure of the V700 specimens fracture surface [figure 5. 43] shows again a very rough status. There are a lot remaining pores and caviations on the fracture face and thus the surface is uneven like the SSS surface.

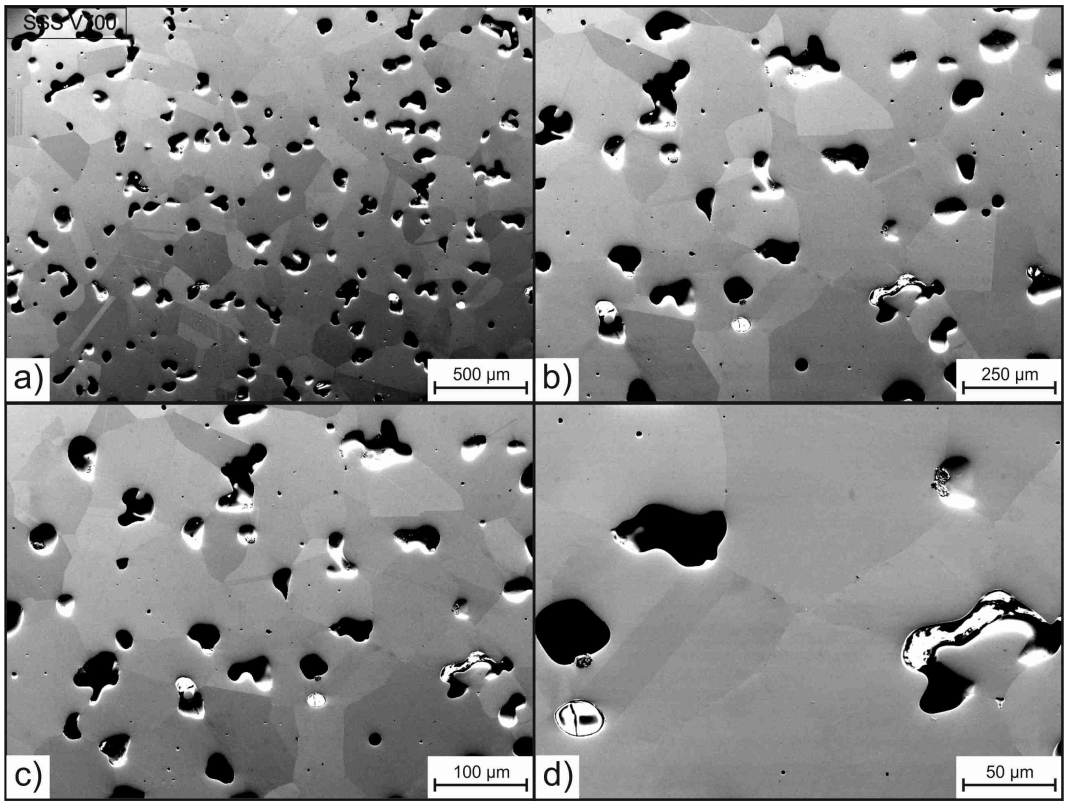

Figure 5. 42.: Overview of the densified powder mass, polished V700 specimen

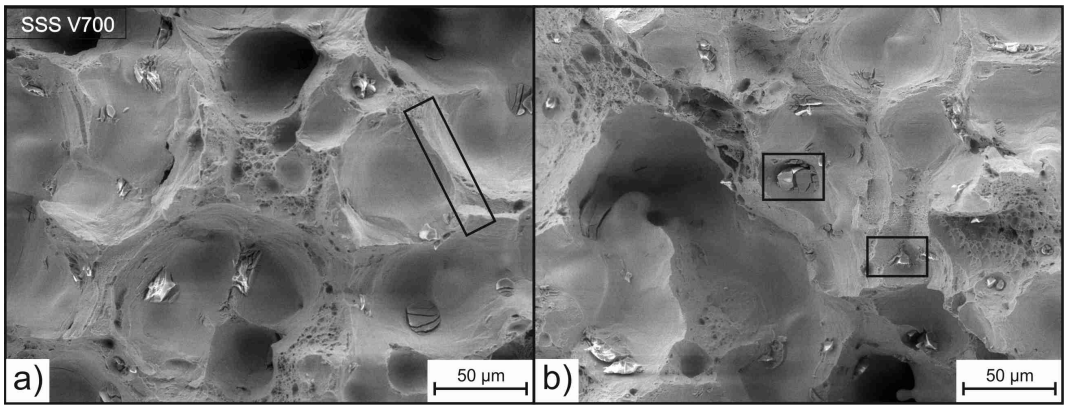

Figure 5. 43.: Overview of fracture surface, V700 specimen

In addition to that the former sintering necks are visible very well [a)] they show the fracturing path of this sample and confirm the densification by only solid state sintering. In opposite to the SSS sample large particulates of irregular shape can be seen on this surface [b)].

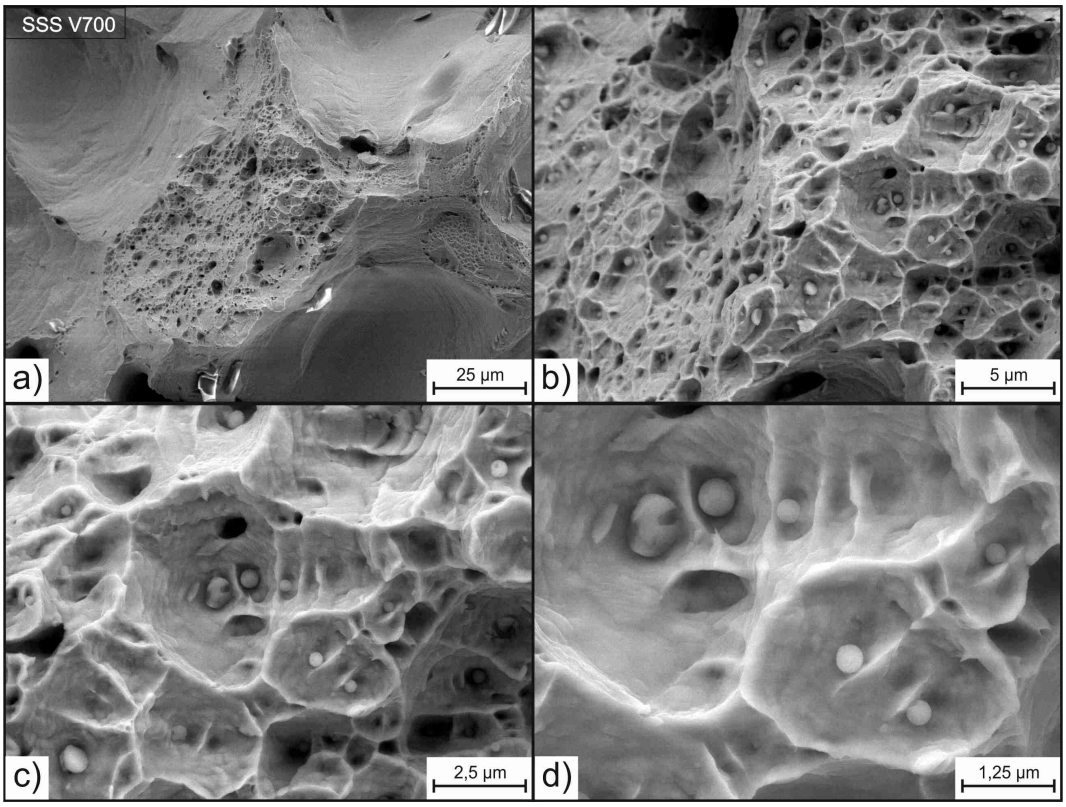

Figure 5. 44.: Closeup of the spherical particulates distributing in the densified powder mass, V700 specimen

Figure 5. 44 further depicts a sintering neck of the V700 sample and its failure mechanism. These sintering necks, as the only connections between the former powder particles, fractured similar to the SSS sample ductile around enclosed, spherical particulates. Therefore the failure mode is interparticle and transgranular.

Figure 5. 45 in addition shows a large area that was fractured very ductile. A closer look at such an area shows furthermore small particulates and hence a transparticle intergranular dimple ductile fracturing is estimated.
Further figure 5. 45 shows a large, spherical included particulate in the V700 sample [c) and d)] with a size of about 2 μm.

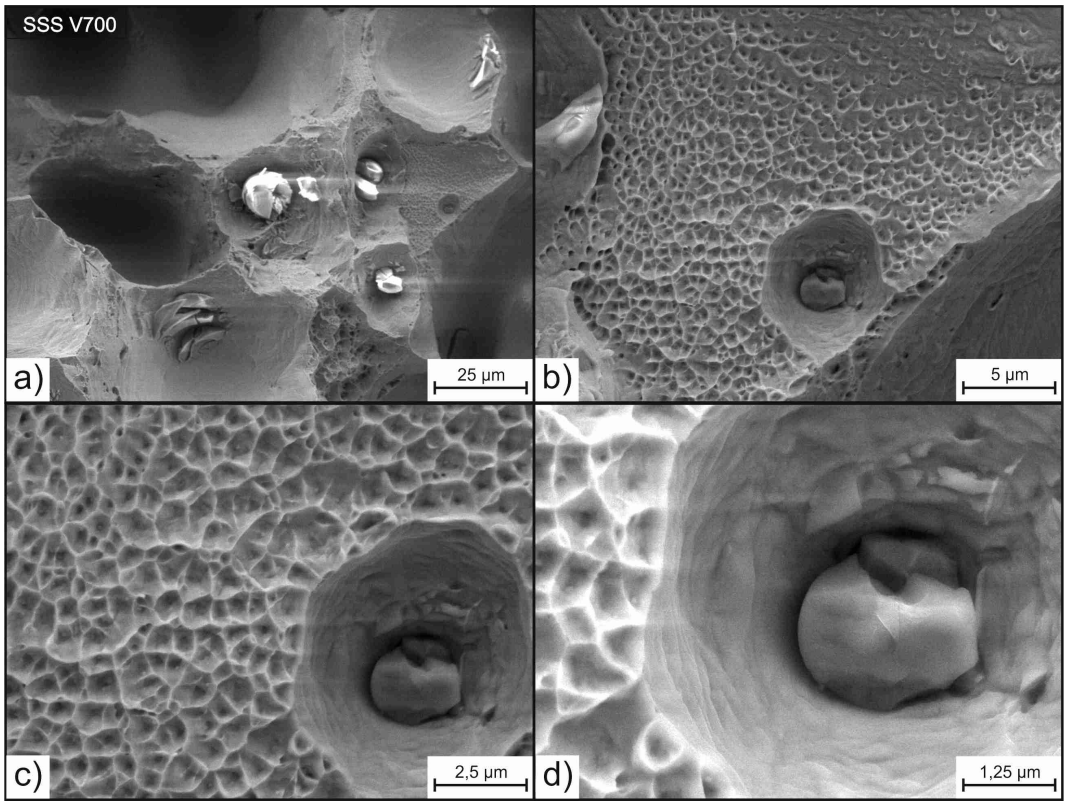

Figure 5.45.: Closeup of a large particulate distributing in a fracture site, V700 specimen

Other large particulates of the V700 fracture surface can be seen in figure 5.46, these are even larger than the particulates considered before. They do not seem to have been included in the matrix and lie furthermore in former pores loosely. Moreover their brittle disruption and charging during SEM examination suggests an oxidic character. This type of particulate is very common in this sample and as visible in the overview they exist in nearly every pore.

Loose, flaky particulates like in figure 5.47 can be found in the V700 sample as well. These particulates seem to coat the surface of some fractured sites and are an assembly of small, angular flakes. The matrix around this particulates appears metallic and evaporation lines can be seen clearly. Thus the flakes only overlie on the surface and aren't connected to it directly.

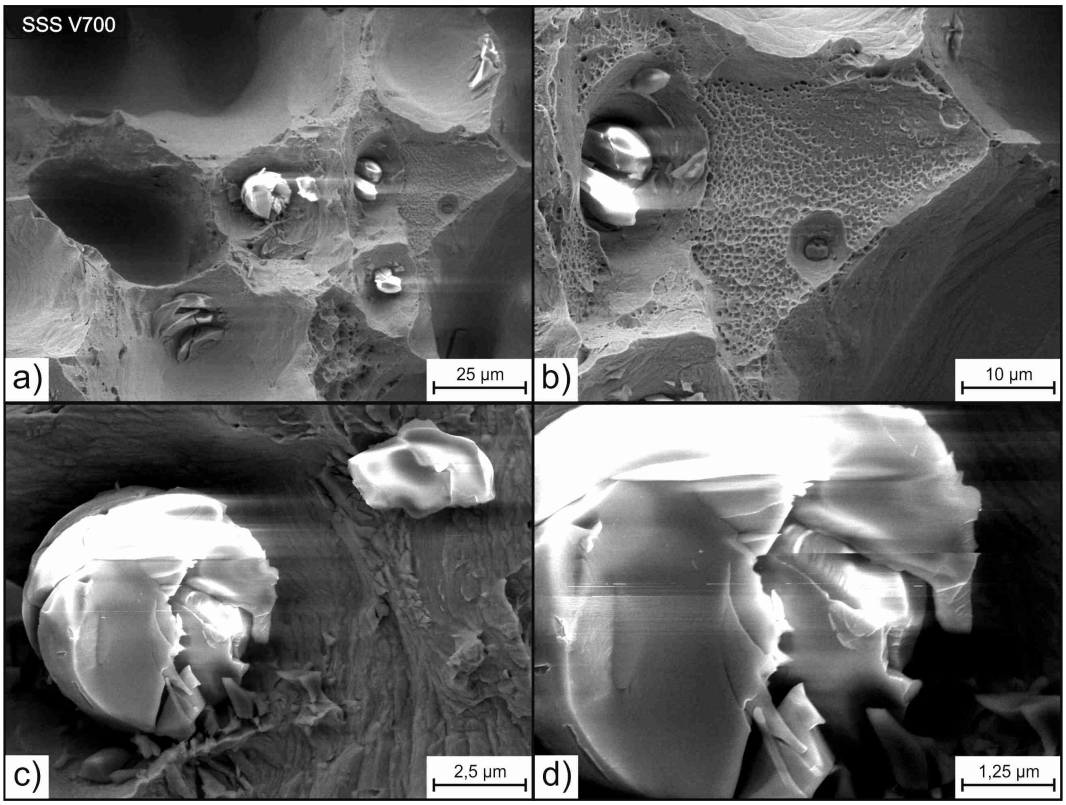

Figure 5. 46.: Closeup of a large, loose, oxidic particulate in a pore, V700 specimen

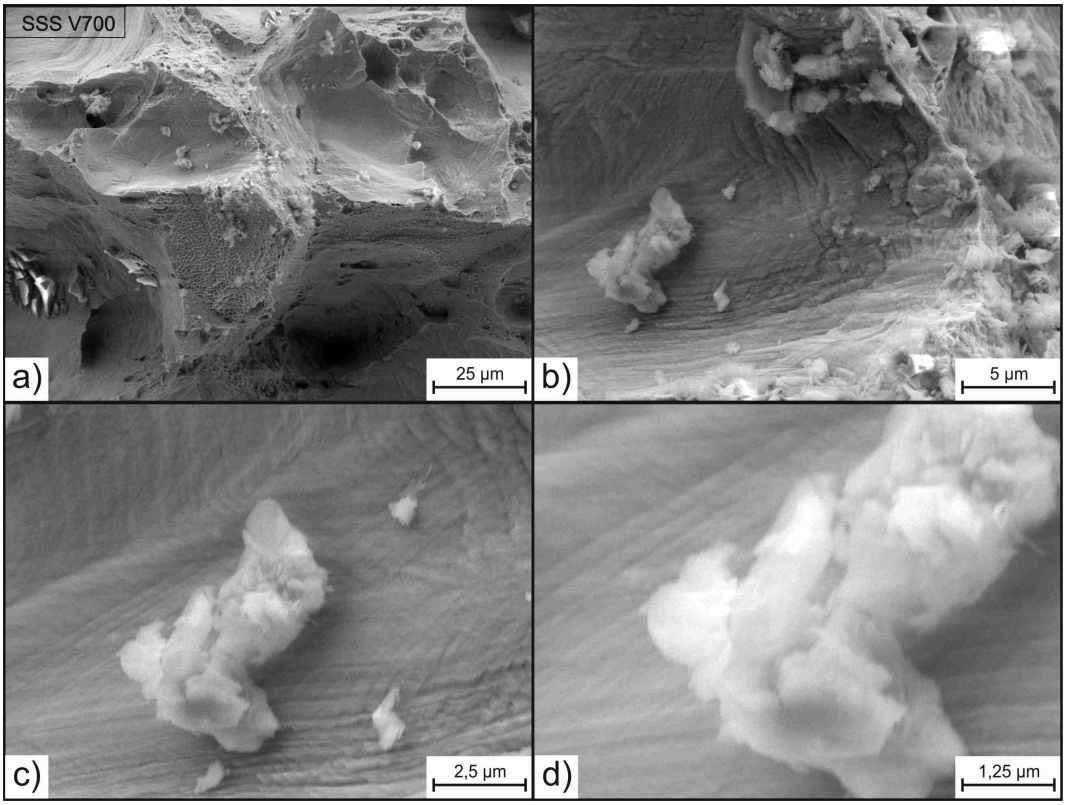

Figure 5. 47.: Closeup of a loose, flaky, oxidic particulate on the fracture surface, V700 specimen

To complete the analysis of the V700 surface EDX measurements clarify the composition and the character of each particulate. These analyses are depicted in appendices B. 36 to B. 39.

The spherical particulates which are enclosed in the sintering necks are analyzed in appendix B. 36. This analysis shows that they are oxides and mainly consist out of oxygen, manganese, silicon, chromium and iron. Yet in comparison to former oxides of this type their silicon content is rather low (4 to 6 at.-%). They contain more chromium and iron than before measured and only little aluminum is measured. This can be underlined by measurements B. 42 and B. 43 which show likewise low Si-fractions and follow the same trends.

The large particulate of figure 5. 44 is analyzed in appendix B. 37. Though this results show only very little oxygen in this particle the manganese amount is huge (83 at.-%) and underlines that this is an oxidic particulate. It can be assumed that this is an manganese based, oxidic particulate enclosed in the consolidated powder mass.

The other large particulates analyzed in appendix B. 38 are oxides too, they show a large fraction of oxygen in spectrum 2 and 3 and are manganese based (50 to 60 at.-%). Further they contain only little silicon. This amount is only about 5 at.-% and slightly over the iron and chromium contents which are additionally very low. Thus these oxides tend to be manganese oxides of higher purity.

The flaky particulates of figure 5. 47 in contrast contain much less manganese. The EDX analyses of these particulates resulted in a composition of only oxygen and iron and showed that these are pure iron oxide flakes.

Further figures and EDX results that underline the conclusions about the V700 specimen are attached in the appendices B. 40 to B. 44.

5.3.3. Solid state sintering with dwelling at 1050°C under vacuum

XPS analysis

Dwelling the powder mass at 1050°C under vacuum during sintering outcame a again very similar surface composition as for the sintering process without additional heat-treatment. The surface mainly consists of carbon, oxygen, chromium, manganese and iron and other elements are only measured in lower contens [table 5. 5 and figure 5. 48].

Table 5. 5.: Content of elements on the fracture surface of the V1050 sample, in at.-%

Content/ Element	C	N	O	Si	S	Cr	Mn	Fe	Se	Mo	Ni
Fracture surface	19.7	3.9	42.9	1.9	0	4.6	8.3	17.9	0.4	0.4	0.1
Etched 1 nm	5.0	2.2	44.9	2.1	0	6.5	9.4	29.1	0.3	0.4	0.2
Etched 5 nm	4.3	2.4	44.1	2.0	0	6.8	9.9	29.7	0.4	0.5	0.1
Etched 10 nm	3.5	2.0	44.2	1.8	0	7.7	9.8	30.5	0	0.6	0
Etched 50 nm	2.9	1.7	37.5	1.5	0	11.1	11.5	33.0	0	0.8	0

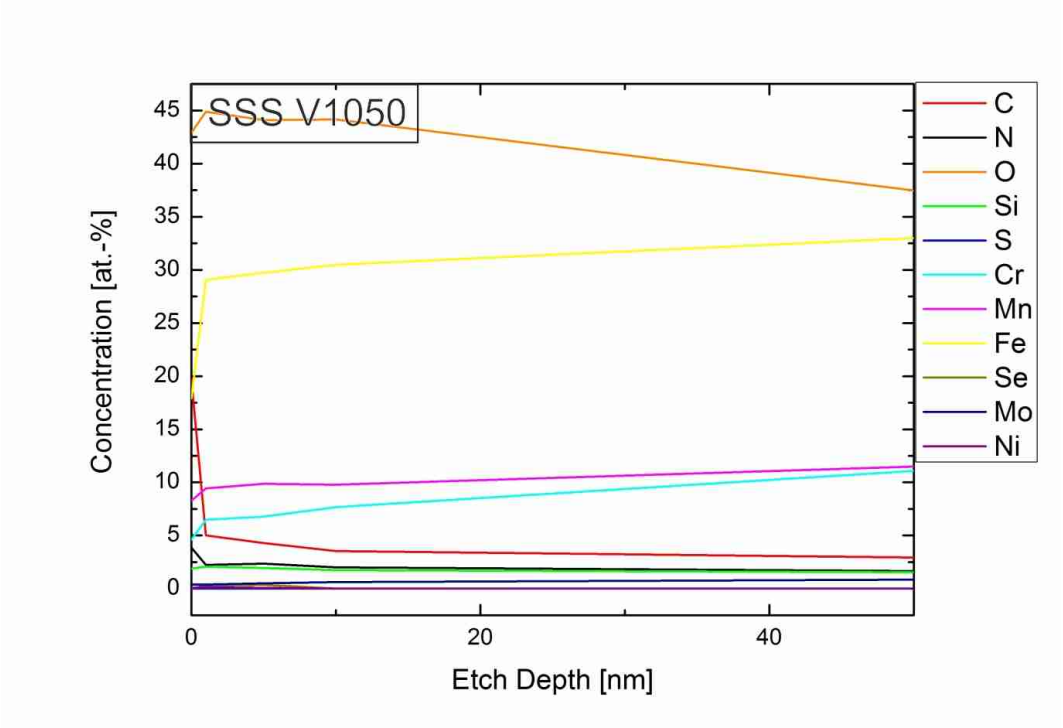

Figure 5. 48.: Development of the element content distribution with etching depth, V1050 specimen

Characteristic features of this element distribution are on the one hand a lower manganese content compared to the other samples which is only 8.3 at.-% at the as-fractured surface and increases to only 11.5 at.-% in 50 nm etch depth.

On the other hand the oxygen content is higher as in the other samples, 43 at.-% at the as-fractured surface and 37.5 at.-% in 50 nm etch depth. It does not decrease strongly during ion etching and stays even in 50 nm etch depth high.

Further no sulfur and very little selenium is detected on the surface which differs from the SSS and especially from the V700 sample.

Taking no light elements into account [figure 5.49], the lower manganese amount on the as-fractured surface and in ion etched state can be seen even better. Only 25 at.-% on the pure fracture surface are manganese and the fraction even decreases to 19.8 at.-% in 50 nm etch depth. In opposite the iron content is higher as usual and accounts 54 at.-% to 62 at.-%.

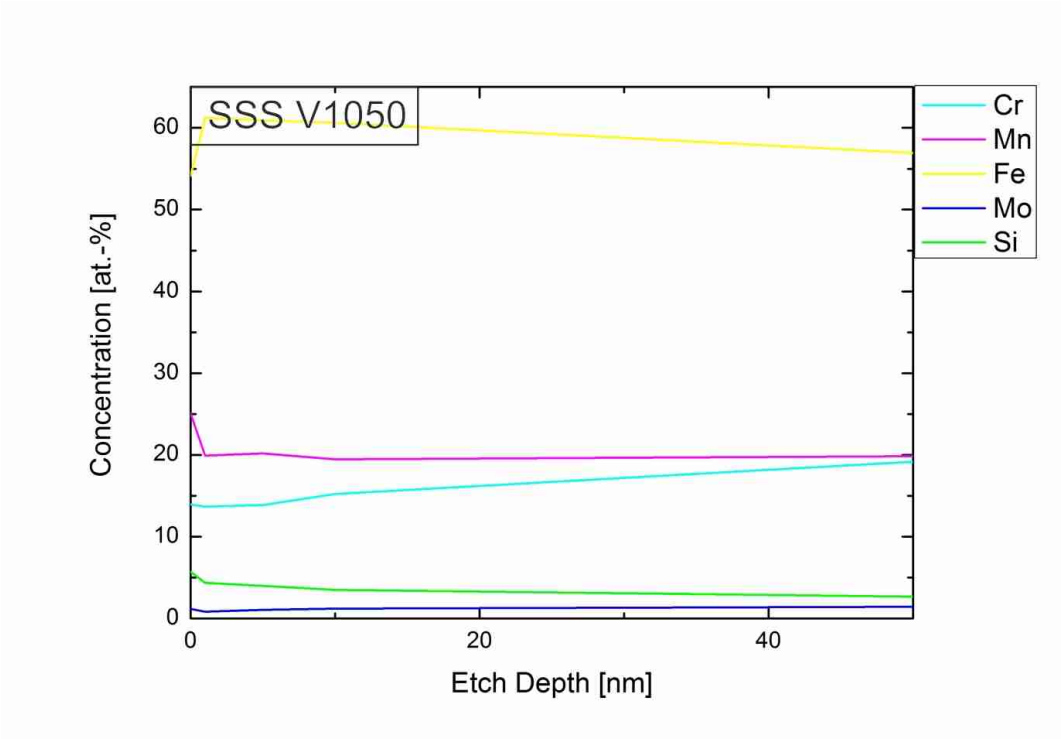

Figure 5.49.: Relative concentration of metallic elements over etching depth, V1050 specimen

Considering the high resolution narrow scans (appendices B.45 to B.47) and the presentation of the content of metallic state [figure 5.50] it becomes clear that a larger amount of iron in this sample is in oxidic state. The metallic Fe content is much lower as till now detected and stays around 80 % till 50 nm etch depth.

The metallic manganese amount instead is two till three times higher as for earlier discussed solid state sintered samples, it ranges from 42.7 % on the as-fractured surface to 30.8 % in 50 nm etch depth.

The metallic chromium contend indeed does not differ much from the other sintered samples and accounts 70 % to 60 %.

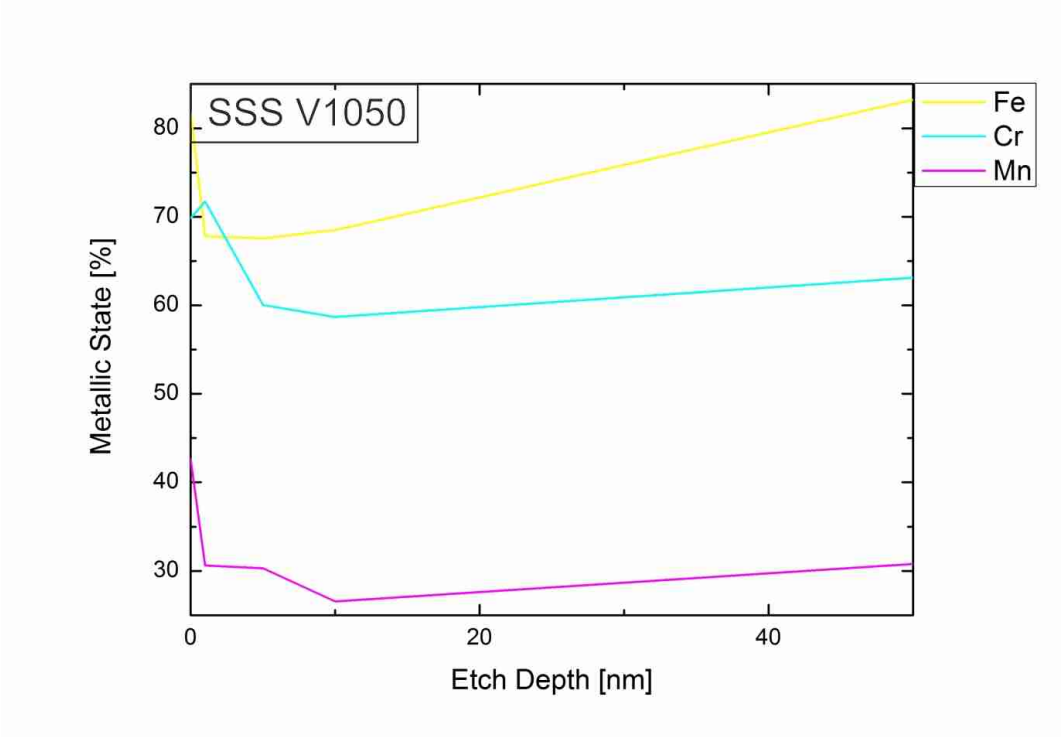

Figure 5. 50.: Content of the metallic state of Fe, Cr and Mn over the etching depth, V1050 specimen

This can further be seen in figure 5. 51 too. The normalized cation concentration shows a lower amount of manganese cations and a higher amount of iron cations of the total oxide sum. Furthermore the silicon fraction on the oxidic state is quite high too, 16.8 % at the surface decreasing to 8 % at 50 nm etch depth.

The depiction in figure 5. 52 reflects this as well, the total oxide amount stays as high as before measured in solid state sintered samples but the fraction of cations is redistributed. A high iron cation amount of 20 at.-% from 1 nm to 10 nm etch depth and an amount of silicon cations from 5.7 at.-% to 2.7 at.-% from the surface to 50 nm etch depth can be measured, while the manganese cation amount is constant about only 14 at.-%.

Hence the V1050 sample comprehends more lower stable iron oxide than the before considered samples and less higher stable manganese oxide.

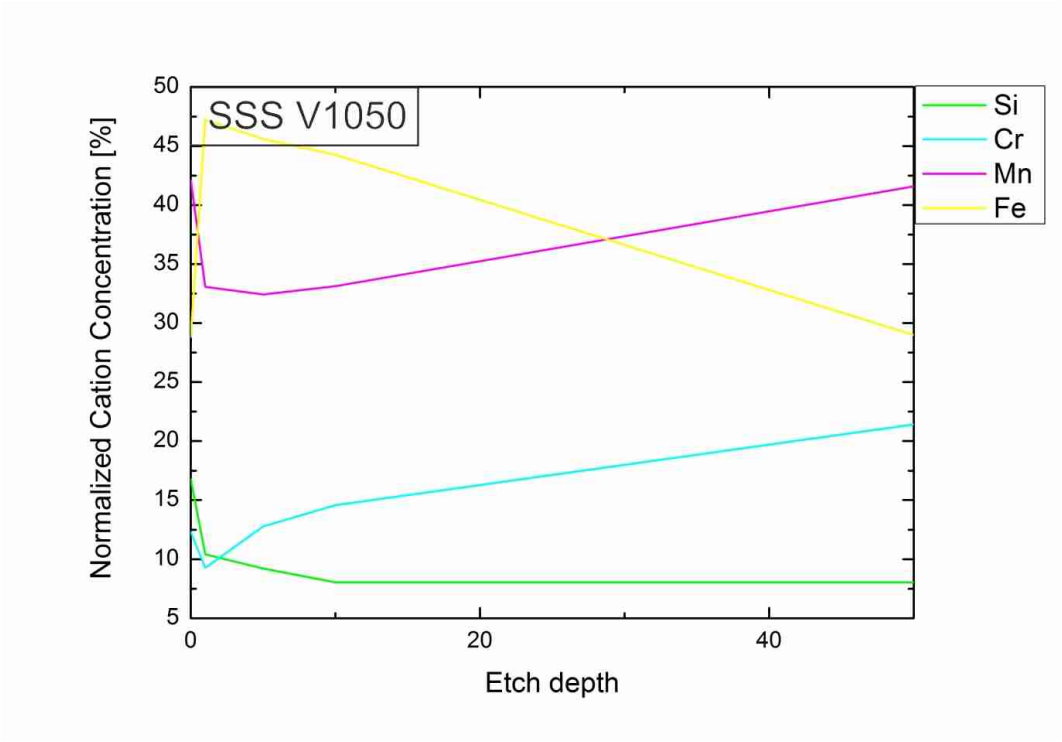

Figure 5. 51.: Normalized relative cation concentration of the oxidic state, V1050 specimen

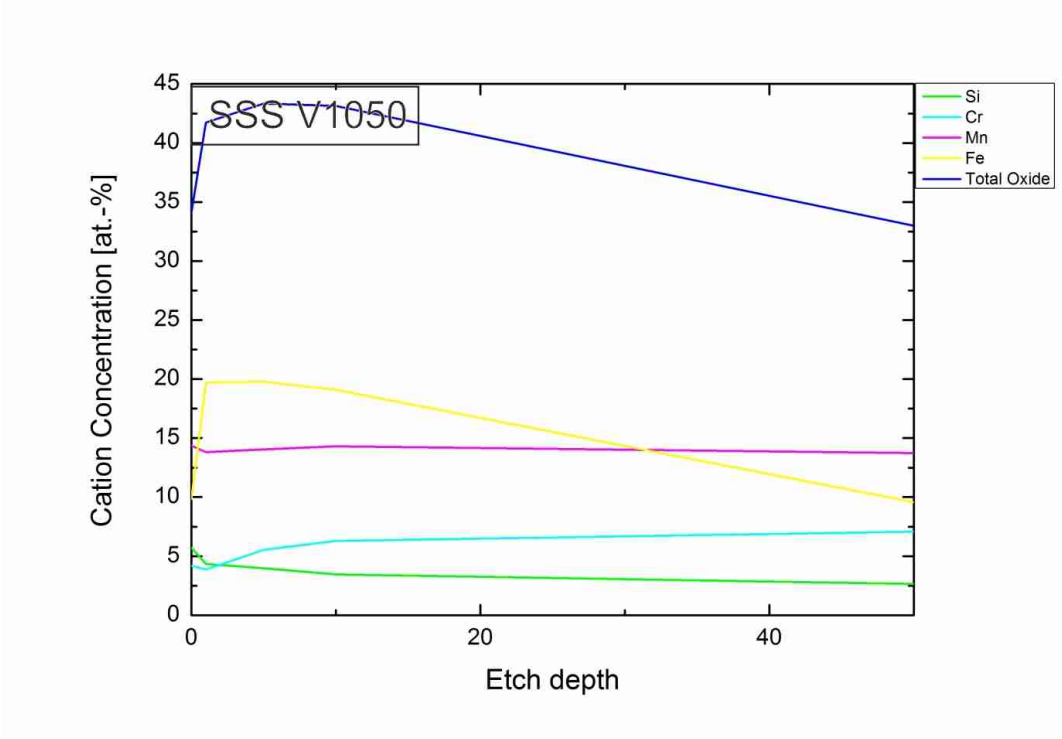

Figure 5. 52.: Total sum of the cations and single cation concentrations depicted over the etching depth, V1050 specimen

SEM and EDX

The state of the V1050 sample after manufacturing [figure 5. 53] is a highly porous powder mass with a lot of little pores and large, agglomerated pores [a) and b)]. Compared to the SSS and the V700 powder mass the number of pores is increased and much less densified matrix area is visible. From the SEM pictures the grain size can be estimated to 100 μm and the state of the microstructure as free of precipitation [c) and d)].

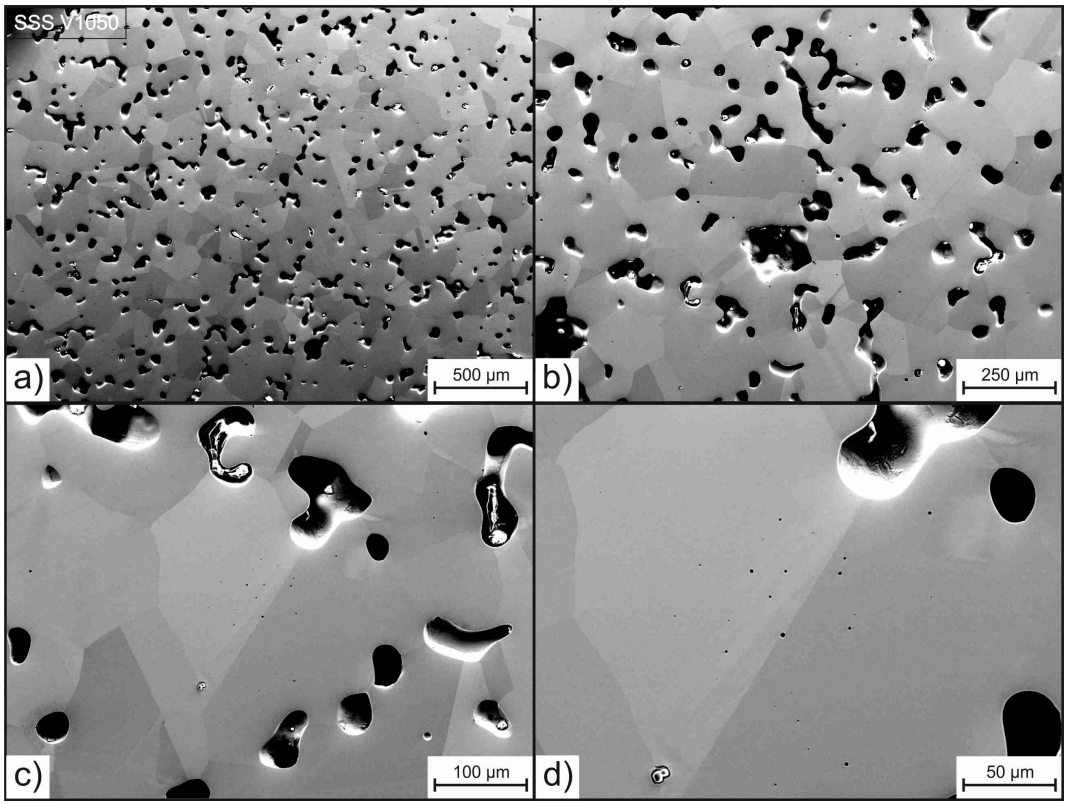

Figure 5. 53.: Overview of the densified powder mass, polished V1050 specimen

Figure 5. 54 underlines this result as it shows a much more fine porous structure which is weakly densified. The pores don't seem to be closed and are still connected to each other a lot. Furthermore this surface is very rough like the surface of every till now considered solid state sintered sample. It shows large differences in hight of the profile and can't be reduced to one plane level properly. Moreover the sintering necks appear much thinner than before presented and less particulates can be seen in the pores.

Figure 5. 55 distinguishes the former sintering necks and the fracturing of this sample. The fracturing again looks very ductile with a lot of elongation. Therefore the fracturing is inter-particle and transgranular again and the matrix fails concentrated around particulates.

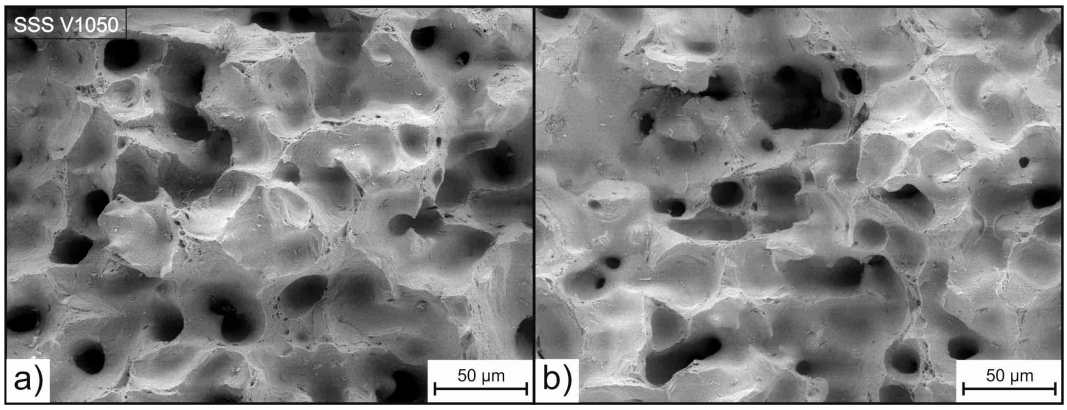

Figure 5. 54.: Overview of fracture surface, V1050 specimen

Furthermore the fracturing is very punctual and the connections of the powder particles are focused on small contact areas. The sintering necks besides this points appear very thin and undersized [Figure 5. 55 a) to e)].

In figure 5. 56 additionally large, agglomerated particulates of spherical shape are presented. These particulates can be found at several places in the sample and seem to be connected to the clean, metallic matrix. Around them the matrix is metallic because evaporation lines are pronounced clearly. But on this matrix thin, flaky particulates assembly at this place as well.

The last considered site of this sample shows a sintering neck coated with a network of flaky particulates. These particulates can be found at divers places of the V1050 fracture surface and shall be examinated here exemplarily. Most of the flakes appear transparent and lie on the metallic matrix they are sharp and angular and agglomerate to a layer [b) and c)]. Additional particulates look more circular and have no spikes [d)]. These particulates further appear brighter and distribute on the spiky flake layer.

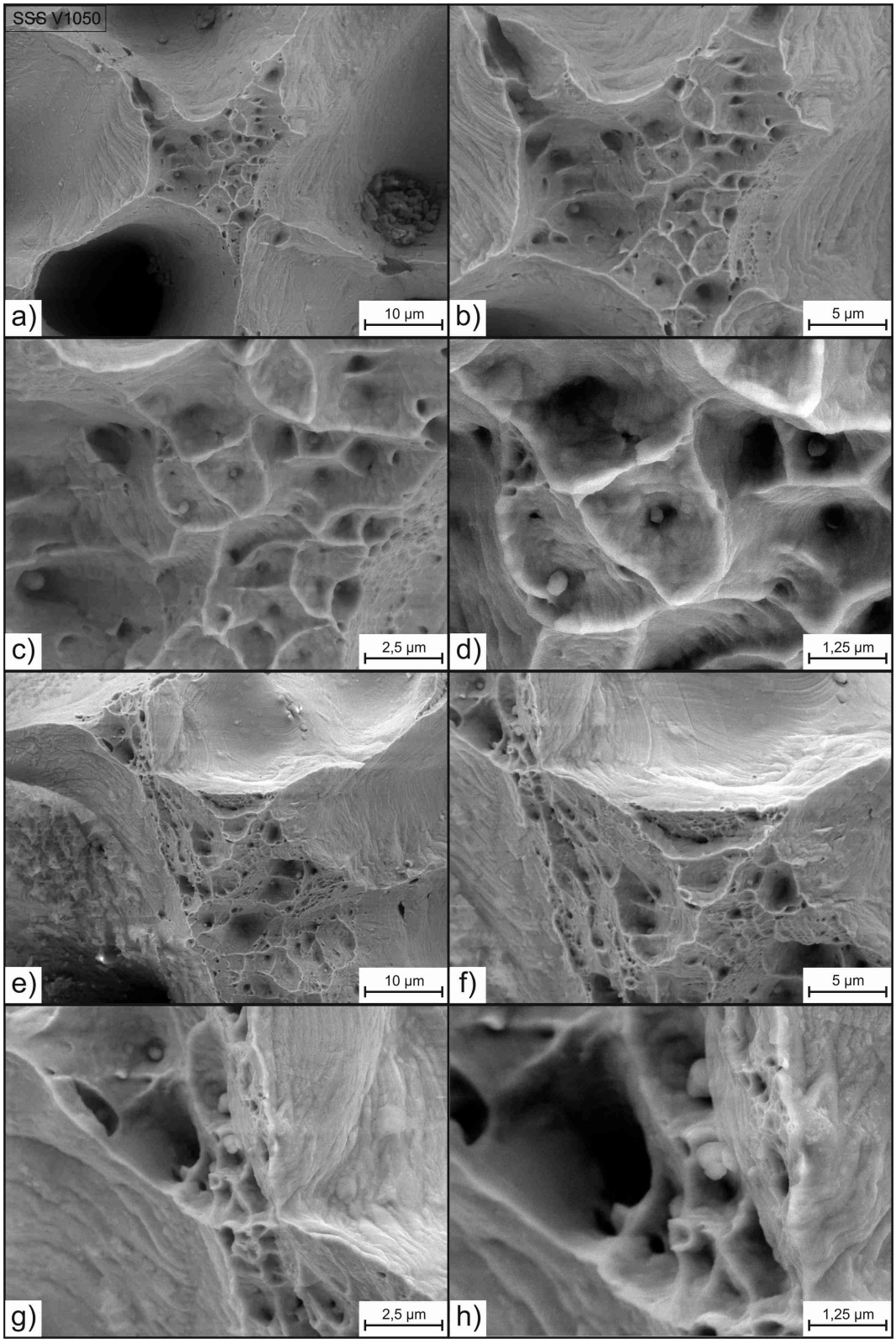

Figure 5. 55.: Closeup of a typical fracture site and enclosed spherical particulates, V1050 specimen

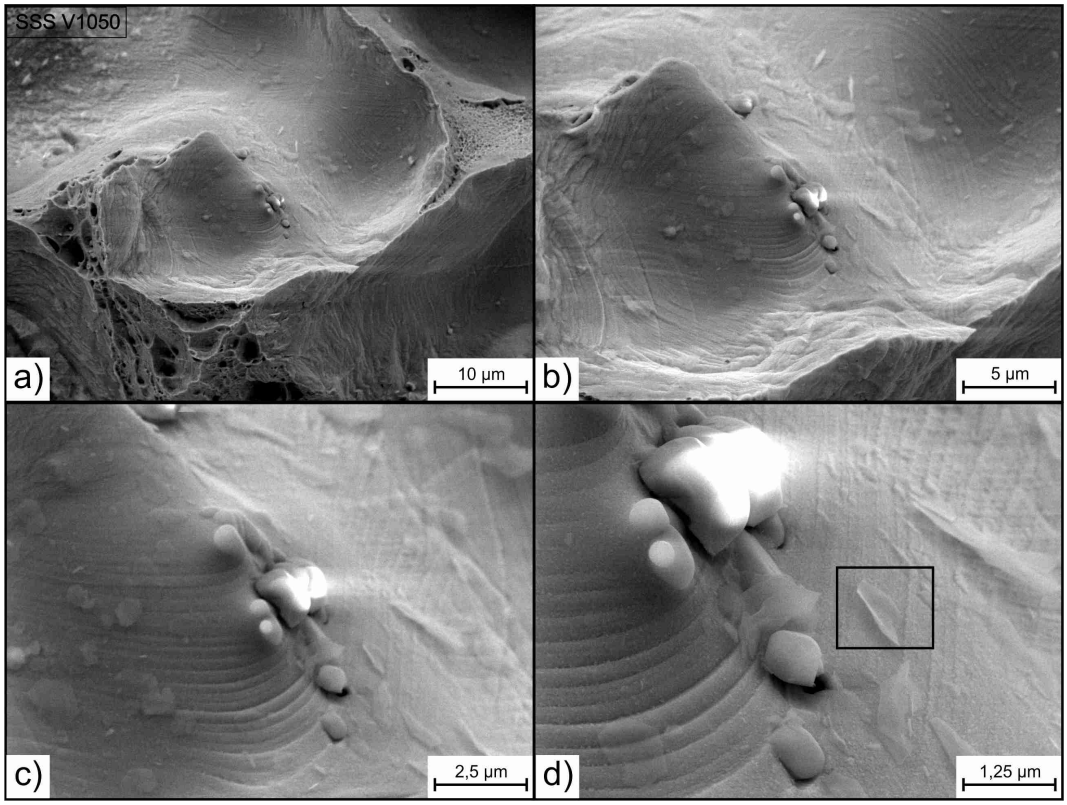

Figure 5. 56.: Agglomerated, large, oxidic particulates embedded in the densified steel matrix, V1050 specimen

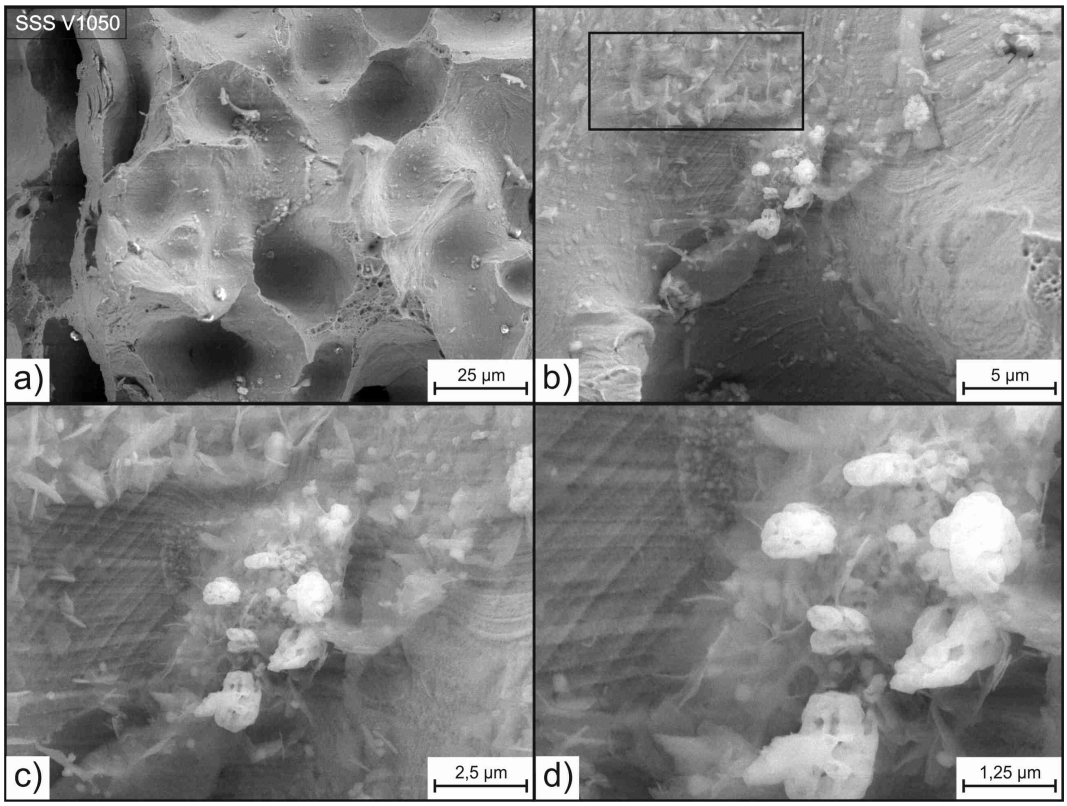

Figure 5. 57.: Sintering necks coated with flaky, inhomogeneous oxides, V1050 specimen

Following the EDX results of the V1050 sample are presented in appendices B. 48 to B. 51.

At first the EDX results of the spherical particulates enclosed in the sintering necks are presented in appendices B. 48 and B. 49. These results show a high amount of oxygen and manganese. Additionally they contain a large amount of aluminum (13.5 to 17.3 at.-%) and quite low chromium amounts (2.2 to 6 at.-%). Therefore it can be suggested that these particulates are Mn-Al-O-oxides.

The larger, agglomerated particulates of figure 5. 56 are analyzed in appendix B. 50. Spectra 1 and 2 of this measurement show the presence of oxides at this site. The particulates contain about 65 at.-% oxygen, 11 at.-% manganese and 20 at.-% aluminium and are identified as Mn-Al-O-oxides.
Outstanding at this measurement is a very stable ratio of 1:2 for manganese and aluminum. Spectrum 3 of this analysis shows additionally the existence of a titanium-nitride. The high nitrogen amount of 44 at.-% and the titanium fraction of 36.3 at.-% leaves no doubt about the character of this particulate.

Also the high chromium (11.7 at.-%) and the low manganese (2.9 at.-%) amount needs to be mentioned which boarders this measurement even more from the spectra 1 and 2. The matrix of this analysis [spectrum 4] furthermore shows an high amount of oxygen (20 at.-%) as well. As earlier mentioned flakes can be seen on the surface which could be the cause for this high oxygen amount. However the considering of only the metallic elements shows the typical 1:1:3 ratio of chromium, manganese and iron and allows no conclusions about the origin of the matrix oxide value.

The analysis of the flaky particulates [appendix B. 51] of figure 5. 57 shows mainly the results that the flake network consist of oxygen, manganese and iron [spectrum 3] and that the brighter particulates [spectra 1 and 2] are selenides with an high oxygen content.
The selenides mainly consist of 23 to 30 at.-% of selenium and 35 to 40 at.-% of oxygen. They show only lower amounts of chromium, manganese, aluminum, molybdenum and iron and further contain small fractions of sulfur.

Further figures and EDX results that underline the conclusions about the V1050 specimen are attached in the appendices B. 52 to B. 54.

5.3.4. Solid state sintering with dwelling at 1150°C under vacuum

XPS analysis

The solid state sintered sample that was dwelled at 1150°C under vacuum during sintering has nearly the identical surface composition as the SSS sample. Only the carbon content is lower and decreases to a lower value during ion etching. Thus all trends and developments of the SSS element distribution apply for the V1150 sample as well [table 5.6 and figure 5.58].

Table 5.6.: Content of elements on the fracture surface of the V1150 sample, in at.-%

Content/ Element	C	N	O	Si	S	Cr	Mn	Fe	Se	Mo	Ni
Fracture surface	12.4	3.0	41.8	0.8	1.0	5.2	13.7	20.3	1.0	0.8	0
Etched 1 nm	3.4	2.2	44.3	0.3	2.4	6.3	15.1	24.5	1.1	0.4	0
Etched 5 nm	2.9	1.7	42.9	0.4	1.9	7.2	14.2	27.0	1.2	0.7	0
Etched 10 nm	2.7	1.4	40.8	0.4	1.6	7.9	13.8	30.0	0.7	0.6	0
Etched 50 nm	2.4	1.7	28.9	0.9	1.2	12.1	13.3	37.6	0.9	1.1	0

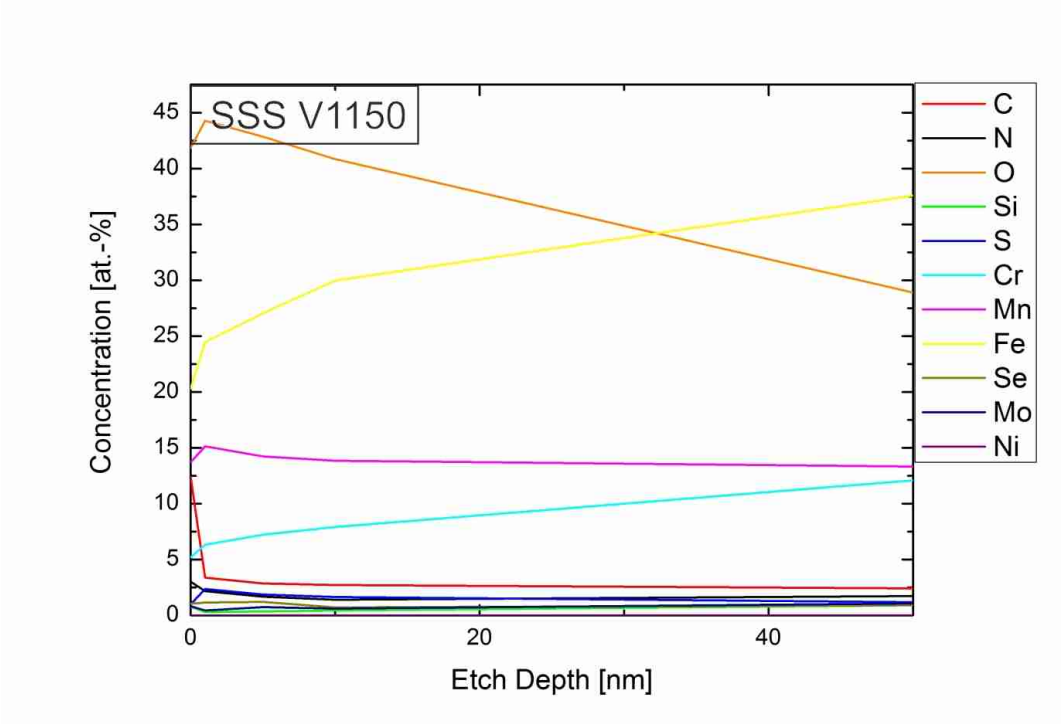

Figure 5.58.: Development of the element content distribution with etching depth, V1150 specimen

Likewise for the relative concentration of only metallic elements [figure 5. 59] no different trends as for the SSS sample can be detected. The only difference is a lower silicon fraction.

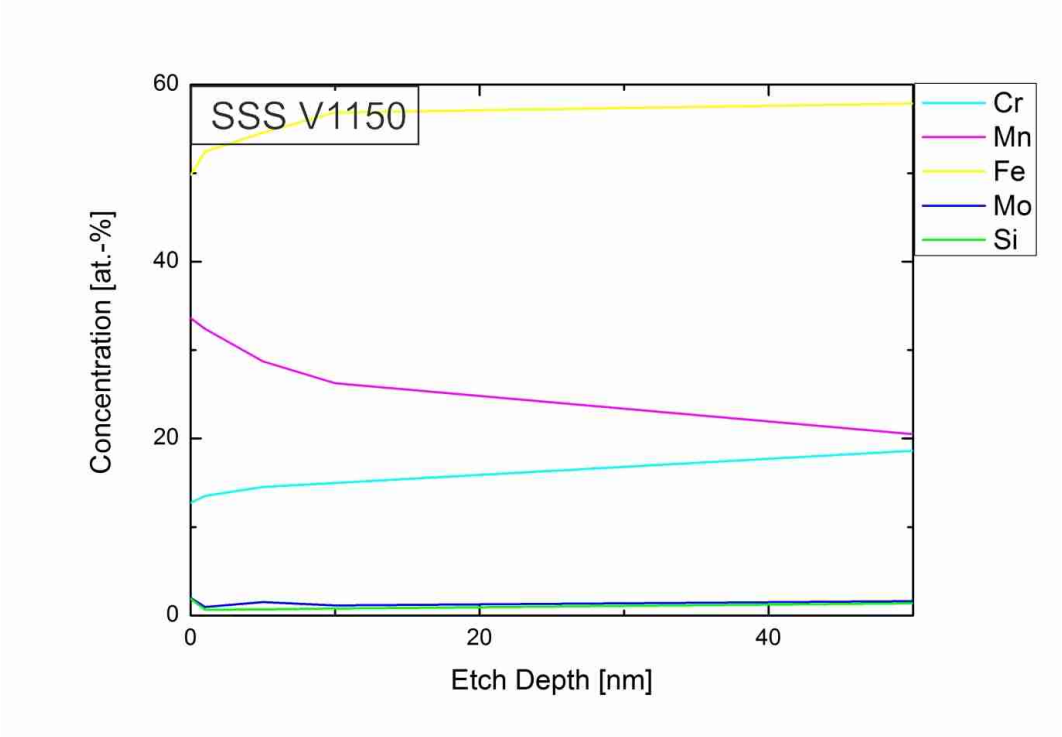

Figure 5. 59.: Relative concentration of metallic elements over etching depth, V1150 specimen

The high resolution narrow scans of the V1150 sample (appendices B. 55 to B. 57) show further a higher fraction of Fe, Cr and Mn in oxidic state.
Figure 5. 60 depicts the metallic contents over the etch depth and shows that the development of their distribution is similar to the development of the already discussed solid state sintered samples.

The amounts of metallic iron and chromium are again rather low and range from 80 % to 70 % for iron and from 80 % to 60 % for chromium till 10 nm etch depth. Manganese amounts are slighly higher as in the SSS sample and range from 22.7 % to 14.5 % till 10 nm etch depth.
In an etch depth of 50 nm the iron and manganese amounts finally are the maximum values and for chromium a quite high value can be measured as well, thus it can be suggested that the oxide amount in general drops with deeper etching depth.
Concluding it has to be pointed out again that the metallic contents of Fe, Mn and especially Cr are very high at the as-fractured surface.

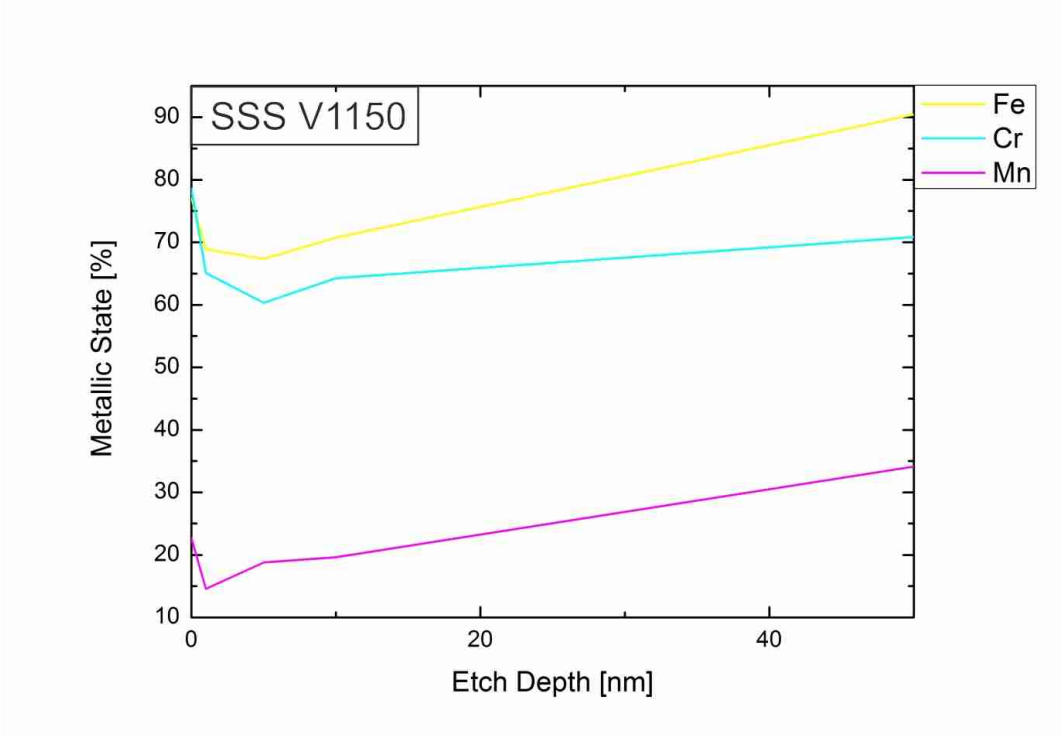

Figure 5. 60.: Content of the metallic state of Fe, Cr and Mn over the etching depth, V1150 specimen

Considering the composition of the oxidic state [figure 5. 61] and the total amount of cations in the V1150 sample [figure 5. 62] the cations are mainly manganese and iron. Till 10 nm etch depth nearly 90 % of the normalized cation concentration are Mn- and Fe-cations, only in deeper etched regions of 50 nm their amount drops to 70 % while the Cr-cation amount rises from before 10 % to over 20 %. Before this chromium and silicon only took a minor part in the cation distribution.

Especially the iron cation amount is very high in the V1150 sample, it's steadily around 15 at.-% till 10 nm etch depth and first drops after 10 nm to 5 at.-%. The chromium content is instead very stable till 50 nm etch depth and levels around 5 at.-%, what further explains the increase of Cr content on the normalized cation concentration. Its not the case that the Cr-cation amount rises, its rather the case that it is stable but the amount of other cations decreases.

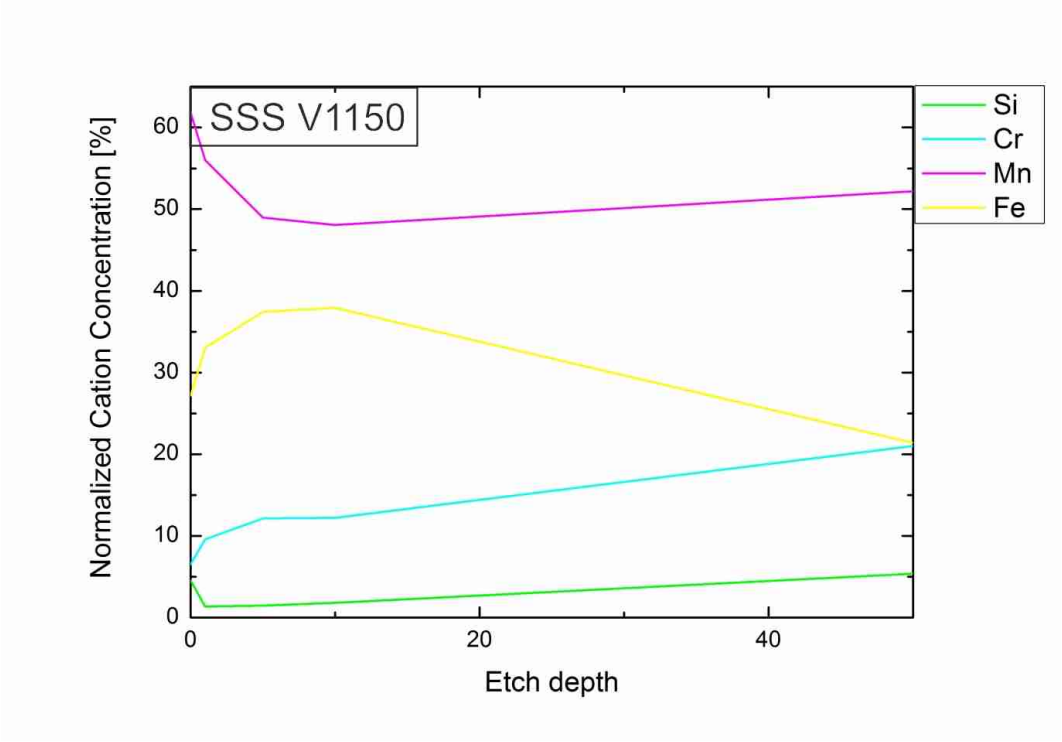

Figure 5. 61.: Normalized relative cation concentration of the oxidic state, V1150 specimen

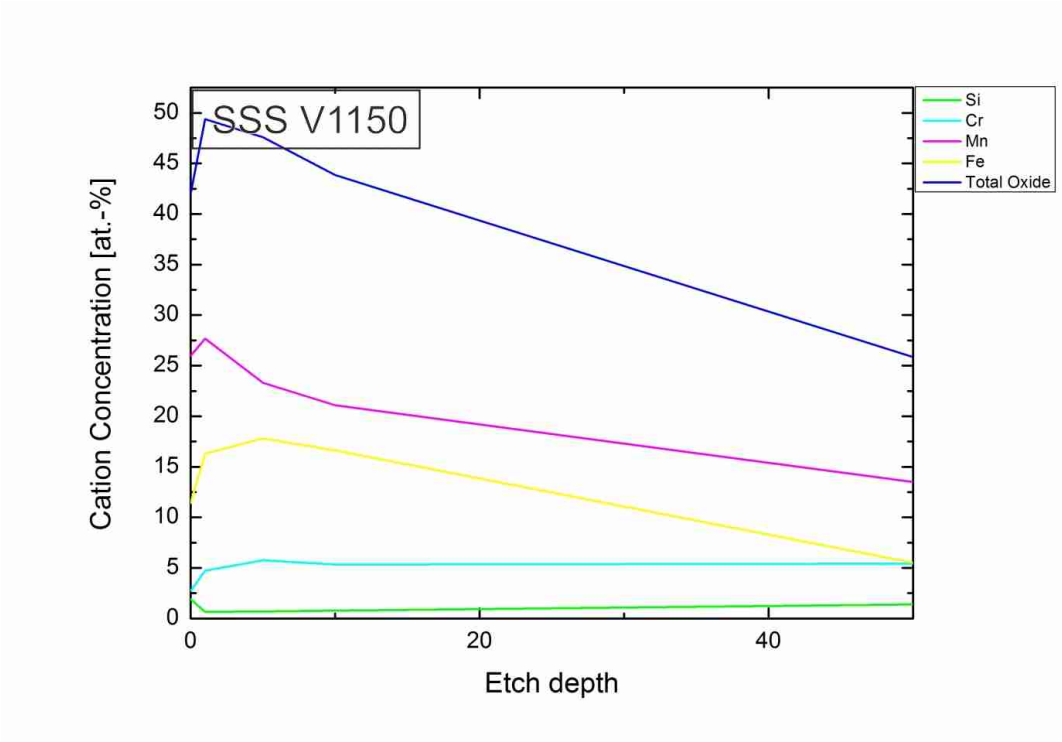

Figure 5. 62.: Total sum of the cations and single cation concentrations depicted over the etching depth, V1150 specimen

SEM and EDX

Figure 5.63 displays the appearance of the densified powder mass after solid state sintering with dwelling at 1150°C under vacuum.
This state is very similar to the V1050 sample and shows a weak densification and high porosity. The grain size can be calculated to 100 μm as well and in figures c) and d) small precipitations in the microstructure can be seen.

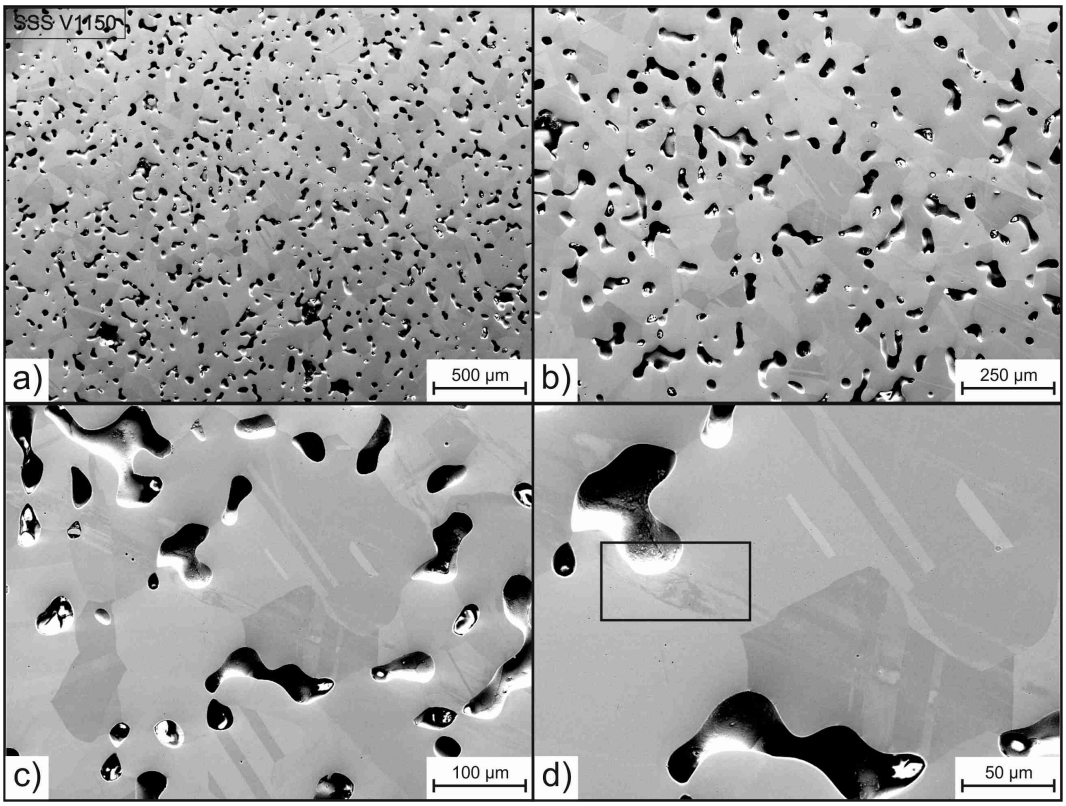

Figure 5.63.: Overview of the densified powder mass, polished V1150 specimen

The depiction of the fracture surface in figure 5.64 presents a very porous state as well. The surface consists of a lot of small pores and large agglomerated caviations [b)]. It is very rough and can't be reduced to one plane level properly because the difference in hight between the top peaks and the bottom is very large.
The fracturing only took place at the peaks of the fracture surface because these are the spots which touched the other particles.
The sintering necks moreover look very rough and show no smooth surface [a)] and further are covered with small particulates themselves.

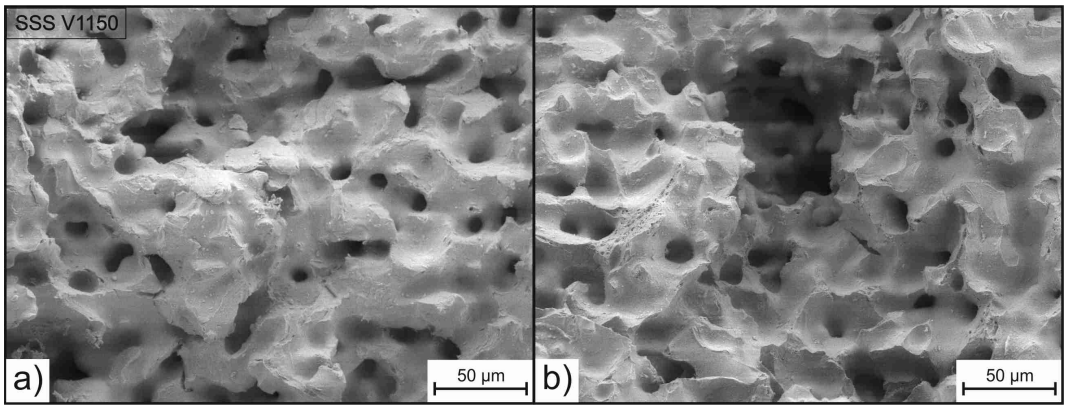

Figure 5.64.: Overview of fracture surface, V1150 specimen

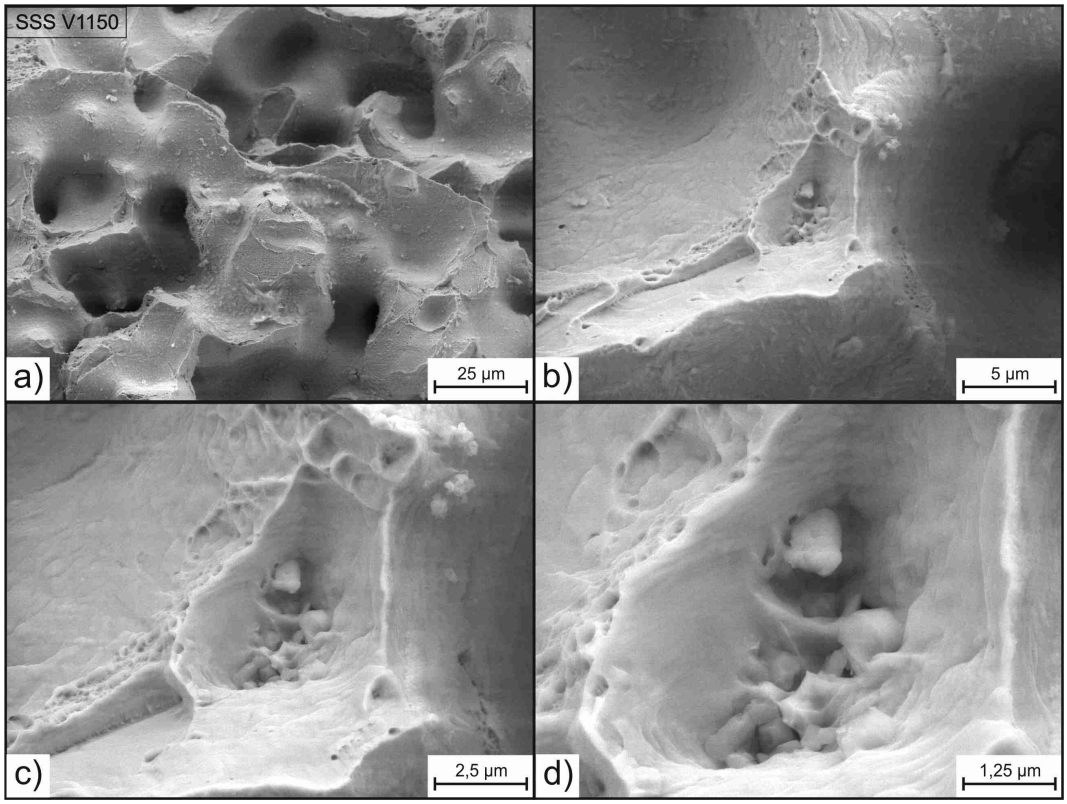

Figure 5.65.: Closeup of the particulates distributing in the densified powder mass, V1150 specimen

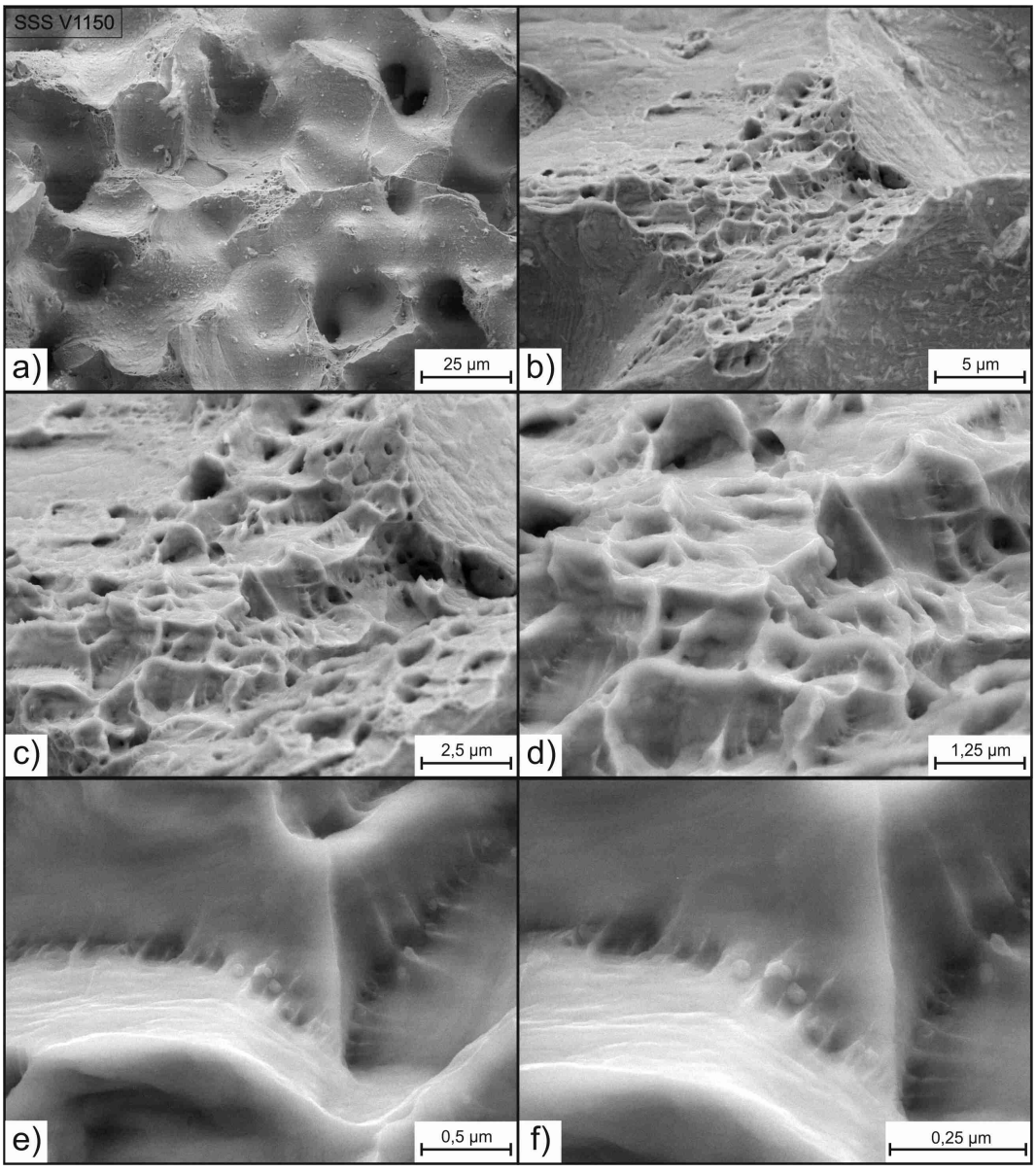

Figure 5. 66.: Typical fracture site with very fine, spherical particulates at the dimple stands, V1150 specimen

Figures 5.65 and 5.66 present typical fracturing places of the V1150 sample. Considering these figures it becomes obvious that the fracturing again was very punctual and that the connected areas are very small.

Figure 5.65 shows particulates in the fractured area, but they are not spherical and rather show a angular shape.
The area depicted in figure 5.66 is fractured rather plane without much elongation and there are no large spherical particulates in the fracture surface. However a closer look at this site shows rather a lot of very small particulates existing at the stand of the dimples. They distribute along the deformation paths and are of spherical shape [figure 5.66 c) and appendix B.62].

Such particulates can further be found in figure 5.67 and appendix B.63 too. These figures depict an intergranular fractured area and show plane fracturing around enclosed particulates.

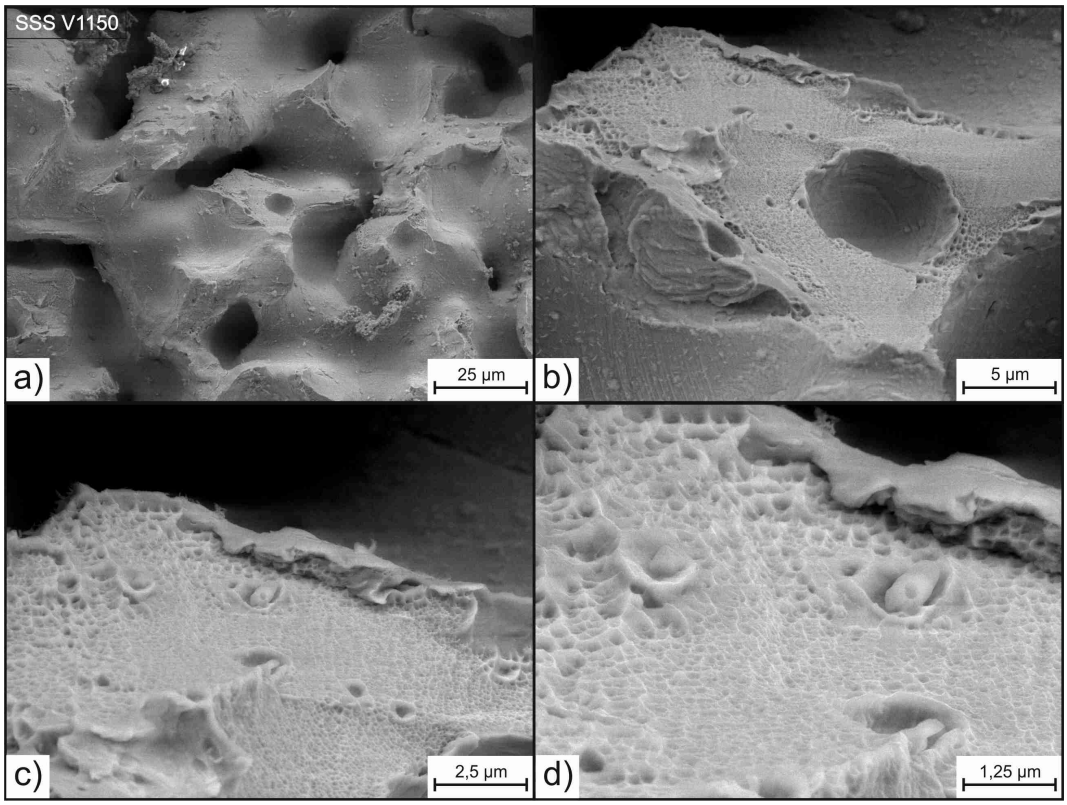

Figure 5.67.: Typical fracture site with very fine and additionally larger spherical particulates, V1150 specimen

Furthermore figures 5.68 and 5.69 show other types of particulates existing in the V1150 sample. These particulates do not distribute in the fractured areas they exist moreover on the surface of the sintering necks. Figure 5.68 presents angular particulates on the metallic matrix and shows that these are included in a flaky layer of spiky particulates.

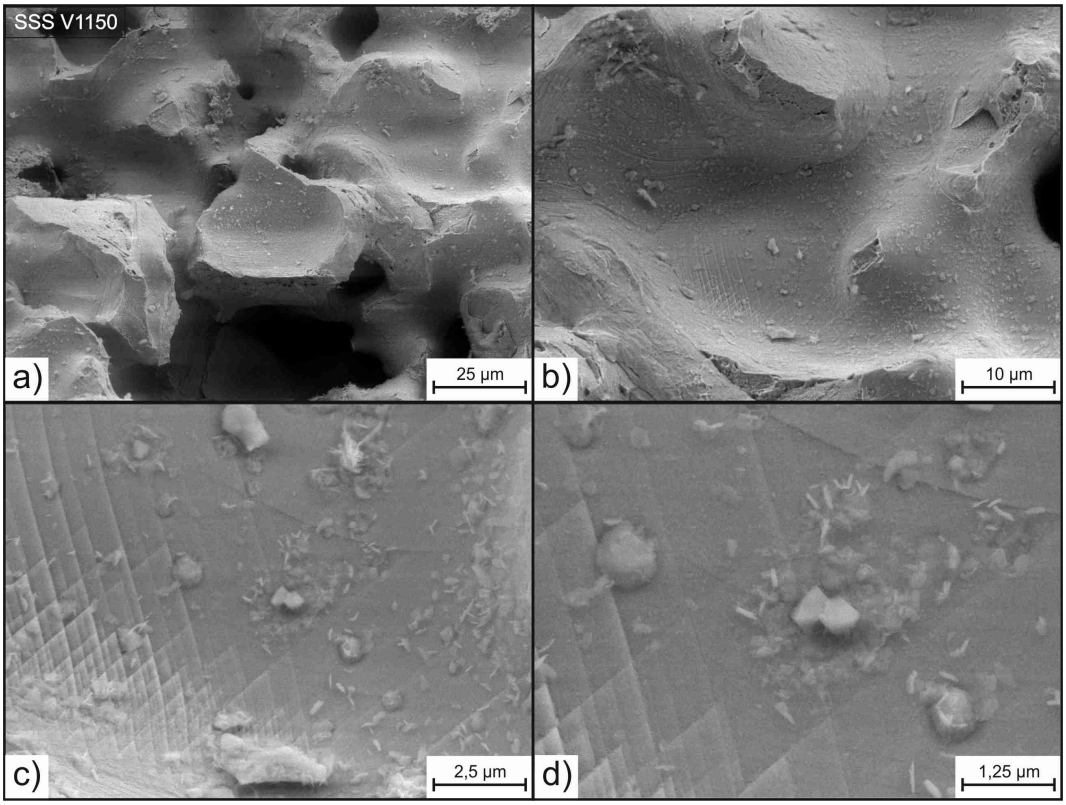

Figure 5.68.: Angular and flaky particulates on the surface of the densified powder mass, V1150 specimen

Figure 5.69 in addition shows some larger oxidic particulates [a)] and a closeup of one of these particulates [c) and d)]. This particulate is rather spherical and surrounded by a flaky layer as well. Additionally it seems to be brittle and cracked.

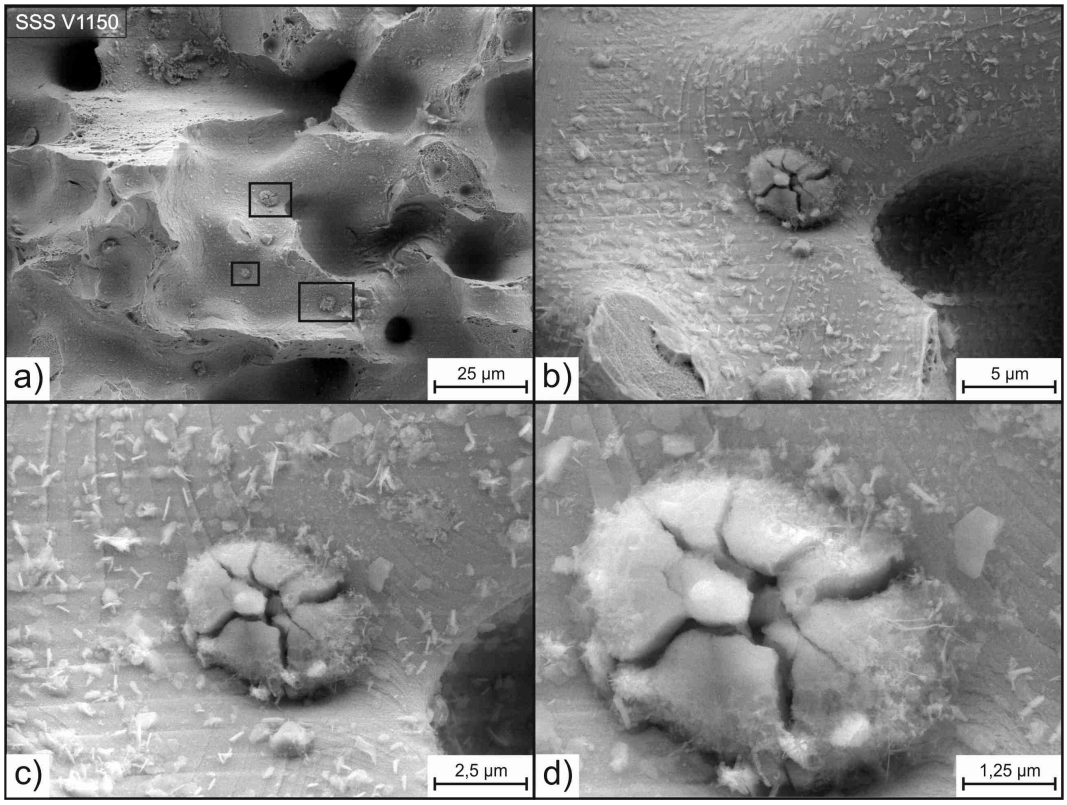

Figure 5. 69.: Large, oxidic particulates on the surface of a former pore, V1150 specimen

To draw further conclusions out of the SEM investigations following EDX analyses are regarded. These are presented in appendices B. 58 to B. 61.

The analysis of the particulates in the fractured areas [appendices B. 58 and B. 59] present an uniform result of their composition.
They show that these are Mn-Al-O-oxides and that their oxygen content is mainly 50 to 60 at.-% while their manganese and aluminum content is about 20 to 30 at.-%. They contain only little chromium (3 to 4 at.-%) and iron (4 to 10 at.-%) and the results of appendix B. 58 even show traces of titanium.

The angular particulates of figure 5. 68 are Mn-O-oxides as well [appendix B. 60]. They contain mainly oxygen (55 to 60 at.-%) and manganese (13 to 18.6 at.-%) and spectra 1 and 2 further show aluminum (12 to 14 at.-%). Furthermore it needs to be mentioned that the Si content is low for higher Al fractions but increases to about 5 at.-% wehen the Al amount decreases.

The composition of the investigated particulate of figure 5. 69 is depicted in appendix B. 61. This analysis shows a mainly composition of oxygen (67 to 71 at.-%) and manganese (20 to 25 at.-%) and especially chromium, aluminum and iron are measured only in traces.

Further figures and EDX results that underline the conclusions about the V1150 specimen are attached in the appendices B. 62 to B. 66.

5.4. Chemical analysis

The results of the chemical analysis due to the nitrogen and oxygen content of the different manufactured specimens are presented in tables 5. 7 and 5. 8.

Table 5. 7.: Nitrogen content of the manufactured samples in mass.-%
Initial value 0.315 mass.-%

Position/ Technique	HIP	SLPS	SSS	V700	V1050	V1150
Top	0.298	0.839	0,893	0.953	0.780	0.779
Deviation	(±0.016)	(±0.026)	(±0.052)	(±0.024)	(±0.041)	(±0.016)
Middle	0.308	0.828	0.882	0.853	0.721	0.833
Deviation	(±0.006)	(±0.002)	(±0.030)	(±0.053)	(±0.031)	(±0.017)
Bottom	0.298	0.856	0.914	0.862	0.744	0.847
Deviation	(±0.028)	(±0.010)	(±0.003)	(±0.019)	(±0.012)	(±0.014)

Table 5. 8.: Oxygen content of the manufactured samples in mass.-%

Position/ Technique	HIP	SLPS	SSS	V700	V1050	V1150
Top	0.055	0.245	0.252	0.221	0.495	0.986
Deviation	(±0.0017)	(±0.0164)	(±0.0132)	(±0.0398)	(±0.0233)	(±0.0213)
Middle	0.038	0.102	0.045	0.137	0.228	0.213
Deviation	(±0.0005)	(±0.0001)	(±0.0067)	(±0.0100)	(±0.0322)	(±0.0117)

These results show that all samples which were produced under increased nitrogen pressure of 1.75 bar (SLPS, SSS, V700, V1050 and V1150) have uptaken a high amount of nitrogen. Their nitrogen content is always higher than the initial amount of 0.315 mass.-% and levels except for the V1050 specimen around the aspired nitrogen value of 0.825 mass.-%. The V1050 specimen contrarily does not reach a nitrogen amount of about 0.825 mass.-% and only contains 0.721 mass.-% to 0.780 mass.-% nitrogen.

The HIP specimen shows a similar nitrogen content like the initial powder and the N fraction does not deviate much from the initial 0.315 mass.-% over the cross section. This was assumed in advance because the HIP specimen has not been produced with direct interaction with a nitrogen atmosphere and was thus not alloyed with further nitrogen.
The results of the oxygen measurements present lowest oxygen contents for the HIP specimen. This sample contains much less oxygen compared to the other specimens and the values do not differ much between the top and the middle. In contrast the SLPS, SSS and V700 specimens contain more oxygen and especially the deviations between top and middle are larger.
The oxygen content of the middle of the SSS specimen is furthermore the lowest value apart from the HIP specimen. The V1050 and V1150 specimens show moreover an even higher oxygen contamination. Their oxygen content even doubles the SLPS, SSS and V700 specimens content.

Additional measurements due to the oxygen content have been performed using a LECO TC-336 instrument (LECO Corporation, St. Joseph, MI). These measurements analyzed the whole sample that was used for XPS analyses before and are presented in table 5.9.

Table 5.9.: Oxygen content of the manufactured samples analyzed by LECO TC-336 instrument, in mass.-%

Oxygen content/ Technique	HIP	SLPS	SSS	V700	V1050	V1150
Content	0.053	0.071	0.049	0.038	0.056	0.044

Chapter 6

Discussion

Considering the density of the different consolidated specimens figure 6. 1 shows that the best results are achieved by using hot isostatic pressing and supersolidus liquid phase sintering. These samples show only small amount of porosity. Though the grain size of the SLPS sample is much larger compared to the HIP sample and the remaining pores appear larger this does not downgrade obtained results because the aspired goal of high density was reached for both samples sufficiently and both are densified homogeneously.

For the solid state sintered samples, the SSS sample without additional treatment appears as the most densified one. It is highly densified compared to the other sintered samples and its density is comparable to the state of the SLPS sample. Therefore the results show that sintering necks develop well during sintering under nitrogen atmosphere. In contrast the other solid state sintered samples with additional dwelling under vacuum during heating stage [figure 6. 1 d) to f)] are much less densified. They contain a much larger amount of porosity, indicating weaker sintering although the same final sintering temperature was set on. The best result of solid state sintering with dwelling under vacuum during heating stage is observed for the V1050 specimen which reaches the highest density. Nevertheless the use of an annealing step before reaching the final sintering temperature did not led to an improved consolidation and rather downgraded the sintering result.

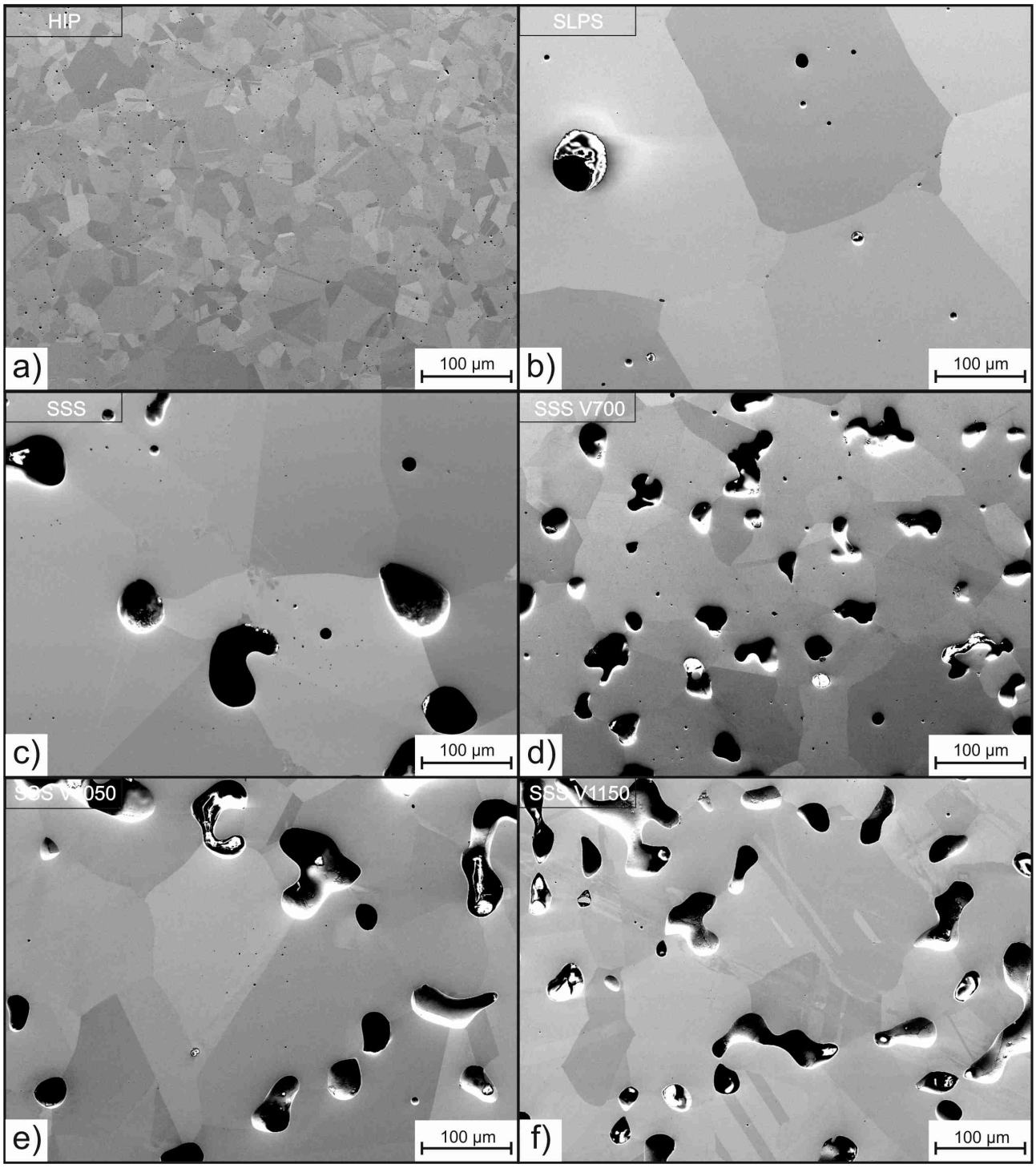

Figure 6. 1.: Different manufacturing techniques compared by their densification, polished specimens

The comparison of the fracture surfaces of the samples in figure 6.2 and 6.3 complete this conclusions.

Due to the nearly pore-free structure the fracture surface of the HIP sample is characterized by fine dimples initiated by fine oxide particulates. Inter- and trans-particle ductile fracture is the main failure mechanism registered for this sample. Presence of larger pores and inclusions in the SLPS sample contrarily results in much larger dimples of the ductile failure on the fracture surface. So coarse oxides and large pores in the SLPS sample result in dimple ductile fracture with much deeper dimples in comparison to the HIP sample.

The large particulates of the SLPS specimen [figure 6.3 b)] are further of the same composition as the HIP oxides [appendix A.1], but their shape and size is changed by the SLPS process strongly. They are concentrated in larger agglomerates, thus have much lower surface coverage than in the HIP sample and lead to stronger inter-particle necks.

Therefore oxide coarsening by the liquid phase of SLPS is advantageous in this case. By means of a liquid the oxides are redistributed/ transformed from fine, spherical particulates to larger agglomerates. The liquid phase in the SLPS sample generates at the same sites in the powder particle structure as the oxides are located, the powder particle surface and the grain boundaries. Thus the oxides are effected by the liquid immediately. They are "pushed" together into the former pores by a directed liquid flow and thus large oxide agglomerates form.

This is advantageous for the final mechanical properties of the SLPS specimen because a lower amount of larger inclusions is always more beneficial than the larger amount of fine inclusions as the total strength of inter-particle necks and therefore the mechanical properties of the consolidated component are improved in general. Larger particulates further lead to lower local stresses because of their size which improves the final mechanical properties of the product even more [35]. Therefore it can be concluded that the SLPS manufacturing in this case leads to better properties compared to the HIP technique. Though even if the final density of HIP and SLPS specimens is comparable, the oxide-shape and distribution provided by SLPS consolidation is much more advantageous.

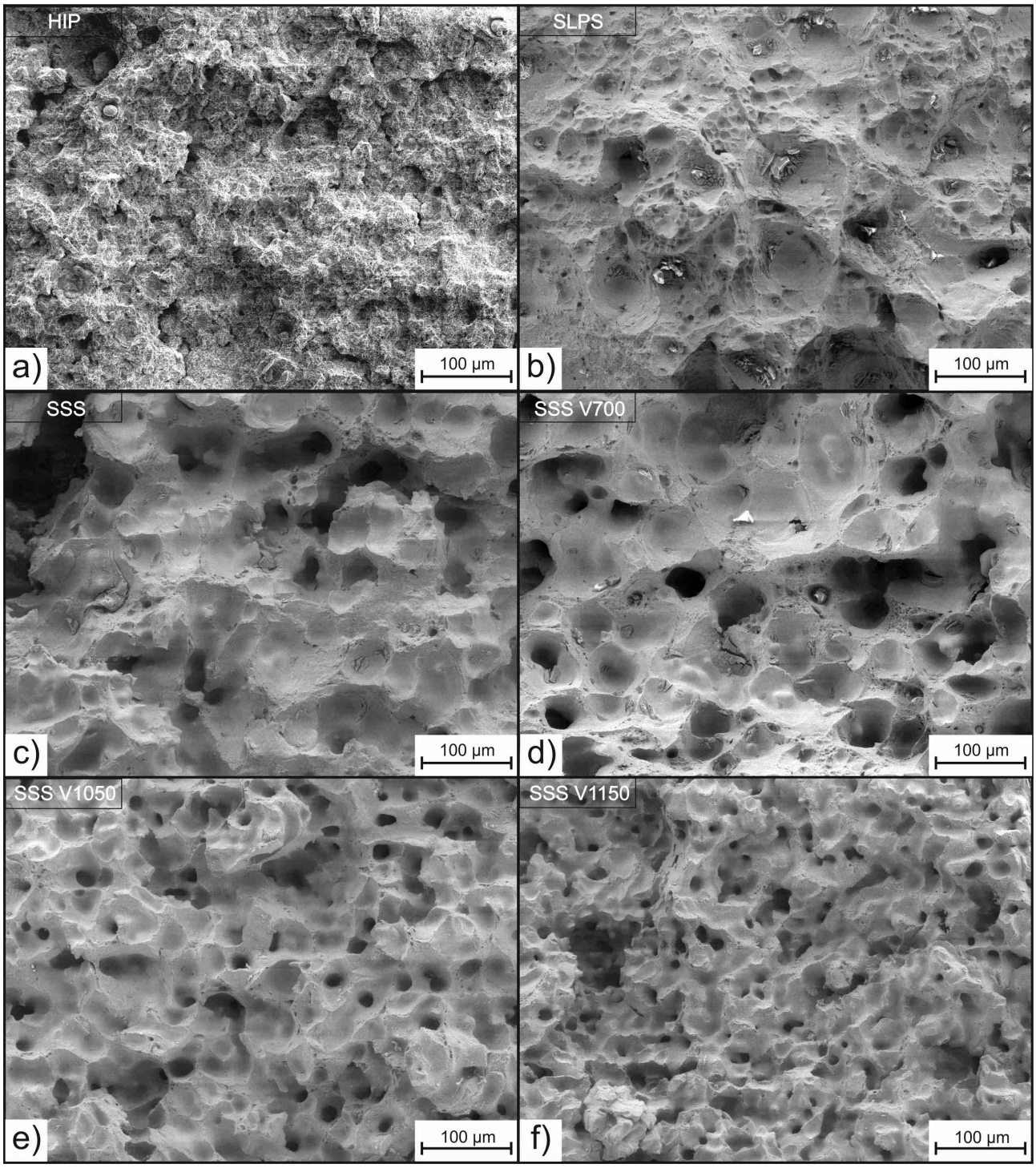

Figure 6. 2.: Comparison of the fracture surface of the different manufacturing techniques

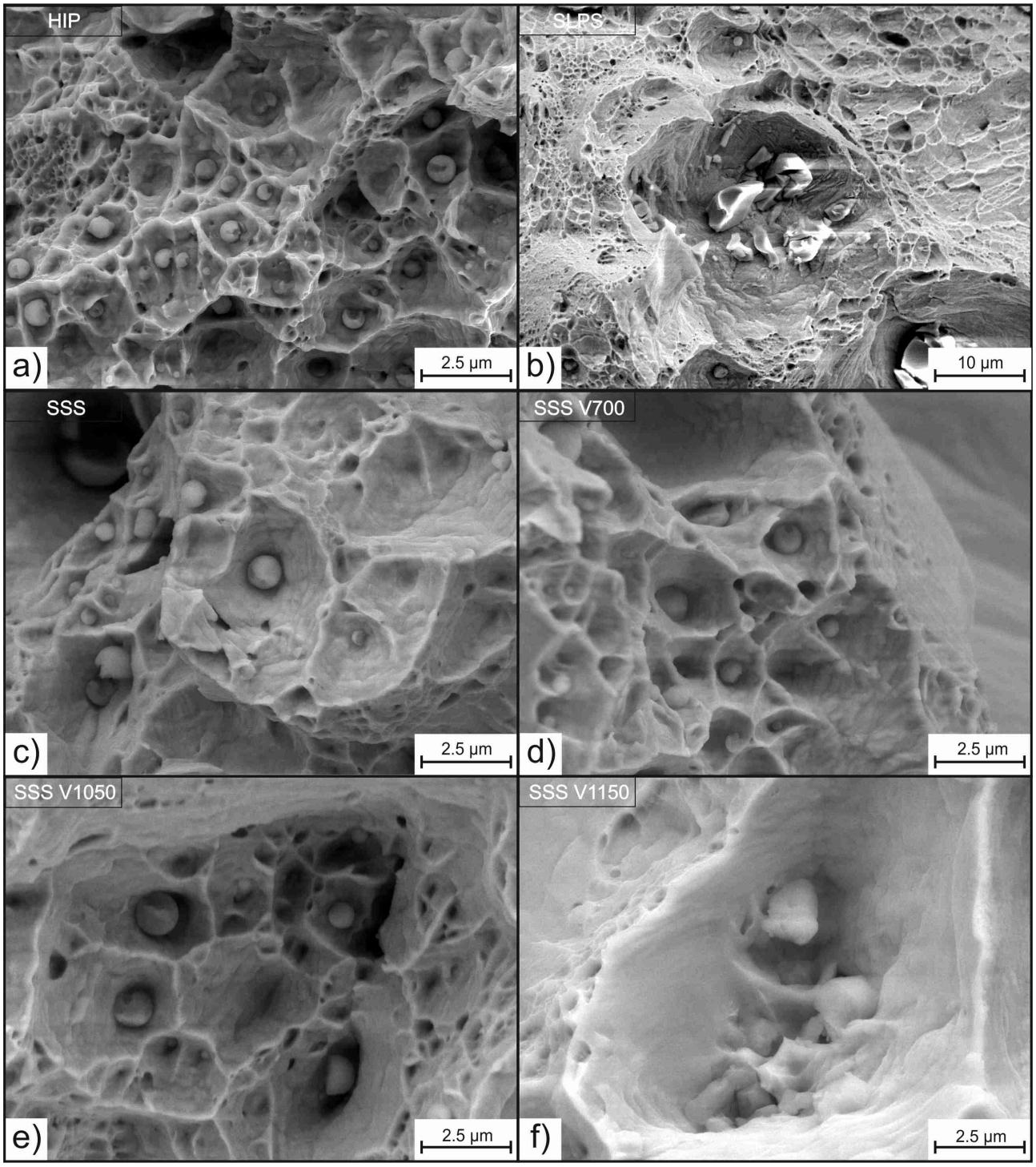

Figure 6.3.: Comparison of the Mn-Si-O-oxides found on the fracture surface of the different samples

The solid state sintered samples in contrast to HIP and SLPS specimens show a much more rough fracture surface [figure 6. 2 c) to f)] due to the large amount of pores. From these samples the sintering necks are best developed in the SSS sample which underlines again the best sintering result under nitrogen atmosphere without additional treatment. The vacuum annealed samples tend to contain more small pores and less developed sintering necks. This trend is more pronounced from V700 to V1150 [figure 6. 2 d) to f)] and underlines the disadvantage of the vacuum dwelling steps at applied vacuum conditions.
Figure 6. 3 c) to f) additionally shows the presence of spherical oxides and their distribution in the sintering necks of the solid state sintered samples. The failure mode of these samples therefore is similar to the HIP sample only the localization at the sintering necks differs.
Thus the sintering results are inferior to the HIP sample because of lower amount of interparticle connections and larger amount of pores. Hence the manufacturing via sintering in this thesis comes to the result that sintering under nitrogen atmosphere without dwelling is more advantageous than dwelling under weak, technical vacuum (0.1 mbar) before final densification. This will be emphasized even more by considering the XPS results later on.

Moreover the vacuum annealed samples and especially the SSS sample depict the state of the powder mass before the appearance of a liquid phase and hence without its influence. Here the oxides are still spherical, small and present in higher amount. Hence these samples further confirm the assumption of a connection between the oxide redistribution and transformation to the presence of a liquid phase in SLPS.

In addition to this topic of consolidating the Fe-19Mn-18Cr-C-N steel powder the solid state alloying of this steel with nitrogen during manufacturing shall be discussed. The results of the chemical analysis are presented in table 5. 7. The initial value of nitrogen in this steel was 0.315 mass.-% and should be raised to 0.825 mass.-% by solid state alloying. Considering these values it is obvious that under increased nitrogen partial pressure produced samples have up-taken a large amount of nitrogen. The nitrogen values of SLPS, SSS, V700 and V1150 are further very close to the aspired value of 0.825 mass.-%.
For these techniques it can be concluded that the alloying through the sintering atmosphere works properly and that the manufacturing leads to the aimed alloy composition. Therefore from a chemical point of view the Fe-19Mn-18Cr-C-N steel can be produced by any of these techniques in a proper way.

The HIP specimen in opposite to this only contains the initial amount of nitrogen. This specimen cannot be alloyed with nitrogen during the manufacturing process. Thus the nitrogen amount cannot be changed during the production and has to be increased in the loose powder. For this aim two possibilities are considered, the first one is to produce the prealloyed powder with a higher nitrogen amount and the second one is to nitride the powder before hot isostatic pressing. Because a melting with a nitrogen amount over 0.6 mass.-% of nitrogen cannot be produced for this steel the first possibility is excluded [5]. The second possibility is connected with an additional manufacturing effort and increases costs because it assumes that the powder has to be heated up under nitrogen atmosphere separately to solid state alloy it before isostatic pressing. This makes the already expensive HIP consolidation even more expensive and handicaps the HIP technique compared to the other applied techniques. Thus the HIP manufacturing is a good way to produce a highly densified product, but makes it complicated to achieve the aspired ideal nitrogen to carbon ratio.

To furthermore evaluate the effect of different manufacturing techniques on the oxide distribution and transformation in Fe-19Mn-18Cr-C-N steel, XPS and EDX analyses are discussed in the following section.
At first it has to be mentioned that the results indicate an ineffectiveness of the ion etching during XPS investigations and thus no accurate information about the chemical composition in deeper etched areas can be given. Looking at straight lines of the element distributions of the XPS results after 5 nm etch depth for more or less all specimens studied indicates this ineffective ion etching at larger etch steps. Further SEM investigations confirm the hypothesis that the ineffective ion etching is connected to the high roughness of the fracture surface. This means that shadowing effects during ion etching and XPS analysis have dominant effect on the XPS curves and trends depicted over the etch depth. Therefore a description of the oxide phase size, distribution and composition at larger etch depth has to be performed very accurately.

Starting this topic firstly the estimated amount of oxide in the different samples shall be pointed out. For this reason the oxygen content of the samples over the etching depth is depicted in figure 6.4. It shows very clearly that the best densified HIP and SLPS samples contain less oxygen compared to the sintered samples and that their oxygen contents levels after the first etching steps. The trend of the O content is very similar for both HIP and SLPS samples and their fractions only differs about 2 at.-%. Hence their oxide content is nearly equal.

The sintered samples in contrast contain much more oxygen in the phases present on the fracture surface. Their oxygen amount starts from about 35 to 45 at.-% at the as-fractured surface to 23 to 37 at.-% in 50 nm etch depth. Thus their oxide content is much higher than those of the HIP and SLPS sample. The depiction of the total sum of oxide in figure 6.5 completes this consideration by following the same trends as the distribution of the oxygen content.
The lower oxide content and constant leveling of the oxygen signal measured for the HIP and SLPS sample can further be explained as following. The porosity of these samples is very low and thus there is no oxide remaining on the pore surface. The oxides in the HIP and SLPS samples are moreover coarse and included in the consolidated powder mass. Due to the coarse nature of this oxides they are not etched away with applied etching steps and therefore their surface coverage and thus intensity of the oxygen signal does not change with the etching steps. The solid state sintered samples in contrast are much more porous. Pores are covered, as the initial powder surface, by a heterogeneous oxide layer formed by a thin and homogeneous iron oxide layer and particulate oxides. Therefore during the etching the iron oxide layer from the pore surface is removed first and then particulate oxides start to be removed. Hence the oxygen signal indicates a continuous decrease with etching depth for solid state sintered samples, even at such high fracture surface roughness. Therefore it can be concluded that the HIP and SLPS processing gives better consolidation and more favorable oxide distribution. Less area is covered by oxides meaning better consolidation due to improvement of the inter-particle connection.

Further on not only the amount of oxide shall be considered. The oxide composition and how it differs between the different manufacturing techniques is important to estimate the oxide transformation from the as-received state.

For this reason the cation composition is depicted in figure 6.6 in total composition of the surface compounds and in figure 6.7 in normalized fractions. Figure 6.6 shows again that the total cation sum and thus the oxide amount of HIP and SLPS is much lower compared to the sintered samples. The XPS results of this specimens show large amounts of manganese and chromium on the oxidic state. SEM and EDX investigations indicate Mn-Si-Cr-O-oxides on the fracture surface as well. Further only very low amount of iron-oxide is detected during XPS analysis.

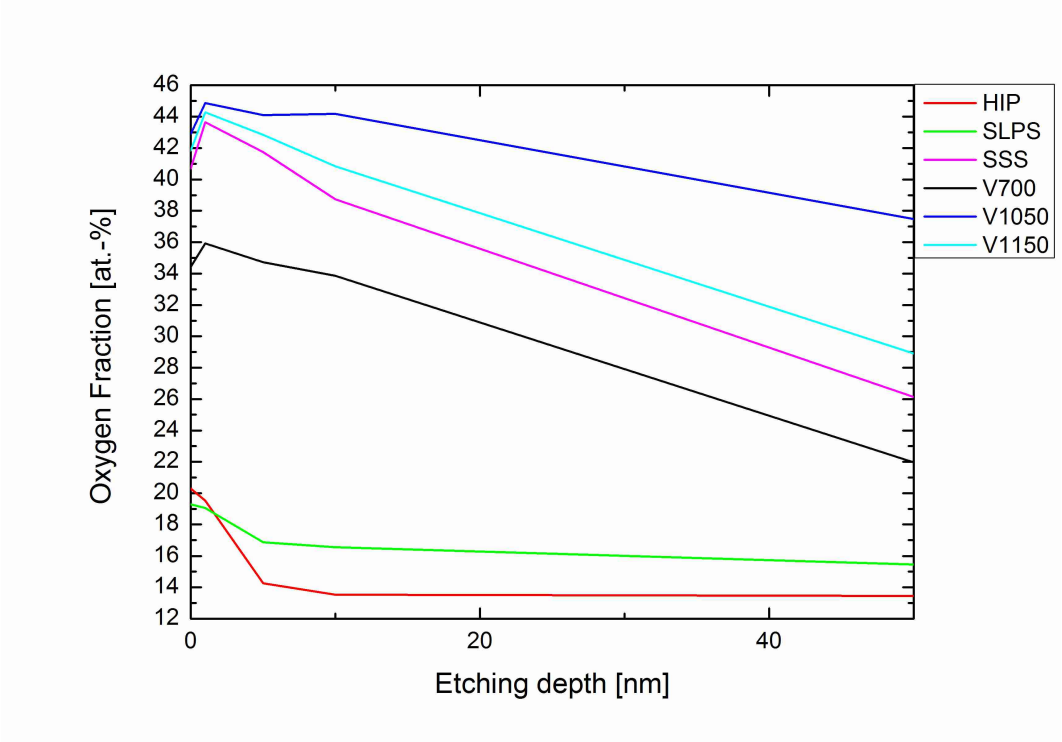

Figure 6. 4.: Oxygen fraction over etching depth for different manufacturing techniques, XPS result

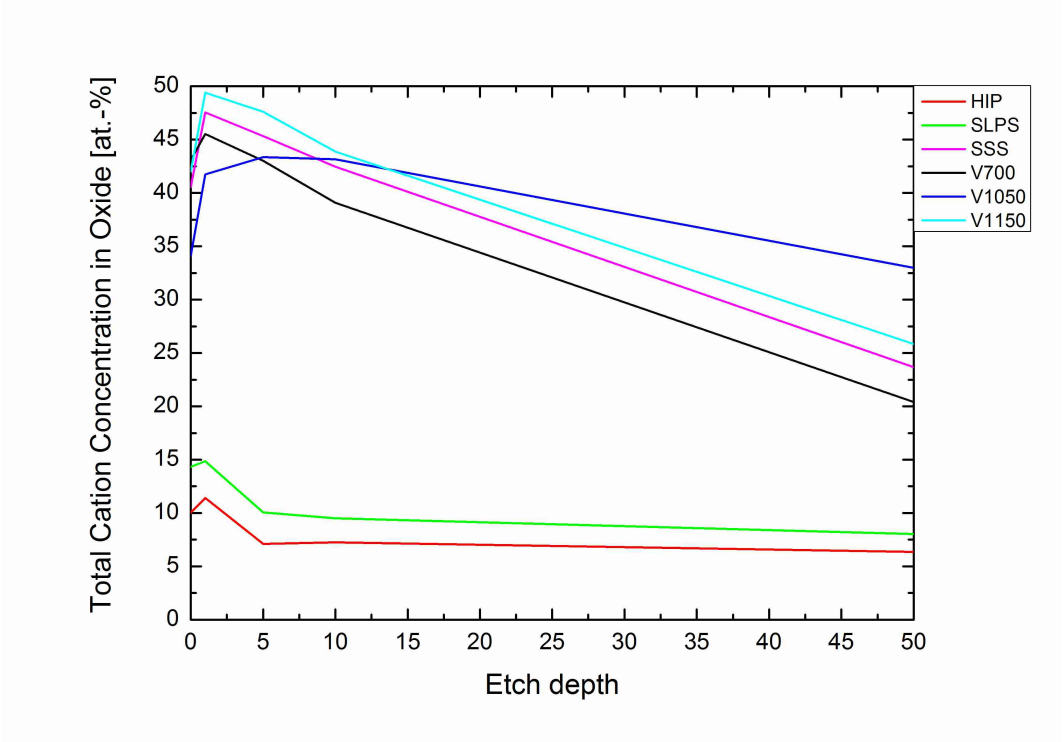

Figure 6. 5.: Total sum of cation concentration and thus sum of oxide amount over etching depth for different manufacturing techniques, XPS result

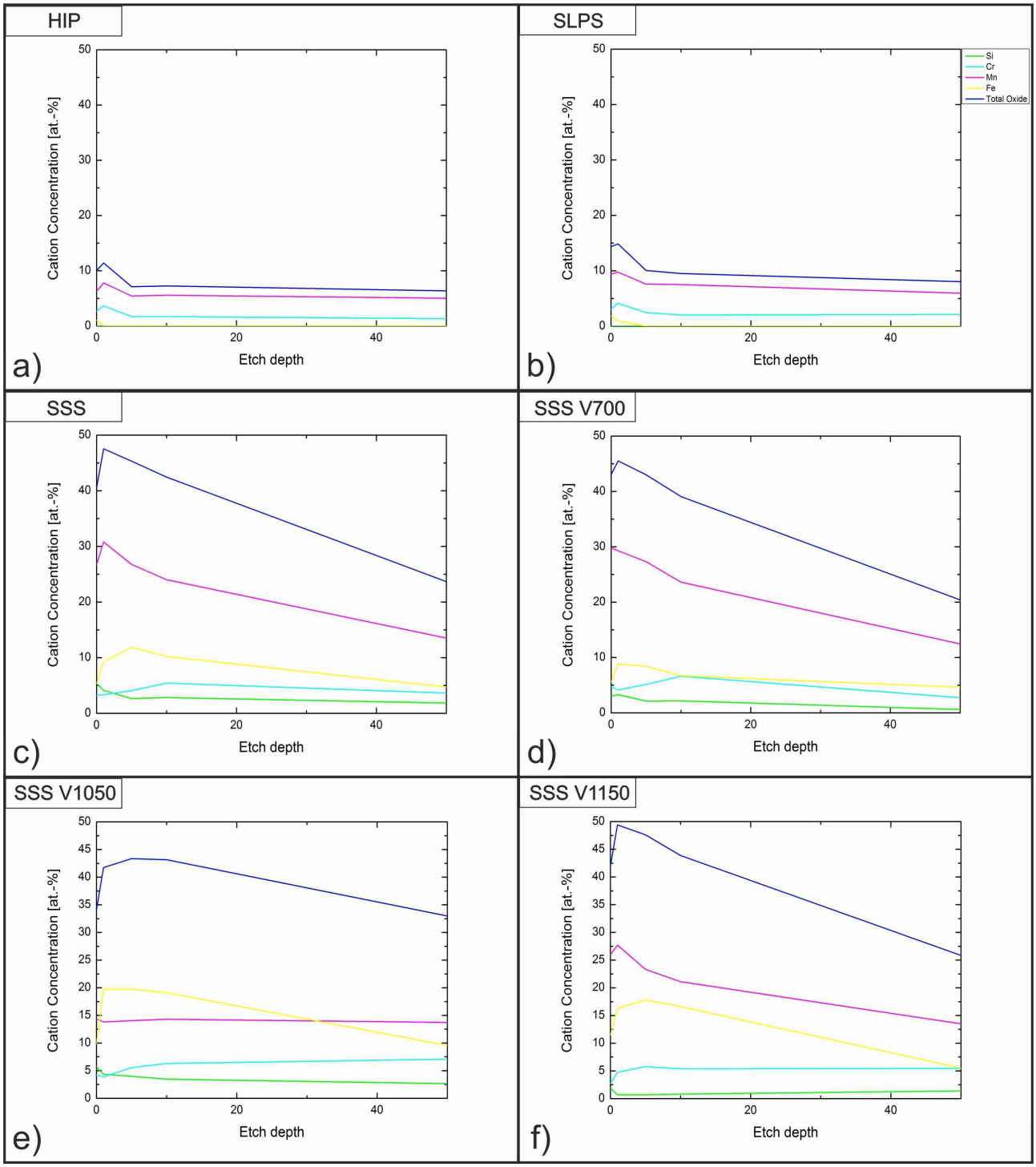

Figure 6. 6.: Total composition of the surface compound of different manufacturing techniques in at.-%, XPS result

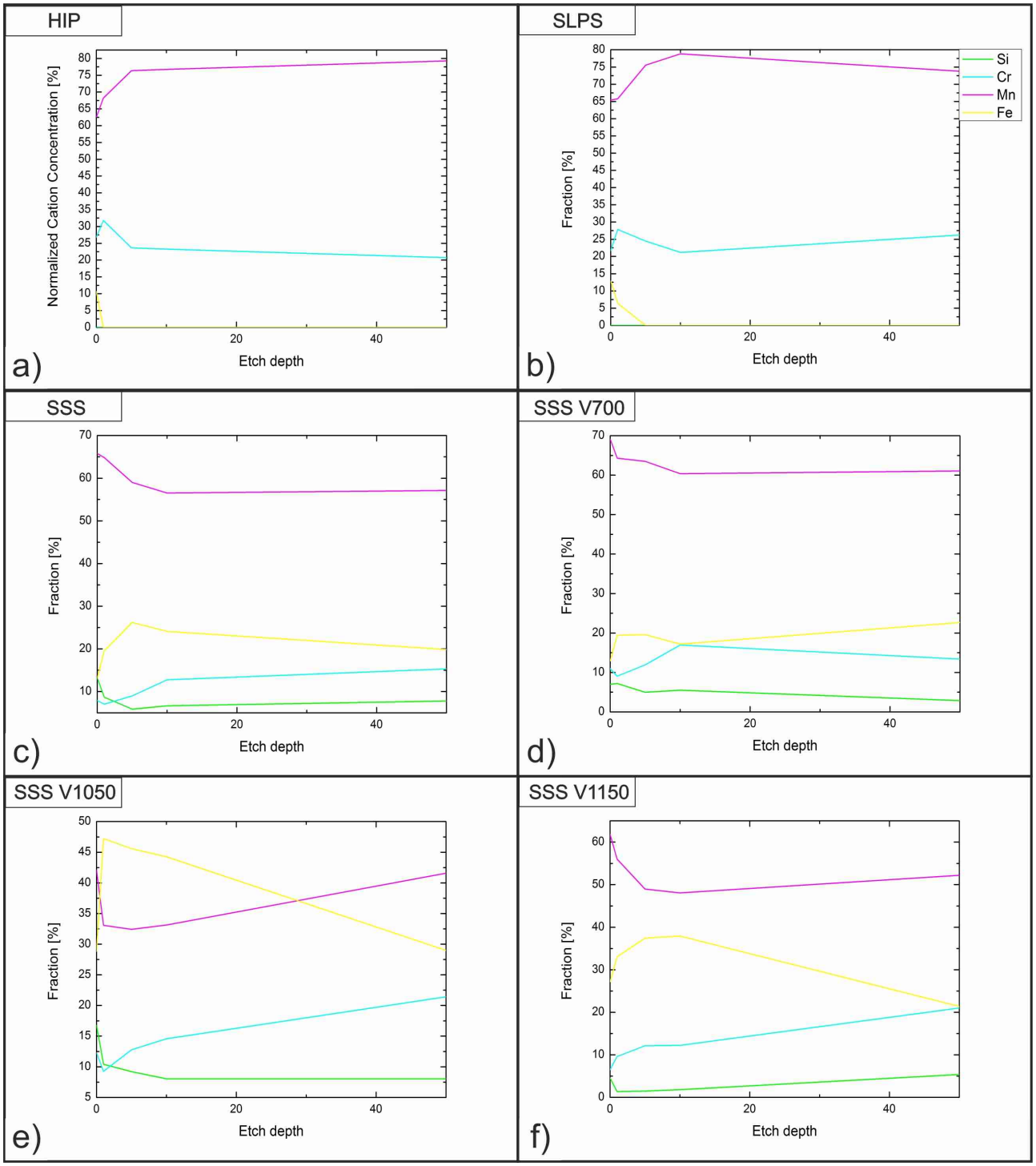

Figure 6. 7.: Comparison of the normalized oxide composition of different manufacturing techniques [%], XPS result

Therefore it is assumed that the iron-oxide layer which was found on the as-received powder surface is reduced/transformed during manufacturing and only more stable oxides are left in the powder mass. Furthermore no single chromium based oxides are found in the densified powder mass either, present oxides are complex Mn-Si-Cr-oxides.
Thus it is assumed that the former " oxide-islands " present on the initial powder surface were enclosed in the powder mass during consolidation and transformed to more stable oxides.
The whole appearance of the fracture surface and the existence of manganese, silicon and chromium in a mixed oxidic state underline previously estimated assumptions [19, 34] which concluded that during heat-treatment the oxides transform from the initial composition into more stable oxides.

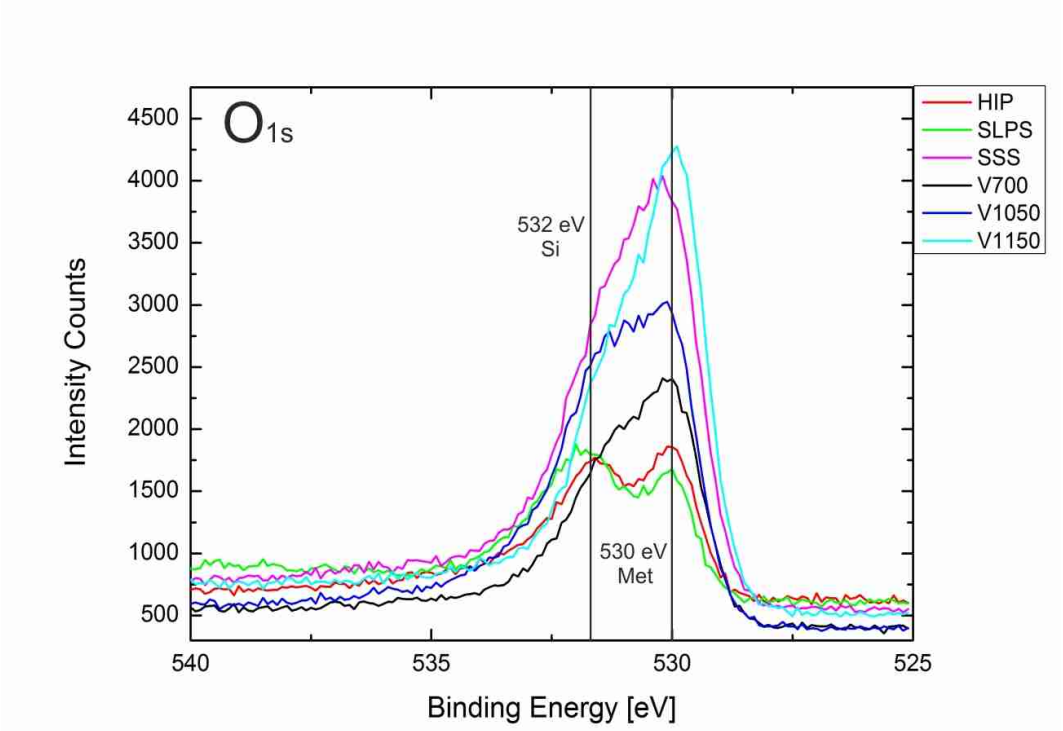

Figure 6. 8.: O 1s peak of the pure fracture surface measured for different manufacturing techniques, XPS result

The shape of the O 1s peak for the differently consolidated samples [figure 6.8] confirms this assumption. For HIP and SLPS specimens it shows a double peak in the oxygen peak which indicates the presence of different oxides. The first peak at around 530 eV is corresponding to oxides formed by Fe, Cr and Mn. The second peak at 532 eV moreover corresponds to oxygen bonded in silicon-based oxides and thus a more stable oxidic state.

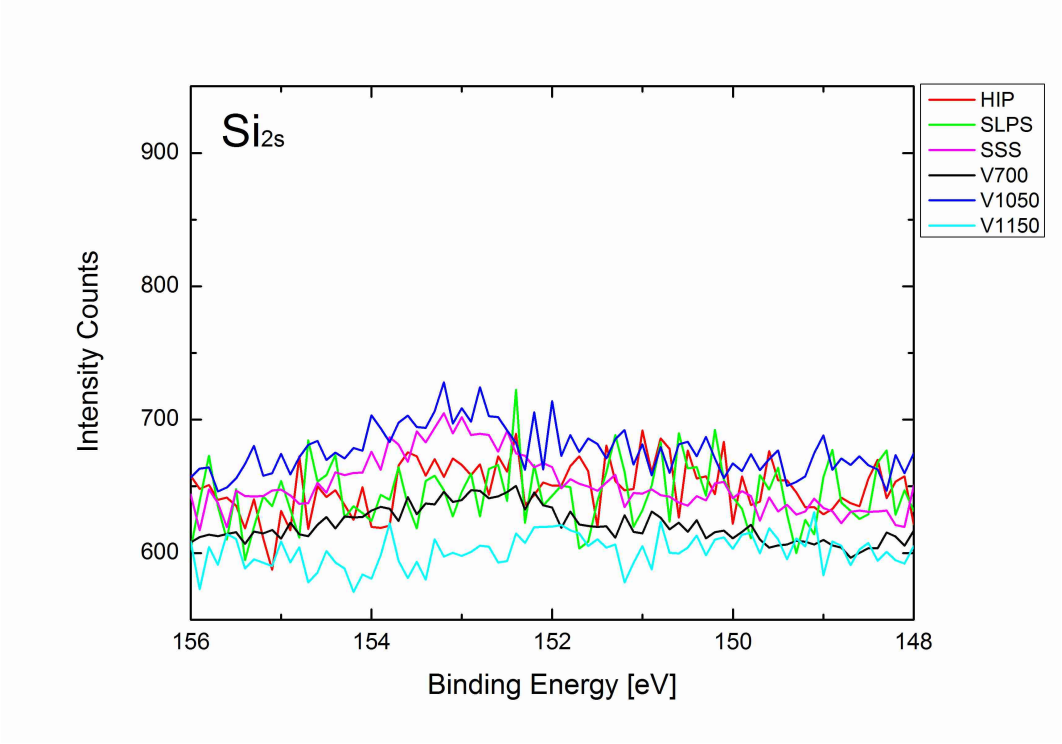

Figure 6.9.: Si 2s peak 1 nm etch depth measured for different manufacturing techniques, XPS result

The previous researches thus estimated the formation of stable spinells of higher binding energy. Hence oxides in HIP and SLPS samples are estimated to be Mn-Si-Cr-O-oxides. Their composition fits quite well to the silicon and manganese containing oxides and confirm the development of the oxides in this material towards more stable Mn-Si-O-oxides.
At this point it has to be mentioned that though silicon could not be quantified during XPS analysis, the measurements show its presences also for the HIP and SLPS sample. This can be seen in figure 6.9 which depicts the measured silicon signal of XPS analysis.

In general oxide transformation processes occur in accordance with the thermodynamic stability of oxides in the line [24, 36, 37]:
$Fe_2O_3 \rightarrow FeO \rightarrow Fe_2MnO_4 \rightarrow Cr_2FeO_4 \rightarrow Cr_2O_3 \rightarrow MnCr_2O_4 \rightarrow MnO/MnSiO_x \rightarrow SiO_2$
Therefore found oxides belong to the very stable manganese and silicon based oxides and it's assumed that they grow at the expense of oxides with lower stability. The existence of manganese based oxides is further very likely for this alloy because of its high manganese amount it tends to Mn-oxides and not to more chromium based oxides.

The analyses of the fracture surface via XPS, SEM and EDX present this state and show as a result a metallic matrix, which contains bulk estimated manganese, chromium and iron contents, and oxides of high stability.
Concluding it can be suggested that the poor reduction conditions of HIP and SLPS manufacturing lead to oxide transformation from a mixed as-received state to only more stable Mn-Si-Cr-complex oxides. These are thus contained in higher amount in the manufactured product in comparison with the based powder.
The transformation of oxides towards the most stable oxide state is very likely for these samples because the conditions of HIP and SLPS under nitrogen atmosphere enable no external influence on reduction of these oxides by the atmosphere. Both systems enable no reducing reactions by the atmosphere and hence a transformation to more stable oxides is the only way to reduce the iron and chromium oxides.

Additionally the advantage or disadvantage of this transformation and redistribution for the manufacturing of a prealloyed steel powder following the C+N concept shall be discussed shortly.
Focusing on the best possible result of manufacturing presence of the inclusions formed by stable oxides in the powder mass does not appear to be unfavorable because the product is well densified with minor loss of the carbon by a carbothermal reduction. Considering the full reduction of any oxides in the powder under for example vacuum condition this would happen by a carbothermal reaction of the prealloyed carbon. This will result in carbon loss of the alloy [36]. This loss of C further cannot be re-established and thus the alloy concept would be changed and the favored C+N ratio not achieved.
Thus the inclusion of stable oxides which bond the oxygen is more advantageous than full oxide reduction. Especially if these oxides can be coarsened and redistributed, as during SLPS consolidation to improve the mechanical properties of the powder compact though containing oxides.

The additionally appearance of Mn-Al-Oxides in the densified powder mass is further evaluated as not characteristic for this steel powder in manufactured state because the Fe-19Mn-18Cr-C-N steel contains only traces of aluminum which cannot lead to such high amounts of Al in oxides. It's rather the case that the powder mass are contaminated by Al during manufacturing and solution annealing because they were handled in an aluminum oxide cup.

The oxide state and the cation distribution in the sintered samples differs much from the HIP and SLPS samples. Firstly the XPS results [figures 6.6 and 6.7] show a much higher oxide content on the fracture surface and large amounts of iron and silicon in oxidic state. Although manganese still constitutes the largest fraction on the total cation sum.

The cations in the solid state sintered samples are in much higher amount in oxidic state compared to the HIP ans SLPS samples. Thus for example the oxidic peak of manganese is much more intensive for these materials in comparison with the HIP and SLPS sample [figure 6.10].

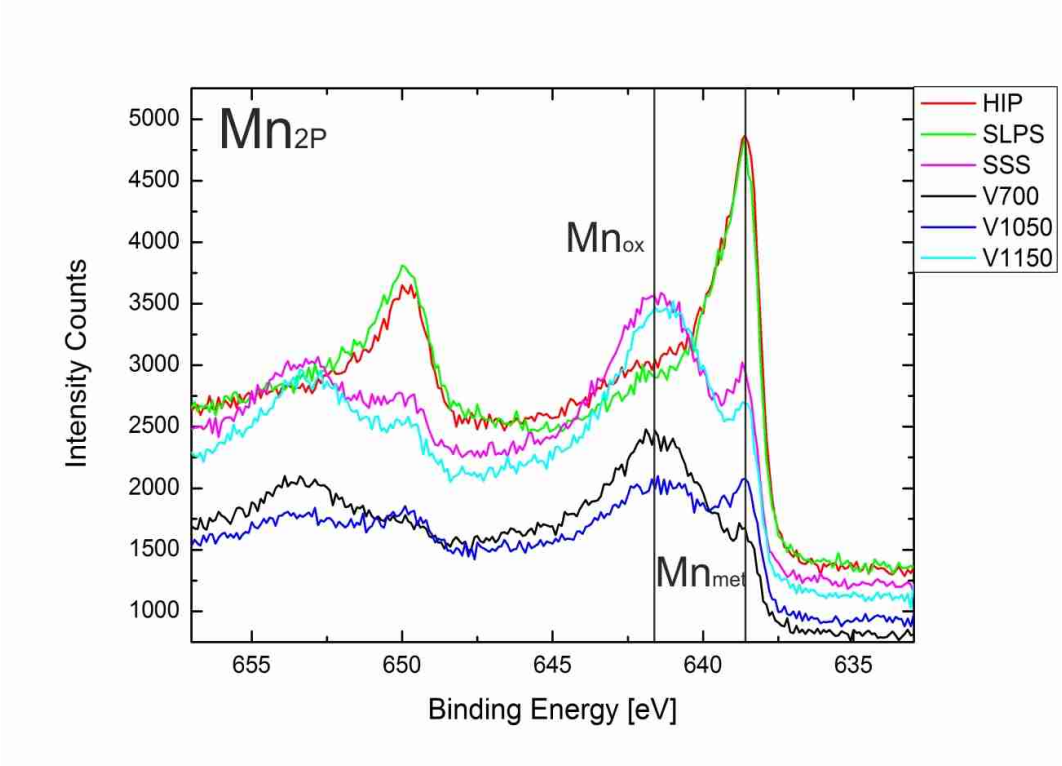

Figure 6.10.: Mn 2p peak of the pure fracture surface measured for different manufacturing techniques, XPS result

The position of the oxygen binding energy peak [figure 6.8] further gives more information about the present oxides, as was described above. For the sintered samples the oxygen peak position at 530 eV indicates that oxides formed by metallic cations (Fe, Cr and Mn) are dominant in contrast to the HIP and SLPS samples. Thus in these samples a larger fraction of oxides of lower stability compared to the HIP and SLPS specimens is present.
The larger fraction of iron oxide can furthermore be connected to the higher porosity of these samples because iron oxide distributes mainly at the pore surface.

The HIP and SLPS samples were well consolidated, thus have much less pores. The sintered samples indeed show high porosity and thus much more iron oxide and total oxide amount.
The SEM and EDX results of the sintered samples complete this consideration because they show presence of iron oxides and increased oxygen content on the pore surface.
In this case the sintering experiment with an included dwelling step under vacuum at 700°C furthermore shows itself as slightly more advantageous as pure sintering under nitrogen atmosphere. It contains less oxide in sum and lower fractions for every element in oxidic state. Dwelling under vacuum at 700°C thus leads to an improved oxide reduction compared to just sintering under nitrogen atmosphere. The reduction during this dwelling step is mostly assumed because of the dissociation of iron oxide. Nevertheless the effect is low and is determined by the quality of the vacuum, that was not good enough in this study.
The dwelling at 1050°C and 1150°C present themselves as more disadvantageous and show no improvement of the oxide reduction. Their oxide amount is similar and they contain more oxygen.
The problem in this case is the high temperature dwelling of the powder under oxidizing conditions. The technical vacuum has a very low quality and thus dwelling in this atmosphere at high temperatures leads to further oxidation of elements like Fe, Cr, Mn and Si.
The problem of these dwelling steps is not only the oxidizing atmosphere, but the high temperature. Dwelling the material at high temperature enforces increased mass-transfer of Cr, Mn and Si from the bulk and thus more oxidation of the powder because of more diffusion of these elements. The dwelling at high temperatures exposes these elements for a longer time to an oxidizing atmosphere, hence this leads to increased oxidation. Using such an oxidizing atmosphere dwelling at high temperatures should be avoided and the heating should be as fast as possible to avoid mass-transfer.
An improvement of the oxide reduction by a dwelling step moreover needs much lower temperatures to prevent this further formation of oxides due to the mass-transfer at high temperatures. A dwelling step temperature should only be high enough to reduce iron-oxide, but low enough to prevent diffusion from the bulk. Additionally the dwelling temperature has to be low enough to avoid evaporation of manganese.
Thus 700°C should be the temperature limit for a dwelling step.

Manganese loss was further measured in higher extent during former investigations in vacuum. The heat-treatment under UHV [19] resulted in an increased evaporation of Mn from 700°C and denies the feasibility of the Fe-19Mn-18Cr-C-N steel to be sintered under vacuum conditions because of this. It was concluded that the loss of manganese would be too high to ensure the aimed properties of the material in the sintered state and thus sintering under UHV was mainly excluded as a feasible manufacturing technique.

The heat-treatment under nitrogen atmosphere in contrast provides much lower manganese loss of the material. It did not change the materials composition and thus did not change the materials properties evidently [34].

The results of this thesis considering this topic show no intense manganese evaporation either. The XPS results show no decrease of the manganese amount on the fracture surface and thus no significant loss during consolidation. Moreover the EDX results considering the matrix show no manganese loss as well. These analyses detect an estimated bulk composition with the manganese, chromium and iron ratio of 1:1:3 and show that Mn is not evaporated from the matrix.

Thus due to high nitrogen pressure and remaining oxides up to high temperatures manganese does not evaporate significantly and the chemical composition of the alloy is not changed evidently.

Therefore the Fe-19Mn-18Cr-C-N steel powder is produced to aimed alloy composition due to prevention of manganese loss by evaporation, carbon loss through carbothermal reduction and additional nitrogen alloying in the case of solid state sintering and supersolidus liquid phase sintering.

Chapter 7

Conclusions and future work

The results of the present work estimate following conclusions about the consolidation and the oxide distribution of the Fe-19Mn-18Cr-C-N steel.
Firstly the steel powder can be consolidated by using SLPS, SSS and V700 without noteworthy manganese and carbon loss due to the minimizing of evaporation or carbothermal reactions. Further these manufacturing techniques lead to the aspired nitrogen content by solid state alloying. Therefore consolidated Fe-19Mn-18Cr-C-N steel compacts have the aspired chemical composition. The HIP manufacturing moreover only prevents manganese and carbon loss, but an increase of the nitrogen content is not possible or economically feasible. This is the main disadvantage of the HIP manufacturing. Though it produces a well consolidated material with very fine grain-size and low oxide amount, it does not allow solid state alloying. Furthermore also the shape of the oxides found in the HIP specimen is disadvantageous because of a large area covered by oxides.
The SLPS sample is good densified as well and achieves a low oxide amount too. Additionally the presence of the liquid phase leads to a more favorable oxide shape and distribution in the consolidated powder mass. Furthermore, in contrast to HIP, SLPS consolidation enables solid state alloying with nitrogen during manufacturing. The main disadvantage of the SLPS manufacturing is the large grain-size after manufacturing. The grains are about six times coarser as in the HIP specimen and thus the mechanical properties supposed to be effected. Hence for the SLPS manufacturing the elimination of the grain growth has to be improved in future studies. In this context it is possible to use finer powder and to shorten the annealing time at the final sintering temperature significant. Thus a coarsening of the microstructure by high temperature annealing would be minimized.

Furthermore a degradation of the other achieved properties by SLPS is not expected by shortening the annealing time because the high densification and oxide redistribution are a consequence of the presence of a liquid phase in SLPS and not of the annealing at high temperatures.
In the case of the solid state sintered samples the V700 specimen has to be pointed out because this manufacturing route leads to an improved oxide reduction compared to the sintering without additional treatment. It leads to lower oxide amount and enables solid state alloying to the aspired nitrogen value as well. The disadvantages are the large grain-size due to the long annealing time (1340°C/ 6 h) and worse consolidation in comparison to the SSS sample.
Therefore it seems to be beneficial to further combine the SLPS manufacturing with this dwelling step at 700°C. It is estimated that this approach will lead to lower total oxide amount in the densified powder mass and further because of the SLPS consolidation to high density and improved oxide distribution in contrast to the sintering route.
The other dwelling steps during heating stage of 1050°C and 1150°C are moreover not applicable for further investigations because of additional oxidation at high annealing temperatures.
It can be finally concluded that a dwelling step under vacuum during heating stage should be limited to a temperature of 700°C in order to improve the oxide reduction. The reason is that till this temperature iron oxide is well reduced and minimal mass-transfer from the bulk allows avoiding of re-oxidation as well as minimizing manganese evaporation.
Further the quality of the used vacuum should be improved to enhance oxide reduction. The quality of the technical vacuum (0.1 mbar) which was used in this work is rather low with high concentration of oxygen. An improvement of the vacuum level and its quality is assumed to effect the oxide reduction strongly and enhance the efficiency of the application of a vacuum dwelling step at 700°C even more.

Appendix A

Tables

Table A. 1.: Composition of the in HIP and SLPS specimen contained manganese based oxides, in at.-%

Sample/ Element	O	Si	Cr	Mn	Al	Mo	Se	Ti	S	Fe
HIP	54.8	6.6	3.6	25.6	–	–	–	–	2.2	7.25
SLPS	62.9	8.1	0.6	21.9	2.5	1.3	1.7	–	1.0	–

Table A. 2.: Grain size and average particle size of the manufactured samples

Feature/ Sample	Powder	HIP	SLPS	SSS	V700	V1050	V1150
Grain size in μm	20	25	150	100	100	100	100
Particulate size in μm	–	0.625	4.000	1.062	0.875	0.750	0.775

Appendix B

Images

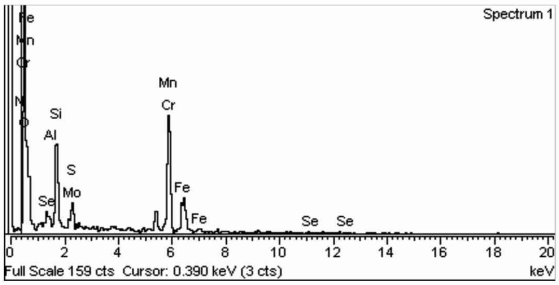

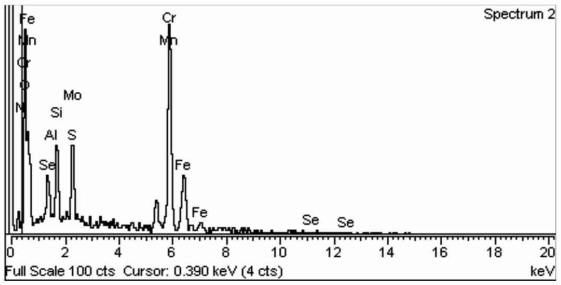

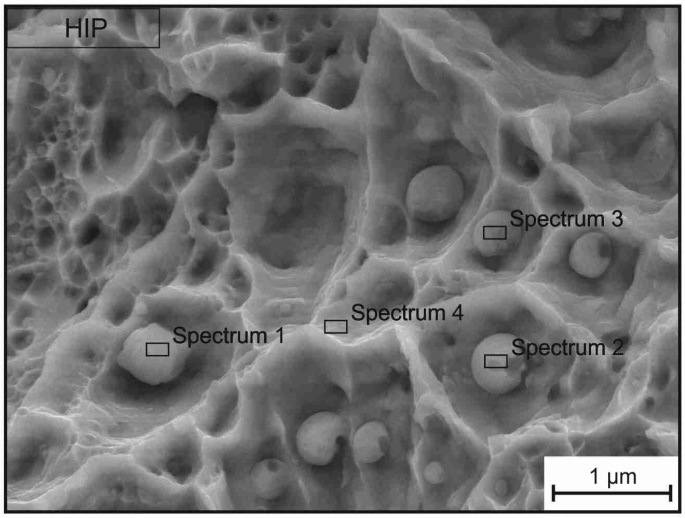

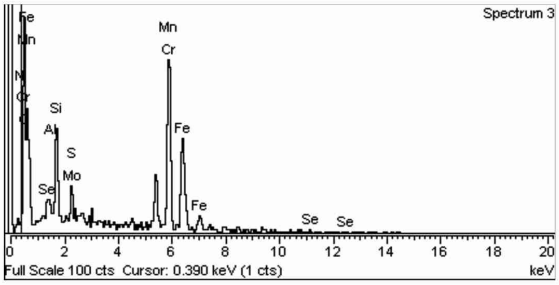

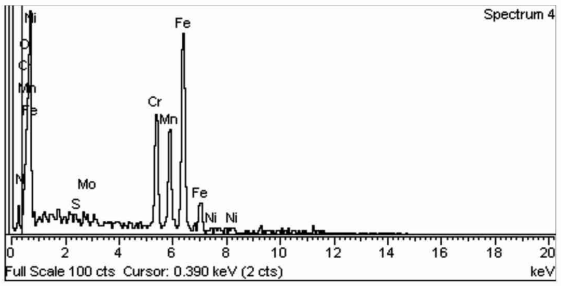

Metallic elements only										
Spectrum	Si	Cr	Mn	Al	Mo	Se	Ti	S	Fe	Total
1 [at.-%]	11.61	8.02	59.33	--	--	--	--	5.39	15.65	100
2	6.80	6.75	60.59	--	3.69	--	--	5.63	16.54	100
3	6.62	11.00	46.26	2.74	3.34	2.07	--	--	27.96	100
4	--	20.48	19.93	--	--	--	--	--	59.59	100

All elements												
Spectrum	N	O	Si	Cr	Mn	Al	Mo	Se	S	Ti	Fe	Total
1 [at.-%]	--	54.79	6.62	3.62	25.56	--	--	--	2.18	--	7.25	100
2	--	45.08	4.70	3.51	30.49	--	2.55	1.76	2.94	--	8.98	100
3	--	42.39	4.81	6.08	24.95	1.91	2.74	1.55	--	--	15.60	100
4	--	--	--	20.48	19.93	--	--	--	--	--	59.59	100

Figure B. 1.: EDX analysis results of the surface particulates of image 5. 12, HIP specimen

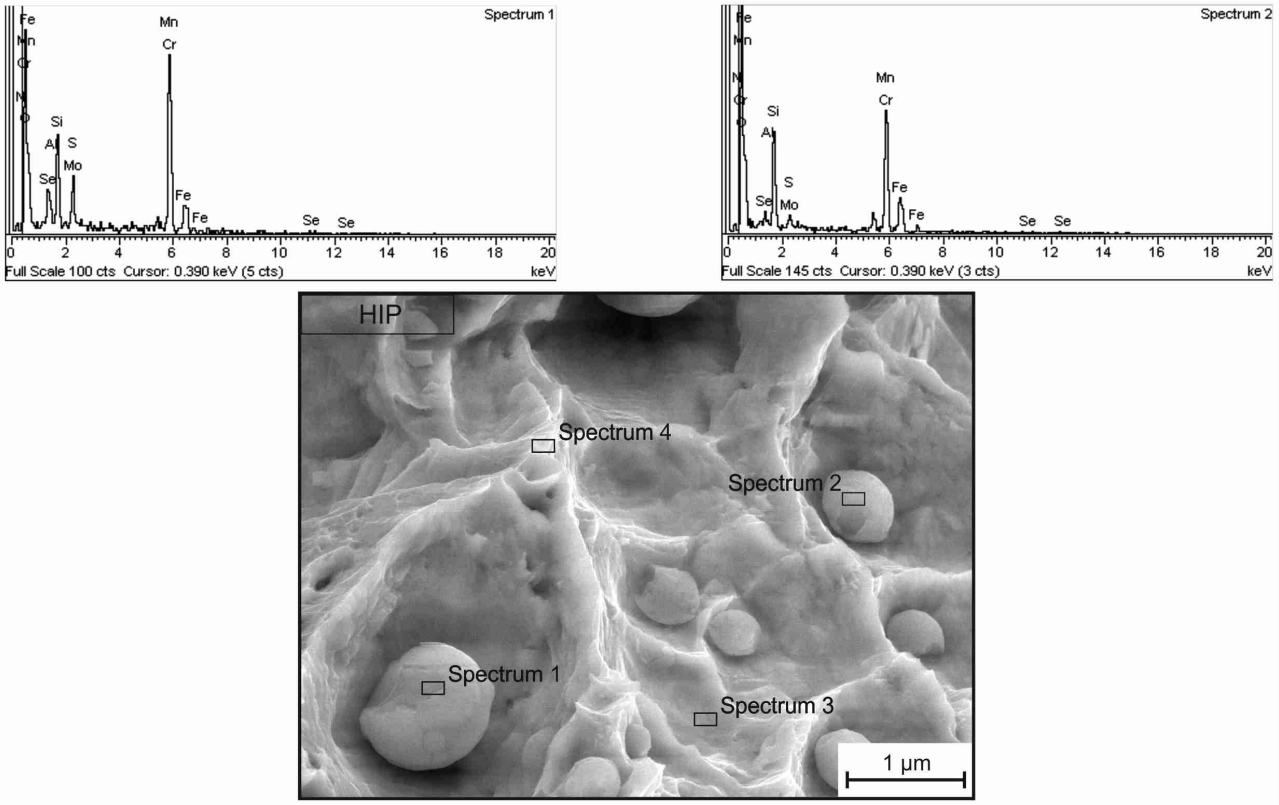

Metallic elements only										
Spectrum	Si	Cr	Mn	Al	Mo	Se	Ti	S	Fe	Total
1 [at.-%]	11.22	3.51	75.81	3.39	6.07	--	--	--	--	100
2	13.58	5.44	63.97	--	--	--	--	--	17.02	100
3	--	17.81	21.42	--	--	--	--	--	60.87	100
4	--	19.50	20.55	--	--	--	--	--	59.95	100

All elements												
Spectrum	N	O	Si	Cr	Mn	Al	Mo	Se	S	Ti	Fe	Total
1 [at.-%]	--	53.29	6.57	--	33.19	2.17	2.53	2.24	--	--	--	100
2	--	57.14	6.87	2.35	26.21	--	--	--	--	--	7.42	100
3	--	--	--	17.81	21.42	--	--	--	--	--	60.87	100
4	--	--	--	19.50	20.55	--	--	--	--	--	59.95	100

Figure B. 2.: EDX analysis results of the analyzed particulate of image **??**, HIP specimen

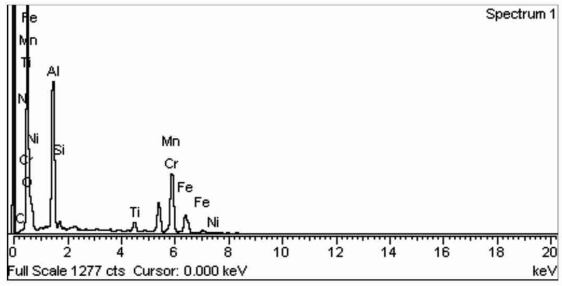

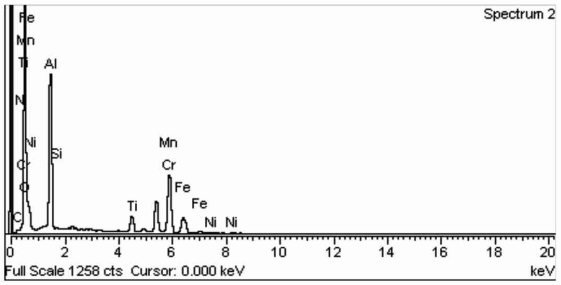

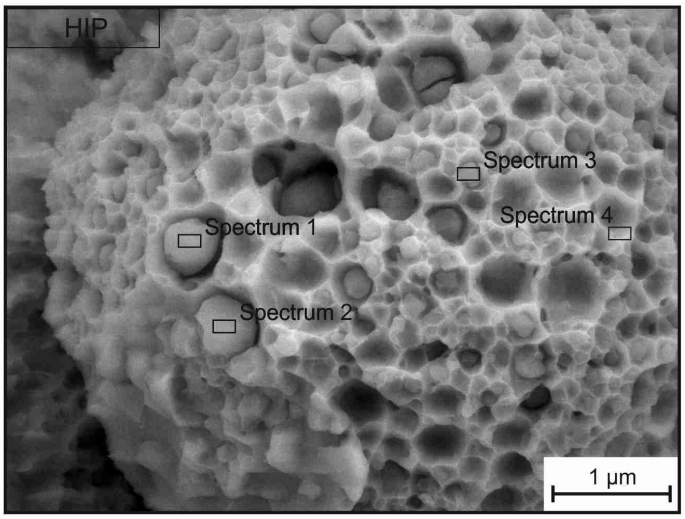

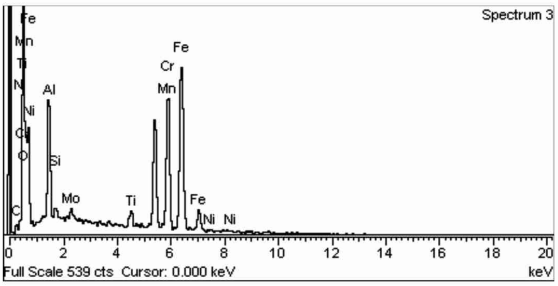

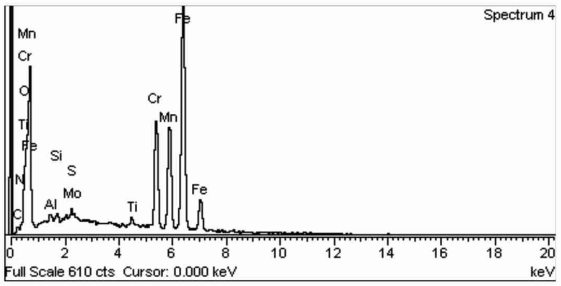

Metallic elements only										
Spectrum	Si	Cr	Mn	Al	Mo	Se	Ti	S	Fe	Total
1 [at.-%]	1.92	14.74	35.72	32.53	--	--	--	--	15.09	100
2	--	17.16	35.41	32.21	--	--	5.64	--	9.58	100
3	1.12	18.03	26.07	9.97	0.08	--	1.75	--	42.26	100
4	--	18.29	19.95	0.87	--	--	0.87	--	60.02	100

All elements												
Spectrum	N	O	Si	Cr	Mn	Al	Mo	Se	S	Ti	Fe	Total
1 [at.-%]	--	60.42	0.73	5.32	12.88	15.06	--	--	--	--	4.29	100
2	--	61.80	--	5.87	12.31	14.25	0.34	--	--	2.05	3.39	100
3	--	35.05	0.84	11.06	15.99	8.67	0.66	--	--	1.18	26.54	100
4	--	5.66	--	17.16	18.71	1.30	--	--	--	0.79	56.38	100

Figure B. 3.: EDX analysis results of the particulates of image 5. 13, HIP specimen

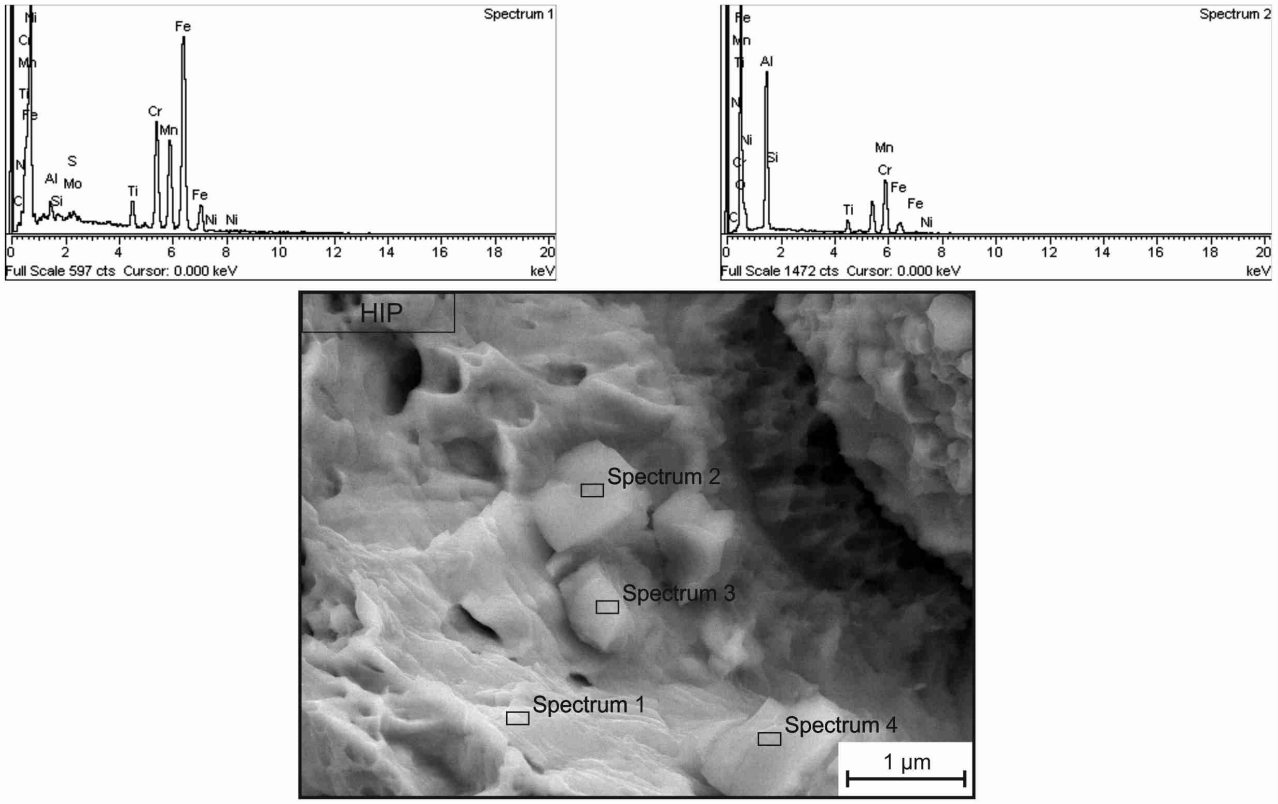

Metallic elements only										
Spectrum	Si	Cr	Mn	Al	Mo	Se	Ti	S	Fe	Total
1 [at.-%]	--	18.76	19.75	1.44	0.70	--	3.24	--	56.11	100
2	--	17.63	35.42	34.94	--	--	5.02	--	6.98	100
3	--	17.48	35.08	33.22	--	--	4.34	--	9.89	100
4	--	14.16	36.92	36.75	--	--	4.93	--	7.23	100

All elements												
Spectrum	N	O	Si	Cr	Mn	Al	Mo	Se	S	Ti	Fe	Total
1 [at.-%]	--	10.91	--	16.58	17.50	1.97	--	--	--	3.01	50.04	100
2	--	63.59	--	5.80	11.77	14.77	--	--	--	--	2.36	100
3	--	62.10	--	5.98	12.18	14.71	--	--	--	1.56	3.46	100
4	--	64.22	--	4.57	11.88	15.22	--	--	--	1.73	2.40	100

Figure B. 4.: EDX analysis results of the bounding surface of image 5. 13, HIP specimen

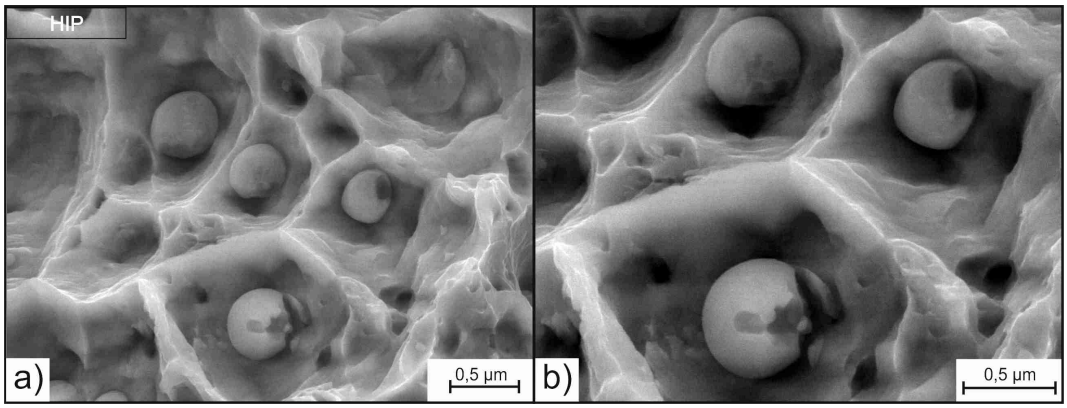

Figure B. 5.: Closeup of the particulates in the densified powder mass of image 5. 12, HIP specimen

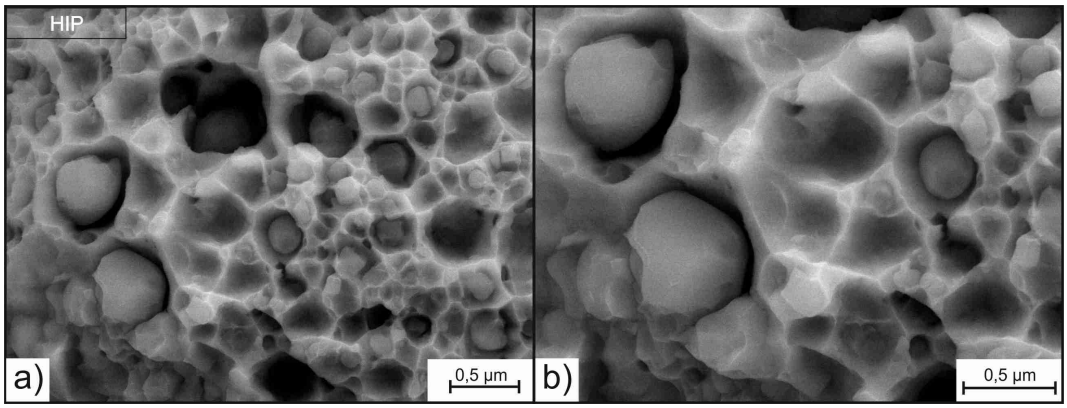

Figure B. 6.: Closeup of the surface of the particle in image 5. 13, HIP specimen

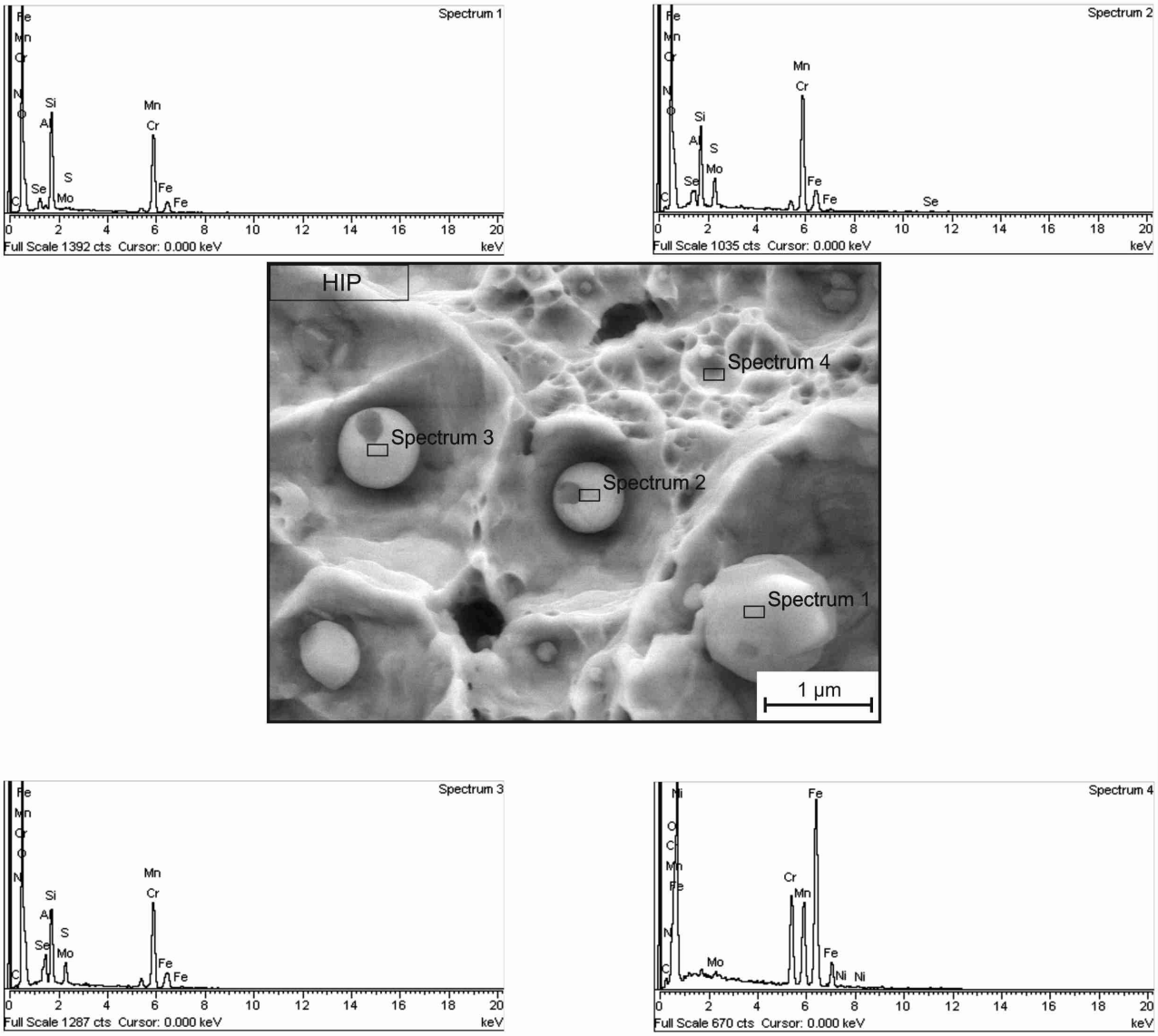

Metallic elements only										
Spectrum	Si	Cr	Mn	Al	Mo	Se	Ti	S	Fe	Total
1 [at.-%]	27.80	2.09	62.93	2.25	--	1.00	--	--	3.94	100
2	14.88	4.42	60.34	3.53	2.26	2.13	--	3.80	8.66	100
3	16.54	4.19	56.56	6.50	2.52	1.91	--	3.44	8.35	100
4	--	19.16	19.67	--	--	--	--	--	61.16	100

All elements												
Spectrum	N	O	Si	Cr	Mn	Al	Mo	Se	S	Ti	Fe	Total
1 [at.-%]	--	64.63	11.10	0.73	21.45	0.75	--	--	--	--	1.34	100
2	--	58.24	7.17	1.78	23.75	1.70	1.40	1.06	1.33	--	3.57	100
3	--	62.03	7.14	1.47	20.06	2.92	1.29	0.94	1.07	--	3.10	100
4	--	--	--	19.16	19.67	--	--	--	--	--	61.16	100

Figure B. 7.: EDX analysis results of the surface particulates second side of interest, HIP specimen

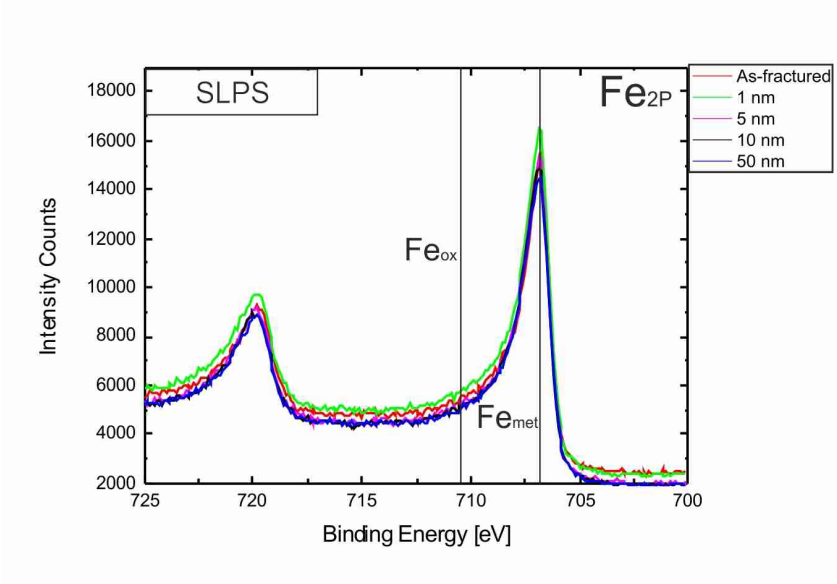

Figure B. 8.: Detailed XPS spectra of Fe 2p peak for SLPS specimen

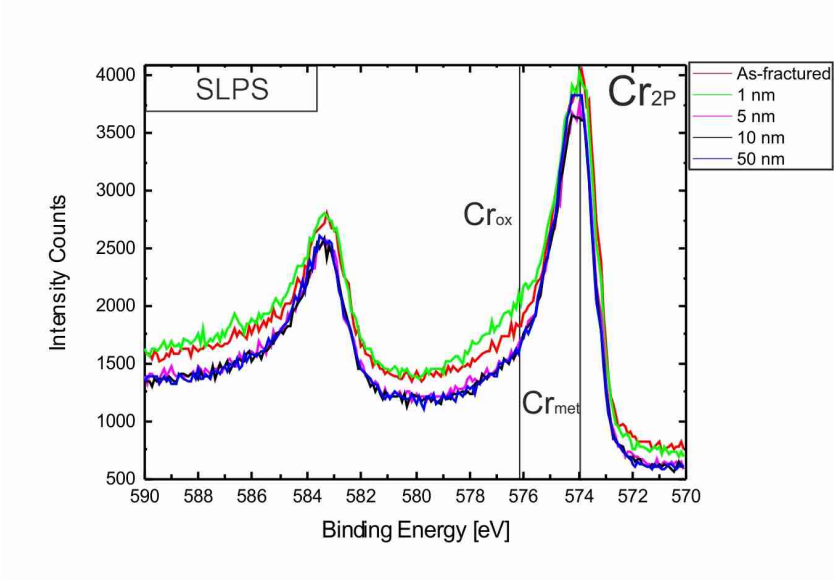

Figure B. 9.: Detailed XPS spectra of Cr 2p peak for SLPS specimen

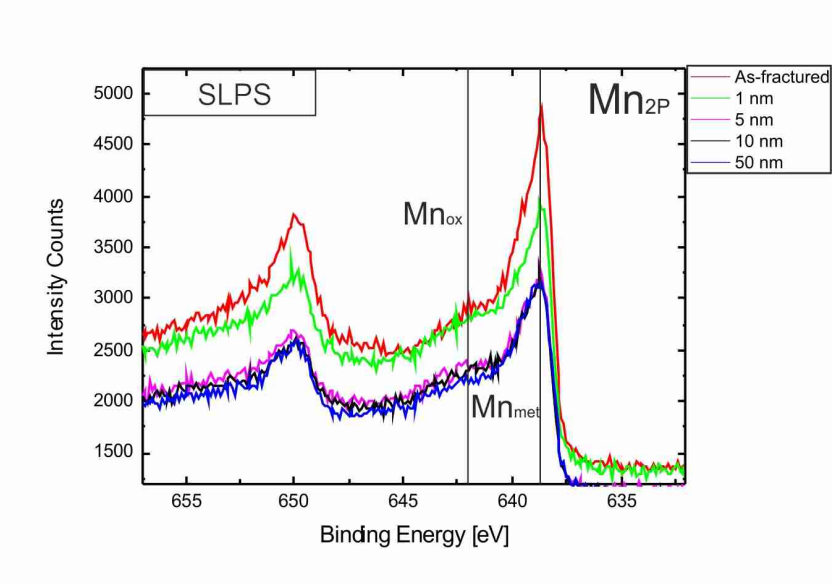

Figure B. 10.: Detailed XPS spectra of Mn 2p peak for SLPS specimen

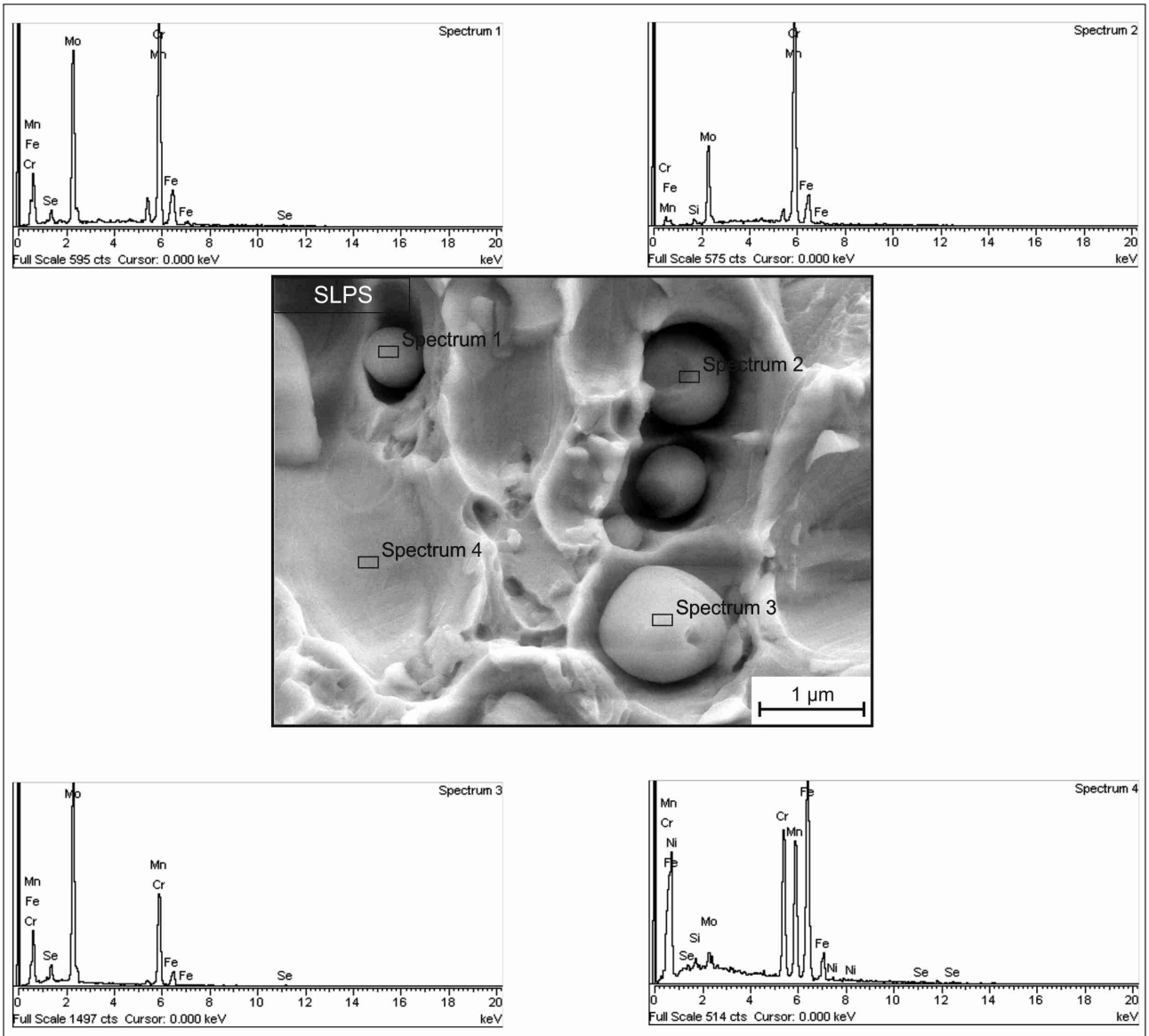

Metallic elements only										
Spectrum	Si	Cr	Mn	Al	Mo	Se	Ti	S	Fe	Total
1 [at.-%]	--	6.13	63.56	--	6.58	1.09	--	14.43	8.21	100
2	0.68	3.70	68.27	--	4.11	--	--	17.67	5.57	100
3	--	1.73	51.40	--	13.00	2.36	--	24.47	3.05	100
4	0.77	23.98	24.56	--	0.71	--	--	--	49.98	100

All elements												
Spectrum	N	O	Si	Cr	Mn	Al	Mo	Se	S	Ti	Fe	Total
1 [at.-%]	--	6.63	--	5.55	56.95	--	8.75	1.30	13.11	--	7.72	100
2	--	4.23	0.10	2.85	58.06	--	5.71	--	24.33	--	4.76	100
3	--	6.86	--	1.47	44.60	--	16.78	2.74	24.90	--	2.65	100
4	4.02	--	1.01	22.41	23.26	--	1.45	--	--	--	47.84	100

Figure B. 11.: EDX analysis results of the spherical particulates of image 5. 21, SLPS specimen

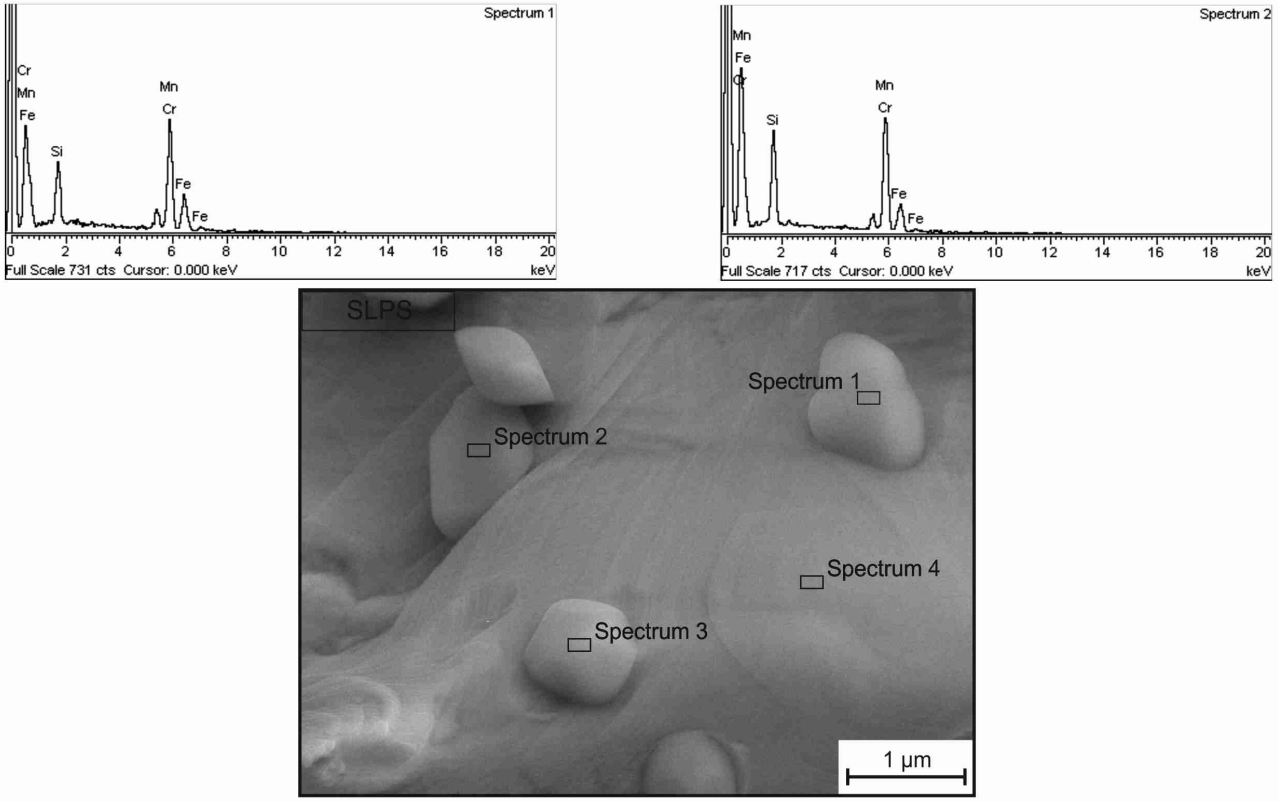

Metallic elements only										
Spectrum	Si	Cr	Mn	Al	Mo	Se	Ti	S	Fe	Total
1 [at.-%]	19.73	8.65	56.05	1.49	--	--	--	--	15.58	100
2	27.04	5.51	57.84	--	--	--	--	--	9.61	100
3	30.20	4.11	58.37	--	--	--	--	0.86	6.46	100
4	1.29	22.90	20.14	2.56	--	--	--	1.19	54.49	100

All elements												
Spectrum	N	O	Si	Cr	Mn	Al	Mo	Se	S	Ti	Fe	Total
1 [at.-%]	--	47.50	10.54	4.50	29.54	--	--	--	--	--	8.02	100
2	--	60.50	10.67	2.15	23.00	--	--	--	--	--	3.68	100
3	--	67.32	10.01	1.30	19.13	--	--	--	0.26	--	1.98	100
4	--	--	1.29	22.90	20.14	2.56	--	--	1.19	--	54.49	100

Figure B. 12.: EDX analysis results of the large, spherical particulates of image 5. 23, SLPS specimen

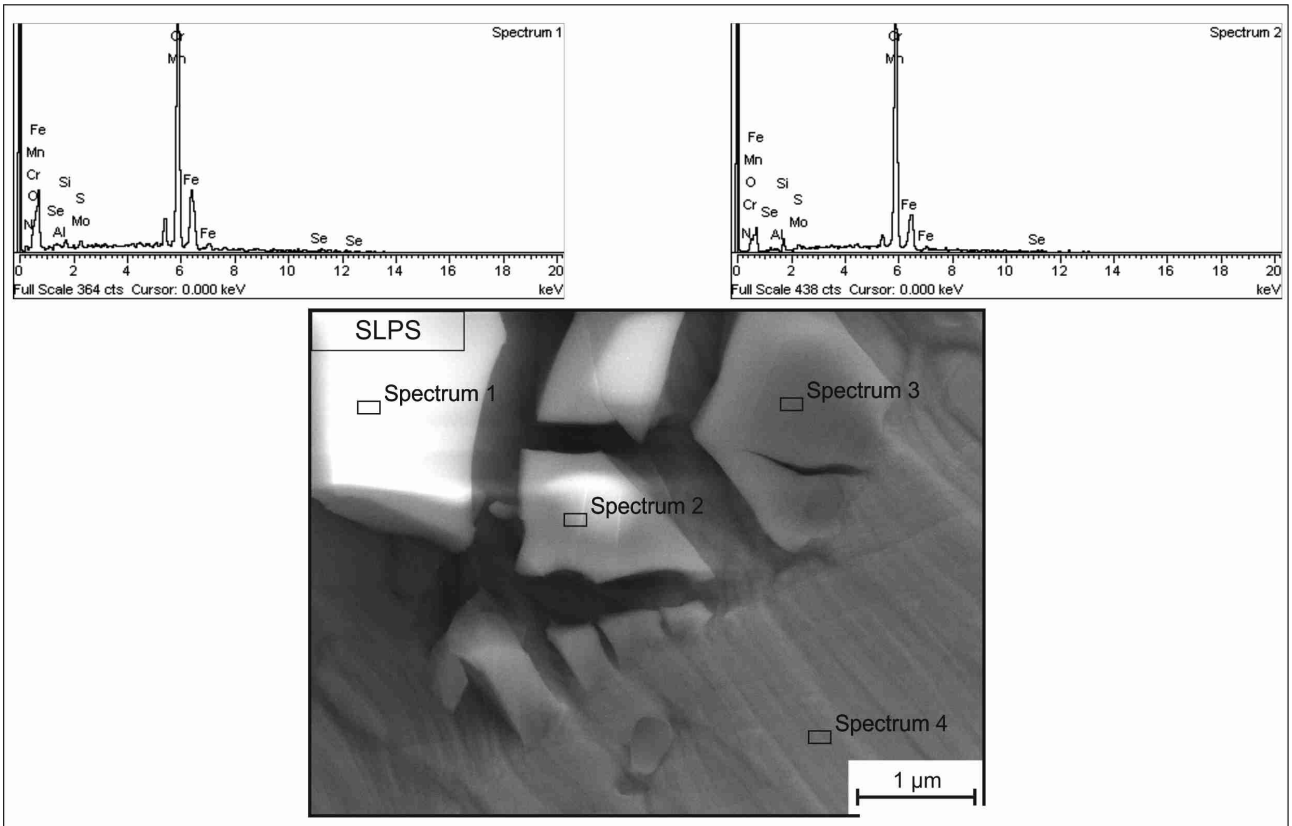

Metallic elements only										
Spectrum	Si	Cr	Mn	Al	Mo	Se	Ti	S	Fe	Total
1 [at.-%]	1.31	7.90	71.28	--	--	--	--	--	19.51	100
2	1.66	4.63	87.04	--	--	--	--	--	6.66	100
3	12.45	3.31	69.83	2.46	2.59	1.86	--	--	7.51	100
4	--	19.30	21.32	--	--	--	--	--	59.39	100

All elements												
Spectrum	N	O	Si	Cr	Mn	Al	Mo	Se	S	Ti	Fe	Total
1 [at.-%]	--	3.96	1.25	7.59	68.46	--	--	--	--	--	18.74	100
2	--	3.85	1.59	4.46	83.69	--	--	--	--	--	6.41	100
3	--	30.97	8.35	2.30	48.53	1.64	1.75	1.24	--	--	5.22	100
4	5.02	--	--	18.33	20.25	--	--	--	--	--	56.40	100

Figure B. 13.: EDX analysis results of the agglomerated, angular particulates of image 5.25, SLPS specimen

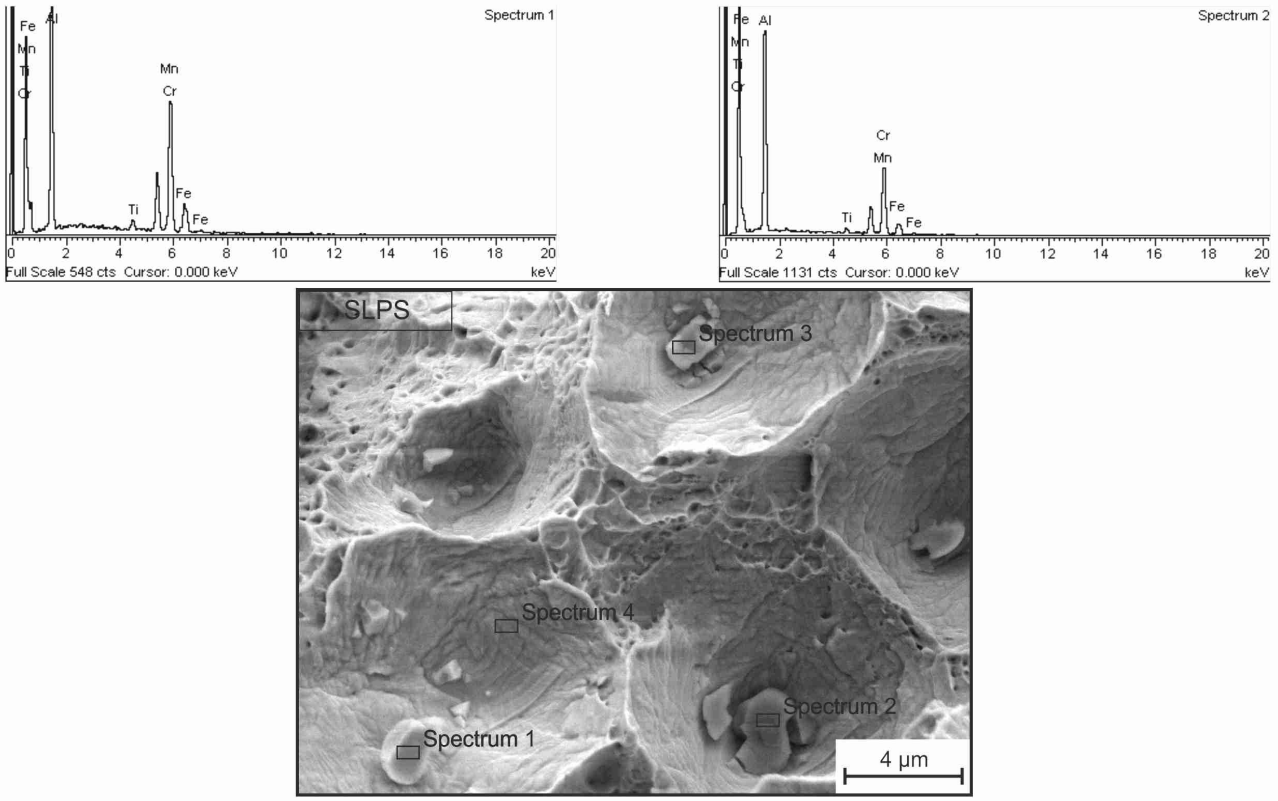

Metallic elements only										
Spectrum	Si	Cr	Mn	Al	Mo	Se	Ti	S	Fe	Total
1 [at.-%]	--	16.85	47.22	26.92	--	--	1.66	--	7.35	100
2	--	13.80	39.58	39.90	--	--	1.73	--	4.98	100
3	3.84	10.84	44.52	33.94	1.38	--	1.51	1.53	2.43	100
4	1.09	18.26	19.22	2.56	1.07	--	--	--	60.36	100

All elements												
Spectrum	N	O	Si	Cr	Mn	Al	Mo	Se	S	Ti	Fe	Total
1 [at.-%]	--	44.09	--	8.52	24.24	18.40	--	--	--	0.88	3.87	100
2	--	59.36	--	5.00	14.49	18.64	--	--	--	0.65	1.86	100
3	--	60.49	1.52	3.90	15.86	15.62	0.70	--	0.45	0.58	0.88	100
4	--	--	1.09	18.26	19.22	--	1.07	--	--	--	60.36	100

Figure B. 14.: EDX analysis results of the angular particulates of image 5. 24, SLPS specimen

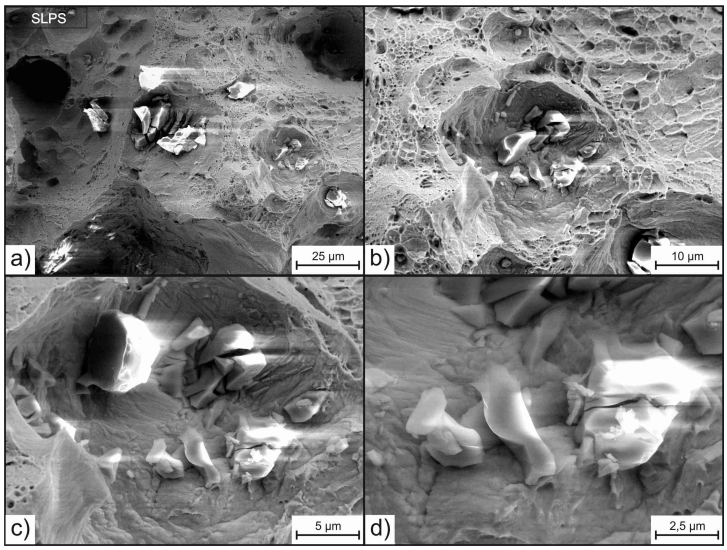

Figure B. 15.: Agglomerated, angular particulates distributing in pores second side of interest, SLPS specimen

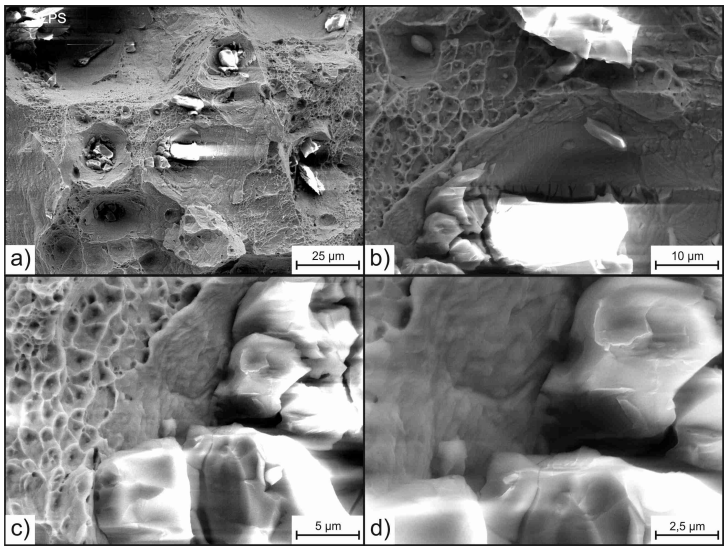

Figure B. 16.: Agglomerated, angular particulates distributing in pores third side of interest, SLPS specimen

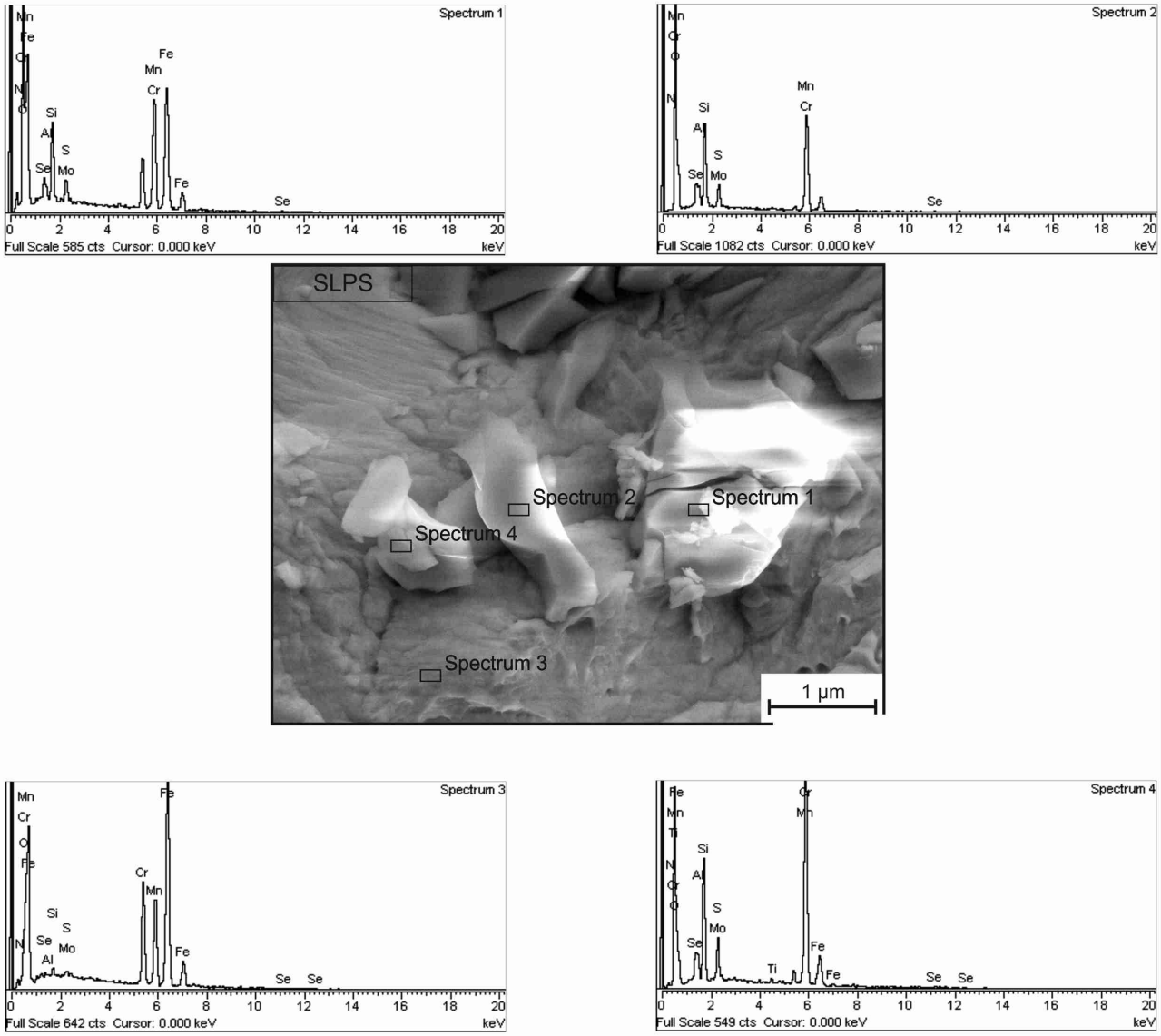

Metallic elements only										
Spectrum	Si	Cr	Mn	Al	Mo	Se	Ti	S	Fe	Total
1 [at.-%]	10.34	11.67	29.26	3.17	1.34	2.39	--	1.33	40.50	100
2	23.04	1.48	57.01	7.06	3.62	4.82	--	2.97	--	100
3	--	18.46	19.75	--	--	--	--	--	61.79	100
4	--	16.59	62.61	4.72	3.38	3.07	0.93	2.18	3.34	100

All elements												
Spectrum	N	O	Si	Cr	Mn	Al	Mo	Se	S	Ti	Fe	Total
1 [at.-%]	3.29	39.57	5.62	6.76	16.90	1.71	0.74	1.29	0.74	--	23.38	100
2	--	62.92	8.06	0.57	21.93	2.46	1.28	1.72	1.05	--	--	100
3	--	--	--	18.46	19.75	--	--	--	--	--	61.79	100
4	--	48.61	8.14	1.67	32.77	2.30	1.68	1.51	1.09	0.48	1.75	100

Figure B. 17.: EDX analysis results of the agglomerated, angular particulates of image B. 15, SLPS specimen

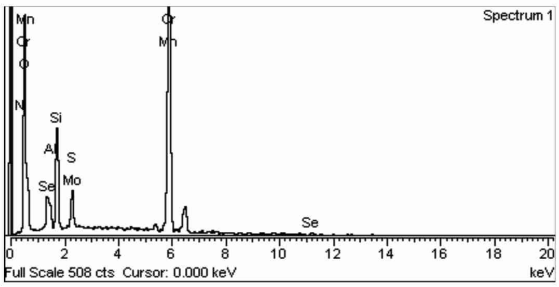

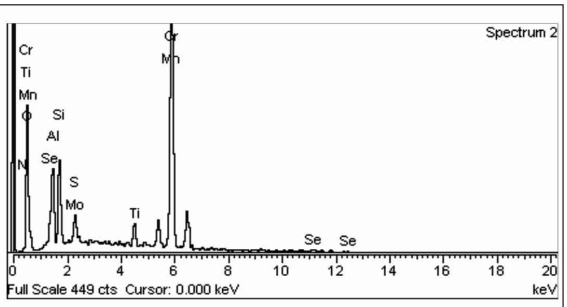

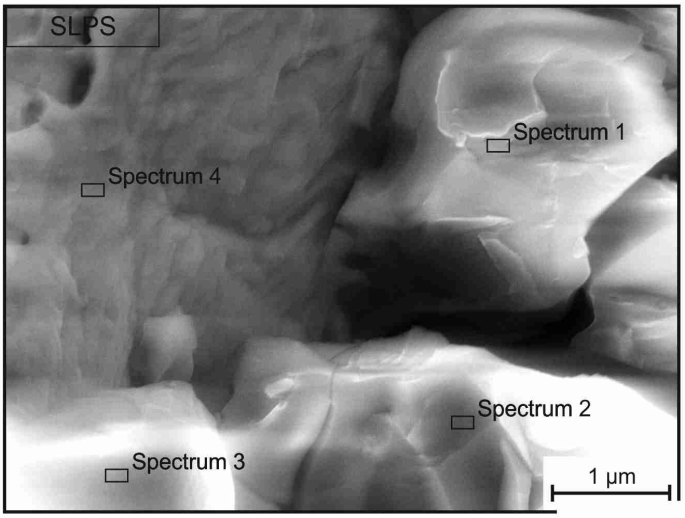

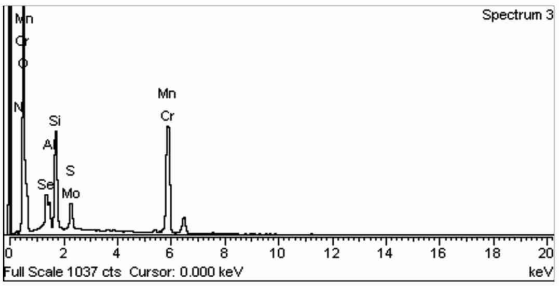

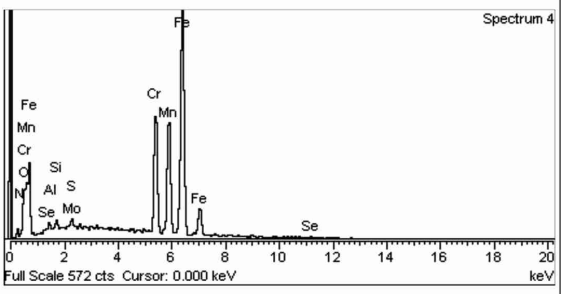

Metallic elements only										
Spectrum	Si	Cr	Mn	Al	Mo	Se	Ti	S	Fe	Total
1 [at.-%]	17.04	1.31	66.98	4.36	3.69	3.56	--	--	3.05	100
2	10.82	5.57	64.27	10.99	11.71	1.70	3.23	1.64	--	100
3	22.78	1.02	57.43	6.54	3.29	5.94	--	3.01	--	100
4	0.89	19.52	22.06	--	--	--	--	--	57.52	100

All elements												
Spectrum	N	O	Si	Cr	Mn	Al	Mo	Se	S	Ti	Fe	Total
1 [at.-%]	--	48.92	8.12	0.70	34.72	2.06	1.79	1.25	--	--	2.35	100
2	--	38.83	6.38	3.44	39.82	6.47	1.07	1.00	0.98	--	--	100
3	--	61.80	8.20	0.40	22.76	2.34	1.20	2.20	1.10	--	--	100
4	--	4.69	0.85	18.61	21.03	--	--	--	--	--	54.82	100

Figure B. 18.: EDX analysis results of the agglomerated, angular particulates of image B. 16, SLPS specimen

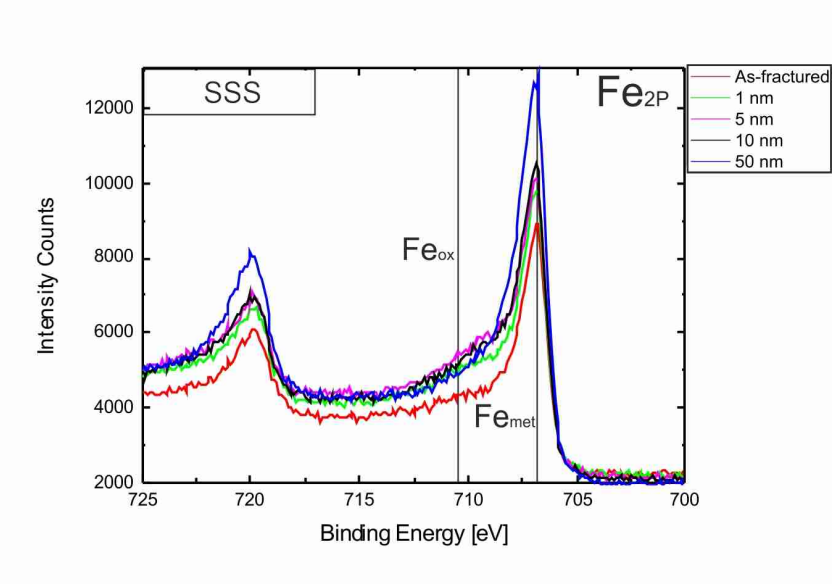

Figure B. 19.: Detailed XPS spectra of Fe 2p peak for SSS specimen

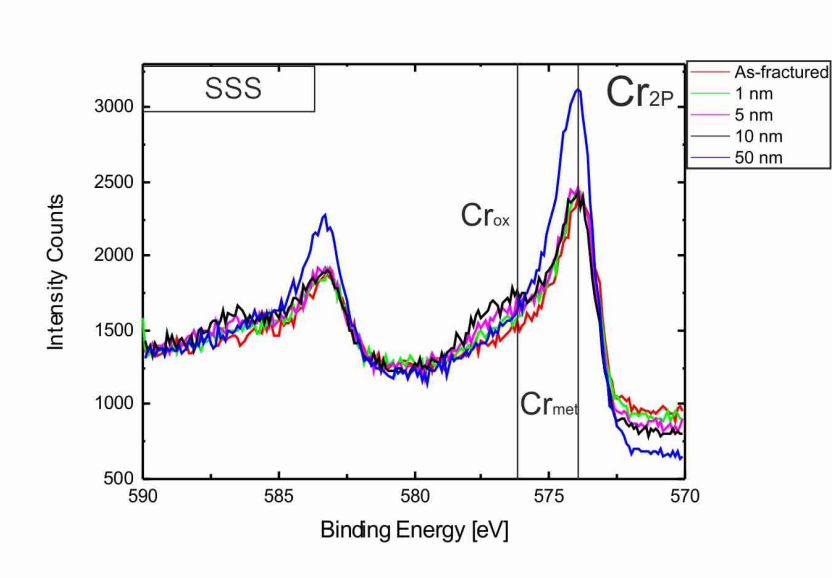

Figure B. 20.: Detailed XPS spectra of Cr 2p peak for SSS specimen

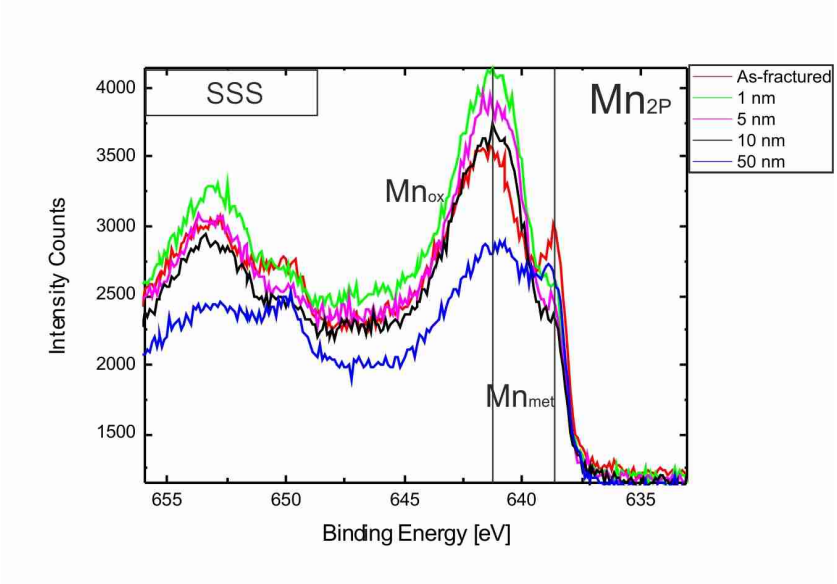

Figure B. 21.: Detailed XPS spectra of Mn 2p peak for SSS specimen

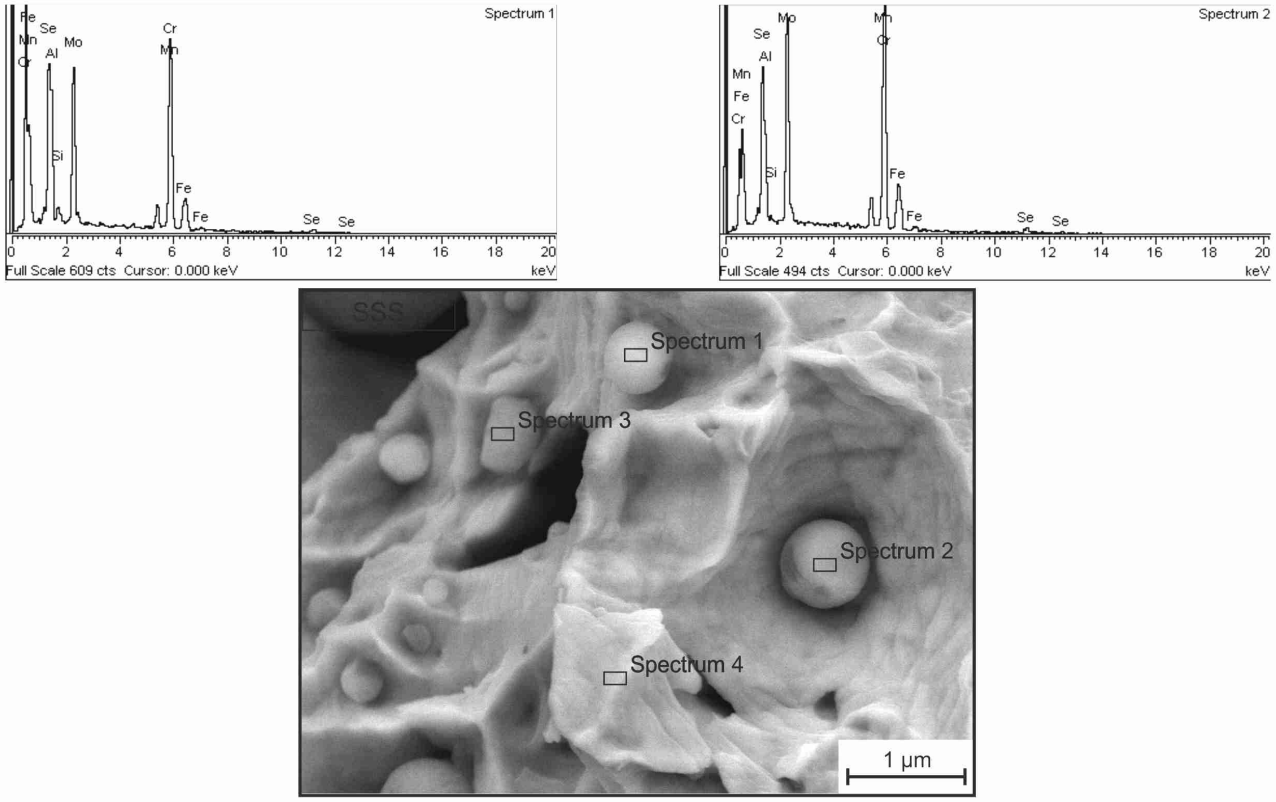

Metallic elements only										
Spectrum	Si	Cr	Mn	Al	Mo	Se	Ti	S	Fe	Total
1 [at.-%]	0.91	4.90	47.87	13.35	5.39	9.21	--	10.91	7.47	100
2	--	7.47	50.40	7.47	6.72	8.67	--	11.98	8.45	100
3	0.93	9.61	42.59	28.86	2.57	--	--	4.68	10.77	100
4	0.68	18.79	19.07	--	--	--	--	0.99	60.47	100

All elements												
Spectrum	N	O	Si	Cr	Mn	Al	Mo	Se	S	Ti	Fe	Total
1 [at.-%]	--	46.97	0.60	2.33	22.75	8.52	3.79	6.18	5.11	--	3.75	100
2	--	21.93	--	4.51	35.74	7.52	7.01	8.61	8.43	--	6.25	100
3	--	56.13	0.36	3.78	16.62	14.85	1.49	0.69	1.72	--	4.37	100
4	4.01	--	0.88	17.70	18.47	--	0.89	--	--	--	58.05	100

Figure B. 22.: EDX analysis results of the spherical particulates of image 5. 33, SSS specimen

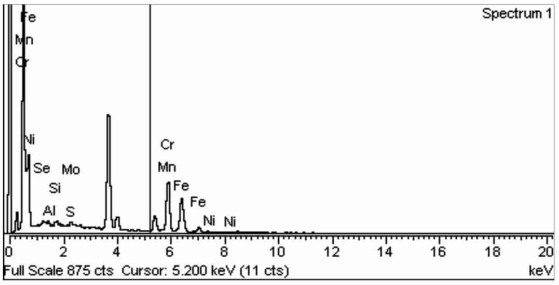

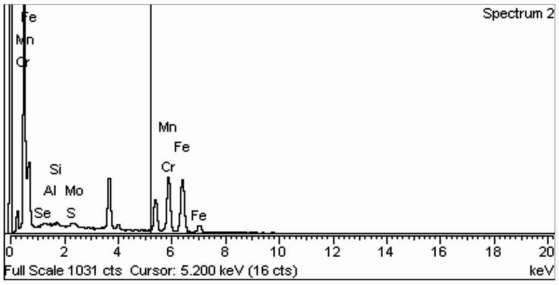

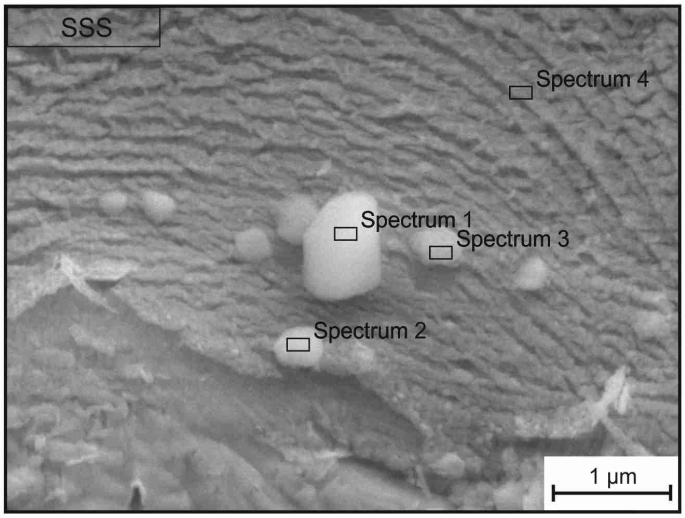

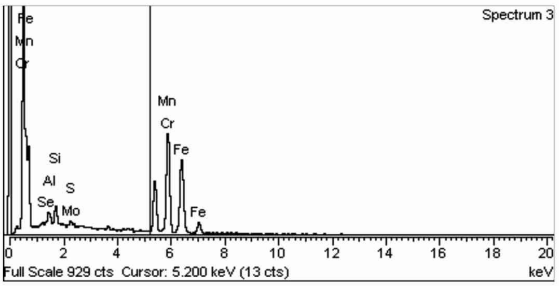

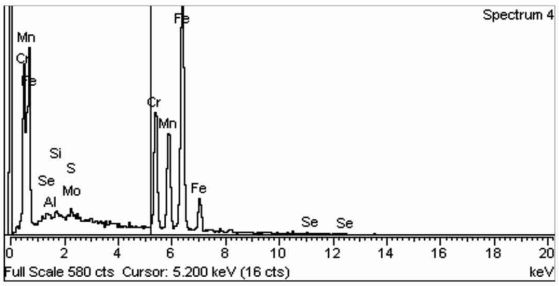

Metallic elements only										
Spectrum	Si	Cr	Mn	Al	Mo	Se	Ti	S	Fe	Total
1 [at.-%]	--	12.53	48.71	--	--	--	--	--	38.77	100
2	--	17.81	35.33	--	--	--	--	--	46.87	100
3	3.84	16.59	39.35	2.88	--	--	--	--	37.33	100
4	--	20.16	19.78	--	--	--	--	--	60.06	100

All elements											
Spectrum	N	O	Si	Cr	Mn	Al	Mo	Se	S	Ti	Fe	Total
1 [at.-%]	2.16	67.85	--	3.79	14.60	--	--	--	--	--	11.59	100
2	2.07	61.11	--	6.61	13.02	--	--	--	--	--	17.19	100
3	--	50.08	1.79	8.36	19.75	1.32	--	--	--	--	18.69	100
4	--	25.92	--	14.97	14.66	--	--	--	--	--	44.45	100

Figure B. 23.: EDX analysis results of the particulates of image 5. 34, SSS specimen

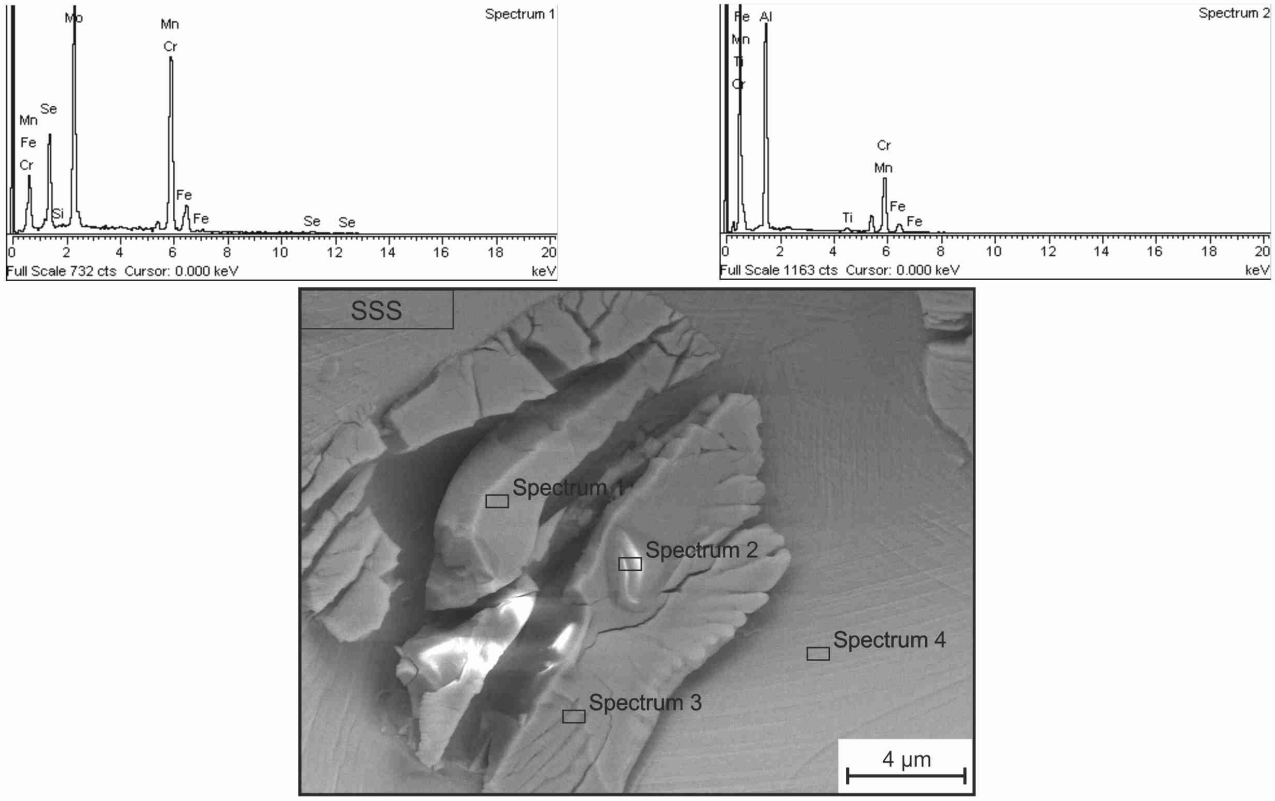

Metallic elements only										
Spectrum	Si	Cr	Mn	Al	Mo	Se	Ti	S	Fe	Total
1 [at.-%]	--	1.93	53.59	1.30	11.57	10.16	0.49	17.58	3.39	100
2	--	9.80	37.44	47.13	--	--	1.38	--	4.25	100
3	6.56	2.29	62.91	--	5.43	6.47	--	12.14	4.20	100
4	--	17.98	21.24	--	1.20	--	--	--	59.58	100

All elements												
Spectrum	N	O	Si	Cr	Mn	Al	Mo	Se	S	Ti	Fe	Total
1 [at.-%]	--	--	--	1.93	53.59	1.30	11.57	10.16	17.58	0.49	3.39	100
2	--	63.55	--	3.23	12.37	18.88	--	--	--	--	1.45	100
3	--	40.51	4.52	1.22	33.47	1.68	4.56	5.56	6.26	--	2.23	100
4	--	--	--	17.98	21.24	--	1.20	--	--	--	59.58	100

Figure B. 24.: EDX analysis results of the particulates of image 5. 35, SSS specimen

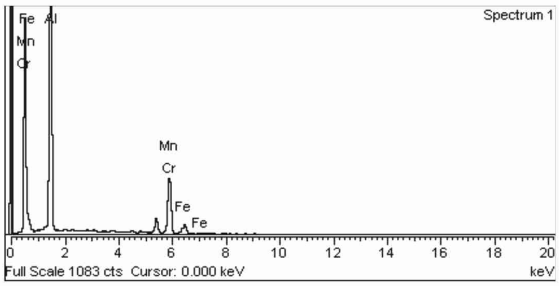

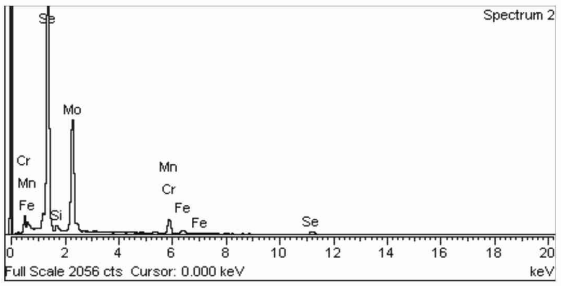

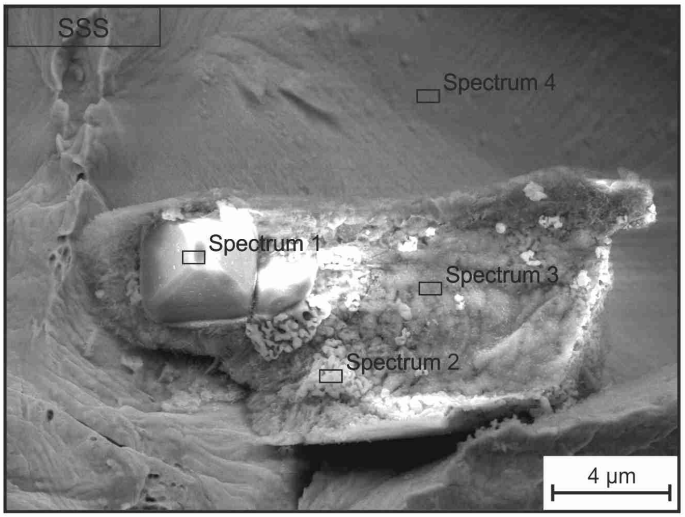

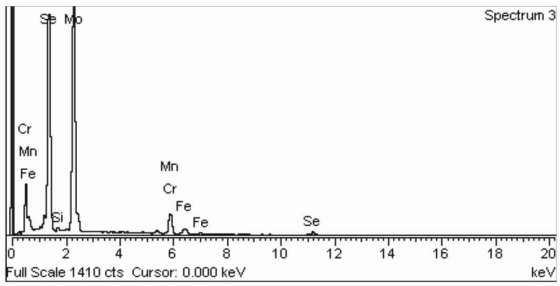

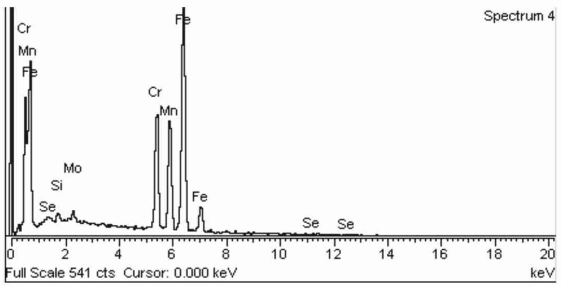

Metallic elements only										
Spectrum	Si	Cr	Mn	Al	Mo	Se	Ti	S	Fe	Total
1 [at.-%]	--	8.05	38.73	49.52	--	--	--	--	3.70	100
2	1.62	1.23	11.59	6.38	12.84	38.02	--	31.28	3.41	100
3	--	1.11	12.55	--	18.39	25.29	--	39.61	3.04	100
4	--	19.90	21.00	--	0.52	--	--	--	58.59	100

All elements												
Spectrum	N	O	Si	Cr	Mn	Al	Mo	Se	S	Ti	Fe	Total
1 [at.-%]	--	61.41	--	2.83	13.60	20.83	--	--	--	--	1.32	100
2	--	25.15	1.10	0.67	6.68	5.22	11.00	30.52	17.65	--	2.01	100
3	4.67	41.44	--	0.51	5.65	1.77	11.66	15.78	17.07	--	1.45	100
4	2.37	20.71	0.65	15.05	16.18	--	--	--	--	--	45.03	100

Figure B. 25.: EDX analysis results of the particulate of image 5. 36, SSS specimen

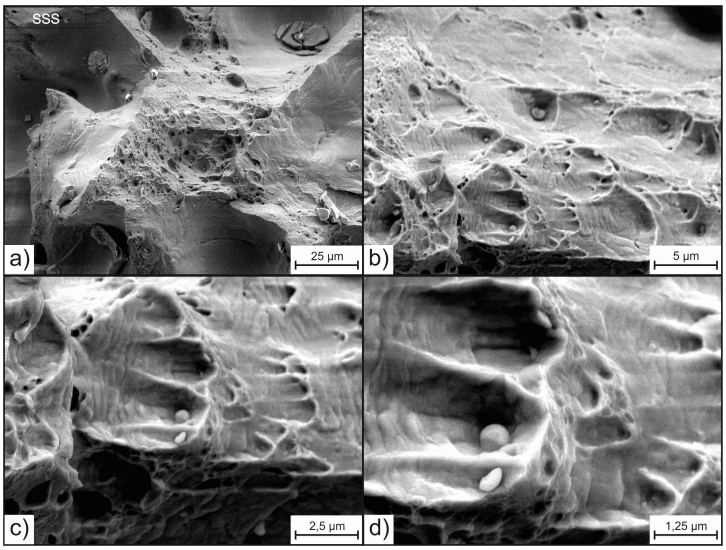

Figure B. 26.: Closeup of the spherical particulates distributing in the densified powder mass second site of interest, SSS specimen

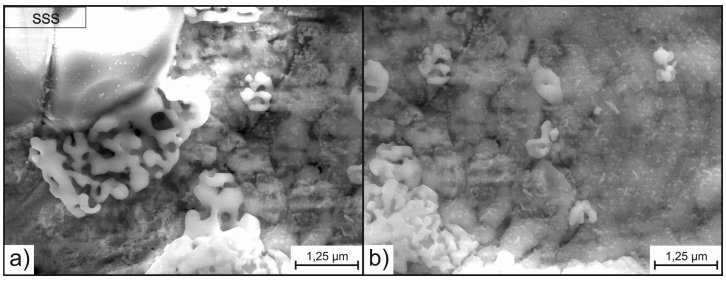

Figure B. 27.: Closeup of the loose, irregular shaped particulate of image 5. 36, SSS specimen

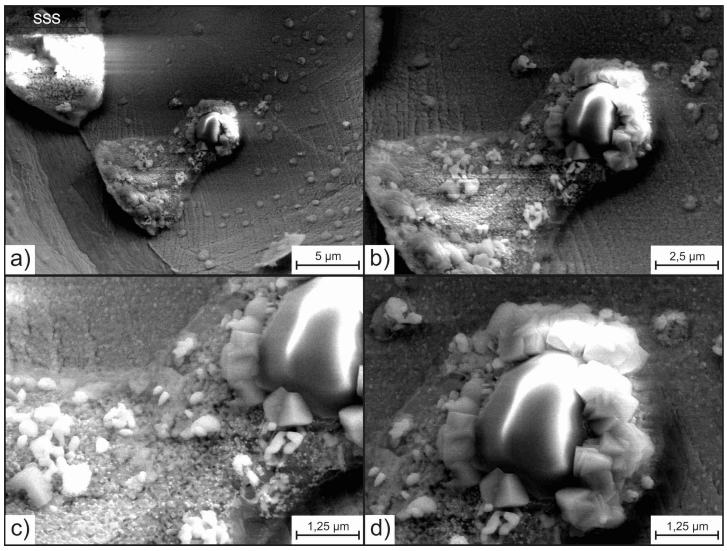

Figure B. 28.: Loose, irregular shaped particulate in former sintering pore second site of interest, SSS specimen

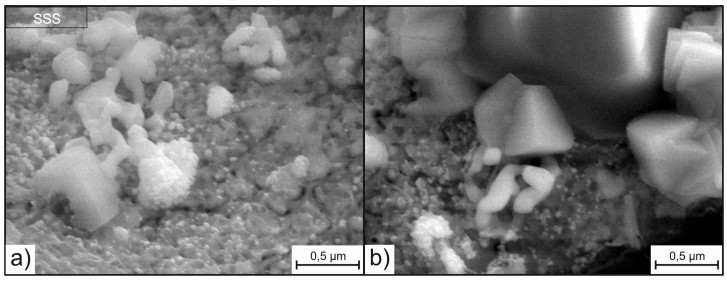

Figure B. 29.: Closeup of the loose, irregular shaped particulate of image B. 28, SSS specimen

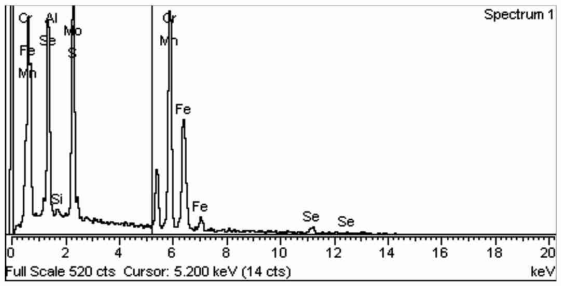

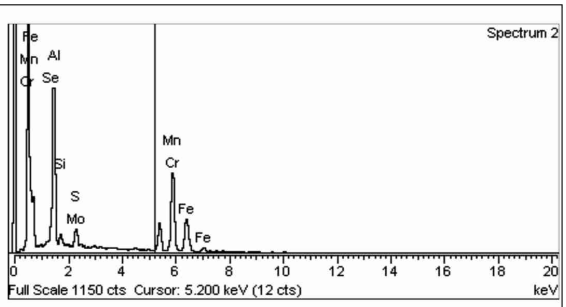

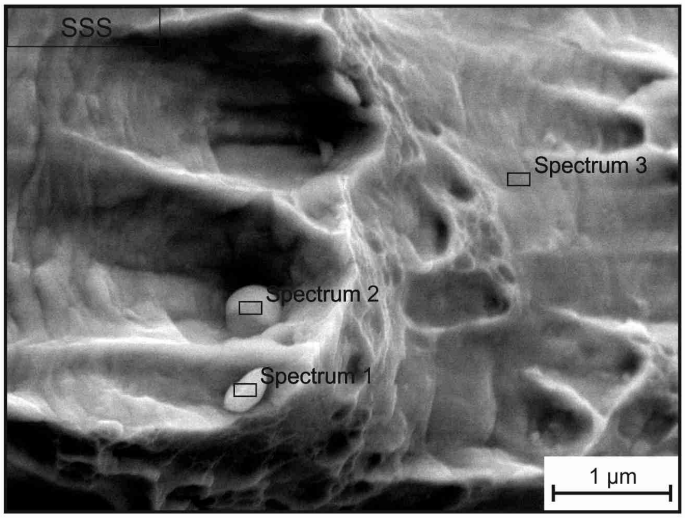

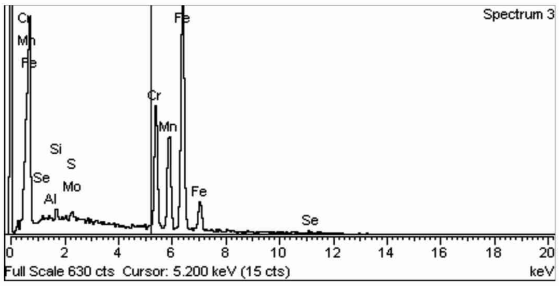

Metallic elements only										
Spectrum	Si	Cr	Mn	Al	Mo	Se	Ti	S	Fe	Total
1 [at.-%]	--	8.07	36.83	2.63	8.85	12.75	--	9.17	21.70	100
2	2.19	9.51	34.07	33.90	--	--	--	3.04	17.30	100
3	1.06	18.98	18.95	--	1.00	--	--	--	60.00	100

All elements												
Spectrum	N	O	Si	Cr	Mn	Al	Mo	Se	S	Ti	Fe	Total
1 [at.-%]	--	8.20	--	7.42	33.88	2.39	8.10	11.66	8.39	--	19.96	100
2	--	54.42	0.92	4.46	15.96	14.81	--	--	1.34	--	8.09	100
3	3.45	--	1.02	18.33	18.30	--	0.96	--	--	--	57.94	100

Figure B. 30.: EDX analysis results of the spherical particulates of image B. 26, SSS specimen

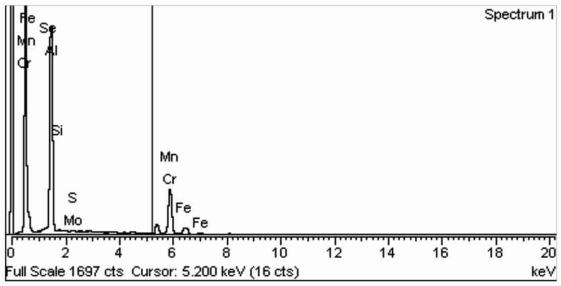

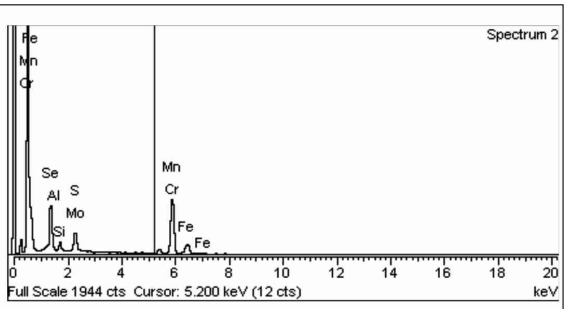

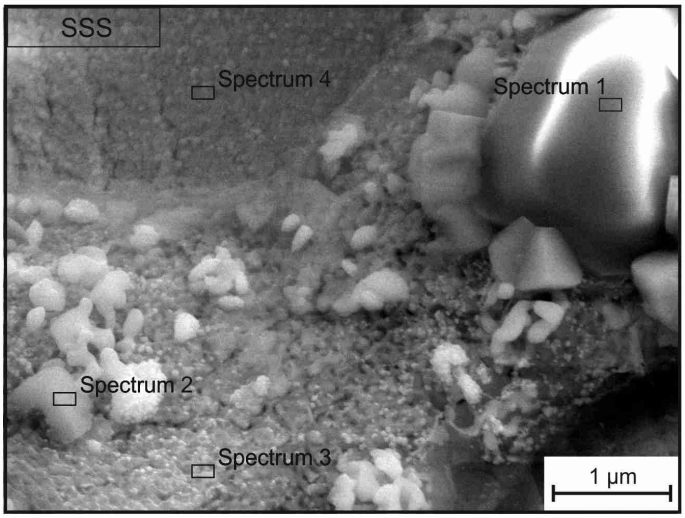

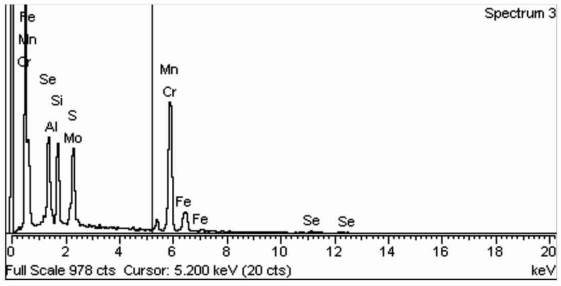

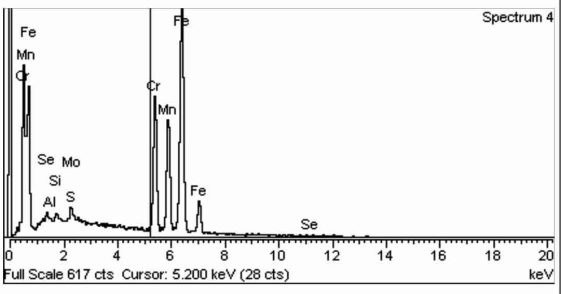

Metallic elements only										
Spectrum	Si	Cr	Mn	Al	Mo	Se	Ti	S	Fe	Total
1 [at.-%]	--	6.17	32.37	58.59	--	--	--	--	2.87	100
2	3.59	3.85	55.36	3.66	5.82	16.66	--	3.10	7.96	100
3	15.81	2.91	47.71	4.74	4.66	11.34	--	8.01	4.82	100
4	0.83	20.02	21.56	--	--	1.00	--	--	56.59	100

All elements												
Spectrum	N	O	Si	Cr	Mn	Al	Mo	Se	S	Ti	Fe	Total
1 [at.-%]	--	65.41	--	2.19	11.52	19.87	--	--	--	--	1.02	100
2	1.38	74.87	0.73	0.95	13.69	0.73	1.28	3.70	0.68	--	1.98	100
3	--	57.88	6.26	1.26	20.80	1.86	1.89	4.69	3.25	--	2.11	100
4	2.43	25.62	0.58	14.45	15.53	--	--	0.69	--	--	40.70	100

Figure B. 31.: Additionally EDX analysis results of the particulates of image B. 28, SSS specimen

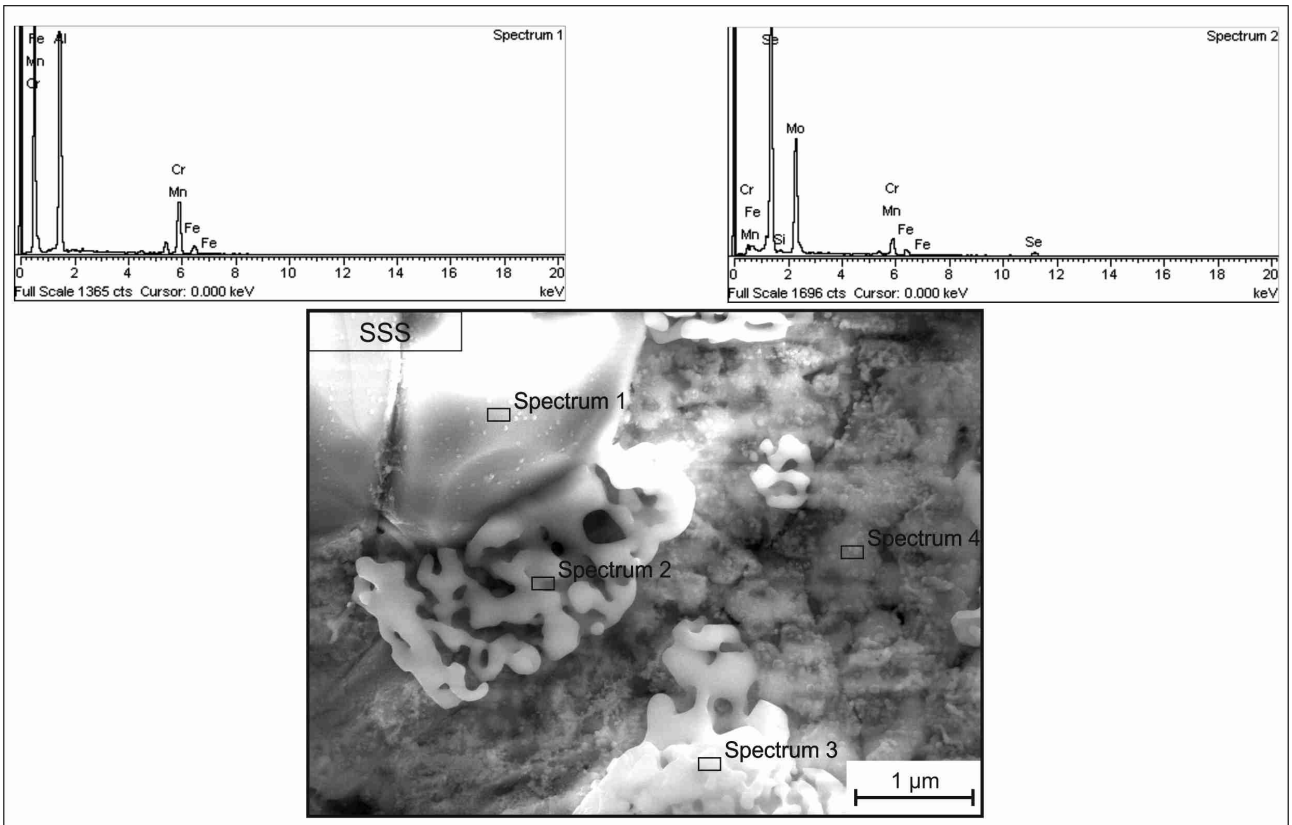

Metallic elements only										
Spectrum	Si	Cr	Mn	Al	Mo	Se	Ti	S	Fe	Total
1 [at.-%]	--	7.41	39.13	51.22	--	--	--	--	2.24	100
2	1.70	2.23	14.38	--	11.71	35.95	--	29.17	4.86	100
3	0.95	1.20	5.91	5.23	15.28	36.05	--	32.12	3.26	100
4	--	0.83	5.30	--	19.71	30.29	--	41.33	2.54	100

All elements												
Spectrum	N	O	Si	Cr	Mn	Al	Mo	Se	S	Ti	Fe	Total
1 [at.-%]	--	63.55	--	2.43	12.86	20.42	--	--	--	--	0.73	100
2	--	14.85	1.31	1.45	9.80	--	11.92	33.31	19.67	--	3.28	100
3	--	21.58	--	0.76	3.71	4.76	13.48	33.88	19.81	--	2.02	100
4	--	31.29	--	0.47	3.00	2.36	15.52	23.39	22.49	--	1.48	100

Figure B. 32.: Additionally EDX analysis results of the particulate of image 5. 36, SSS specimen

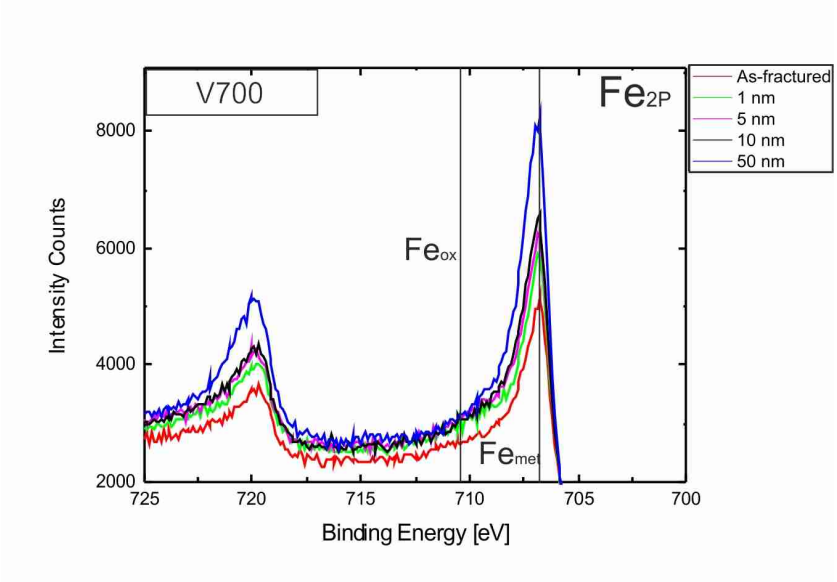

Figure B. 33.: Detailed XPS spectra of Fe 2p peak for V700 specimen

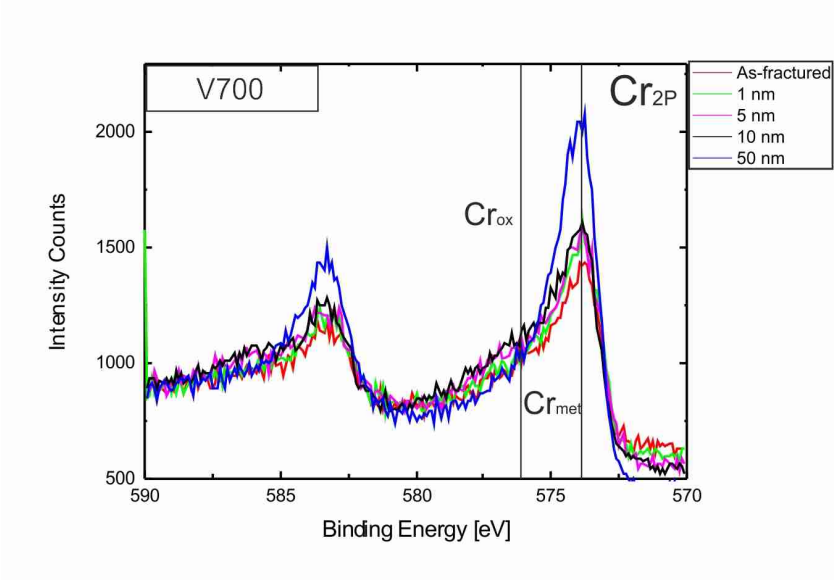

Figure B. 34.: Detailed XPS spectra of Cr 2p peak for V700 specimen

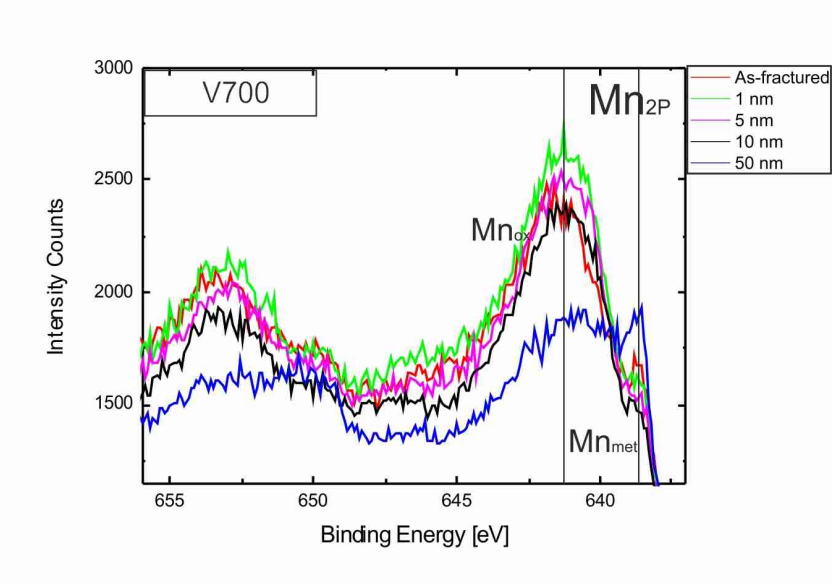

Figure B. 35.: Detailed XPS spectra of Mn 2p peak for V700 specimen

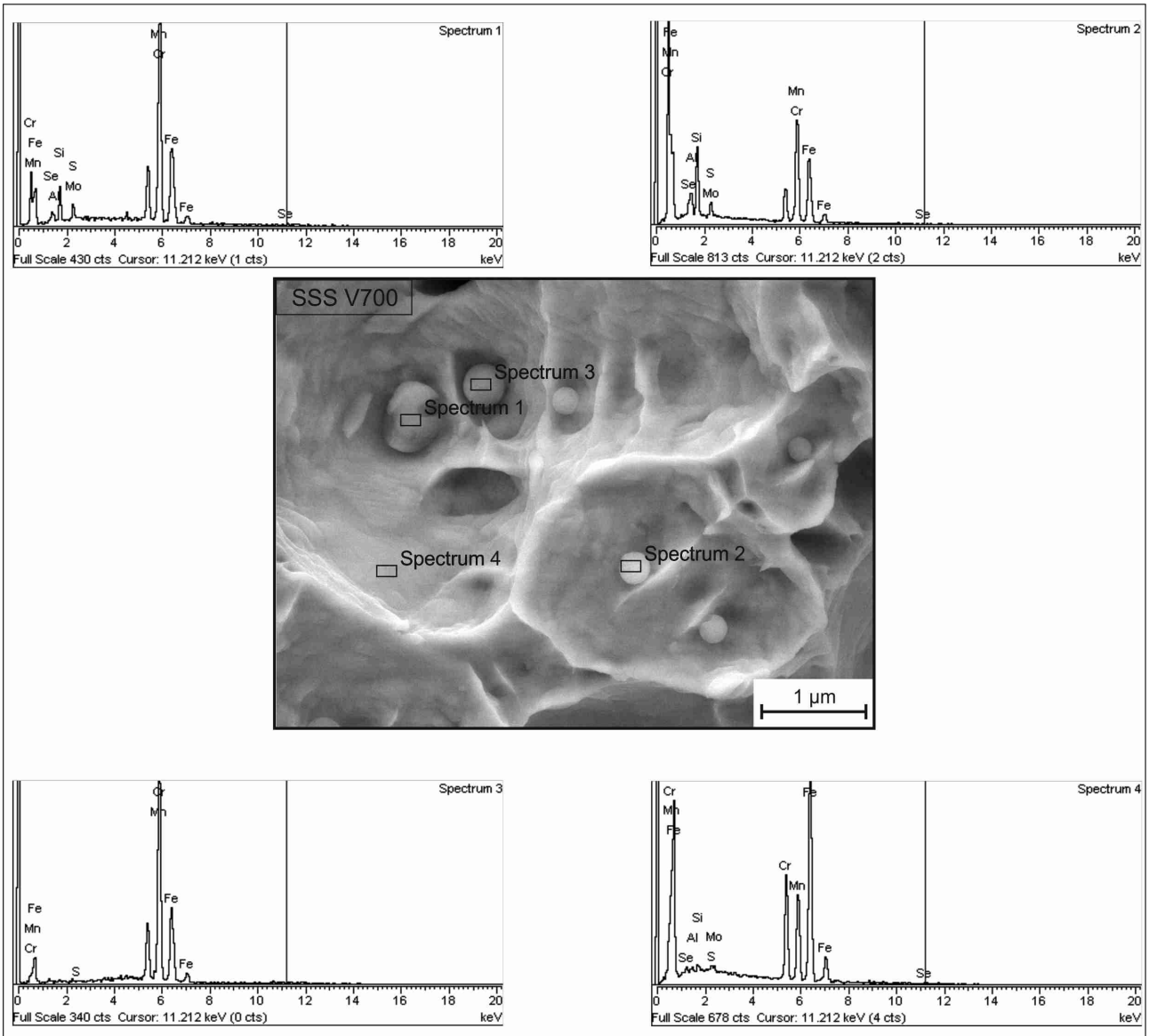

Metallic elements only										
Spectrum	Si	Cr	Mn	Al	Mo	Se	Ti	S	Fe	Total
1 [at.-%]	4.56	12.42	55.48	1.27	1.50	--	--	--	24.77	100
2	12.29	10.47	38.77	6.03	1.75	2.03	--	--	28.66	100
3	--	13.19	60.42	--	--	--	--	--	26.38	100
4	0.80	19.28	19.41	--	--	--	--	--	60.51	100

All elements												
Spectrum	N	O	Si	Cr	Mn	Al	Mo	Se	S	Ti	Fe	Total
1 [at.-%]	--	13.52	3.90	10.75	48.03	1.08	1.29	--	--	--	21.44	100
2	--	48.92	5.94	5.44	20.11	2.89	0.86	0.98	--	--	14.86	100
3	--	--	--	13.19	60.42	--	--	--	--	--	26.38	100
4	4.15	--	0.76	18.48	18.61	--	--	--	--	--	57.99	100

Figure B. 36.: EDX analysis results of the spherical particulates of image 5. 44, V700 specimen

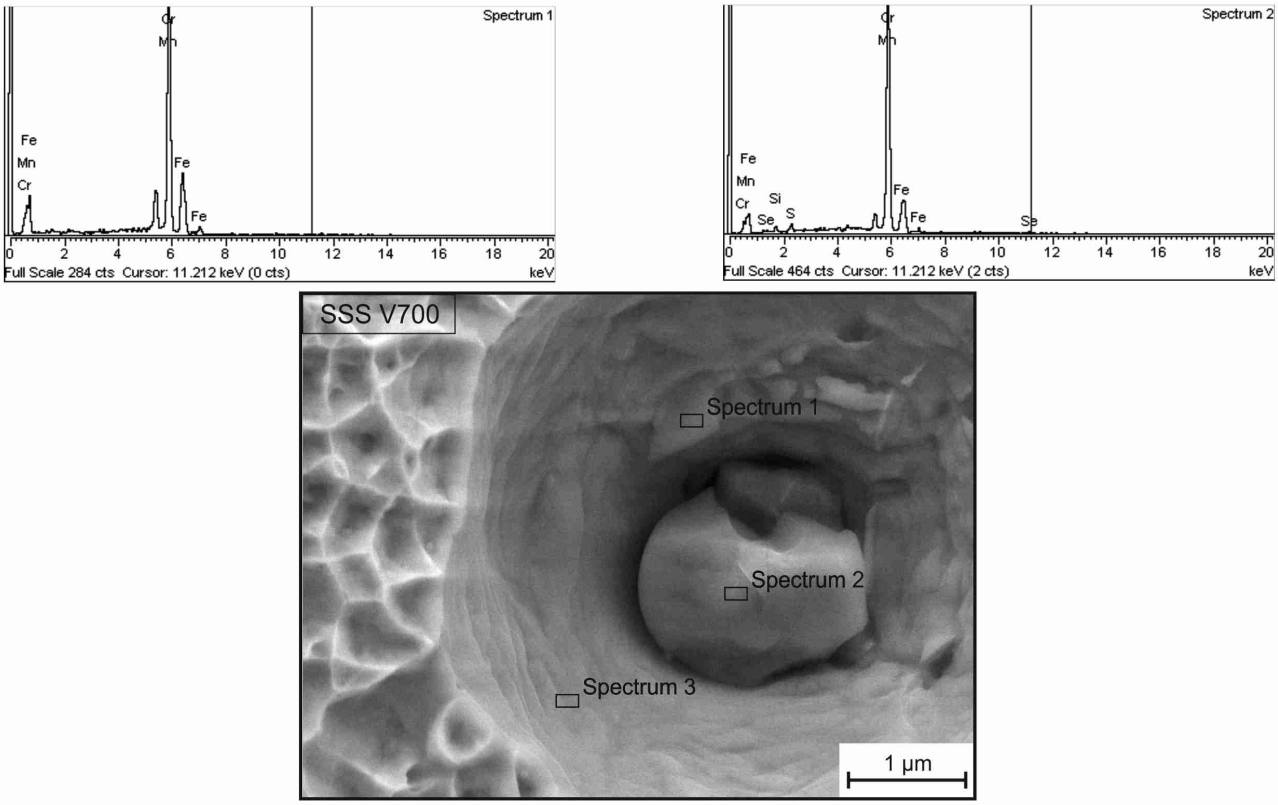

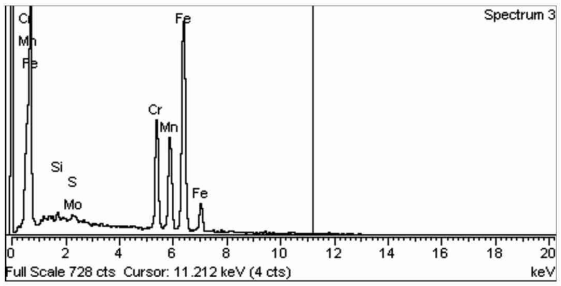

Metallic elements only										
Spectrum	Si	Cr	Mn	Al	Mo	Se	Ti	S	Fe	Total
1 [at.-%]	--	10.62	67.45	--	--	--	--	--	21.93	100
2	0.88	4.53	86.25	--	--	--	--	0.83	7.50	100
3	1.50	18.97	19.75	--	--	--	--	--	59.78	100

All elements												
Spectrum	N	O	Si	Cr	Mn	Al	Mo	Se	S	Ti	Fe	Total
1 [at.-%]	--	--	--	10.62	67.45	--	--	--	--	--	21.93	100
2	--	3.88	0.85	4.35	82.91	--	--	--	0.79	--	7.21	100
3	3.78	--	--	18.26	19.01	--	--	--	--	--	57.52	100

Figure B. 37.: EDX analysis results of the large particulate of image 5. 45, V700 specimen

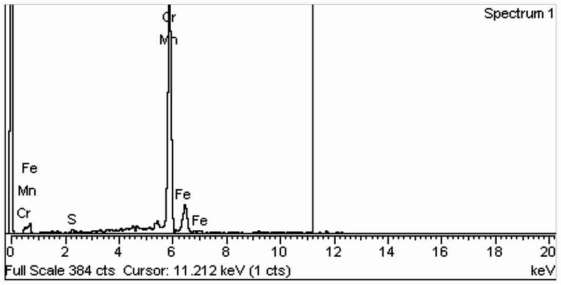

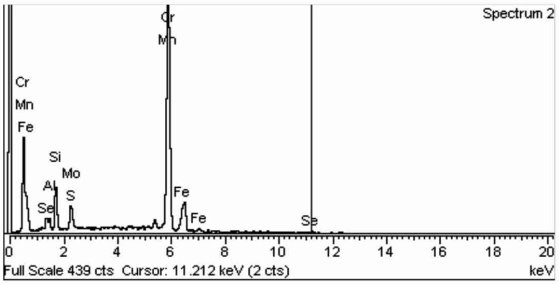

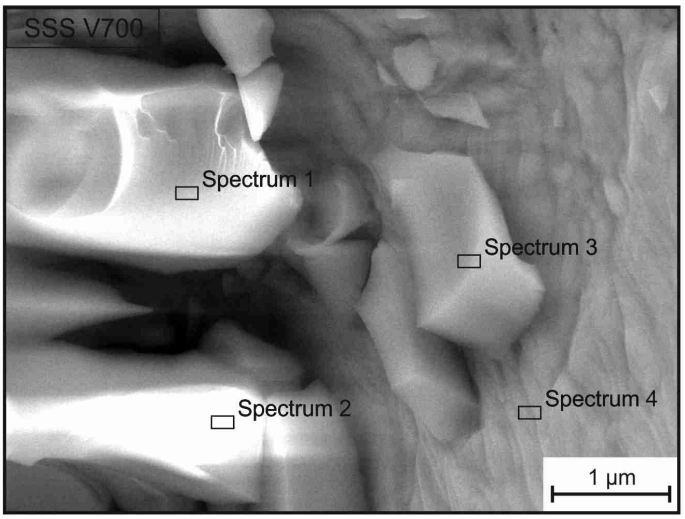

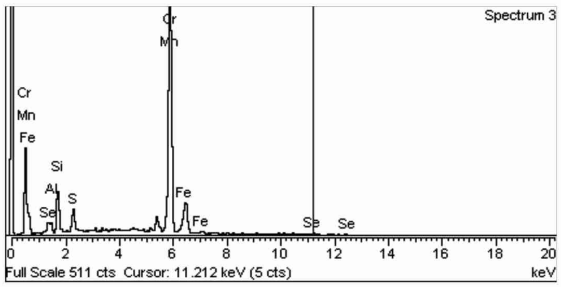

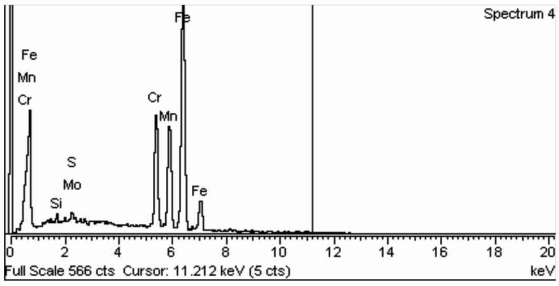

Metallic elements only										
Spectrum	Si	Cr	Mn	Al	Mo	Se	Ti	S	Fe	Total
1 [at.-%]	--	1.79	93.11	--	--	--	--	--	5.10	100
2	6.89	2.39	77.32	2.77	2.15	1.81	--	1.41	5.26	100
3	7.30	3.39	77.12	2.34	--	1.42	--	3.38	5.04	100
4	0.82	17.96	21.08	--	1.21	--	--	--	58.93	100

All elements												
Spectrum	N	O	Si	Cr	Mn	Al	Mo	Se	S	Ti	Fe	Total
1 [at.-%]	--	--	--	1.79	93.11	--	--	--	--	--	5.10	100
2	--	32.38	4.50	1.62	52.58	1.80	1.42	1.18	0.94	--	3.58	100
3	--	26.99	5.19	2.48	56.55	1.65	--	1.01	2.43	--	3.70	100
4	2.86	3.56	0.76	16.82	19.73	--	1.13	--	--	--	55.15	100

Figure B. 38.: EDX analysis results of loose, oxidic particulates out of a pore, V700 specimen

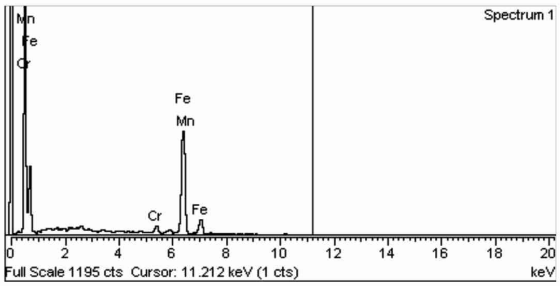

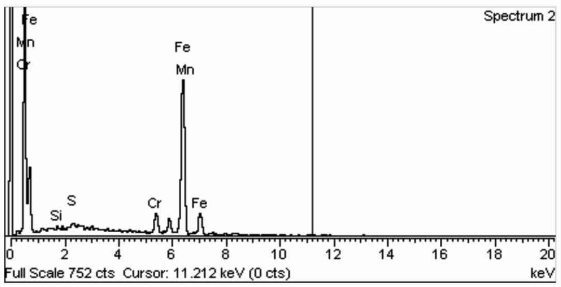

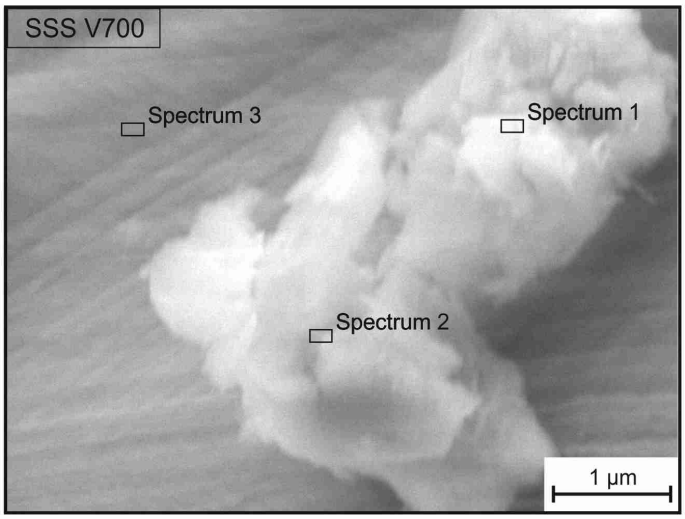

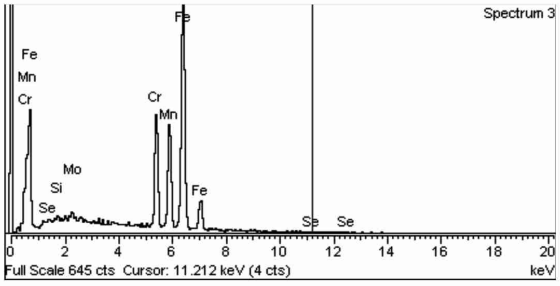

Metallic elements only										
Spectrum	Si	Cr	Mn	Al	Mo	Se	Ti	S	Fe	Total
1 [at.-%]	--	3.75	1.61	--	--	--	--	--	94.64	100
2	1.17	6.49	5.48	--	--	--	--	--	86.86	100
3	0.76	19.16	19.91	--	0.55	--	--	--	59.62	100

All elements												
Spectrum	N	O	Si	Cr	Mn	Al	Mo	Se	S	Ti	Fe	Total
1 [at.-%]	--	64.01	--	1.38	0.58	--	--	--	--	--	34.04	100
2	--	54.15	0.49	3.02	2.51	--	--	--	--	--	39.83	100
3	4.24	--	0.72	18.35	19.07	--	0.52	--	--	--	57.09	100

Figure B. 39.: EDX analysis results of the flaky particulate of image 5. 47, V700 specimen

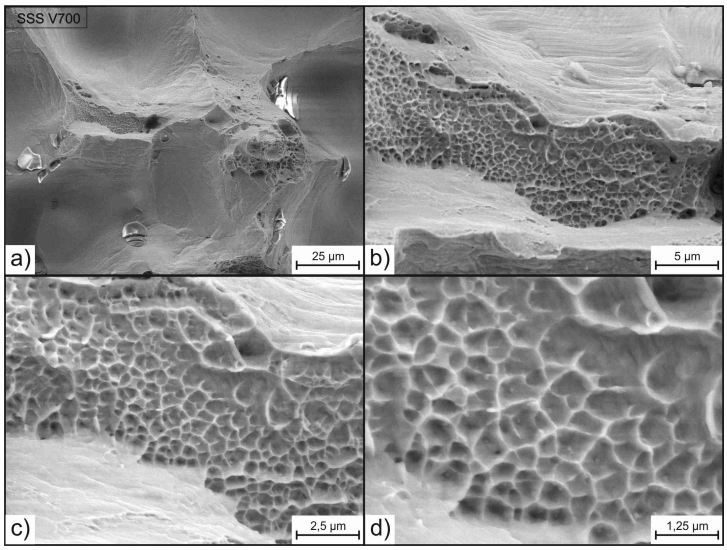

Figure B. 40.: Characteristic fracture site with very small particulates, V700 specimen

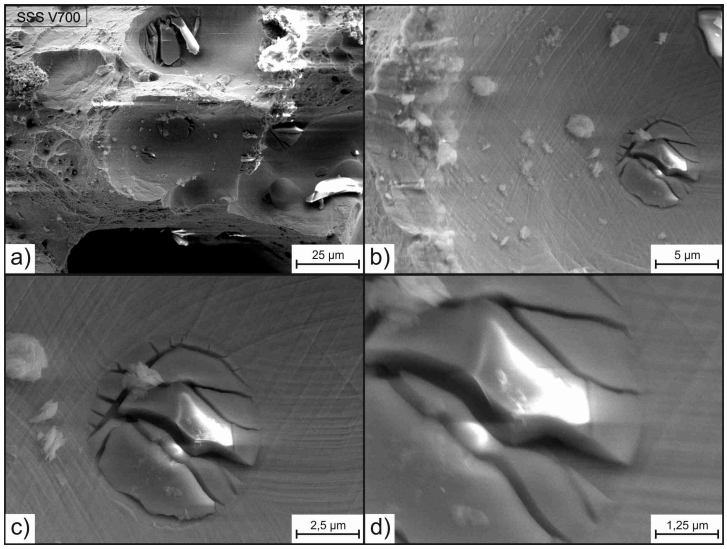

Figure B. 41.: Closeup of an oxidic particulate in a pore, V700 specimen

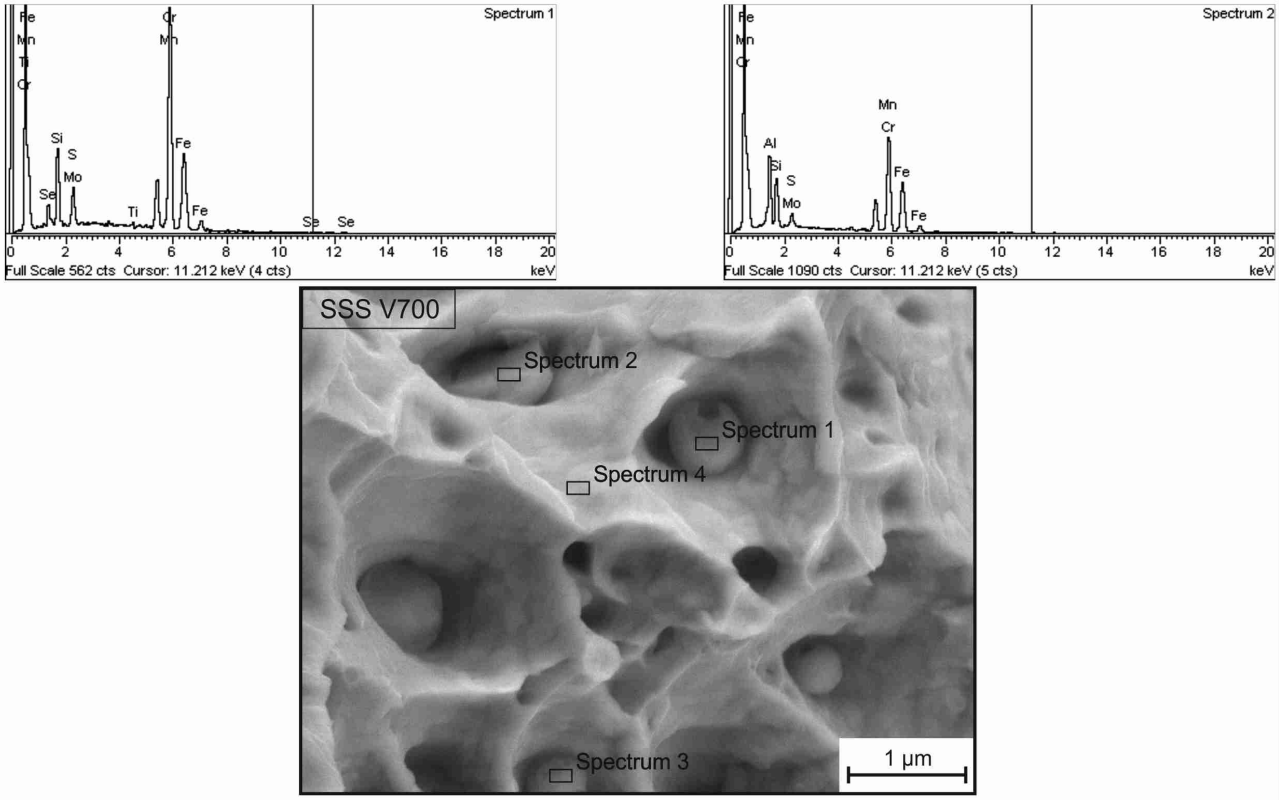

Metallic elements only										
Spectrum	Si	Cr	Mn	Al	Mo	Se	Ti	S	Fe	Total
1 [at.-%]	9.82	9.73	52.90	--	2.46	1.66	--	1.92	21.52	100
2	10.40	10.42	37.61	15.56	1.47	--	--	--	24.53	100
3	3.29	10.34	58.23	--	1.02	--	--	--	27.21	100
4	--	19.45	19.65	--	--	--	--	--	60.90	100

All elements												
Spectrum	N	O	Si	Cr	Mn	Al	Mo	Se	S	Ti	Fe	Total
1 [at.-%]	--	41.38	5.51	5.75	31.25	--	1.40	0.92	1.09	--	12.71	100
2	--	53.13	4.59	5.00	18.01	6.89	0.67	--	--	--	11.73	100
3	--	6.01	3.07	9.72	54.74	--	0.95	--	--	--	25.49	100
4	--	--	--	19.45	19.65	--	--	--	--	--	60.90	100

Figure B. 42.: EDX analysis results of the spherical particulates distributing in the densified powder mass second site of interest, V700 specimen

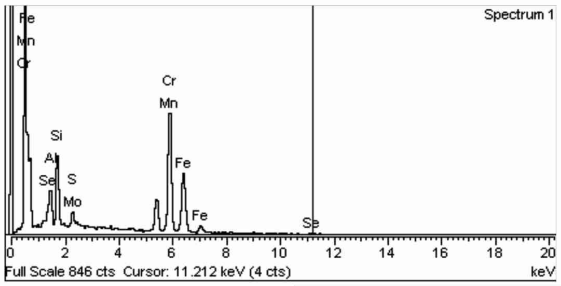

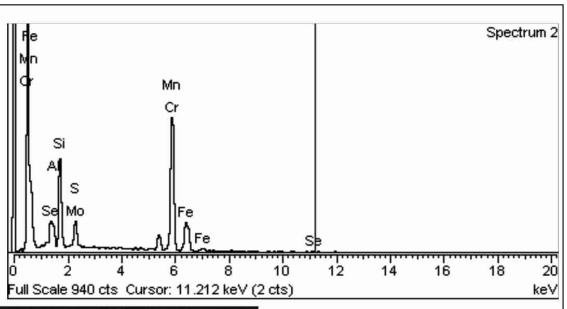

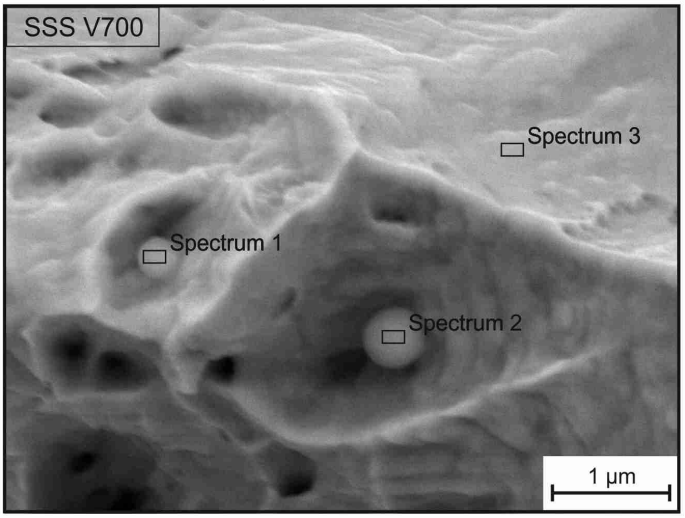

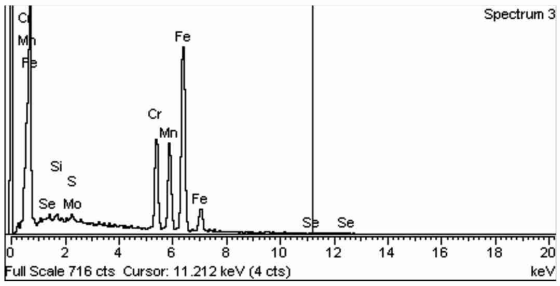

Metallic elements only										
Spectrum	Si	Cr	Mn	Al	Mo	Se	Ti	S	Fe	Total
1 [at.-%]	12.22	9.91	44.24	6.63	1.86	--	--	--	25.14	100
2	17.01	4.73	52.71	--	2.62	3.35	--	2.80	11.51	100
3	--	19.03	19.48	--	--	--	--	--	61.49	100

All elements												
Spectrum	N	O	Si	Cr	Mn	Al	Mo	Se	S	Ti	Fe	Total
1 [at.-%]	--	50.24	5.76	5.01	22.33	3.10	0.90	--	--	--	12.68	100
2	--	55.31	7.19	2.16	24.12	2.21	1.13	1.42	1.21	--	5.27	100
3	3.75	--	--	18.32	18.75	--	--	--	--	--	59.18	100

Figure B. 43.: EDX analysis results of the spherical particulates distributing in the densified powder mass third site of interest, V700 specimen

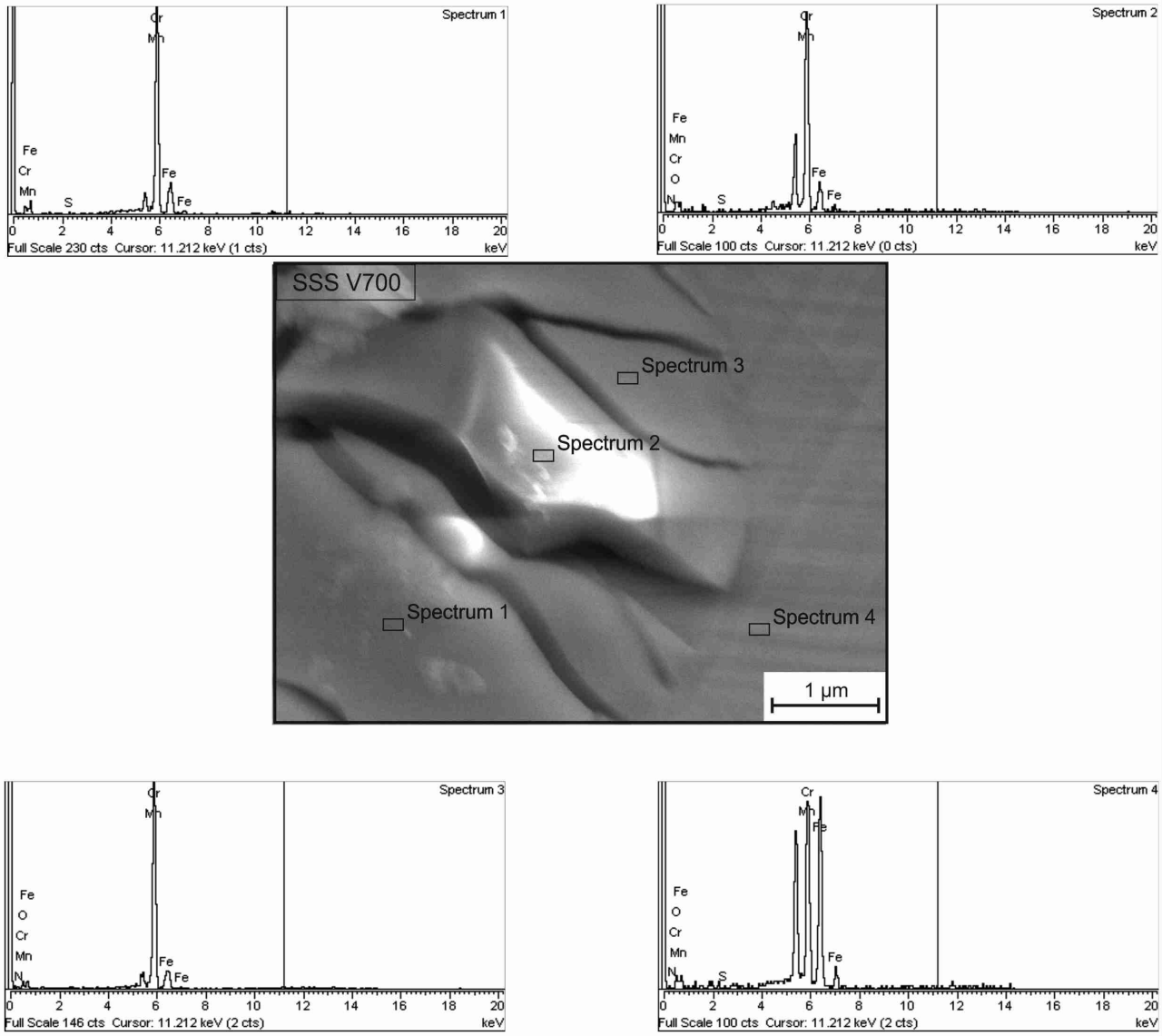

Metallic elements only										
Spectrum	Si	Cr	Mn	Al	Mo	Se	Ti	S	Fe	Total
1 [at.-%]	--	5.69	83.77	--	--	--	--	--	10.54	100
2	--	19.48	71.57	--	--	--	--	--	8.96	100
3	--	4.54	88.80	--	--	--	--	--	6.66	100
4	--	22.83	33.94	--	--	--	--	--	43.23	100

All elements												
Spectrum	N	O	Si	Cr	Mn	Al	Mo	Se	S	Ti	Fe	Total
1 [at.-%]	--	3.31	--	5.50	80.99	--	--	--	--	--	10.19	100
2	--	--	--	19.48	71.57	--	--	--	--	--	8.96	100
3	--	--	--	4.54	88.80	--	--	--	--	--	6.66	100
4	--	--	--	22.83	33.94	--	--	--	--	--	43.23	100

Figure B. 44.: EDX analysis results of the loose oxidic particulates of image B. 41, V700 specimen

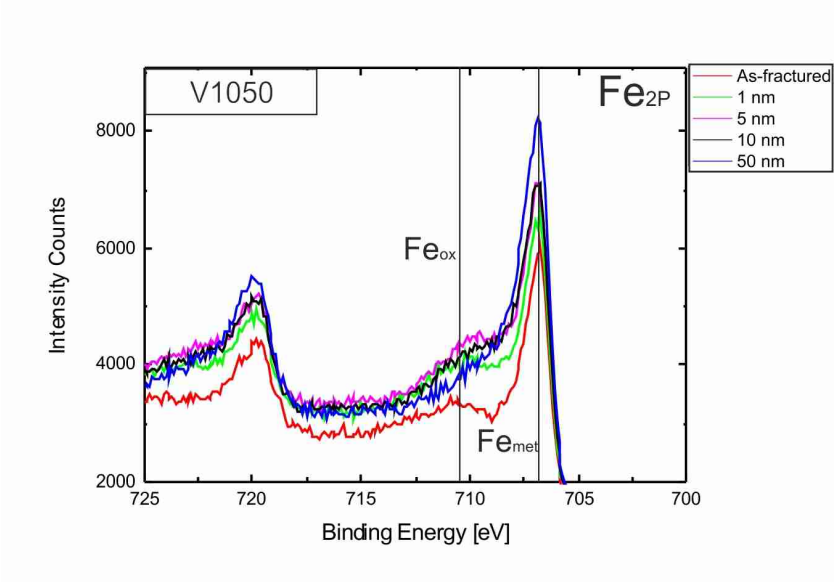

Figure B. 45.: Detailed XPS spectra of Fe 2p peak for V1050 specimen

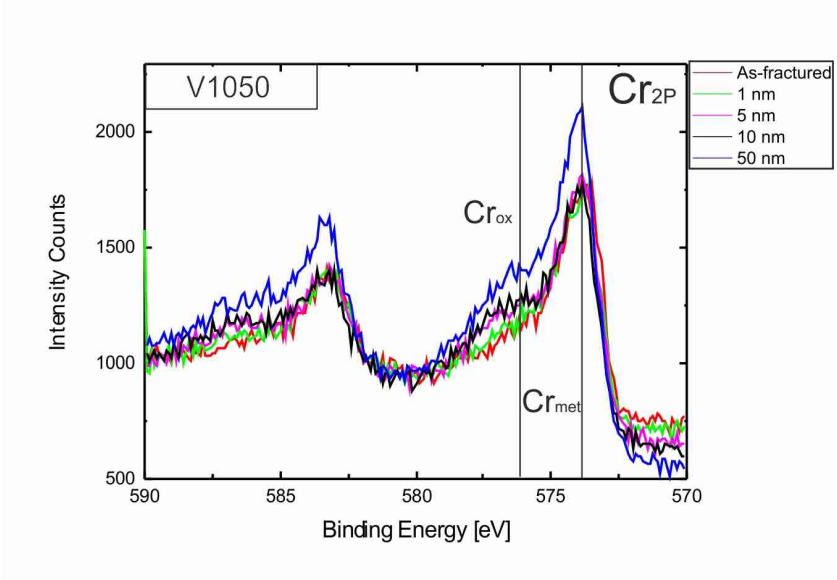

Figure B. 46.: Detailed XPS spectra of Cr 2p peak for V1050 specimen

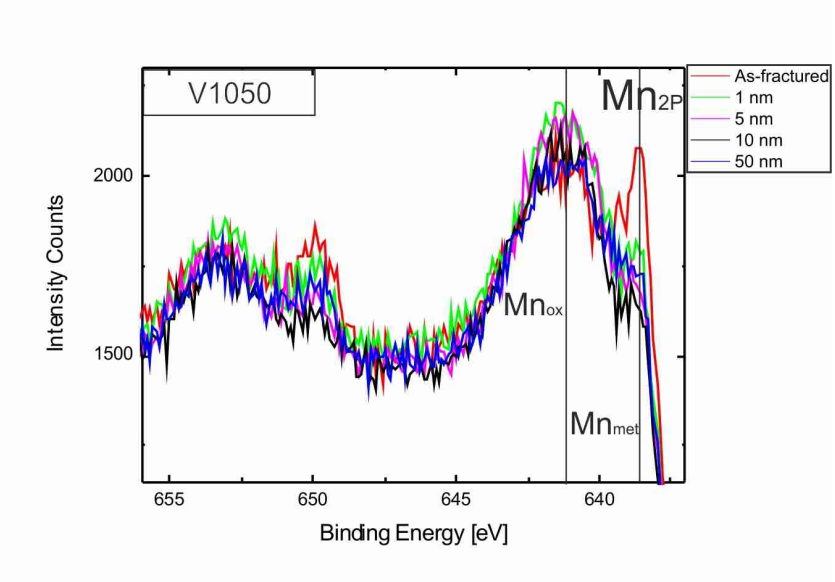

Figure B. 47.: Detailed XPS spectra of Mn 2p peak for V1050 specimen

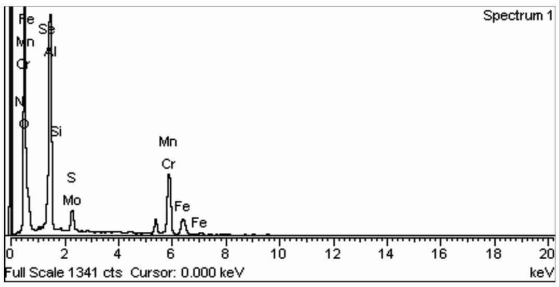

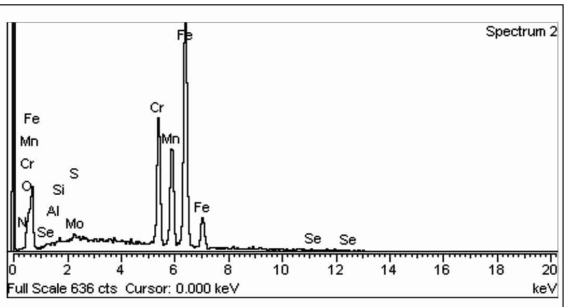

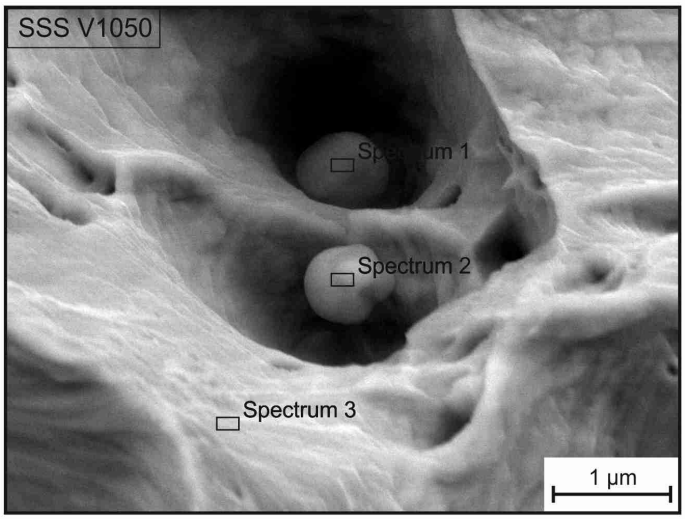

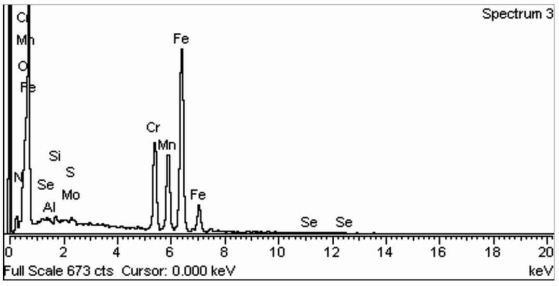

Metallic elements only										
Spectrum	Si	Cr	Mn	Al	Mo	Se	Ti	S	Fe	Total
1 [at.-%]	--	5.66	33.12	46.77	3.27	--	--	2.41	8.77	100
2	--	20.28	19.34	--	0.87	--	--	--	59.51	100
3	1.07	18.84	19.02	--	--	--	--	--	61.07	100

All elements												
Spectrum	N	O	Si	Cr	Mn	Al	Mo	Se	S	Ti	Fe	Total
1 [at.-%]	--	61.98	--	2.22	13.00	17.29	1.19	--	0.88	--	3.44	100
2	--	--	--	20.28	19.34	--	0.87	--	--	--	59.51	100
3	5.98	--	1.00	17.72	17.88	--	--	--	--	--	57.41	100

Figure B. 48.: EDX analysis results of the spherical particulates of image 5. 55, V1050 specimen

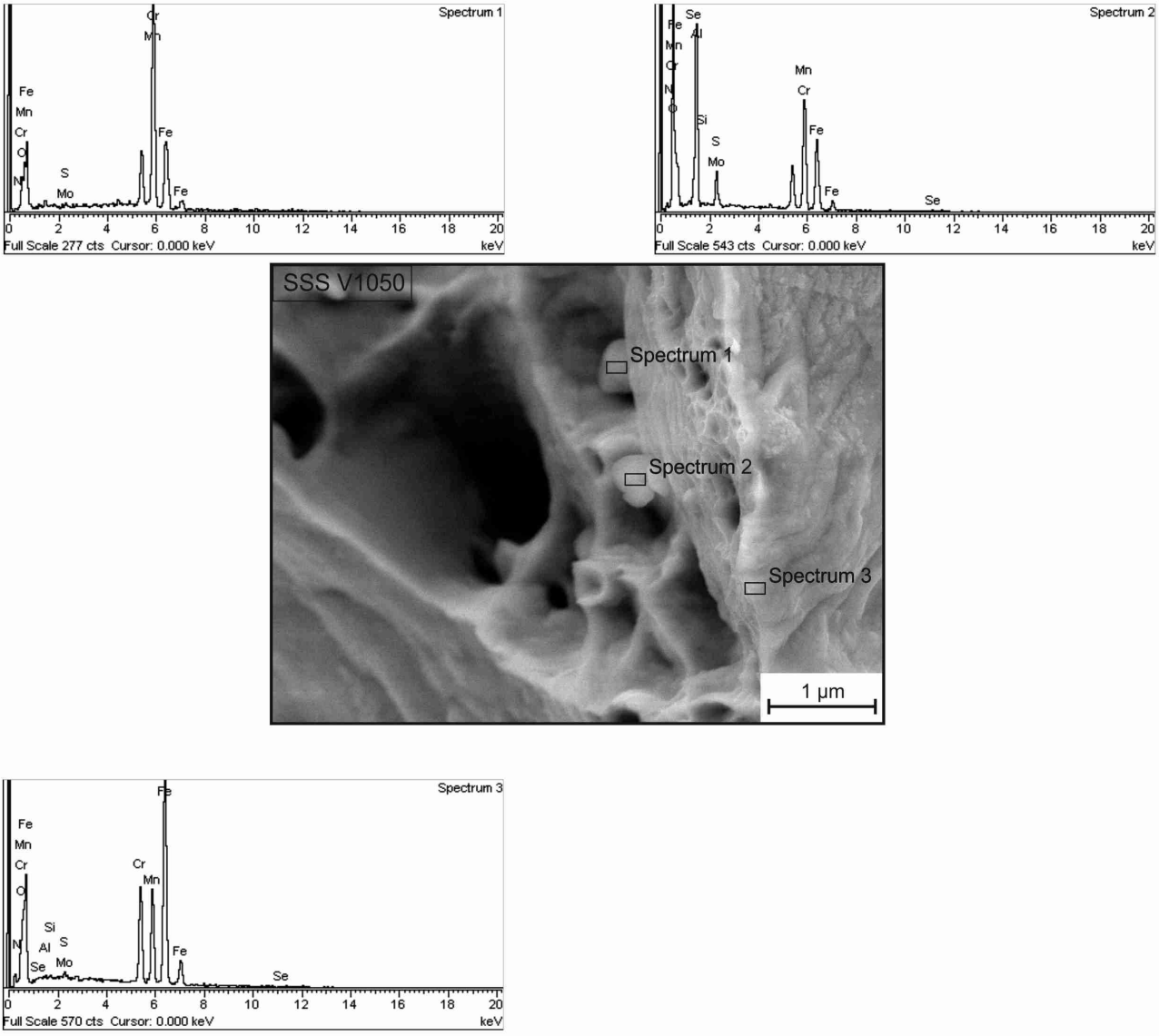

Metallic elements only										
Spectrum	Si	Cr	Mn	Al	Mo	Se	Ti	S	Fe	Total
1 [at.-%]	--	13.93	60.35	--	--	--	--	--	25.72	100
2	--	10.46	32.81	26.11	2.82	--	--	2.10	25.69	100
3	--	18.42	20.25	--	--	--	--	--	61.33	100

All elements												
Spectrum	N	O	Si	Cr	Mn	Al	Mo	Se	S	Ti	Fe	Total
1 [at.-%]	--	9.18	--	12.66	54.81	--	--	--	--	--	23.35	100
2	--	46.17	--	5.74	17.98	13.46	1.48	--	1.10	--	14.07	100
3	2.69	5.25	--	16.97	18.64	--	--	--	--	--	56.45	100

Figure B. 49.: EDX analysis results of the spherical particulates of image **??**, V1050 specimen

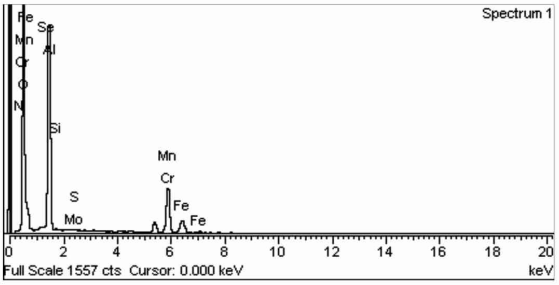

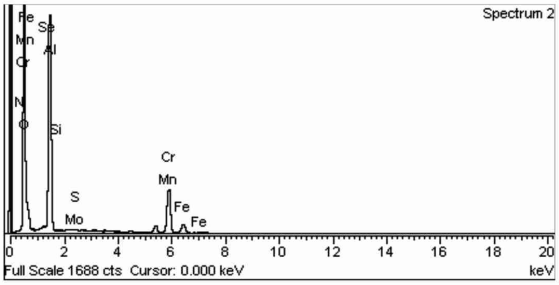

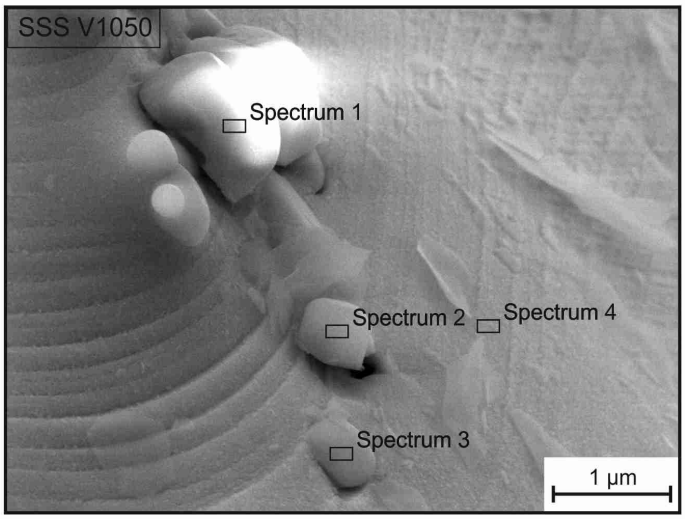

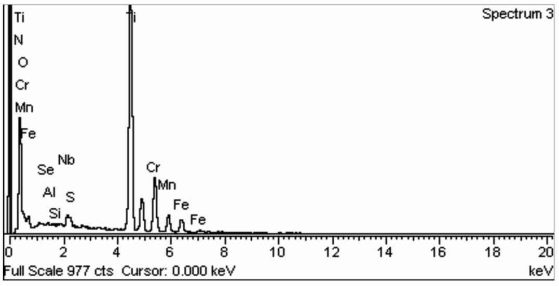

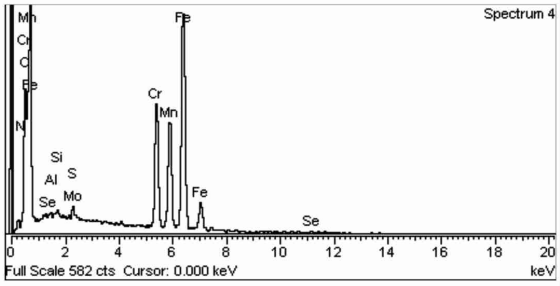

Metallic elements only										
Spectrum	Si	Cr	Mn	Al	Mo	Se	Ti	S	Fe	Total
1 [at.-%]	--	5.90	29.63	55.86	--	--	--	--	8.61	100
2	--	3.87	31.43	59.39	--	--	--	--	5.31	100
3	--	21.06	5.15	--	1.57	--	64.53	--	7.70	100
4	--	20.30	20.48	--	---	--	--	--	59.22	100

All elements												
Spectrum	N	O	Si	Cr	Mn	Al	Mo	Se	S	Ti	Fe	Total
1 [at.-%]	--	64.06	--	2.19	10.99	19.57	--	--	--	--	3.19	100
2	--	65.44	--	1.37	11.17	20.12	--	--	--	--	1.89	100
3	44.04	--	--	11.67	2.87	--	0.85	--	--	36.29	4.28	100
4	--	21.65	--	15.93	16.06	--	--	--	--	--	46.36	100

Figure B. 50.: EDX analysis results of the embedded particulates of image 5. 56, V1050 specimen

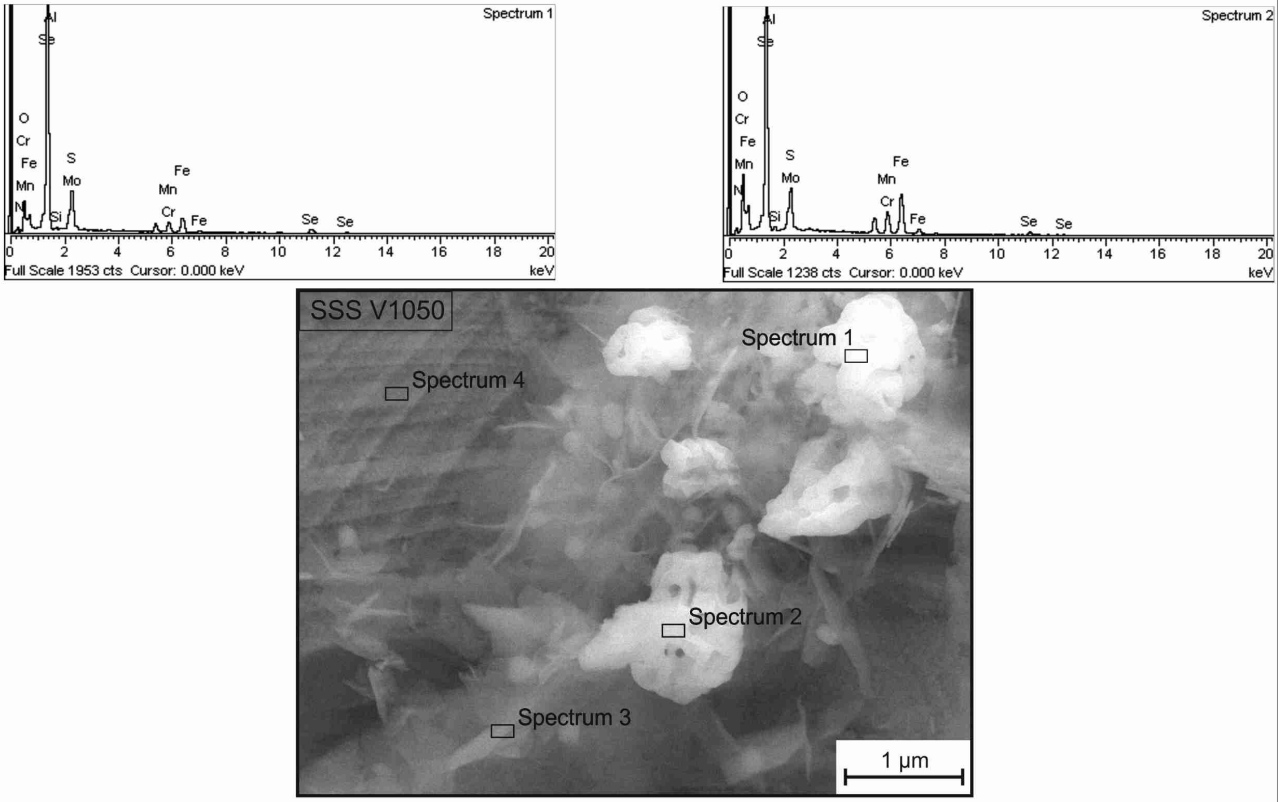

Metallic elements only										
Spectrum	Si	Cr	Mn	Al	Mo	Se	Ti	S	Fe	Total
1 [at.-%]	--	5.78	7.23	7.52	5.76	49.46	--	8.84	15.41	100
2	--	7.54	11.81	5.44	5.56	38.87	--	4.18	26.58	100
3	1.44	14.11	35.39	--	1.37	2.72	--	--	44.96	100
4	--	19.14	19.56	--	1.31	--	--	--	60.00	100

All elements												
Spectrum	N	O	Si	Cr	Mn	Al	Mo	Se	S	Ti	Fe	Total
1 [at.-%]	4.86	35.44	--	3.49	4.37	4.19	3.31	29.80	5.08	--	9.33	100
2	--	40.24	--	4.57	7.17	3.05	3.22	23.19	2.42	--	16.15	100
3	1.95	41.85	0.76	7.98	19.96	--	0.74	1.42	--	--	25.33	100
4	--	18.05	--	15.71	16.04	--	1.06	--	--	--	49.15	100

Figure B. 51.: EDX analysis results of the flaky particulates of image 5. 57, V1050 specimen

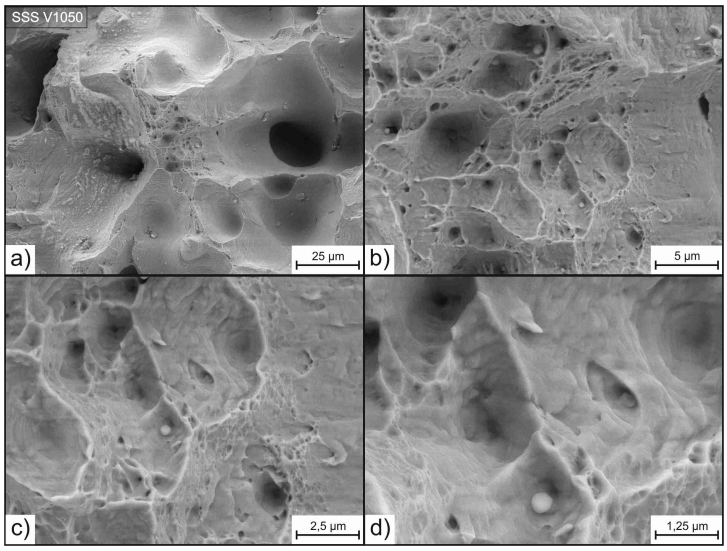

Figure B. 52.: Closeup of the spherical particulates distributing in the densified powder mass second site of interest, V1050 specimen

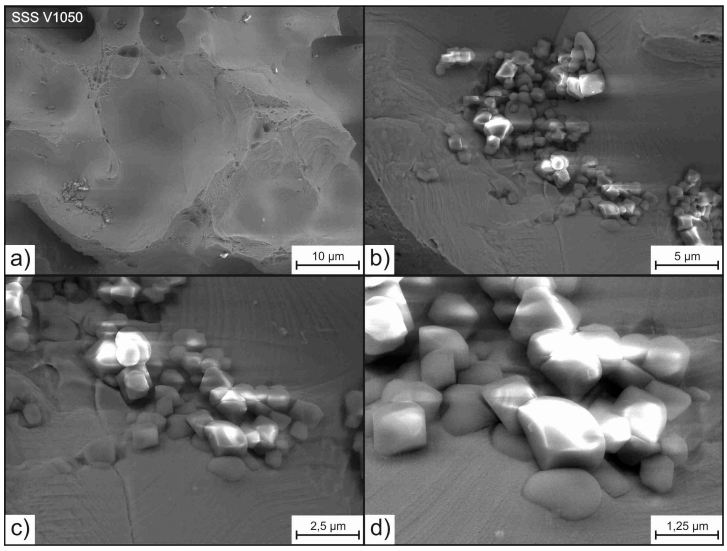

Figure B. 53.: Agglomareted, large, oxidic particulates in parts embedded in the densified steel matrix, V1050 specimen

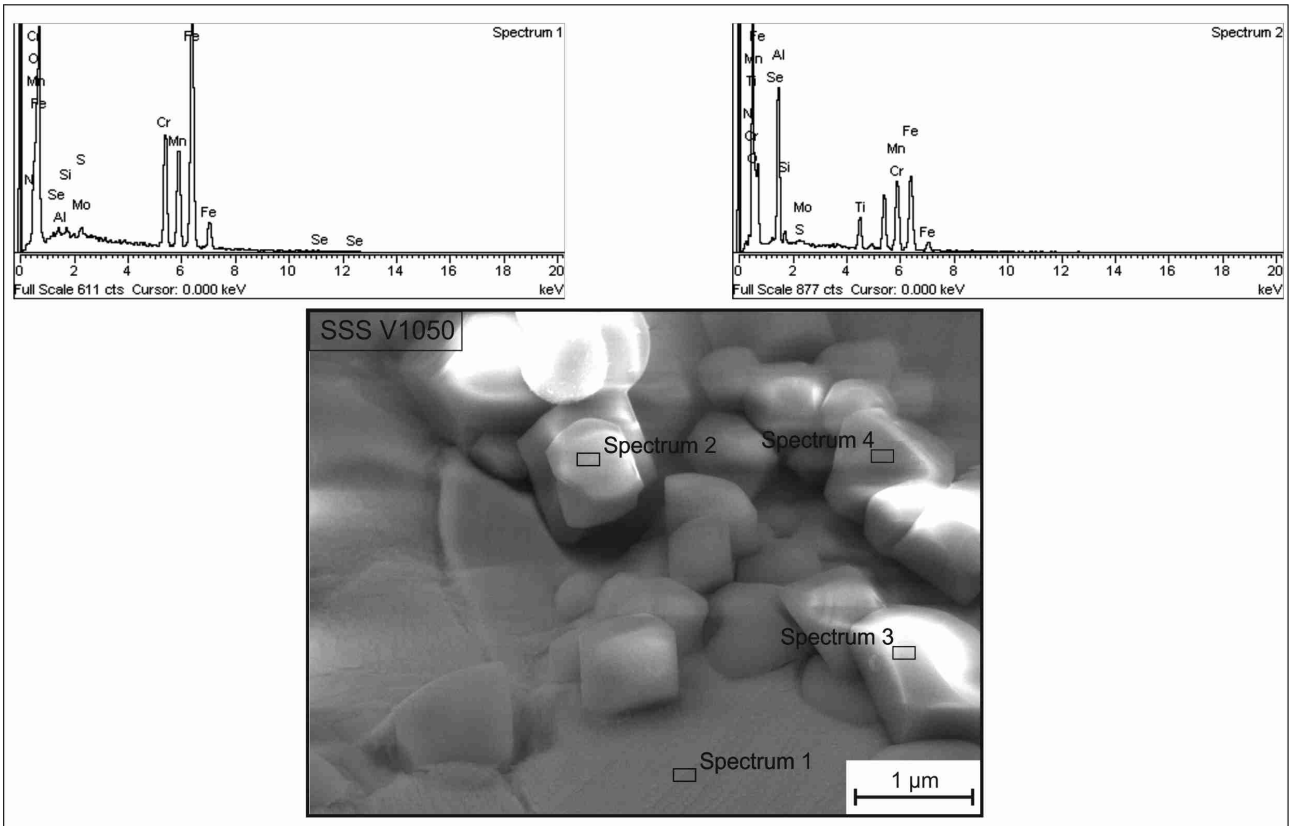

Metallic elements only										
Spectrum	Si	Cr	Mn	Al	Mo	Se	Ti	S	Fe	Total
1 [at.-%]	1.00	19.44	19.20	--	1.04	--	--	--	59.32	100
2	2.01	13.88	22.40	24.48	--	--	6.24	--	30.98	100
3	--	3.62	31.05	61.70	--	--	0.87	--	2.76	100
4	--	2.72	31.25	62.75	--	--	1.03	--	2.25	100

All elements												
Spectrum	N	O	Si	Cr	Mn	Al	Mo	Se	S	Ti	Fe	Total
1 [at.-%]	--	8.50	0.91	17.80	17.57	--	0.95	--	--	--	54.27	100
2	6.17	48.63	0.84	6.43	10.35	10.40	--	--	--	2.89	14.29	100
3	--	65.85	--	1.26	10.86	20.76	--	--	--	0.30	0.97	100
4	--	66.43	--	0.93	10.73	20.79	--	--	--	0.35	0.77	100

Figure B. 54.: EDX analysis results of the partly embedded particulates of image B. 53, V1050 specimen

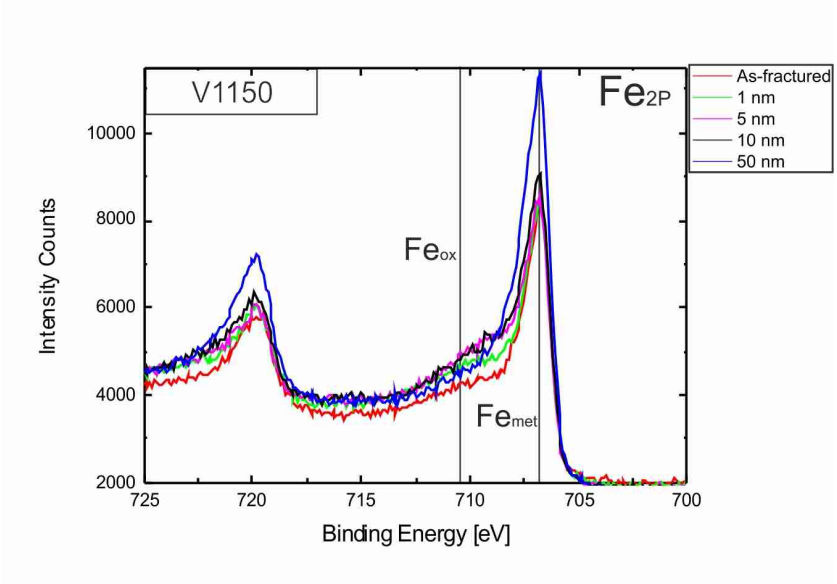

Figure B. 55.: Detailed XPS spectra of Fe 2p peak for V1150 specimen

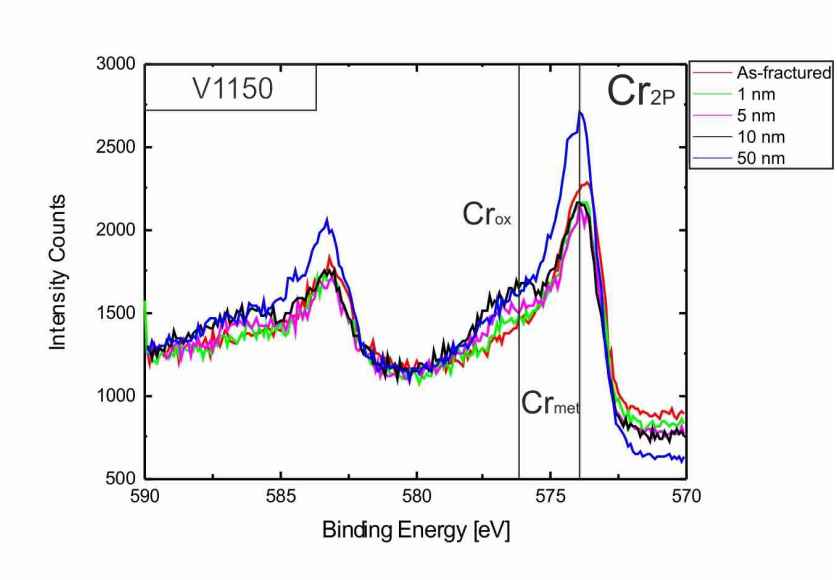

Figure B. 56.: Detailed XPS spectra of Cr 2p peak for V1150 specimen

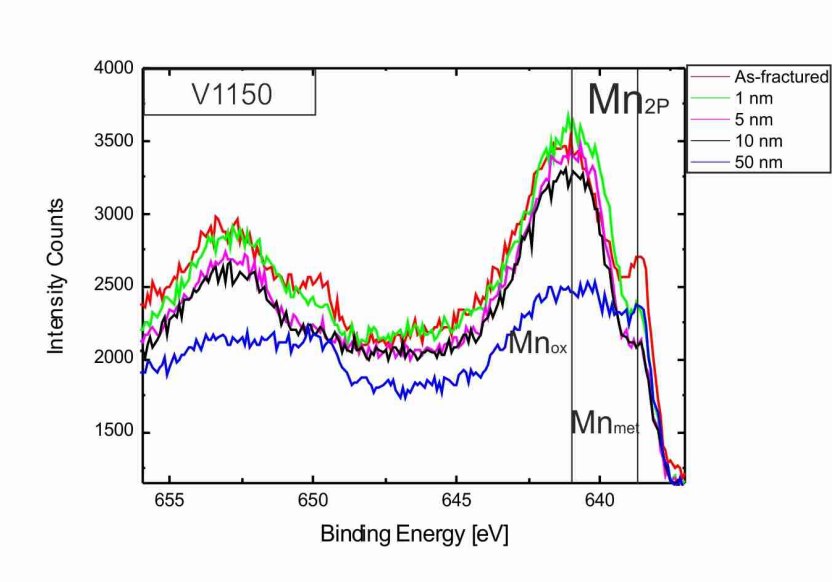

Figure B. 57.: Detailed XPS spectra of Mn 2p peak for V1150 specimen

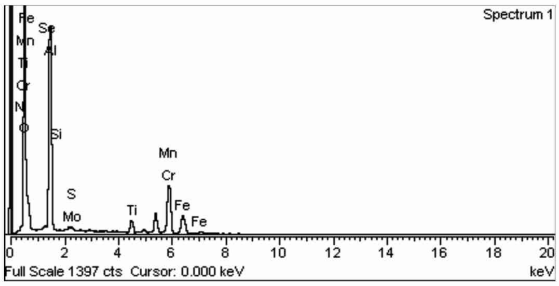

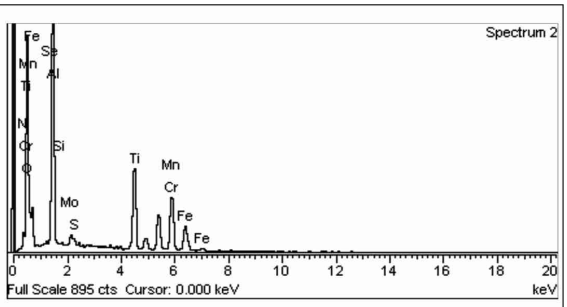

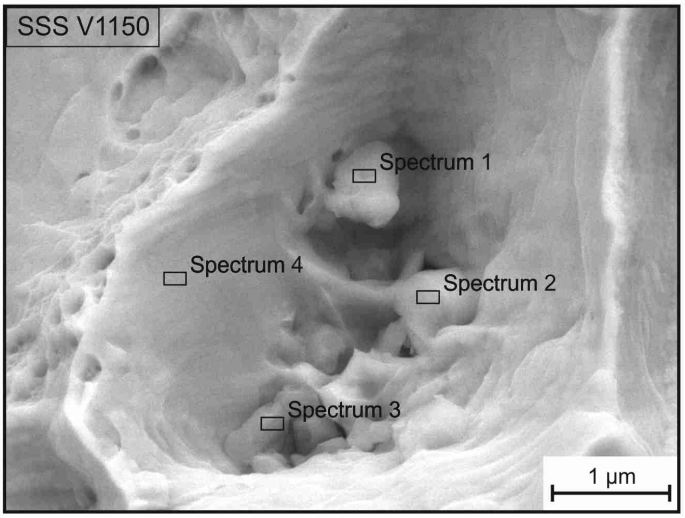

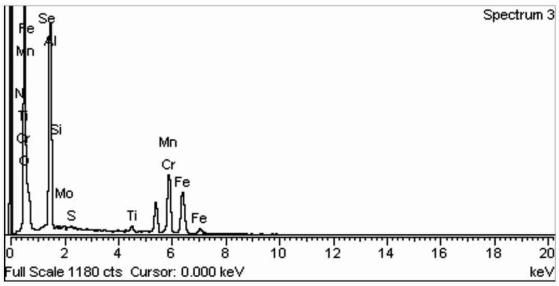

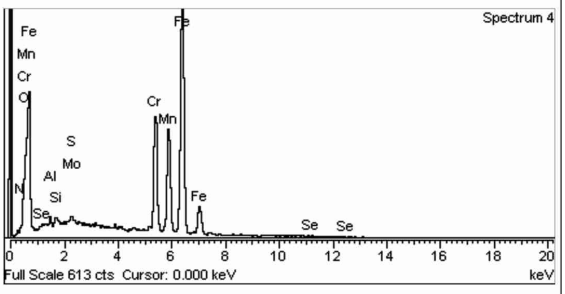

Metallic elements only										
Spectrum	Si	Cr	Mn	Al	Mo	Se	Ti	S	Fe	Total
1 [at.-%]	--	8.33	27.80	48.41	--	--	4.36	--	11.10	100
2	--	11.81	21.42	36.85	--	--	19.00	--	10.92	100
3	--	10.50	24.56	41.16	--	--	1.71	--	22.07	100
4	--	18.96	19.76	1.30	--	--	--	--	59.97	100

All elements												
Spectrum	N	O	Si	Cr	Mn	Al	Mo	Se	S	Ti	Fe	Total
1 [at.-%]	5.05	61.02	--	2.92	9.77	15.81	--	--	--	1.53	3.90	100
2	6.74	57.68	--	4.29	7.82	12.52	--	--	--	6.98	3.98	100
3	--	55.87	--	4.78	11.15	17.42	--	--	--	0.78	10.00	100
4	3.31	--	--	18.34	19.11	1.26	--	--	--	--	57.99	100

Figure B. 58.: EDX analysis results of the particulates of image 5. 65, V1150 specimen

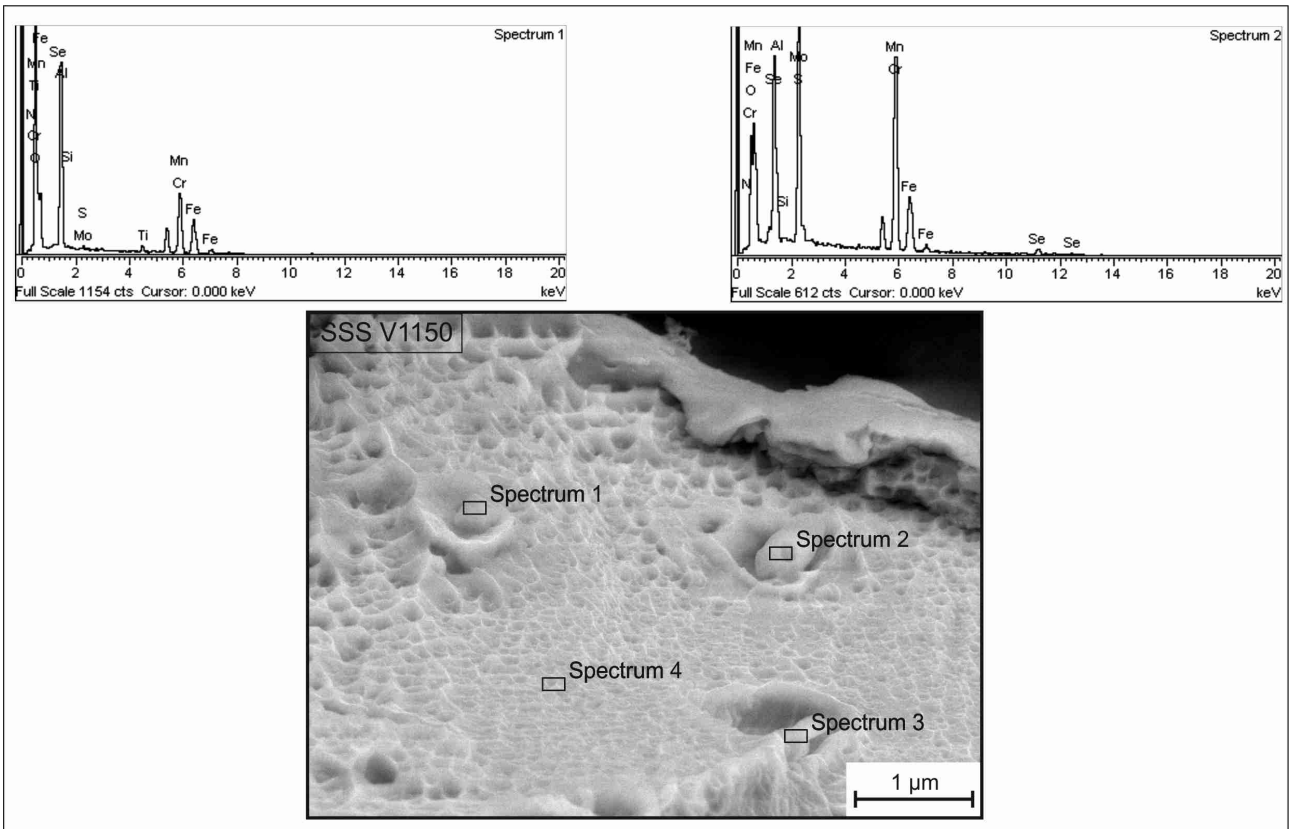

Metallic elements only										
Spectrum	Si	Cr	Mn	Al	Mo	Se	Ti	S	Fe	Total
1 [at.-%]	--	9.68	27.79	41.17	--	--	1.84	--	19.52	100
2	--	5.61	40.10	7.90	8.95	12.95	--	12.47	12.02	100
3	1.17	18.51	19.81	1.68	--	--	--	--	58.82	100
4	1.22	18.68	21.25	--	--	--	--	--	58.84	100

All elements												
Spectrum	N	O	Si	Cr	Mn	Al	Mo	Se	S	Ti	Fe	Total
1 [at.-%]	3.97	56.10	--	4.00	11.46	15.67	--	--	--	--	8.03	100
2	--	27.29	--	4.11	29.44	5.59	6.44	9.33	8.96	--	8.83	100
3	--	--	1.17	18.51	19.81	1.68	--	--	--	--	58.82	100
4	4.26	8.63	1.05	16.30	18.52	--	--	--	--	--	51.25	100

Figure B. 59.: EDX analysis results of the particulates on the fracture surface of image 5. 67, V1150 specimen

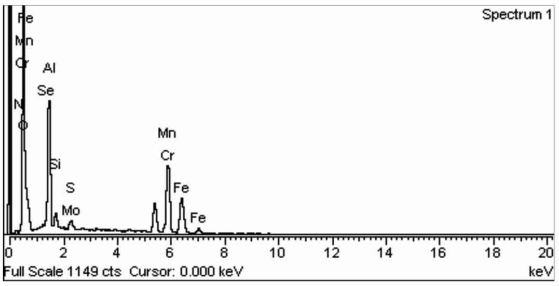

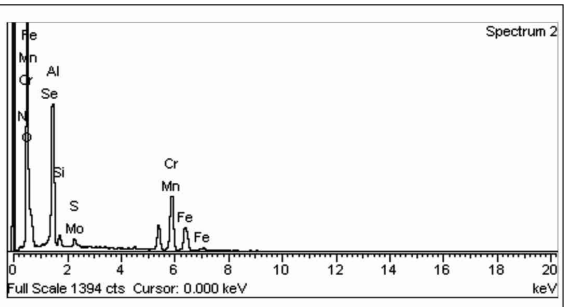

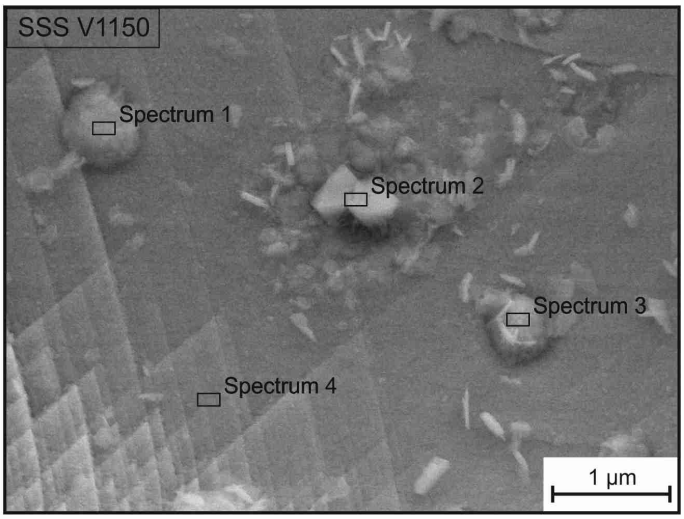

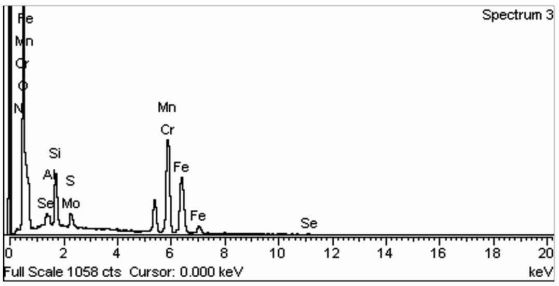

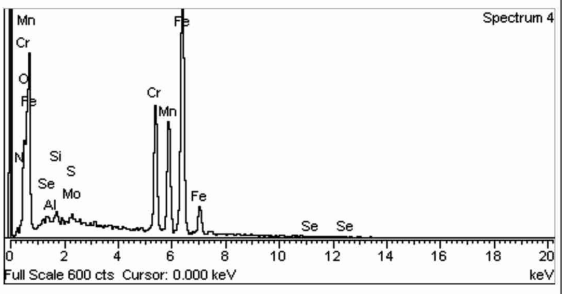

Metallic elements only										
Spectrum	Si	Cr	Mn	Al	Mo	Se	Ti	S	Fe	Total
1 [at.-%]	3.86	11.10	33.59	30.03	1.12	--	--	--	20.29	100
2	3.07	11.41	31.46	36.98	1.21	--	--	--	15.86	100
3	12.43	11.66	39.82	2.91	1.72	2.33	--	--	29.14	100
4	1.18	19.90	20.90	--	0.97	--	--	--	57.05	100

All elements												
Spectrum	N	O	Si	Cr	Mn	Al	Mo	Se	S	Ti	Fe	Total
1 [at.-%]	--	57.07	1.53	4.91	14.84	12.24	0.46	--	--	--	8.94	100
2	--	60.99	1.09	4.61	12.69	13.79	0.45	--	--	--	6.38	100
3	--	54.01	5.35	5.45	18.60	1.23	0.76	0.99	--	--	13.60	100
4	--	12.61	0.97	16.71	17.53	--	0.81	--	--	--	47.83	100

Figure B. 60.: EDX analysis results of the angular particulates on the surface of image 5. 68, V1150 specimen

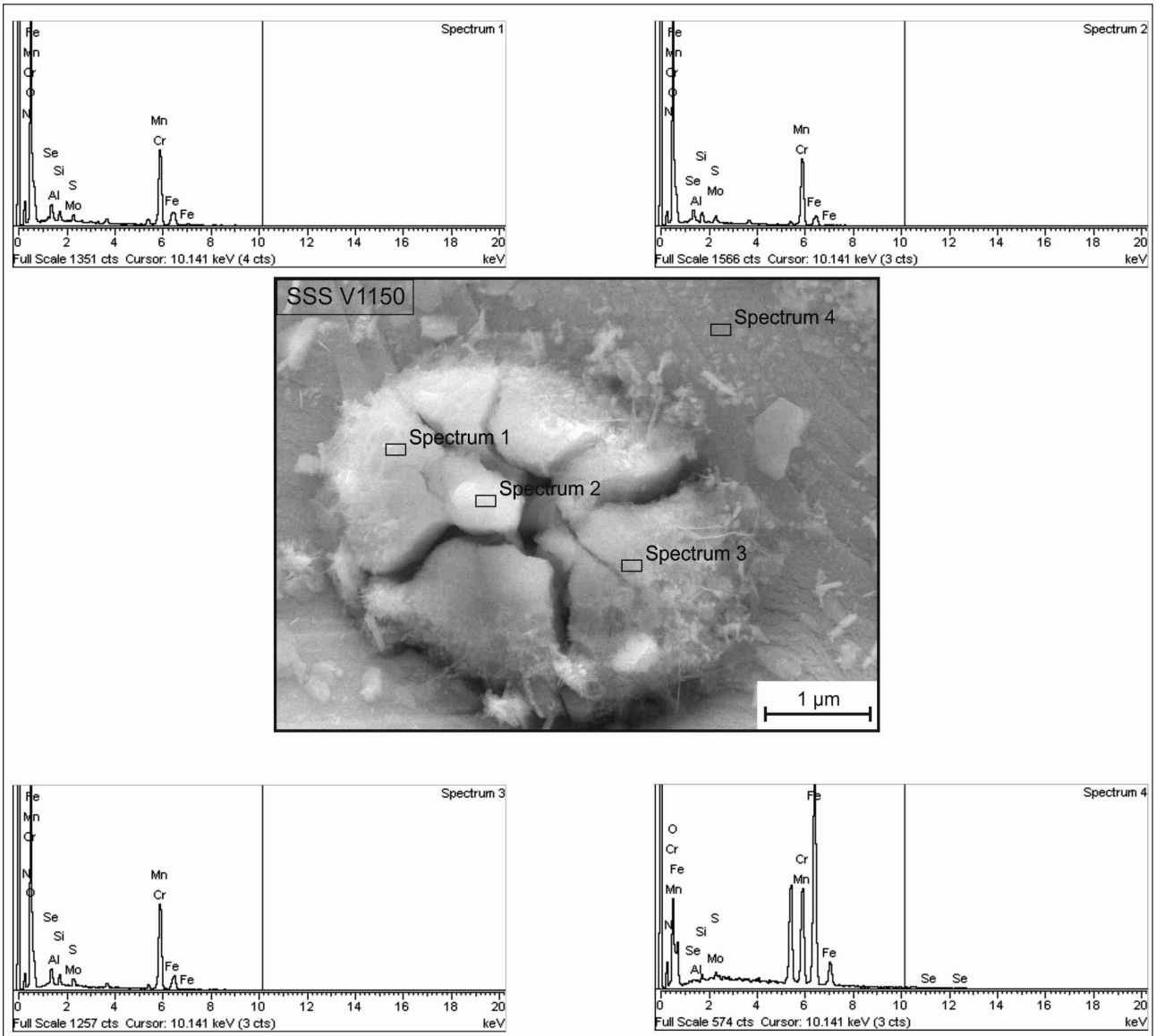

Metallic elements only										
Spectrum	Si	Cr	Mn	Al	Mo	Se	Ti	S	Fe	Total
1 [at.-%]	4.97	3.94	68.43	2.51	--	7.43	--	1.85	10.88	100
2	6.55	3.36	72.85	2.26	2.37	6.05	--	--	6.56	100
3	5.12	2.90	77.75	--	--	6.22	--	1.63	6.37	100
4	0.91	18.80	21.70	--	--	--	--	--	58.59	100

All elements												
Spectrum	N	O	Si	Cr	Mn	Al	Mo	Se	S	Ti	Fe	Total
1 [at.-%]	1.74	67.33	1.35	1.25	21.63	0.67	--	2.05	0.53	--	3.44	100
2	1.52	71.00	1.58	0.94	20.49	0.53	0.61	1.47	--	--	1.85	100
3	1.92	66.72	1.42	0.92	24.78	--	--	1.73	0.48	--	2.03	100
4	--	19.65	0.71	15.14	17.45	--	--	--	--	--	47.06	100

Figure B. 61.: EDX analysis results of the large oxide of image 5. 69, V1150 specimen

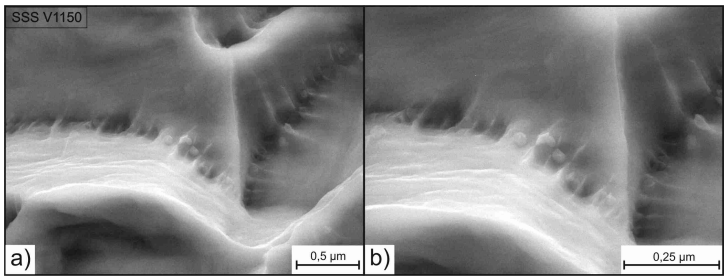

Figure B. 62.: Closeup of the fine particulates at the dimple stands of image 5. 66, V1150 specimen

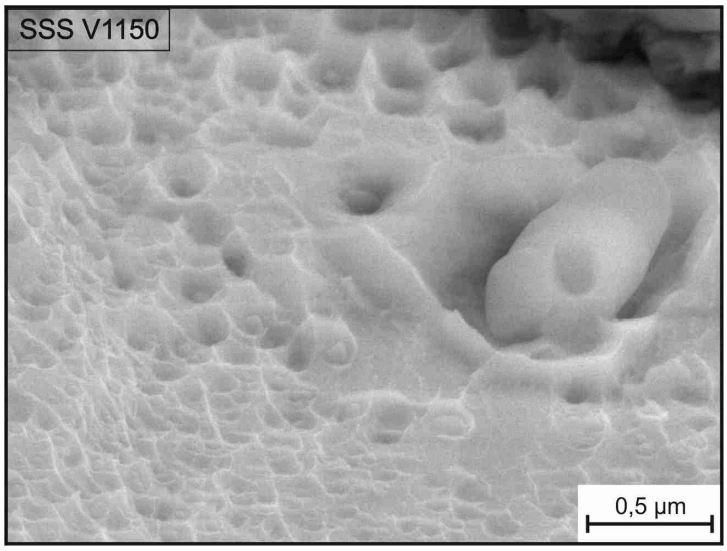

Figure B. 63.: Closeup of the fine particulates on the fracture surface of image 5. 67, V1150 specimen

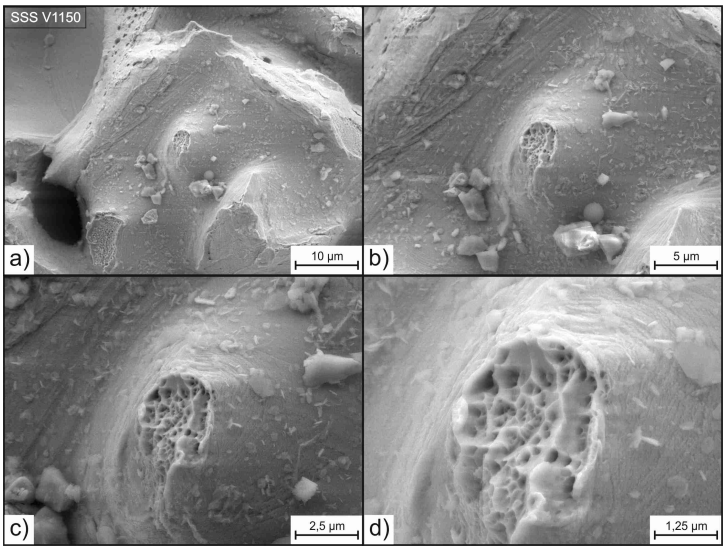

Figure B.64.: Fractured, former sintering neck surrounded by irregular and flaky particulates, V1150 specimen

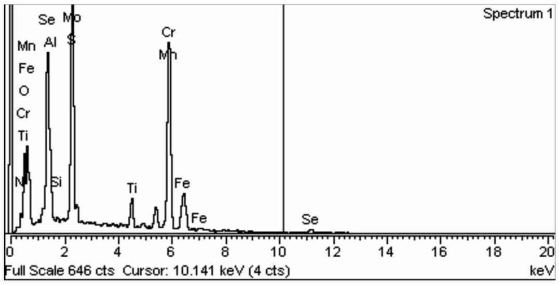

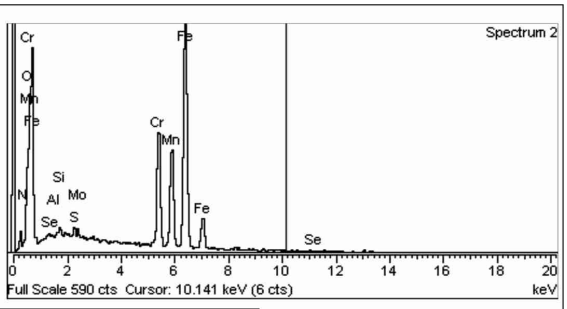

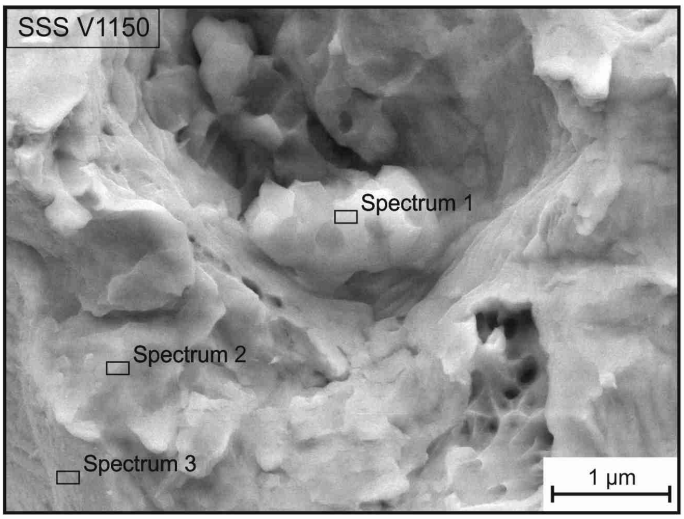

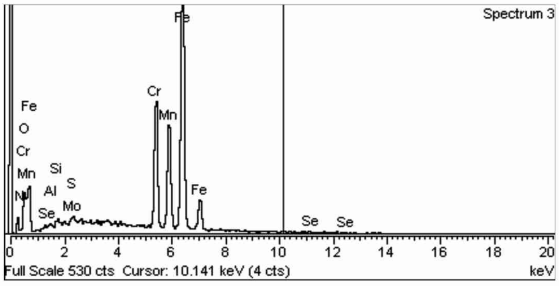

Metallic elements only										
Spectrum	Si	Cr	Mn	Al	Mo	Se	Ti	S	Fe	Total
1 [at.-%]	--	3.95	41.07	8.92	8.73	12.43	3.93	13.97	7.01	100
2	--	19.75	19.27	--	1.18	--	--	--	59.80	100
3	--	19.75	19.51	--	--	--	--	--	60.73	100

All elements												
Spectrum	N	O	Si	Cr	Mn	Al	Mo	Se	S	Ti	Fe	Total
1 [at.-%]	10.66	20.62	--	2.74	28.58	5.94	5.93	8.44	9.48	2.72	4.88	100
2	3.78	--	--	19.00	18.55	--	1.13	--	--	--	57.54	100
3	--	5.43	--	18.69	18.46	--	--	--	--	--	57.43	100

Figure B. 65.: EDX analysis results of the particulates in the fracture surface second site of interest, V1150 specimen

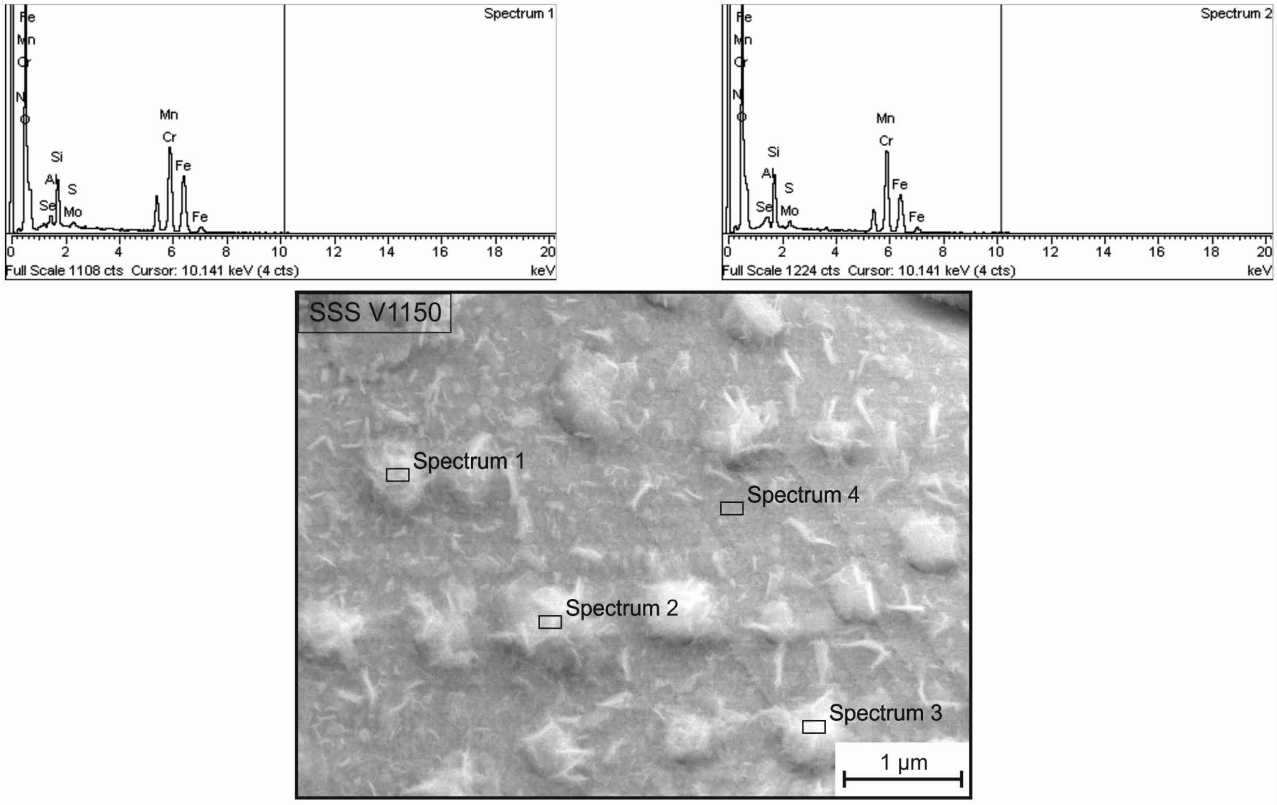

Metallic elements only										
Spectrum	Si	Cr	Mn	Al	Mo	Se	Ti	S	Fe	Total
1 [at.-%]	11.78	13.12	39.67	2.80	--	--	--	--	32.63	100
2	14.93	9.19	45.03	3.52	1.22	1.17	--	--	24.96	100
3	14.22	12.46	43.41	1.53	1.21	--	--	--	27.18	100
4	0.95	17.13	28.38	--	0.95	--	--	--	52.59	100

All elements												
Spectrum	N	O	Si	Cr	Mn	Al	Mo	Se	S	Ti	Fe	Total
1 [at.-%]	--	55.73	4.86	5.91	17.78	1.16	--	--	--	--	14.55	100
2	1.80	59.57	5.35	3.61	17.75	1.24	0.42	0.40	--	--	9.84	100
3	--	58.95	5.44	5.19	18.05	0.59	0.48	--	--	--	11.30	100
4	3.11	23.84	0.76	14.01	14.59	--	0.77	--	--	--	42.93	100

Figure B. 66.: EDX analysis results of the angular particulates on sintering neck surface second site of interest, V1150 specimen

References

[1] H. Berns and V. G. Gavriljuk. "High nitrogen steels: Structure, properties, manufacture, applications". Springer, Berlin, Germany, 1 edition (1999).

[2] S. Riedner. "Hochfeste nichtrostende austenitische CrMn-Stähle mit (C+N)". PhD thesis, Ruhr-Universität, Bochum, Germany (2010).

[3] H. Berns and W. Theisen. "Eisenwerkstoffe: Stahl und Gusseisen". Springer, Berlin, Germany, 4 edition (2008).

[4] H. Berns; B. Hussong; S. Riedner, and F. Wischnowski. Effect of Carbon on Stainless Austenitic CrMnCN Steel Castings. Steelresearch Journal **2010** (02.12.2010) 3, page 245–250.

[5] S. Riedner; N. Nabiran, and H. Berns, editors. "Stainless austenitic steel with 0.85 mass% C+N for castings", Proceedings of 10-th International Conference on High Nitrogen Steels, Moscow, Russia (2009).

[6] H. Berns and V. G. Gavriljuk, editors. "Stainless Austenitic Steel of Superior Strength", International Conference on Super-high Strength Steels, Rom, Italy (2005).

[7] B. D. Shanina; V. G. Gavriljuk; A. Konchits, and S. P. Kolesnik. The Influence of Substitutional Atoms upon the Electron Structure ot the Iron-based Transition Metal Alloys. Journal of Physics-Condensed Matter **1998** 10, page 1825–1838.

[8] R. M. German. "Powder metallurgy and particulate materials processing: The processes, materials, products, properties, and applications". Metal Powder Industries Federation (2005).

[9] W. Schatt and K. Weiters. "Pulvermetallurgie: Technologien und Werkstoffe". VDI-Verlag, Düsseldorf, Germany (1994).

[10] G.C Kuczynski, editor. "Sintering and related phenomena: Proceedings of the third International conference on sintering and related phenomena", International Conference of Sintering, University of Notre Dame, France (1972).

[11] D. Stöver. Pulvermetallurgie. Script (2010).

[12] E. Hryha and E. Dudrova. The Sintering Behaviour of Fe-Mn-C Powder System, Correlation between Thermodynamics and Sintering Process, Manganese Distribution and Microstructure. Materials Science Forum **2007** 534-536, page 761–764.

[13] W. Schatt. "Sintervorgänge: Grundlagen". VDI-Verlag, Düsseldorf, Germany (1992).

[14] S. Weber. "Gezielte Ausnutzung des Stofftransportes zur Herstellung neuartiger PM-Hartverbundwerkstoffe auf Eisenbasis". PhD thesis, Ruhr-Universität, Bochum, Germany (2005).

[15] R. M. German. Supersolidus liquid-phase sintering of prealloyed powders: Metallurgical And Materials Transactions. A-Physical Metallurgy And Materials Science **1997** 28.

[16] R. M. German. An Update on the Theory of Supersolidis Liquid Phase Sintering. Publication (2007).

[17] D. Chasoglou; E. Hryha, and L. Nyborg, editors. "Effect of Atmosphere Composition on the Surface Interactions during Sintering of Chromium-alloyed PM Steels", Euro PM2011, Barcelona, Spain (2011).

[18] H. Karlsson. "Role of Surface Oxides in Sintering of Chromium-Alloyed Steel Powder". PhD thesis, Chalmers University of Technology, Gothenburg, Sweden (2005).

[19] A. Weddeling. Surface Analysis of Austenitic Fe-18Cr-19Mn-C-N Powder. Bachelor Thesis (2011).

[20] D. Chasoglou. Surface Characteristics of Water Atomized Pre-alloyed Steel Powders and their effect on Sintering. (2010).

[21] D. Chasoglou; E. Hryha, and L. Nyborg, editors. "Surface Interactions During Sintering of Chromium-alloyed PM Steels in Different Atmospheres", PM2010 World Congress, Florence, Italy (2010).

[22] D. Chasoglou; E. Hryha, and L. Nyborg, editors. "Oxide Distribution in Prealloyed Water Atomized Steel Powder", PM2010 World Congress, Florence, Italy (2010).

[23] E. Hryha. Surface composition of steel powders prealloyed with manganese. Applied Surface Science **2010** 256, page 3946–3961.

[24] E. Hryha and L. Nyborg, editors. "Oxide Transformation During Sintering of Cr and Mn Prealloyed Water Atomized Steel Powder", Euro PM2011, Barcelona, Spain (2011).

[25] E. Hryha and L. Nyborg, editors. "Surface Analysis of Prealloyed Steel Powders: Qualitative and Quantitative Aspects", PM2010 World Congress, Florence, Italy (2010).

[26] J. Moulder; W. Stickle; P. Sobol, and K. Bomben. Handbook of X-ray Photoelectron Spectroscopy. (1992).

[27] A. Klein. Grundlagen der Röntgenphotoelektronenspektroskopie. Script (2008).

[28] J. Watts and J. Wolstenholme. "Surface Analysis by XPS and AES". John Wiley & Sons Ltd., West Sussex, England (2003).

[29] J. Goldstein. Scanning electron microscopy and x-ray microanalysis: a text for biologists, materials scientists, and geologists. Plenum Press New York **1992** 2, page 23–27.

[30] L. Reimer. "Scanning Electron Microscopy". Springer, Berlin, Germany (1985).

[31] Zeiss GmbH. Handbuch für die Rasterelektronenmikroskope SUPRA(VP) und ULTRA.

[32] Eltra GmbH. Spezifikationen ONH 2000.

[33] N. J. Bernauer. "Einfluss von Kohlenstoff als Legierungselement in stickstofflegierten Chrom-Mangan-Stählen". PhD thesis, ETH Zurich, Zurich, Swiss (2004).

[34] K. Zumsande; A. Weddeling; E. Hryha; S. Huth; L. Nyborg; S. Weber; N. Krasokha, and W. Theisen. Characterisation of the surface of Fe-19Mn-18Cr-C-N during heat treatment in nitrogen atmosphere - an XPS study. **2012**.

[35] E. Dudrova and M. Kabatova. Fractography of Sintered Iron and Steels. Powder Metallurgy Progress **2008** 2, page 59–75.

[36] E. Hryha and L. Nyborg, editors. "Oxide Transformation During Sintering Of Prealloyed Water Atomized Steel Powder", Florence, Italy (2010).

[37] E. Hryha and E. Dudrova. "Application of Thermodynamics to Biological and Materials Science: The Sintering Behaviour of Fe-Mn-C Powder System, Correlation between Thermodynamics and Sintering Process, Manganese Distribution and Microstructure Composition, Effect of Alloying Mode". INTECH (2011).